INAUGURAL-DISSERTATION

zur
Erlangung der Doktorwürde
der
Gesamtfakultät für Mathematik,
Ingenieur- und Naturwissenschaften
der
Ruprecht-Karls-Universität
Heidelberg

vorgelegt von

Finn Luca Sebastian

Tag der mündlichen Prüfung
10.10.2025

Raman and Chiroptical Spectroscopy of Carbon Nanotubes with Luminescent Defects

Gutachter

Prof. Dr. Jana Zaumseil

Prof. Dr. Ralph Krupke

Abstract

Semiconducting single-wall carbon nanotubes (SWCNTs) – nanoscale cylinders made entirely of carbon – hold potential for optoelectronics, optical biosensors, and high-contrast imaging due to their stable and narrowband near-infrared (NIR) photoluminescence (PL). Upon covalent chemical modification with luminescent defects, the optical properties of SWCNTs can be significantly enhanced as new red-shifted excitonic emission features lead to increased PL quantum yields (PLQYs) and enable room-temperature single-photon emission. The continuous development of synthetic protocols for functionalization in aqueous environments and organic solvents has created numerous methods for tailoring the optical properties of SWCNTs to achieve specific properties. Far less progress has been made with regard to the methods for precise spectroscopic characterization of luminescent defects. Their density and distribution on the nanotube lattice is typically unknown. However, integration of SWCNTs into devices, single-photon sources and diagnostic tools requires precisely defined properties, *e.g.*, single defects on individual SWCNTs to ensure sufficient purity of quantum emission. In addition to metrological aspects, the identification of parameters which determine sample performance can guide the rational design of synthetic strategies for brighter SWCNTs and discovery of novel properties of luminescent defects.

This thesis introduces a robust method for the absolute quantification of luminescent defects in SWCNTs. Based on Raman spectroscopy and spectrally resolved PLQY measurements in combination with exciton diffusion models, this approach facilitates the identification of samples with maximum brightness for imaging applications or single defects for quantum light sources. The systematic study of small-diameter SWCNT species at different Raman laser excitation wavelengths yields a unified empirical expression, which enables the assessment of defect densities in a straightforward and reproducible manner for any excitation energy, and reveals a strong dependence of the defect-related Raman response on nanotube diameter. It is further shown that this absolute quantification approach can be used to distinguish different types of luminescent defects and to determine the presence of oxygen defect clusters as opposed to individual aryl defects on the nanotube lattice. Building upon the identification of favorable reaction conditions, photocatalysis is explored for functionalization of SWCNTs with luminescent oxygen defects. This strategy facilitates the introduction of a large number of luminescent defects with uniform binding configuration in concentrated samples, which makes them accessible for chiroptical spectroscopy. Consequently, this enables the first observation of chiral, defect-localized excitonic states in SWCNTs.

Kurzfassung

Halbleitende einwandige Kohlenstoffnanoröhren (engl. *single-wall carbon nanotubes*, SWCNTs) – nanoskalige, zylindrische Strukturen aus Kohlenstoff – besitzen aufgrund ihrer stabilen und schmalbandigen Photolumineszenz (PL) im nahen Infrarotbereich (NIR) großes Potenzial für den Einsatz in optoelektronischen Bauelementen, als optische Sensoren und für die medizinische Bildgebung. Durch chemische Funktionalisierung mit lumineszenten Defekten können die optischen Eigenschaften von SWCNTs dabei erheblich verbessert werden, wobei neue, rotverschobene Emissionsbanden zu erhöhten PL-Quantenausbeuten (engl. *PL quantum yields*, PLQYs) führen und Einzelphotonenemission bei Raumtemperatur ermöglichen. Die stetige Entwicklung neuer Synthesemethoden für Dispersionen von SWCNTs in wässriger Umgebung oder organischen Lösemitteln hat dabei vielseitige Möglichkeiten zur gezielten Veränderung ihrer optischen Eigenschaften hervorgebracht. Weitaus weniger Fortschritte wurden jedoch bei der Entwicklung von Methoden zur spektroskopischen Charakterisierung lumineszenter Defekte erzielt. In der Regel ist daher die genaue Dichte und Verteilung der Defekte auf den funktionalisierten Kohlenstoffnanoröhren unbekannt. Für die Verwendung von SWCNTs in elektronischen Bauelementen, als Einzelphotonenquellen oder als optische Sensoren sind jedoch präzise definierte Eigenschaften erforderlich, so z. B. einzelne Defekte auf SWCNTs, um eine ausreichende Reinheit der Einzelphotonenemission zu gewährleisten. Ein besseres Verständnis der Verteilung und Struktur lumineszenter Defekte kann zudem zur Entwicklung von Synthesestrategien beitragen, um die Helligkeit von SWCNTs weiter zu verbessern und neue Eigenschaften von Defekten zu ermitteln.

Die vorliegende Arbeit führt eine robuste Methode zur absoluten Quantifizierung von lumineszenten Defekten in SWCNTs ein. Basierend auf Raman-Spektroskopie und spektral aufgelösten PLQY-Messungen ermöglicht dieser Ansatz in Kombination mit Exzitonen-Diffusionsmodellen die direkte Identifizierung von Proben mit einzelnen Defekten für den Einsatz als Einzelphotonenquellen, oder solchen mit maximaler Helligkeit für die Anwendung in der biologischen Bildgebung. Weiterhin führt eine systematische Untersuchung von SWCNT-Spezies mit kleinen Durchmessern bei verschiedenen Anregungswellenlängen in Raman-Messungen zu einem empirischen Ansatz für die Bestimmung der Defektdichten für verschiedene Anregungsenergien. Dabei zeigt sich eine deutliche Abhängigkeit der defektspezifischen Raman-Aktivität vom Durchmesser der Nanoröhren. Dieser universelle Ansatz zur absoluten Quantifizierung von Defekten eignet sich außerdem zur Unterscheidung verschiedener Arten von lumineszenten Defekten. Für Sauerstoffdefekte kann

dabei eine Tendenz zur Bildung lokaler Cluster festgestellt werden, wohingehen Aryl-Defekte isoliert auf Kohlenstoffnanoröhren auftreten. Darüber hinaus werden erstmalig photokatalytische Reaktionen, welche unter milden und präzise kontrollierbaren Reaktionsbedingungen ablaufen, zur Funktionalisierung von SWCNTs mit lumineszenten Sauerstoffdefekten untersucht. Diese Strategie ermöglicht die Einführung einer großen Anzahl von Defekten mit einheitlicher Bindungskonfiguration in konzentrierten Dispersionen, wodurch diese für chiroptische Spektroskopie zugänglich werden. Die hierbei erstmals beobachtete optische Aktivität von Defekt-Exzitonen zeigt, dass sich die chiralen Eigenschaften von Kohlenstoffnanoröhren auch in lokalisierten exzitonischen Zuständen wiederfinden.

Danksagung

Diese Dissertation wurde erst durch die Beiträge zahlreicher wunderbarer, hilfsbereiter Menschen möglich, denen ich im Folgenden danken möchte.

An erster Stelle gilt mein Dank **Prof. Dr. Jana Zaumseil** für die herzliche Aufnahme in ihrer Arbeitsgruppe und die großartige Unterstützung während der Anfertigung meiner Doktorarbeit. Ich danke Dir für das mir entgegengebrachte Vertrauen, die beispiellose Gestaltungsfreiheit, die Du mir in all meinen Forschungsprojekten ermöglicht hast, sowie die Chance zur Teilnahme an zahlreichen internationalen Konferenzen und Mitwirkung bei so vielen spannenden Kollaborationen. Es hat mir große Freude bereitet, Mitglied Deiner Gruppe zu sein.

Herzlich bedanken möchte ich mich außerdem bei **Prof. Dr. Ralph Krupke** für seine Bereitschaft, das Zweitgutachten dieser Arbeit zu übernehmen.

Ich danke allen ehemaligen und aktuellen Mitgliedern der Arbeitsgruppe **Nanomaterials for Optoelectronics** für die tolle Zusammenarbeit, den regen Austausch und die schöne gemeinsame Zeit. Ein besonderer Dank geht an das **TRIFECTs Team** um **Ali**, **Felix**, **Nicolas**, **Sonja**, **Simon** und **Sebastian**, das ich zu meiner großen Freude als neuestes und letztes Mitglied komplettieren durfte. Ihr habt unsere gemeinsamen Projekte, aufschlussreichen Diskussionen und unterhaltsamen Konferenzreisen zu den besten Erfahrungen meiner Promotion gemacht und wart immer Garanten für gute Laune. **Simon** möchte ich zudem für das Korrekturlesen dieser Arbeit danken.

Für ihre Motivation, Kreativität und Mithilfe geht mein herzlicher Dank an **Felicitas Becker**, **Leon Kaminski**, **Lukas Siegel**, **Hiroyuki Fujinami** und **Pylyp Filippov**, deren Forschungsarbeiten ich betreuen und begleiten durfte.

Danken möchte ich außerdem allen Kooperationspartnern für ihren Beitrag zu dieser Arbeit und für die spannenden Projekte, die wir gemeinsamen angestoßen haben. Im Besonderen gilt mein Dank **Dr. Han Li** (Universität Turku) und **Dr. Benjamin S. Flavel** (Karlsruher Institut für Technologie) sowie **Dr. Somen Nandi** und **Dr. Laurent Cognet** (Universität Bordeaux). **Dr. Clement Deleau** und **Dr. Yuichiro Kato** (RIKEN, Wako, Japan) sowie **Dr. Yohei Yomogida** (Universität Hokkaidō, Sapporo, Japan) und **Prof. Dr. Kazuhiro Yanagi** (Tokio Metropolitan Universität, Hachiōji, Japan) möchte ich herzlich für ihre wunderbare Gastfreundschaft und die produktive Zusammenarbeit danken.

Bei allen Mitarbeiterinnen und Mitarbeitern des Lehrstuhls für Angewandte Physikalische Chemie bedanke ich mich für die tatkräftige Unterstützung. Insbesondere **Joachim Eger-Constantin**, **Peter Jeschka**, **Günter Meinusch** und **Ali Ghajar** waren stets eine große Hilfe bei Reparaturen und technischen Fragen aller Art. Weiterhin bedanken möchte ich mich bei **Klaus Schmitt** und den Mitarbeitern der **Feinmechanischen Werkstatt** für die Beratung und Anfertigung technischer Bauteile für die vielzähligen Projekte. **Anja Ihli**, **Isabella Haffelder**, **Tatjana Enns**, **Karin Jordan** und **Benjamin Scherke** danke ich für ihre Hilfe bei administrativen Fragen sowie die schnelle und verlässliche Versendung zahlreicher Pakete mit Proben.

Ganz besonders dankbar bin ich für die wunderbaren Freundschaften, die die vergangenen Jahre geprägt haben. **Christoph**, **Felix**, **Leon**, **Nils**, **Paul**, **Timon**, **Valentin**, **Annika**, **Sophie**, **Aleks** und **Simon**, ich kann Euch nicht genug danken für die unzähligen lustigen Erlebnisse, die hoffentlich niemals endenden Running Gags, all die Reisen, Spieleabende und gemeinsamen Jahreswechsel.

Meinen Eltern **Gerlinde** und **Jörg** und meinem Bruder **Mika** bin ich von ganzem Herzen dankbar für ihre Gelassenheit, Ruhe und unermüdliche Unterstützung. Mein allergrößter Dank aber gilt Dir, **Constanze**, für all die wunderschönen Momente und Deinen bedingungslosen Rückhalt. Danke, dass Du immer für mich da bist, und ich blicke voller Vorfreude auf alles, was wir noch zusammen erleben und entdecken werden.

Contents

Abstract I

Kurzfassung III

Danksagung V

Contents VII

1 Introduction 1

2 Background 5

2.1 Single-wall carbon nanotubes 5

2.1.1 Structure 6

2.1.2 Synthesis 7

2.1.3 Purification and sorting 8

2.1.4 Electronic structure 12

2.1.5 Optical properties and excitons 15

2.1.6 Circular dichroism 19

2.2 Luminescent defects 22

2.2.1 Exciton dynamics and optical properties 23

2.2.2 Role of defect structure 27

2.2.3 Covalent functionalization of SWCNTs 28

2.2.4 Oxygen defects 31

2.3 Raman spectroscopy of SWCNTs 34

2.3.1 Phonon structure 34

2.3.2 Raman scattering processes 35

2.3.3 Defect characterization and quantification 41

3 Unified quantification of luminescent defects in SWCNTs 45

4 Spectroscopic identification of defect clustering in SWCNTs 77

5 Photocatalytic creation and circular dichroism of luminescent defects 113

6 Conclusion and Outlook 161

Abbreviations 171

Bibliography 173

Eidesstattliche Versicherung 201

1 Introduction

Numerous fundamental advances in information, telecommunication, and imaging technology have been enabled by the discovery, characterization, and deterministic modification of bulk and low-dimensional materials with unique optical and electronic properties. For optical fiber technology and biological imaging, semiconducting materials that emit light in the near-infrared (NIR) spectral region from 1.0 - 1.6 μm are particularly relevant due to minimized optical attenuation and optimal biological tissue transparency.[1] NIR-light sources such as inorganic III-V compound semiconductors, lanthanide complexes, and halide perovskites offer limited tunability and their fabrication requires scarce resources or toxic chemicals,[2,3] while small organic molecules often suffer from insufficient long-term photostability.[4] Simultaneously, the rising demand for NIR single-photon sources in quantum communication applications[5] and customizable emitters for medical diagnostics[6] calls for the development of more emitters with increased versatility and well-defined optical properties.

Owing to their narrowband photoluminescence (PL) in the NIR and high ambipolar charge carrier mobilities, single-wall carbon nanotubes (SWCNTs) are promising candidates for the applications outlined above. They combine mechanical flexibility with processability in aqueous and organic solvents.[7,8] Semiconducting SWCNTs exist as a variety of different species with distinct diameters and optical band gaps, depending on the precise structure of the hexagonal, sp^2-hybridized carbon lattice. With high specific surface areas and exceptional stability under prolonged optical or electrical excitation, they are ideal targets for the development of tunable and robust NIR-light sources. In super-resolution microscopy (SRM), which has been established for emitters in the visible spectral region, SWCNTs could offer unprecedented deep tissue penetration with spatial resolution beyond the diffraction limit.[9] The highly exposed sidewalls of and reduced dielectric screening in one-dimensional SWCNTs lead to a pronounced dependence of the NIR emission energy and intensity on the surrounding environment, making specifically functionalized SWCNTs a powerful framework for optical (bio)sensors.[10] However, these advantages come along with a fundamental limitation of the nanotube NIR emission efficiency. The sensitivity to dielectric perturbations, high charge carrier mobilities, and fast diffusion of excited electron-hole pairs (excitons) to quenching sites result in low PL quantum yields (PLQYs) of <1% in dispersion and approximately ten-fold lower PLQYs are observed for solid-state, thin films of SWCNTs.[11]

However, the discovery of luminescent defects created by controlled covalent modification of SWCNTs has opened up one pathway to increased PLQYs. Upon local incorporation of atomic oxyen defects in the nanotube lattice *via* oxidation or covalent attachment of aryl compounds, energetically lower-lying potential wells are created, which efficiently trap fast-diffusing band-edge excitons. Optical emission from these states occurs with significantly longer PL lifetimes and at further red-shifted emission wavelengths.[12,13] Of particular interest is the quasi zero-dimensional nature of these defect states, *i.e.*, one luminescent defect state can only be populated with one exciton at a time. With optical trap depths of hundreds of meV, this enables the observation of room-temperature single-photon emission (SPE),[14] which is a prerequisite for efficient quantum key distribution and computing technology with low energy consumption.[15,16]

The availability of purified, high-quality semiconducting SWCNTs from different liquid-phase sorting methods has significantly contributed to progress in the field of luminescent defects.[17,18] Synthetic protocols for the functionalization of SWCNTs have advanced to the point where different defect types with distinct binding configurations can be introduced selectively to the SWCNT lattice in aqueous environments and organic solvents. However, the exact number of defects or their distribution on the SWCNTs is usually not known, which presents a significant challenge for the identification of samples for SPE or with precise numbers of binding sites for molecular analytes. Additionally, systematic studies of the relation between reaction conditions and nanotube PL brightness as well as defect density and distribution could guide the rational development of synthetic strategies for achieving even higher PLQYs, better biocompatibility, and improved selectivity towards binding configurations for NIR emission at wavelengths in the telecom range. The work presented in this thesis addresses several of the challenges outlined above by combining previously established spectroscopic techniques and newly developed metrological approaches for the study of pristine and functionalized SWCNTs. Furthermore, a new synthetic method for controlled nanotube functionalization is presented and applied to uncover the chiroptical properties of luminescent defects. The structure of this thesis is briefly outlined below.

Chapter 2 provides an introduction to the fundamental principles, theoretical concepts, and current state of the research area of SWCNTs, their optical and chiroptical properties, as well as luminescent nanotube defects. Particular attention is paid to Raman spectroscopy as a versatile and sensitive tool for the characterization of pristine and functionalized SWCNTs. Partially influenced by experimental work carried out before and in the beginning of this dissertation project,[19] **Chapter 3** explores

the development of a unified method for the quantification of luminescent defects. Inspired by the seminal work on graphene, a systematic and combined study of the Raman response and PLQYs of pristine and functionalized SWCNTs identifies a linear relation between defect density and integrated Raman D/G^+ intensity ratios. The application of the developed metric at different Raman excitation laser energies and to several small-diameter SWCNT species reveals that the Raman response of defect-related phonon modes strongly depends on the nanotube diameter. Additionally, intermediate frequency modes in the low-frequency region of Raman spectra are analyzed and unambiguously assigned to defect-activated phonon modes. These findings present both a starting point for future theoretical studies and a straightforward practical method for the characterization of luminescent defects.[20]

A comparative study of previously developed functionalization methods already provides valuable insights into the structure and distribution of luminescent defects in SWCNTs, as detailed in **Chapter 4**. The absolute quantification and comparison of luminescent oxygen and aryl defects, introduced by a variety of chemical approaches, indicates that functionalization methods based on reactive oxygen species exhibit a strong tendency for the formation of clusters of closely spaced oxygen defects. In comparison, aryl defects are more likely to occur as individual, evenly spaced defects. PL measurements of individual oxygen-functionalized SWCNTs at cryogenic temperature enable a statistical determination of absolute defect numbers and support the hypothesis of oxygen defect clusters.[21]

Chapter 5 builds on the identification of favorable reaction conditions for the creation of luminescent oxygen defects. Using photocatalysis with suitable anthraquinone derivatives, oxygen defects can be introduced in a controlled and selective procedure without the need for toxic compounds or metal ions. In addition to PLQYs as high as 3.6% in aqueous dispersions, the presented approach enables the direct functionalization of SWCNTs wrapped by biocompatible polymers. It is also applicable to organic solvent dispersions and even suitable for the spatially controlled introduction of luminescent defects in SWCNT thin films. By functionalization of concentrated dispersions of sorted carbon nanotube enantiomers, they become accessible for chiroptical spectroscopy and the observation of optical activity in zero-dimensional defect states. This enables the direct spectroscopic determination of the relative size of free band-edge and trapped defect excitons from absorption dissymmetry factors.[22]

Chapter 6 summarizes and discusses the obtained results in a broader context of the research area and identifies open questions and possible future objectives.

2 Background

This Chapter outlines the fundamental concepts and current state of research, which this thesis builds upon. Following an introduction to structure, synthesis and purification of single-wall carbon nanotubes, their electronic, optical and chiroptical properties are described. The second section covers the creation and photophysics of luminescent nanotube defects. Finally, Raman spectroscopy is introduced as an essential technique for the characterization of pristine and functionalized carbon nanotubes.

2.1 Single-wall carbon nanotubes

The continuous downscaling of electronic and photonic devices has created a demand for materials with sub-nanometer thickness and atomically defined structures.[23–26] Naturally, a classification of such low-dimensional materials into zero-, one-, and two-dimensional structures (0D, 1D, and 2D, respectively) depending on their size and aspect ratio has emerged. Low-dimensional allotropes of carbon have been a particular focus of fundamental and applied nanomaterial research in recent decades, as they are synthetically accessible from a variety of carbon sources and present a versatile platform for chemical functionalization.[27] The discovery of the 2D carbon allotrope graphene in 2004 established the field of 2D materials,[28] which since has shifted its focus from processing and characterization of single 2D sheets[29,30] to the engineering of stacked heterostructures with intriguing electronic and optical properties.[31–34] The spherical fullerenes, theoretically predicted in 1970 and first synthesized in 1985,[35,36] are commonly regarded as 0D structures and investigated as components for photovoltaic cells,[37] nanoelectronics[38] and biomedicine.[39] Among 1D carbon allotropes, graphene nanoribbons and single-wall carbon nanotubes (SWCNTs) stand out due to their diversity in geometrical and electronic structure.[27,40] Since the discovery of SWCNTs in 1991,[41] research efforts have aimed to exploit their charge transport properties for transistor technology,[42,43] their mechanical strength for lightweight and durable fiber-based materials,[44,45] and their high Seebeck coefficients for thermoelectric heat conversion.[46,47] Additionally, SWCNTs are investigated as candidates for light-emitting devices,[48,49] quantum optics,[50–52] and healthcare applications such as drug delivery,[53] metabolite sensing,[10] or high-contrast tissue imaging.[54,55]

2.1.1 Structure

SWCNTs are hollow cylinders of sp^2-hybridized carbon atoms arranged in a hexagonal lattice. With typical lengths of several hundred nm and diameters on the order of 1 nm, they are classified as 1D materials.[7,56] Conceptually, SWCNTs can be viewed as rolled-up sheets of graphene. Depending on the connection pattern of carbon atoms, which is created in this roll-up process, structurally different SWCNT species are obtained. These species are defined by a circumferential roll-up vector $\vec{C}_h$, which connects superposed carbon atoms, and is expressed as a linear combination

$$\vec{C}_h = n\vec{a}_1 + m\vec{a}_2, \tag{2.1}$$

where n, m are integers and $\vec{a}_1$, $\vec{a}_2$ denote the primitive unit vectors of the graphene lattice. $\vec{a}_1$ and $\vec{a}_2$ have lengths of $a = 0.246\,nm$, as derived from the carbon-carbon bond length $a_{C\text{-}C} = 0.142\,nm$ in graphene according to $a = \sqrt{3}\,a_{C\text{-}C}$.[57] Irrespective of stereochemical aspects, SWCNTs with distinct integer pairs (n, m) are termed "chiralities". The diameter d_t and chiral angle θ ($\angle(\vec{C}_h, \vec{a}_1)$) of a specific chirality can be calculated according to[57,58]

$$d_t = \frac{|\vec{C}_h|}{\pi} = \frac{a\sqrt{n^2 + nm + m^2}}{\pi} \tag{2.2}$$

and

$$\cos\theta = \frac{2n + m}{2\sqrt{n^2 + nm + m^2}}. \tag{2.3}$$

The periodic lattice geometry along the longitudinal SWCNT axis is defined by the translation vector $\vec{T}$, which denotes the smallest graphene lattice vector orthogonal to $\vec{C}_h$. Consequently, d_t and $\vec{T}$ define the SWCNT unit cell, which differs in size depending on the chiral indices (n, m). The construction of (6,5) and (5,5) SWCNTs from the sp^2-hybridized graphene lattice is depicted exemplarily in Figure 2.1.

Owing to their hexagonal lattice geometry, unique SWCNT chiralities (n, m) are obtained only for chiral angles θ between 0° and 30°. In the case of $\theta = 0°$, the resulting SWCNTs with $(n, 0)$ are called zigzag, whereas armchair SWCNTs are characterized by $\theta = 30°$ and equal chiral indices (n, n). From a stereochemical perspective, zigzag and armchair carbon nanotubes are achiral. In contrast, SWCNTs with $0° < \theta < 30°$ are chiral with enantiomeric pairs (n, m) and $(n+m, -m)$. Chapter 2.1.6 is dedicated to a discussion of the resulting optical activity and circular dichroism of SWCNT enantiomers.

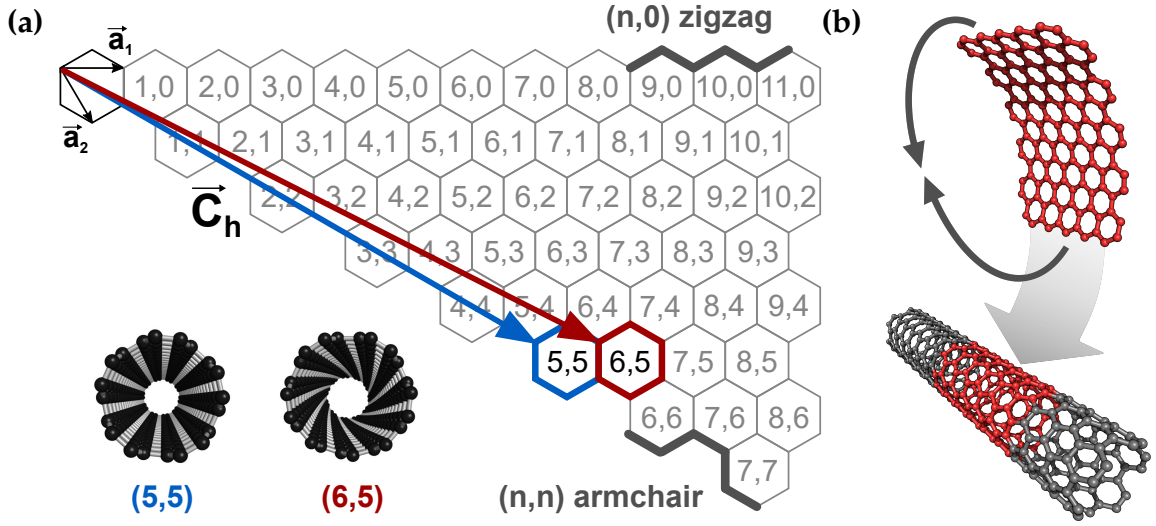

Figure 2.1: (a) Distinct species of SWCNTs are conceptually obtained from superposing different carbon atoms in a roll-up process of the flat graphene lattice. The corresponding roll-up vector $\vec{C}_h$ is a linear combination of the primitive lattice vectors $\vec{a}_1$ and $\vec{a}_2$. The respective scalars define the indices used to label the generated SWCNT species. The achiral and chiral geometry of (5,5) (blue) and (6,5) (red) SWCNTs, respectively, can be inferred directly from the existence or absence of mirror planes in their molecular structure (bottom left). Roll-up directions that result in zigzag and armchair SWCNTs are indicated in gray. **(b)** Visualization of the theoretical roll-up process to generate SWCNTs from a graphene sheet.

2.1.2 Synthesis

The production of SWCNTs on a commercial scale is based on the evaporation or the decomposition of gaseous carbon sources at elevated temperatures to achieve nanotube growth from catalyst nanoparticles.[59,60] Operating at temperatures above 1200 °C, arc discharge,[61,62] laser ablation,[63–65] and plasma torch[66] syntheses generally produce SWCNTs with diameters of $\approx 1-2$ nm. While high-quality SWCNTs can be obtained with these methods, they are difficult to scale up and have high resource demands.[60] For these reasons, high-temperature processes were gradually replaced by chemical vapor deposition (CVD) synthesis, which offers improved scalability and typically proceeds at temperatures <1200 °C with a lower boundary of $\approx$ 550 °C.[67] In CVD synthesis, particles of catalytically active transition metals, *e.g.*, Fe, Ni, Co or corresponding alloys are exposed to gaseous hydrocarbons such as methane, acetylene, or carbon monoxide.[59,68,69] Following decomposition of the carbon precursors, hemispherical, fullerene-like cap structures nucleate at the catalyst surface and the emerging nanotubes elongate upon continuous carbon supply to the SWCNT-catalyst interface.[70] SWCNTs are obtained for catalyst particle sizes of few nanometers, whereas larger particles promote the growth of multi-wall carbon nanotubes (MWCNTs).[59] Prior lithographic patterning of the catalyst enables spatial control over nucleation sites, and even free-standing SWCNTs spanning across

pillars or trenches can be generated.[71,72] Among CVD methods, the HiPCO (high-pressure carbon monoxide) and CoMoCAT (cobalt-molybdenum catalyst) process have found widespread use for large-scale production of small-diameter SWCNTs. In the HiPCO process, carbon monoxide is employed as carbon source and converted at elevated pressure ($1 - 10\,\text{atm}$) by catalyst particles formed from thermal decomposition of iron pentacarbonyl ($Fe(CO)_5$) at $800 - 1200\,°C$. This method produces SWCNTs with diameters ranging from 0.8 nm to 1.3 nm.[73,74] The CoMoCAT process utilizes a bimetallic cobalt-molybdenum alloy catalyst on SiO_2 or MgO carriers at temperatures ranging from $700 - 950\,°C$. Under these conditions, SWCNTs with a narrow diameter distribution of $0.7 - 1.0\,\text{nm}$ are obtained.[75] While the choice of carbon precursor and catalyst support affects the outcome in terms of chirality and diameter distribution,[76,77] the CoMoCAT process predominantly leads to the growth of (6,5) and (7,5) SWCNTs, with a minor presence of (8,4), (8,3), (7,6) and (6,4) species.[78] Post-synthetic processing usually involves treatment with hydrofluoric acid to dissolve the catalyst substrate.[77,78]

Advances in carbon nanotube CVD synthesis were closely accompanied by theoretical attempts to elucidate the underlying nucleation and growth mechanisms.[70,79–84] While many complex aspects of SWCNT growth dynamics remain unresolved, it is evident that initial stages of nanotube formation are largely stochastical in nature and shaped by high configurational entropy as well as strong fluctuations regarding nanotube structure.[82,83] Thus, even precisely controlled reaction conditions yield mixtures of SWCNTs with respect to chirality, length, diameter and electronic type (semiconducting or metallic),[85] while more selective processes based on template molecules[86] or solid-state catalysts[87,88] only provide access to specific species in higher purity. Consequently, protocols for SWCNT purification and sorting are required in order to make them accessible for (opto-)electronic and biomedical applications.

2.1.3 Purification and sorting

The raw soot obtained during SWCNT growth usually also contains residual catalyst particles and amorphous carbon. The SWCNTs form bundles held together by strong van der Waals interactions between the extended π-systems of individual nanotubes. Thus, purification of the raw material is required and, depending on the desired application, sorting of SWCNTs by electronic type, diameter or even species is necessary.[89] Due to the small entropy of mixing, SWCNTs are virtually insoluble in common solvents or solvent systems. Few solvents such as *N*-methyl-2-pyrrolidone and *N*-cyclohexyl-2-pyrrolidone can provide some limited dispersion stability.[90–92] Thus, the standard approach for liquid-phase processing of SWCNTs is the addition

of stabilizers or surfactants that prevent re-aggregation after debundling of SWCNTs by sonication (bath sonication, tip sonication[93]) or mechanical shearing (stirring,[94] shear force mixing[95]). The dispersion step is typically followed by centrifugation to separate remaining SWCNT bundles and other impurities as sediment, while the supernatant contains the dispersed SWCNTs. Selectivity for the electronic type, diameter or nanotube species is introduced either by use of selective dispersion agents or post-dispersion sorting techniques.

In organic solvents, typically toluene or *ortho*-xylene, dispersions of semiconducting SWCNTs with exceptional purity can be obtained by selective polymer wrapping with polyfluorene-, polythiophene-, or polycarbazol-derived (co)polymers.[96–100] Initially reported by Nish *et al.*,[101] this process combines dispersion and sorting in a single step, as the polymer exhibits a high affinity for distinct nanotube species. Figure 2.2a schematically demonstrates the selective extraction of (6,5) and (7,5) SWCNTs from CoMoCAT material with poly[(9,9-dioctylfluorenyl-2,7-diyl)-*alt*-(6,6'-2,2'-bipyridine)] (PFO-BPy),[102] and poly(9,9-dioctylfluorene) (PFO),[101] respectively. While the structure-property relationships relevant to selective polymer wrapping are not fully understood, theoretical studies suggest that the polymer backbone facilitates π-electron interactions with the nanotube surface, whereas alkyl chains enable efficient steric stabilization in organic solvents of low polarity.[103,104] Particularly the integration in electronic devices requires high purities of semiconducting SWCNTs, a demand that is met by polymer wrapping which can achieve purities of up to 99.8% in a single separation step.[105] If carried out under mild exfoliation conditions, polymer wrapping can yield long SWCNTs ($\approx 1.6\,\mu$m) with only few defects and high photoluminescence quantum yields (PLQYs, $\approx 2\%$) suitable for use in light-emitting devices, as introduced by Graf *et al.*, who employed shear force mixing with PFO-BPy in toluene to prepare nearly monochiral dispersions of (6,5) SWCNTs.[11,95,106] A fundamental drawback of polymer wrapping is the limited range of wrapping polymers with selectivity towards distinct nanotube species. In contrast, the accessibility of virtually any SWCNT species present in the raw material is a major benefit of aqueous sorting techniques such as aqueous two-phase extraction (ATPE) or gel chromatography.

ATPE relies on the competition of different molecular surfactants for adsorption on SWCNT sidewalls, which directs the partitioning between a more hydrophobic upper phase and a more hydrophilic lower phase.[107–110] The phase boundary is formed due to the difference in density of two polymers (*e.g.*, poly(ethylene glycol (PEG), upper phase and dextran, lower phase), once their concentrations surpass a critical threshold. Upon addition of surfactant-covered SWCNTs, their partitioning

between the two phases is governed by the difference in chemical potential of each SWCNT species. This separation process can be described by the separation coefficient K_i, expressed as the ratio of concentrations in the upper phase ($c_{U,i}$) and lower phase ($c_{L,i}$):[109]

$$K_i = \frac{c_{U,i}}{c_{L,i}} = \exp\left(-\frac{\mu^0_{U,i} - \mu^0_{L,i}}{k_B T}\right). \tag{2.4}$$

Here, $\mu^0_{U,i}$ and $\mu^0_{L,i}$ denote the standard chemical potentials of the SWCNT species in the upper and lower phases, respectively, k_B is the Boltzmann constant and T the absolute temperature. The chemical potential of SWCNT species in the two phases is closely related to their coverage with surfactant molecules, and minor changes already strongly influence the partition coefficient. This effect can be utilized to select single species from a sample containing several chiralities. Most commonly, a binary surfactant system of the bile salt sodium deoxycholate (DOC) and sodium dodecyl sulfate (SDS) is employed for the separation of small-diameter SWCNT species, while ternary surfactant systems were shown to facilitate efficient separation of large-diameter species[111] and even carbon nanotube enantiomers.[112] The planar and rigid structure of DOC, an amphiphilic steroid compound, leads to dense packing of the molecule on the hydrophobic nanotube surface.[113,114] Exposure of the hydrophilic side of DOC to the surrounding aqueous environment enables efficient SWCNT dispersion, while small-diameter SWCNTs are covered preferentially by DOC.[115,116] The amphiphilic properties of SDS result from its polar, anionic head group connected to a non-polar alkyl chain, which adopts a longitudinal orientation on the nanotube surface to maximize van der Waals interactions.[117] In contrast to DOC, this preferential morphology of SDS layers on the SWCNT surface favors the coverage of larger-diameter species,[118] as a circumferential orientation of SDS molecules is energetically suppressed with increasing lattice curvature. At low concentrations, SDS molecules will assume a disordered and sparse coverage of the SWCNT sidewalls, but typical concentrations used in ATPE sorting exceed the critical micelle concentration (CMC) of SDS and lead to the formation of stabilizing micelles around SWCNTs.[118,119] In the actual ATPE process, increased coverage of SWCNTs with DOC leads to their transition to the lower, more hydrophilic phase containing dextran, whereas higher SDS coverage drives the respective species to the upper, more hydrophobic, PEG-rich phase.[109] For a schematic depiction of the ATPE sorting procedure, see Figure 2.2b. Initially, the SWCNT raw material is dispersed in DOC, followed by step-wise addition of SDS while the concentration of DOC is kept constant. SWCNTs with diameters larger than the targeted species are driven to the upper phase, which is subsequently replaced until the desired species is collected.

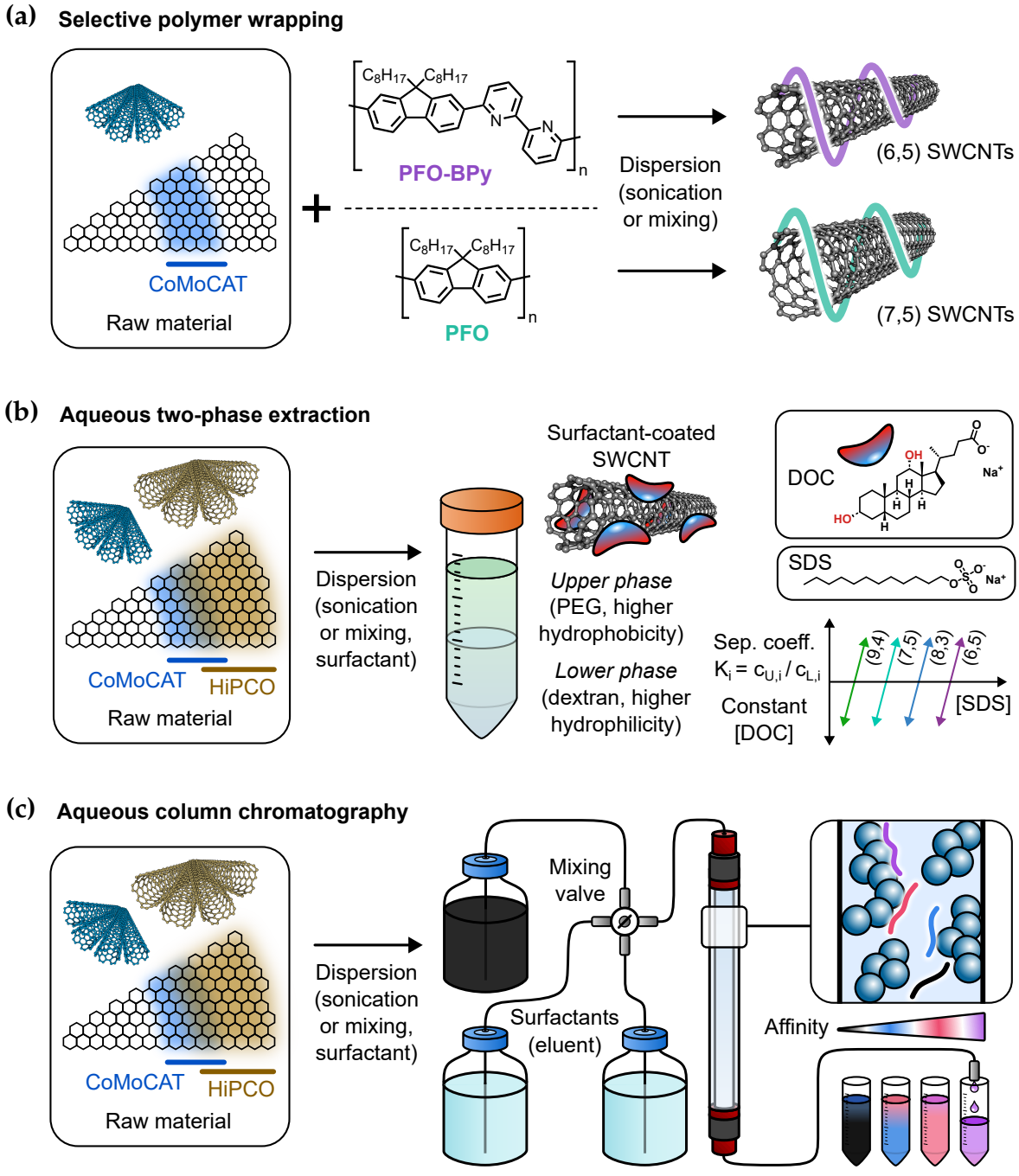

Figure 2.2: (a) Selective polymer wrapping to prepare SWCNT dispersions in organic solvents: CoMoCAT raw material and polyfluorene-based copolymers (PFO-BPy or PFO) are combined and processed by sonication or prolonged stirring. The resulting dispersions contain nearly monochiral (6,5) and (7,5) SWCNTs, respectively. **(b)** SWCNT sorting by aqueous two-phase extraction: DOC-dispersed carbon nanotube raw material is added to a two-phase system of poly(ethylene glycol) (PEG) and dextran in water. An increase of the SDS concentration at constant concentration of DOC leads to step-wise transfer of single SWCNT species to the top phase, depending on the corresponding separation coefficient K_i. **(c)** Schematic of SWCNT purification using aqueous column chromatography: The adsorption affinity of SWCNTs depends on their surface coverage with surfactants, which enables gradual removal from the stationary phase by changing the surfactant type and concentration in the column.

The process concludes with the separation of semiconducting and metallic SWCNTs by addition of sodium cholate (SC) and oxidative reagents, *e.g.*, sodium hypochlorite (NaOCl).[109] While the integration of ATPE-sorted carbon nanotubes in high-performance transistors is still limited by residual metallic SWCNTs,[120] continuously refined ATPE sorting protocols currently enable the extraction of virtually any SWCNT species contained in the raw material.[110,121]

Separation of surfactant-coated SWCNTs by diameter, species, and electronic type can also be achieved by gel adsorption chromatography,[122–124] as schematically shown in Figure 2.2c. Chromatography columns are usually loaded with gel beads of crosslinked allyl dextran/*N*,*N*'-methylenebisacrylamide copolymers, which exhibit unspecific adsorption characteristics. Similar to ATPE, SWCNT sorting is facilitated by adjustment of the surfactant concentration, which governs SWCNT surface coverage and therefore the interaction with the stationary phase.[125] Initially, unsorted SWCNT material, typically stabilized in a binary surfactant system of SDS and SC, is transferred into an equilibrated column. After elution of unbound material, including metallic SWCNTs, the addition of more concentrated surfactant solutions enables gradual elution of other species with varying affinity to the stationary phase, taking advantage of the difference in hydrophobicity of SWCNT-surfactant systems. Often performed as a multi-column procedure,[123] precise tuning of surfactant environments and increasing levels of automation currently provide high-resolution and large-scale separation of SWCNTs down to the level of carbon nanotube enantiomers.[125–130] While the precise interplay of parameters that control the adsorption and elution process are complex,[131] the separation order was demonstrated to closely follow the smallest C−C bond curvature radius (*i.e.*, the largest bond curvature). As SWCNTs with smaller bond curvature radii tend to experience lower surface coverage by surfactants, the corresponding species exhibit stronger adsorption to the gel.[123] However, the exact separation order depends on the chosen surfactant system,[125] and the interactions between SWCNTs and the stationary phase are also highly sensitive to the temperature.[132]

2.1.4 Electronic structure

Similar to the geometrical structure of SWCNTs, their electronic structure can be derived from the conceptual roll-up process of sp^2-hybridized graphene. In graphene, a highly delocalized π-electron system results from the interaction of the $2p_z$ orbitals with perpendicular orientation relative to the planar hexagonal lattice. With only two carbon atoms per primitive unit cell, one bonding π-band and one anti-bonding π*-band are obtained. The nearest-neighbor tight-binding formalism is sufficient to provide an analytical approximation to the electronic band structure near the Fermi

level (±3 eV).[133,134] Assuming electron-hole symmetry, the energy dispersion relation for the bonding (valence) and anti-bonding (conduction) bands in reciprocal space reduces to a Hückel model with the nearest-neighbor carbon-carbon interaction energy γ (typically set to 3.1 eV) as only adjustable parameter:[135]

$$E(\vec{k})^{\pm} = \pm\gamma\sqrt{1 + 4\cos\frac{\sqrt{3}k_x a}{2}\cos\frac{k_y a}{2} + 4\cos^2\frac{k_y a}{2}}. \tag{2.5}$$

Here, $\vec{k}$ denotes the wave vector and the Fermi level is arbitrarily set to zero.[56,134] A graphical representation of the valence band in the first Brillouin zone reveals points of three-fold symmetry, commonly referred to as K and K′ (compare Figure 2.3a). Consequently, with the six-fold (hexagonal) symmetry of the carbon lattice, the symmetry of the K and K′ points constitutes a valley degeneracy of two. At the K points, the energy dispersion relation becomes approximately linear as the valence and conduction bands of graphene are in contact (see Figure 2.3b), making it a semi-metal or zero-band gap semiconductor.

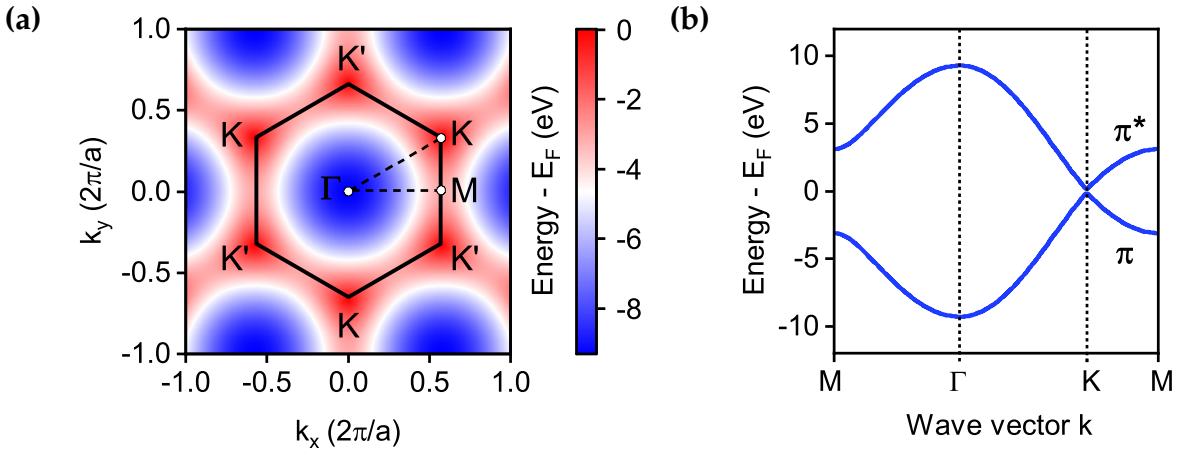

Figure 2.3: (a) Contour diagram of the valence band of graphene showing the first Brillouin zone. Points of high symmetry (K, K′, Γ, M) are marked. **(b)** Energy dispersion of the valence (π) and conduction (π^*) bands of graphene along the path M-Γ-K-M, as traced in **(a)**, calculated according to the tight-binding formalism.

To obtain the electronic band structure of SWCNTs, their reciprocal lattice is constructed from the real space geometry using the so-called zone-folding model.[136] By applying the reciprocity condition[56]

$$\exp\left[i(\vec{K}_a + \vec{K}_c)(\vec{C}_h + \vec{T})\right] = 1 \tag{2.6}$$

one obtains the nanotube Brillouin zone from the reciprocal lattice vectors $\vec{K}_a$ along the SWCNT axis and $\vec{K}_c$ with circumferential orientation. Upon roll-up of

the graphene sheet, additional periodic boundary conditions are imposed on the wave vectors $\vec{K}_a$ and $\vec{K}_c$. In circumferential direction, the resulting quantiziation of the wave vector is given by

$$q = j|\vec{K}_c| = \frac{2\pi j}{|\vec{C}_h|} = \frac{2j}{d_t}, \tag{2.7}$$

where $j = 0, 1, ..., j_{max}$. While identical boundary conditions apply along the longitudinal direction, the corresponding allowed wave vectors k are closely spaced in the limit of long SWCNTs ($L \gg |\vec{T}|$) and can be approximated as quasi-continuous.[56,134] The obtained wave vectors constitute the subbands of a nanotube in the form of 1D cuts through the graphene band structure (see Figure 2.4a,c). Consequently, the band structure of a nanotube can be calculated as the sum of these subbands. For armchair (5,5) and chiral (6,5) SWCNTs, the band structure is illustrated in Figure 2.4b,d. If the cutting lines intersect the K point, as is the case for (5,5) SWCNTs, the nanotube does not have a band gap and is classified as metallic. The absence of an intersection at the K points leads to a band gap and semiconducting properties (*e.g.*, (6,5) SWCNTs). The close relation between the real space and band structure enables the determination of the electronic type of SWCNTs from their chiral indices (n, m), where nanotubes with $(n - m) \bmod 3 = 0$ are metallic and all others are semiconducting. The band gap of semiconducting SWCNTs primarily depends on the nanotube diameter and can be estimated as $E_g = 2\gamma \frac{a_{C\text{-}C}}{d}$ in a first-order approximation.[56] A visualization of the correlation between nanotube diameter and optical transition energies for semiconducting and metallic SWCNTs has found widespread application in the form of so-called Kataura plots, *e.g.*, for the identification of SWCNT species.[137,138] In small-diameter SWCNTs, the hexagonal lattice symmetry can induce significant trigonal warping effects, which lead to an anisotropy in the electronic and phonon energy dispersions.[139]

The total density of states (DOS) distribution $g_{tot}(E)$ can be calculated directly from the corresponding SWCNT band structure according to:

$$g_{tot}(E) = \sum_j g(E, j) = \sum_j \frac{1}{\pi} \left| \frac{\partial k}{\partial E} \right|. \tag{2.8}$$

Here, $g(E, j)$ denotes the DOS of the j-th subband (see Equation 2.7). Characteristic for 1D solids, sharp features termed van Hove (vH) singularities emerge in the DOS distribution of SWCNTs (see Figure 2.5a).[56,140] The DOS at the Fermi level is finite for metallic SWCNTs, but zero for semiconducting species. Thus, luminescence upon

optical or electrical excitation can occur in semiconducting SWCNTs, but is prevented in metallic species due to fast non-radiative carrier relaxation.

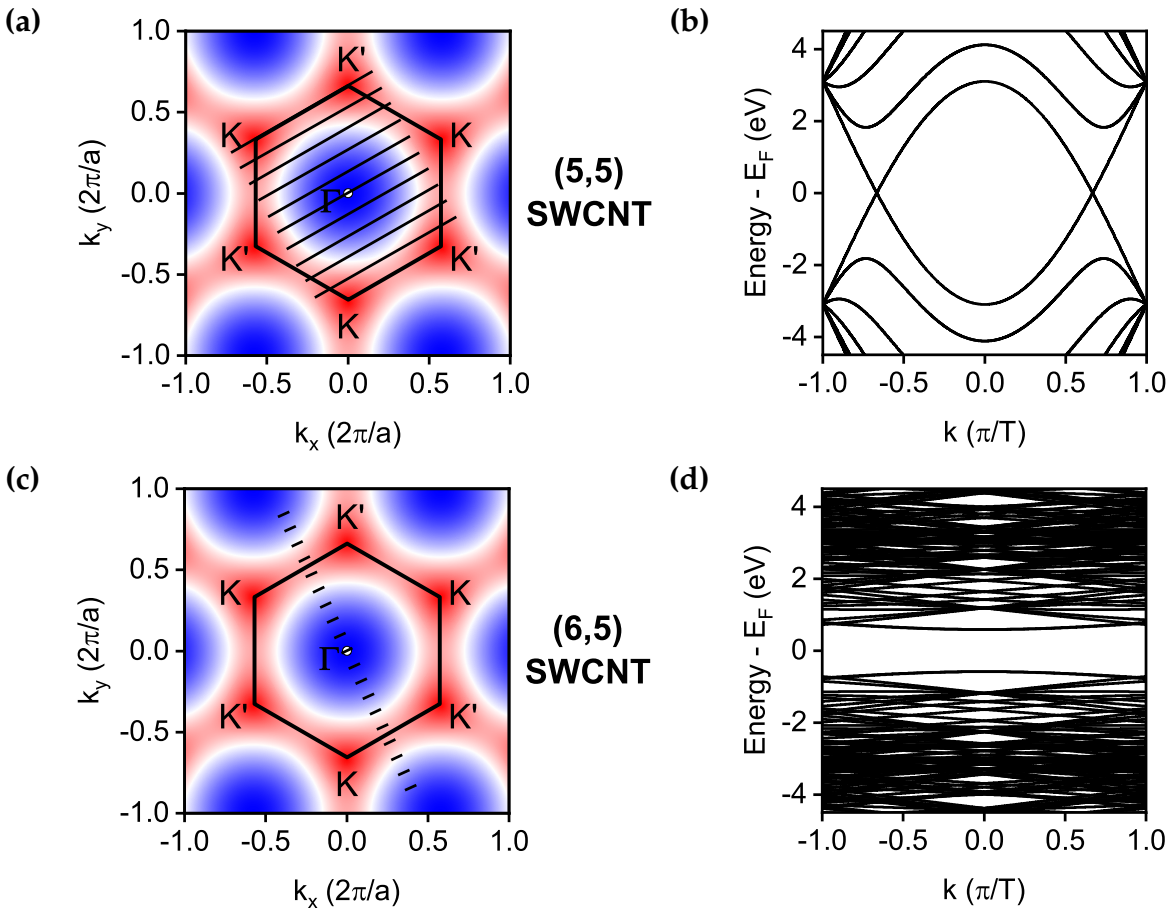

Figure 2.4: Electronic structure of SWCNTs according to the tight-binding and zone-folding approach. **(a,c)** Contour diagrams of the valence band of graphene in the first Brillouin zone. The cutting lines visualize the symmetry constraints which yield the allowed wave vectors for (5,5) and (6,5) SWCNTs. **(b,d)** The absence of a band gap in the band structure of (5,5) SWCNTs leads to metallic properties, whereas semiconducting (6,5) SWCNTs possess a band gap.

2.1.5 Optical properties and excitons

The DOS distribution derived from the tight-binding model or DFT calculations[141,142] readily provides a framework to estimate the energies of optical transitions in semiconducting SWCNTs. In a single-particle picture, optical absorption transitions can be viewed as electronic excitation between vH singularities of the valence and conduction band. The respective transition rate from the initial to the final state depends on their coupling strength and DOS (Fermi's golden rule).[42] Thus, the features in optical absorption spectra of SWCNTs can be regarded as transitions between vH singularities of the valence (v_1, v_2, ...) and conduction band (c_1, c_2, ...). The predominant

E_{ii} transitions are those which occur between the i-th vH singularity of the valence and the conduction band, while E_{ij} transitions are much weaker.[143] The reason for this observation lies in the strong anisotropy of optical absorption processes in SWCNTs. Parallel to the nanotube axis, only E_{ii} transitions are dipole-allowed, whereas E_{ij} transitions require optical excitation with perpendicular polarization. However, the absorption cross section is sigificantly larger along the 1D nanotube lattice due to the antenna effect,[144,145] thus, in practice only E_{ii} transitions are observed. The lowest energy transition is denoted as E_{11} and corresponds to the electronic transition across the band gap E_g for semiconducting SWCNTs.

A more detailed analysis of spectral position, shape, and dynamics of optical transitions of SWCNTs, however, reveals that the single-particle picture is insufficient to accurately describe the nature of electronic states in carbon nanotubes.[137,146–148] The 1D character of SWCNTs results in reduced dielectric screening and thus strong interactions between electrons and holes (see Figure 2.5b) and many-body interactions have to be considered in the description of excited states.[149] Strong electrostatic interactions between holes and electrons result in the formation of bound electron-hole pairs (excitons).[150] Due to 1D confinement, excitons in SWCNTs share characteristics of both tightly-bound Frenkel and delocalized Wannier-Mott excitons, as they possess electron-hole coherence lengths of several nm and binding energies of hundreds of meV.[147,151] In the many-body picture, repulsive interactions between the electrons in the conduction band and those remaining in the valence band further lead to a self-energy contribution E_{self}, which increases the effective band gap. On the other hand, the binding energy E_b leads to a reduction of the optical transition energy, and the effective E_{11} transition energy can be expressed as:

$$E_{11} = E_g + E_{self} - E_b. \tag{2.9}$$

In total, the transition energy increases compared to the band gap, as E_{self} is larger than E_b in SWCNTs.[147,149]

Considering the trigonal symmetry of the K and K' points in the hexagonal nanotube lattice, one obtains a two-fold valley degeneracy in SWCNTs, which again causes a four-fold degeneracy of each possible excitonic state. The electron and hole can either reside in the K or K' valley, which provides four possible configurations KK, K'K', KK', and K'K (compare Figure 2.5c). In conjunction with the spin of charge carriers, each configuration additionally splits into one singlet and three triplet states. Thus, every E_{ii} transition corresponds to 16 excitons in total. The weak spin-orbit coupling in SWCNTs leads to low intersystem crossing yields and all 12 triplet excitons are

optically dark.[152] Of the remaining singlet excitons, the intervalley excitons KK' and K'K possess a finite center-of-mass momentum, as electron and hole are located at different K points. Therefore, only indirect (momentum-forbidden) transitions are possible for intervalley excitons, and they are optically dark. The even-parity, zero center-of-mass momentum exciton is also dark, as a change in parity between the initial and final state is required in a one-photon absorption or emission process. This leaves the odd-parity, zero momentum singlet exciton as the only bright state for a given E_{11} transition.[148] A qualitative picture based on this model for singlet excitons is presented in Figure 2.6a. The bright excitonic state (E_{11}(B)) is located a few meV (Δ_{BD}) above the parity-forbidden, zero-momentum dark state (E_{11}(D)), which leads to a reduction in E_{11} photoluminescence (PL) intensity for temperatures below $\approx$ 50 K.[153] Population of the degenerate K-momentum dark excitons (E_{11}(K)), which are 25 meV (Δ_{BK}) above the bright state, can be achieved by coupling to a D phonon of finite momentum K.[154]

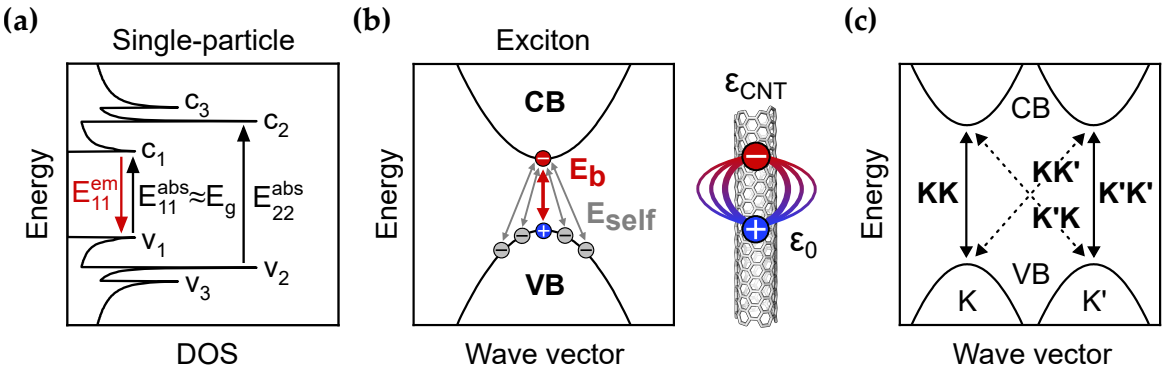

Figure 2.5: (a) In the single-particle framework, optical transitions in semiconducting SWCNTs occur between van Hove singularities of the valence and conduction band in the DOS (absorption in black, emission in red). **(b)** Illustration of many-body effects occurring in SWCNTs due to low dielectric screening and expansion of the electric field lines into the surrounding vaccuum with permittivity ε_0. The electron-hole (exciton) binding energy E_b and self-energy E_{self} due to electron-electron repulsion appear as corrective terms for the band gap energy E_g. **(c)** The two-fold valley degeneracy in SWCNTs due to the trigonal symmetry of K and K' points creates a four-fold degeneracy for each excitonic state.

The optical transitions in absorption and emission are depicted exemplarily for (6,5) SWCNTs in Figure 2.6b. At $\approx$ 575 nm, absorption into the E_{22} state is visible, whereas the E_{11} absorption feature occurs at $\approx$ 1000 nm. At slightly lower wavelengths ($\approx$ 860 nm for (6,5) SWCNTs), the so-called phonon sideband (PSB) is observed, which results from brightening of the E_{11}(K) state by coupling to an additional D phonon.[154] Following optical excitation to higher excitonic states (E_{22}, E_{33},...), fast relaxation to the E_{11} band-edge exciton manifold occurs on timescales of

≈ 100 fs.[155,156] Due to the rigidity of the carbon lattice, only small reorganization energies are observed in SWCNTs and radiative relaxation from the E_{11} to the ground state results in PL with Stokes shifts of < 8 nm and narrow linewidths (≈ 30 meV for liquid-dispersed SWCNTs, and < 15 nm for single nanotubes in air at room temperature).[157–159]

Aside from excitonic resonances, PL peaks of lower intensity with red-shifted emission in comparison to the E_{11} exciton, contribute to SWCNT PL spectra (compare Figure 2.6c). As addressed above, coupling of the E_{11} state to a D phonon, presumably due to scattering at lattice defects,[160,161] results in brightening of the K-momentum dark excitonic state, which gives rise to a PSB in emission (X_1). A further red-shifted vibronic sideband, usually referred to as G_1, is caused by coupling of the bright E_{11} exciton to a G phonon.[154,162] The low-energy shoulder of the E_{11} excitonic emission (Y_1) originates from processing-related lattice defects which can act as shallow potential traps for excitons.[154,163]

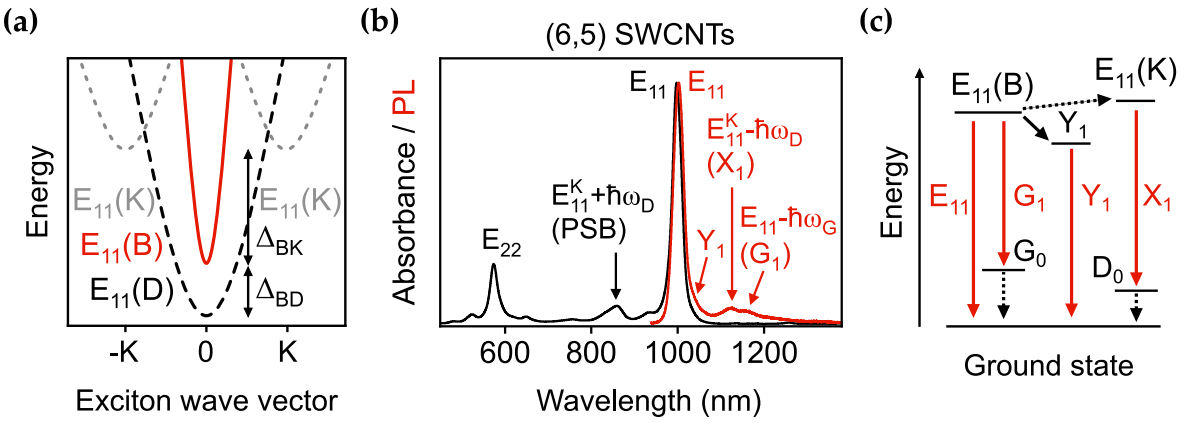

Figure 2.6: (a) Schematic energy dispersion of E_{11} singlet excitons, of which three are dark (E_{11}(K) at -K and K, E_{11}(D)). The steep energy dispersion of the bright singlet exciton (E_{11}(B), red) results from its comparably lower effective mass. **(b)** Assigned absorption (black) and photoluminescence (red) peaks of main excitonic transitions and lower-energy sidebands (Y_1, X_1, G_1) in optical spectra of (6,5) SWCNTs dispersed with PFO-BPy in toluene. **(c)** Qualitative energy diagram of radiative transitions linked to the features labeled in **(b)**. Relaxation processes that include interactions with a phonon are depicted as dashed arrows.

The pivotal role of defects, shallow trap states[154,163] and localized charges[164–166] on carbon nanotube emission becomes evident upon closer inspection of the underlying exciton dynamics. With diffusion coefficients on the order of $2 - 40\,cm^2\,s^{-1}$,[159,167–170] excitons can cover large areas of the SWCNT lattice prior to radiative decay with typical lifetimes of 10 – 100 ps.[48] A corresponding dependence of exciton decay dynamics on nanotube length, reflected in increased effective lifetimes, was demonstrated with

samples of air-suspended SWCNTs.[159,171] Consequently, the interaction with other excitons (*e.g.*, exciton-exciton annihilation (EEA)[165,172]), charges and lattice defects strongly influences the optical response of SWCNTs and transition energies depend on the dielectric environment of the nanotube, *e.g.*, solvent system or surfactant coverage.[173–175] In dispersion, these effects can be described by a solvatochromic model, in which an increase of the dielectric constant in the vicinity of the nanotube results in a decrease of exciton oscillator strength and a red-shift of the PL.[176,177] Extrinsic parameters also impact the emission efficiency in carbon nanotubes, usually expressed in terms of the PLQY. With values on the order of $0.1 - 1\,\%$ in dispersion, SWCNTs exhibit comparably low PLQYs, commonly attributed to non-radiative decay following the efficient intrinsic conversion of bright excitons to energetically lower-lying dark states.[178] At room temperature however, the contribution of structural defects and the surrounding dielectric environment becomes more relevant, as quick diffusion of excitons to quenching sites such as nanotube ends or lattice defects dominates the exciton dynamics.[167,179–181]

2.1.6 Circular dichroism

As indicated in Chapter 2.1.1, SWCNTs exist as helically chiral enantiomers, except for achiral zigzag and armchair species. Corresponding enantiomers of SWCNTs can be constructed as mirror images of each other, are referred to as (n, m) and $(n + m, -m)$ species (compare Figure 2.7a), and share identical mechanical and electronic properties. A distinctive characteristic of chiral materials is the occurrence of circular dichroism (CD), which describes a difference in optical absorption of left- and right-handed circularly polarized light (LCPL and RCPL, respectively).[182] First theoretical studies inferred the presence of CD in SWCNTs based on the tight-binding model within the dipole approximation, and derived dipole selection rules for the interaction of nanotubes with LCPL and RCPL.[183–185] Initial considerations that the magnitude of the CD should decrease with SWCNT diameter as the nanotube curvature is reduced and the lattice approaches that of achiral graphene[183] were corroborated by subsequent first-principles studies.[186,187]

An analytical expression for the CD of SWCNTs within the tight-binding approach is obtained when, beyond the dipole approximation, the local phase factor of the incident circularly polarized light at every carbon atom position is considered.[182] In this case, the conduction band wave vector k_c^σ, obtained upon absorption of circularly polarized light propagating parallel to the nanotube axis, can be expressed as

$$k_c^\sigma = k_v - \sigma K_1 + \tau K_2, \tag{2.10}$$

where $\sigma = \pm 1$, depending on the light polarization. k_v denotes the wave vector of the valence band, while K_1 and K_2 are the reciprocal lattice vectors in circumferential and longitudinal direction, respectively. τ is given by the ratio of nanotube unit cell length T and excitation wavelength λ. Due to the perpendicular orientation of the electric field with respect to the nanotube axis, an angular momentum of K_1 or $-K_1$ is added to k_c^σ for momentum conservation. In the limit of $\tau = 0$, the momentum difference $k_c - k_v$ equals $-\sigma K_1$ and is thus perpendicular to the cutting lines in the Brillouin zone of the SWCNT (compare Figure 2.7b).

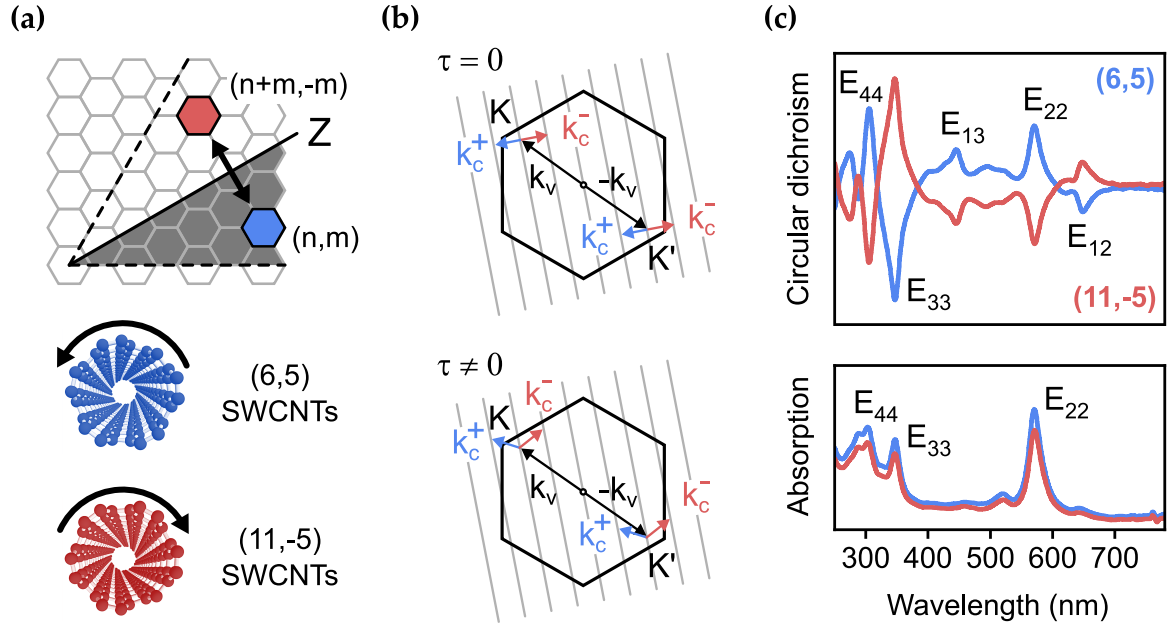

Figure 2.7: (a) Schematic construction of (n, m) and (n + m, −m) (blue and red, respectively) enantiomers of SWCNTs as mirror images (mirror axis Z). Enantiomeric structures with opposite handedness are displayed for (6,5) and (11,-5) SWCNTs (view along the nanotube axis). **(b)** Illustration of the model used to calculate the CD for carbon nanotubes within the tight-binding approach according to Sato *et al.*[182] The conduction band wave vectors k_c^+ (blue arrows) and k_c^- (red arrows), depending on the circular polarization of the light propagating along the nanotube axis, are obtained according to Equation 2.10. When the local phase factor is not considered ($\tau = 0$), the momentum contributions of LCPL and RCPL cancel out upon integration over the Brillouin zone. Otherwise ($\tau \neq 0$), a finite CD signal intensity occurs. **(c)** Exemplary UV-Vis CD (top) and absorption spectra (bottom) of (6,5) and (11,-5) SWCNT enantiomers. The observed excitonic transitions E_{ii} and E_{ij} are indicated.

Consequently, the optical transition probabilities for LCPL and RCPL cancel out upon integration over the complete Brillouin zone, and as a result, no CD is calculated. However, as the phase of the incident light is considered, a wavelength-dependent momentum τK_2 is added and a finite CD is obtained. Similarly, phase difference effects for circularly polarized light propagating perpendicular to the nanotube axis can

be incorporated to yield a complete analytical expression for the CD of SWCNTs.[182] This model precisely reproduces the experimentally determined wavelength dependence and alternating sign of the CD intensity for the progression of E_{ii} transitions.

The separation of carbon nanotube enantiomers has been achieved by a large variety of methods based on selective interactions with chiral surfactants or media. Initial observations of CD in racemic SWCNT samples were enabled by wrapping with chiral DNA strands, which was attributed to coupling between DNA and SWCNT transition moments.[188] The first deterministic enantiomer separation method utilized chiral diporphyrins in methanol-based dispersions,[189,190] while density gradient ultracentrifugation (DGU) was shown to separate nanotube enantiomers in aqueous environments if performed with chiral surfactants.[191] Enantiomer separation has also been reported for ATPE-based sorting techniques utilizing the chiral selectivity of DNA strands[192] or the surfactants DOC and SC.[111,112] To date, the highest enantiomeric purities are obtained with gel chromatography, which combines the enantiomer-selective interactions between SWCNTs and both the surrounding chiral surfactants and chiral moieties in the stationary phase.[116,127,129,193,194] By quantifying the optical response of (6,5) and (11,-5) SWCNT enantiomers dispersed by chiral flavin mononucleotide in various mixing ratios, Wei *et al.* developed a method for the determination of enantiomeric purities from the absorption-normalized CD intensity at the E_{22} optical transition.[128] For (6,5) SWCNTs sorted by length with size exclusion chromatography prior to the enantiomer separation step, enantiomeric purities can exceed 90% for fractions with longest SWCNTs due to maximization of chiral interactions.[130] Similar to selective polymer wrapping in toluene, separation of (6,5) SWCNTs by handedness was demonstrated with polyfluorenes containing a chiral center in the polymer backbone.[195]

The availability of enantiomer-sorted SWCNTs has prompted a number of experimental studies on the relationship between nanotube structure and optical activity. In contrast to optical absorption, the CD signals of E_{ii} and E_{ij} transitions have comparable signal intensities. Therefore, CD spectra can reveal more intricate information about electronic states and the extracted E_{ii} and E_{ij} transition energies were used to clarify the band structure of SWCNTs.[127] Exemplary CD and absorption spectra of (6,5) and (11,-5) SWCNT enantiomers are depicted in Figure 2.7c. Magg *et al.* demonstrated the vibrational optical activity of DGU-separated (6,5) and (11,-5) SWCNT enantiomers in resonance-enhanced Raman measurements.[196] Using Rayleigh scattering circular dichroism, which provides strongly enhanced signal intensities compared to conventional CD spectroscopy, Yao *et al.* showed that identification of nanotube handedness is possible even at the single nanotube level.[197]

Erkens *et al.* demonstrated that hyperspectral PL microscopy can be employed to simultaneously distinguish the handedness of SWCNT enantiomers and their filling content in ensemble measurements.[198]

2.2 Luminescent defects

Along with the development of carbon nanotube dispersion and purification methods (see Chapter 2.1.3), interest in covalent sidewall and non-covalent exo- and endohedral functionalization of SWCNTs to alter their mechanical and electronic properties started to grow. Their high specific surface area combined with the exposure of the nanotube surface makes SWCNTs attractive targets for chemical modification. However, the strain energy of the sp^2-hybridized carbon nanotube lattice, due to the curvature and corresponding misalignment of π-orbitals, is significantly lower compared to reactive fullerenes with rich functionalization chemistry.[199,200] For this reason, the first successful attempts to prepare covalently functionalized SWCNTs utilized particularly reactive compounds and harsh reaction conditions.[201] Reagents employed for SWCNT functionalization included nitrenes and carbenes,[202] diazonium salts,[203,204] ozone,[205,206] oxidizing acids[207] and azomethine ylides.[208] With the goal to increase the solubility of SWCNTs in organic solvents or to use them as catalyst supports, most reaction protocols aimed to achieve high degrees of sidewall functionalization.[201,206,209] Generally, the introduction of lattice defects was demonstrated to be detrimental for the optical properties of SWCNTs, as perturbations of the intrinsic electronic structure promote non-radiative decay of fast-diffusing excitons.

However, Ghosh *et al.* and Piao *et al.* demonstrated that if distinct types of oxygen and sp^3 aryl defects are incorporated in the nanotube lattice in small numbers under precisely controlled conditions, new red-shifted emission features can be observed in PL spectra of SWCNTs.[12,13] Excitons are efficiently localized at these so-called luminescent defects and decay radiatively from these lower energy states. The associated decrease in non-radiative exciton decay at nanotube ends or quenching sites leads to a total increase in PL brightness (compare Figure 2.8).[13,210,211] These findings sparked intensive research of luminescent defects for optoelectronic applications and optical probes, summarized in several comprehensive review articles.[18,212–215] In the literature, luminescent defects are also frequently referred to as "quantum defects" to highlight their quasi zero-dimensional nature enabling single-photon emission,[14,216] or "organic color centers" due to their phenomenological similarity to color centers in inorganic crystals.[212]

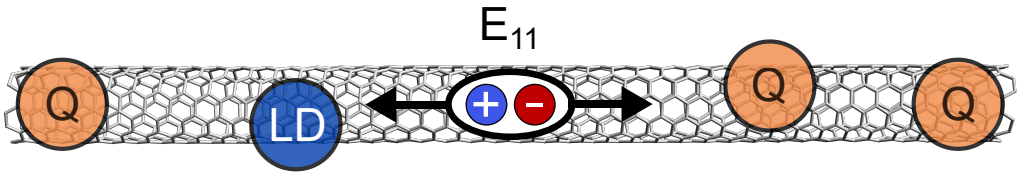

Figure 2.8: Schematic depiction of E_{11} exciton diffusion in SWCNTs with exciton quenching sites (Q) and luminescent defects (LD).

This Chapter provides a condensed overview of the photophysics of luminescent sp^3 aryl defects, available functionalization methods to create them, the influence of attached functional groups on carbon nanotube emission, and concludes with a section dedicated to the characteristics of oxygen defects.

2.2.1 Exciton dynamics and optical properties

Functionalization of SWCNTs with luminescent defects locally modifies the otherwise sp^2-hybridized lattice, as the affected carbon atoms form new σ bonds and acquire significant sp^3 character. This perturbation interrupts the π-conjugation at the defect site and results in symmetry breaking of the electronic structure,[217] as the K and K' valley degeneracy is lifted and a new optically allowed state emerges below the E_{11} exciton, as depicted in Figure 2.9a. The KK and K'K' states, which correspond to the odd-parity $E_{11}(B)$ and even-parity $E_{11}(D)$ excitons with an energy separation of only few meV (compare Δ_{BD} in Figure 2.6a), split and form a two-level system. The lower-energy, stabilized excitonic state is denoted as E_{11}^* and optically bright, whereas the destabilized dark state is referred to as E_{11}^{up}.[153] The presence of this two-level system in the energetic landscape of the SWCNT enables efficient trapping of highly mobile excitons, as the energy associated with the E_{11}^* state is below that of $E_{11}(B)$. The corresponding energy wells on the order of ≈ 100 meV lead to strong confinement and room-temperature stability of trapped excitons.[218] The electron-hole coherence lengths are estimated to be $\approx 2-5$ nm.[219,220] Upon radiative relaxation of trapped excitons to the ground state, red-shifted E_{11}^* emission occurs, accompanied by a reduction in E_{11} emission intensity (see Figure 2.9b). The energy difference $E_{11} - E_{11}^*$ is referred to as optical trap depth ΔE_{opt}. The nanotube diameter and ΔE_{opt} are inversely correlated,[13,221,222] which is attributed to the reduced energetic splitting expected upon functionalization of larger-diameter SWCNTs with less structural strain.

Theoretical studies suggest that both E_{11} and E_{11}^* excitons possess radiative lifetimes on the order of $1-10$ ns.[152,223,224] This picture is contrasted by experimental

studies, which report effective lifetimes of 1 – 10 ps for E_{11} and a few 100 ps for E_{11}^* excitons in SWCNT dispersions.[167,224] In the case of E_{11} excitons, lifetimes are limited by rapid diffusion-limited quenching, which does not apply to E_{11}^* excitons.[225,226] Consequently, functionalization of SWCNTs with luminescent defects can significantly enhance the overall emission efficiency by reduction of non-radiative decay.[13] The magnitude of this effect is heavily dependent on structural parameters such as nanotube length and defect density. Ultra-short SWCNTs with lengths of less than 100 nm exhibit the strongest brightening factors.[55,227] In contrast, CVD-grown and practically defect-free carbon nanotubes suspended in air experience a decrease in PLQY upon gas-phase sp^3 functionalization.[228] In solution-processed SWCNTs, maximum brightening effects are typically restricted to a narrow range of defect densities, as sp^3 defects not only lead to new emissive states, but also perturb the intrinsic electronic structure of the sp^2-hybridized nanotube lattice. As a consequence, further sp^3 functionalization continues to increase the E_{11}^*-to-E_{11} emission intensity ratio, whereas the total PLQY starts to decline.[13,221,222,229–231]

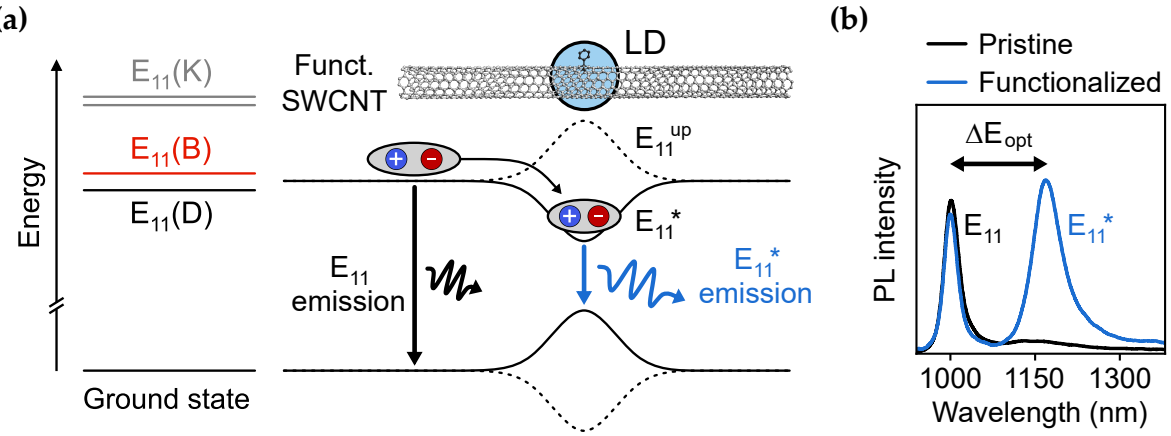

Figure 2.9: (a). Energy level diagram (axis not to scale) illustrating local symmetry breaking upon functionalization of SWCNTs with luminescent defects (LD). Splitting of the excitonic states E_{11}(B) and E_{11}(D) creates a lower-energy bright E_{11}^* state, which enables efficient trapping of highly mobile E_{11} excitons. **(b)** PL spectra of pristine and sp^3-functionalized (6,5) SWCNTs. Radiative decay from the E_{11}^* excitonic state manifests as additional red-shifted emission feature with optical trap depth ΔE_{opt}.

The reduced PL lifetimes of E_{11}^* excitons compared to theoretical predictions suggest that non-radiative relaxation pathways dominate the dynamics of defect-trapped excitons and ultimately set the limit of attainable PLQYs. The main contributions are thermal exciton detrapping, multi-phonon decay, and electronic-to-vibrational energy transfer, which depend on the nanotube species, trap depth, dielectric environment, and temperature (see Figure 2.10).[211,218,224]

Thermal detrapping (TD) describes the process of thermally controlled transfer of trapped excitons back to the E_{11} energy level.[232] The associated detrapping rate is expected to decrease with defect trap depth, which is corroborated by the observation of increased PL lifetimes at longer wavelengths of the defect emission for a given SWCNT species.[224] Temperature-dependent PL spectroscopy revealed a significant discrepancy between the thermal ($\Delta E_{thermal}$, $\approx 80 - 100$ meV) and optical trap depth (ΔE_{opt}, $\approx 160 - 180$ meV). Initial interpretations of this phenomenon as reorganization energy upon lattice deformations occurring during exciton localization are contradictory to the experimentally determined small Stokes shifts ($\approx$ 20 meV),[218,230] which point more towards a substantial energy splitting of the ground state at the luminescent defect site (see Figure 2.9a).[12]

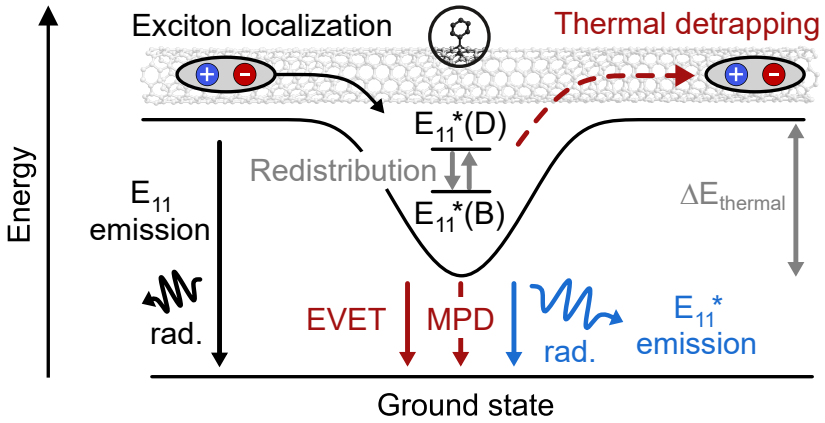

Figure 2.10: Schematic of exciton decay pathways at luminescent sp^3 defects according to the model proposed by He *et al.*[224] Following diffusive trapping of mobile E_{11} excitons, redistribution of the exciton population between dark (E_{11}^*(D)) and bright (E_{11}^*(B)) defect states takes place. Subsequent non-radiative decay pathways (red) include thermal detrapping, electronic-to-vibrational energy transfer (EVET) and multi-phonon decay (MPD). Radiative decay can occur in the form of intrinsic E_{11} emission for free excitons (black), and E_{11}^* emission (blue) from the defect state.

The non-radiative relaxation of trapped excitons under emission of multiple phonons is termed multi-phonon decay (MPD). As trapped excitons show enhanced coupling to phonons, higher MPD rates are observed for defect-localized excitons.[233] In contrast to TD, MPD rates increase with the wavelength of the defect emission for a given SWCNT species, as less phonons are required to reach the ground state ("energy gap law").[234] This offers an explanation for the reduction in defect-state lifetime and emission efficiency of larger-diameter SWCNTs.[211] Electronic-to-vibrational energy transfer (EVET) describes Förster-type resonance energy transfer (FRET) from SWCNTs to the vibrational modes of surrounding solvent molecules, resulting in non-radiative quenching of defect-localized excitons. Especially in the presence of

solvents with broad absorption bands at similar energy as defect states, EVET can contribute significantly to a reduction of PL lifetimes.[224] This effect is pronounced for SWCNTs dispersed with polar surfactants or in polar solvents (*e.g.*, H_2O, MeOH).

Similar to the excitonic state manifold of the E_{11} energy level, a bright singlet state and several dark states exist in defect-localized excitons.[235,236] For aryl and alkyl (sp^3-type) defects, theoretical studies suggest that dark states are energetically located slightly above the bright singlet state.[224] The energy difference is predicted to be small enough that significant redistribution to dark states occurs at room temperature, leading to an apparent biexponential radiative decay of defect-trapped excitons. In this model, the decay dynamics of trapped excitons can be expressed as the sum of a long and short decay component:[224]

$$\tau_{\text{long}}^{-1} = \tau_{\text{TD}}^{-1} + \tau_{\text{MPD}}^{-1} + \tau_{\text{EVET}}^{-1} + k_{\text{other}}, \tag{2.11}$$

$$\tau_{\text{short}}^{-1} = \tau_{\text{rd}}^{-1} + \tau_{\text{long}}^{-1}. \tag{2.12}$$

Here, k_{other} indicates the contribution of the radiative relaxation pathway and other, not specified non-radiative decay paths. The short component is obtained as sum of the rate constant for exciton redistribution τ_{rd}^{-1} and the long decay component. Typical values for the long decay component span from $\approx 100 - 500$ ps, whereas τ_{short} is closer to $60 - 100$ ps, with a strong dependence on dispersion solvent and dielectric environment.[221,224,230,237] Additionally, the presence of luminescent defects in close proximity to an existing defect site was found to shape their emission characteristics. The resulting coupling of luminescent defect states results in strongly correlated emission, which can be employed to estimate distances of few nm between individual defect sites.[238]

A remarkable property of luminescent defects is their quasi zero-dimensional electronic structure. Only one exciton can occupy one defect state at a time, and for an individual defect this prevents the occurrence of simultaneous electron-hole recombination events. This has enabled the observation of single-photon emission (SPE) at room temperature and at telecom wavelengths,[50] a prerequisite for use in quantum communication technology.[5] For SWCNTs with luminescent sp^3 defects, single-photon purities of up to 99 % in the telecom C-band have been demonstrated.[14] The two-level character of the defect state also manifests itself in the form of state-filling effects due to significantly faster defect state population ($\approx$ 10 ps)[167] compared to exciton decay ($\approx$ 100 – 200 ps).[224] Thus, saturation of the PL intensity occurs at much lower excitation power for the E_{11}^* state compared to the intrinsic E_{11} exciton.[239]

Consequently, the defect-to-E_{11} PL intensity ratio cannot serve as a reliable metric for luminescent defect density as it depends on the excitation power.

2.2.2 Role of defect structure

Up to this point, the optical properties of luminescent defects were treated as a result of the nanotube lattice deformations and conversion of carbon atoms from sp^2 to sp^3 hybridization. For luminescent sp^3 defects, however, a more nuanced picture emerges if the electronic structure of the attached functional group is considered. In the case of more electron-withdrawing functional groups, the electrostatically controlled exciton localization is enhanced and a red-shift of the defect emission occurs.[13,240,241] A similar increase in emission wavelength is obtained upon reduction of s character in the hybridization state of the defect carbon atom by functionalization with divalent functional groups.[241,242] In contrast, an increase in the s character, *e.g.*, by functionalization with azides,[243] results in less red-shifted defect emission. To a larger extent, however, the defect emission energy is influenced by the binding configuration of the attached functional group with respect to the nanotube lattice. Carbon nanotube functionalization can proceed *via* radical or ionic mechanisms, and the resulting unpaired electrons or charges of reactive intermediates will delocalize in the vicinity of the initial binding site (*i.e.*, *ortho* and *para* positions, see Figure 2.11a). Subsequent saturation by binding of a second chemical moiety to the nanotube lattice forms a stable, closed-shell system. This can be either another functional group or solvent molecule. The functionalization in different solvent systems was shown to create small wavelength shifts, indicative of the involvement of (fragments of) solvent molecules.[244]

In chiral SWCNTs (*e.g.*, the (6,5) species), six possible binding configurations of different energy can be distinguished.[245] Theoretical studies suggest that each of the topologically different configurations should lead to a distinctive trap depth and defect emission energy,[215] which is supported by the large spectral diversity observed in PL spectroscopy of individual SWCNTs at cryogenic temperature.[238,245] These considerations suggest that in higher-symmetry SWCNTs, the number of distinguishable defect emission features becomes more restricted, which was corroborated by functionalization of achiral zigzag species.[246] As proposed by Saha *et al.*, of the six optically active binding motifs, the *ortho*-L_{90} (also called *ortho*$^{++}$) and *ortho*-L_{30} (or *ortho*$^{+}$) binding configurations dominate the PL spectra of sp^3-functionalized SWCNTs.[246] These configurations are commonly associated with emission peaks in the spectral regions from 1100 – 1200 nm (E_{11}^{*}) and 1200 – 1350 nm (E_{11}^{*-}), respectively (compare Figure 2.11b).[221,230,246] However, the E_{11}^{*-} emission has also been associated with the *para*$^{++}$ configuration,[244,247] and overall, no conclusive picture of the relation between binding motifs and defect emission has been established yet.

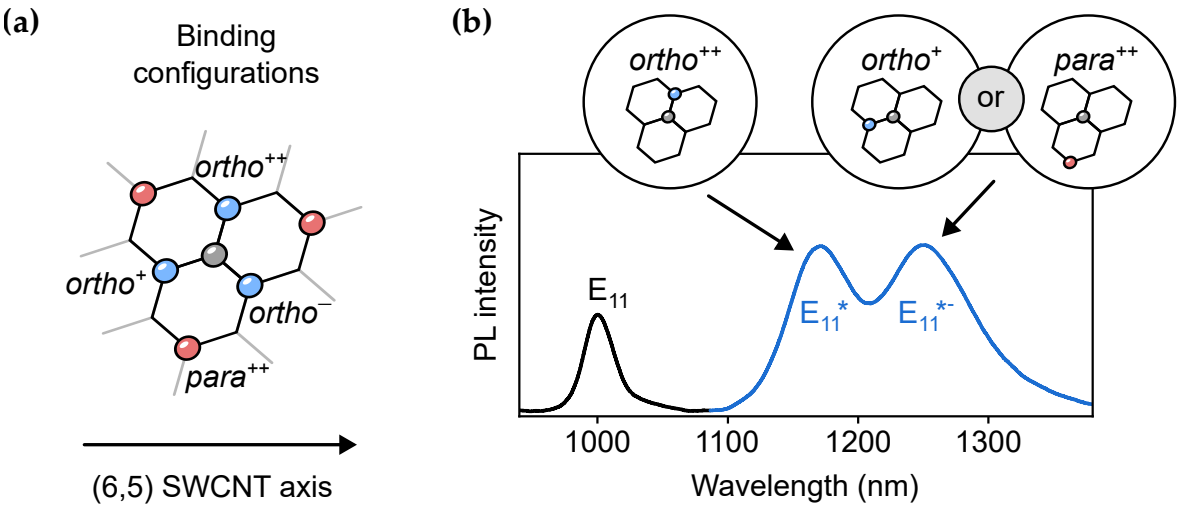

Figure 2.11: (a) Schematic illustration of luminescent sp^3 defect binding configurations in (6,5) SWCNTs. The position of the second attached group in *ortho* (blue) or *para* (red) configuration with respect to the initially bound functional group (gray) determines the emission wavelength of the defect state. **(b)** PL spectrum of (6,5) SWCNTs with binding configurations assigned to the E_{11}^* and E_{11}^{*-} emission peaks. Note that the E_{11}^{*-} peak potentially arises from either the $ortho^+$ or $para^{++}$ configuration.[221,244,247]

2.2.3 Covalent functionalization of SWCNTs

Since the initial reports of luminescent defects in carbon nanotubes,[12,13] a large variety of covalent functionalization methods was developed to tailor their optical properties. The majority of these approaches drew inspiration from previous covalent nanotube chemistry which, for the most part, was intended to create a large number of functional groups on the nanotube lattice.[201,248,249] Precise control of the reaction conditions is required to achieve very sparse and uniform sidewall functionalization. Otherwise, perturbations of the intrinsic electronic structure of SWCNTs result in strong quenching of PL and suppressed NIR emission.[250] The intrinsic reactivity of SWCNTs is governed by the curvature-induced misalignment of π-orbitals, leading to increased reactivity for small-diameter species.[200,246] Regarding the dispersion environment, lower surface coverage generally increases reactivity by providing higher accessibility of the SWCNT sidewall for reactive species. Consequently, nanotube functionalization was preferably explored for small-diameter species (*e.g.*, (6,5) SWCNTs) stabilized by surfactants such as SDS[13] or sodium tridecylbenzenesulfonate (STBS)[12] with a tendency for sparse, unstructured sidewall adsorption.[118,251] Recent developments have expanded the scope of functionalization reactions to polymer-wrapped SWCNTs in organic solvents, other surfactant systems, larger-diameter species, and nanotube thin films.[212,213,221,230,252–257] Figure 2.12 summarizes selected solution-based approaches for covalent SWCNT functionalization.

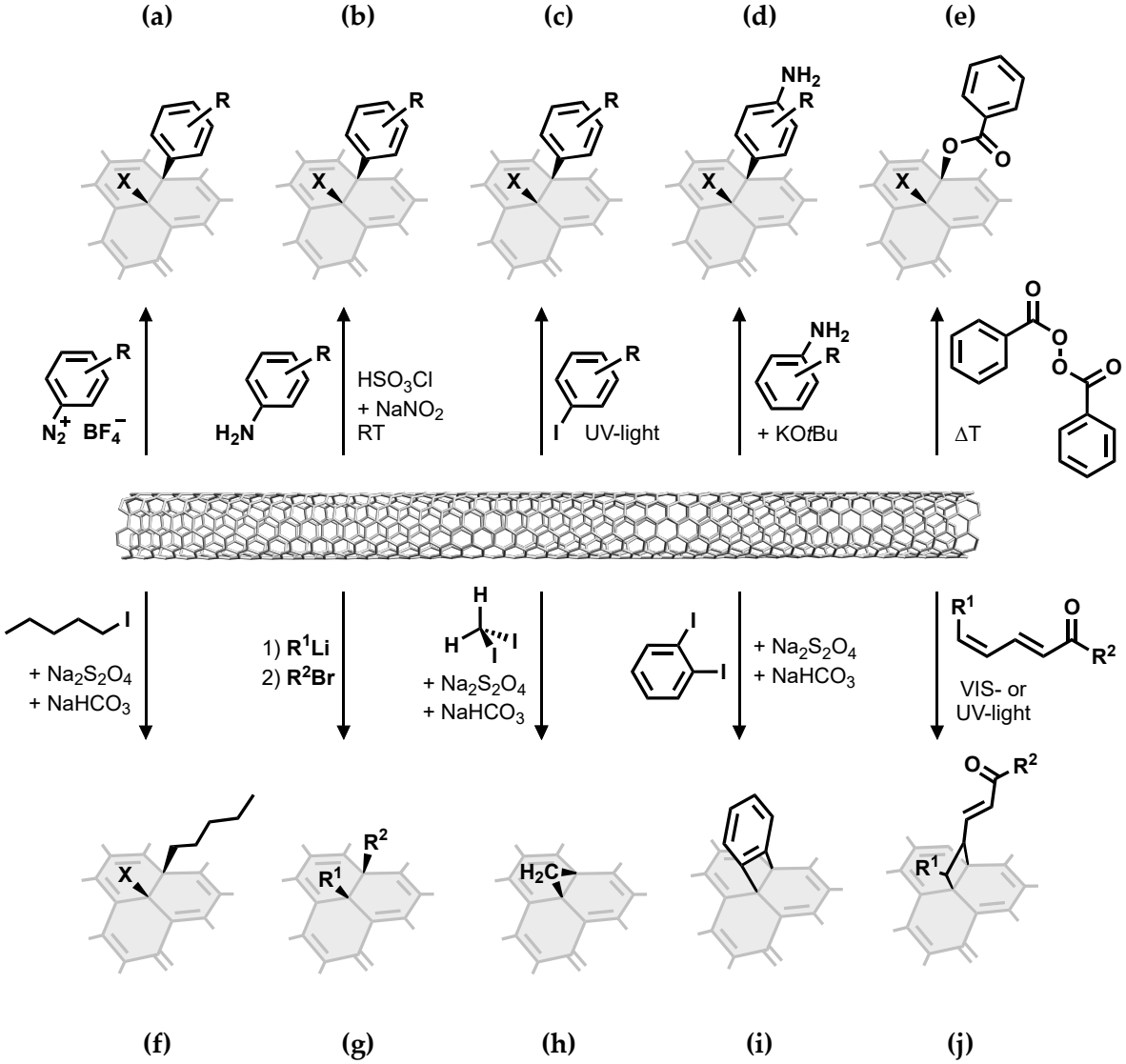

Figure 2.12: Synthetic strategies for the introduction of luminescent sp^3 defects in SWCNTs. Attachment of aryl groups by diazonium chemistry using **(a)** isolated compounds,[13] which is also applicable to polymer-wrapped SWCNTs in organic solvents,[230] or **(b)** *in situ* diazotation.[258] **(c)** Functionalization with activated aryl halides upon UV-light irradiation.[259,260] Luminescent defects in polymer-wrapped SWCNTs *via* **(d)** base-promoted nucleophilic addition of anilines[221] or **(e)** thermal activation of benzoyl peroxide.[252] Introduction of alkyl defects using **(f)** alkyl iodides under mildly reductive conditions or **(g)** organolithium reagents followed by addition of alkyl bromides.[261] Divalent sp^3 defects can be obtained by treatment of SWCNTs with **(h)** alkylene diiodides, **(i)** aryl diiodides,[240] or **(j)** using photo-induced [2+2] cycloaddition reactions of enones.[262]

Diazonium salts have found widespread application for covalent SWCNT functionalization, as they offer a balance between sufficient reactivity and stability. The synthetic preparation of diazonium derivatives from easily accessible precursor molecules is straightforward, which has opened up a large space of defect functionalities ranging from pH detection[263] to *in vivo* imaging,[54,55,264] optical analyte sensing,[265–268] and detection of disease biomarkers.[269] The reaction mechanism proceeds *via* adsorption of diazonium compounds on the nanotube sidewall followed by cleavage of N_2 and radical formation upon single-electron transfer from the SWCNT.[270–273] The Gomberg-Bachmann mechanism represents an alternative pathway for aryl radical formation.[274] The relatively slow reaction rates observed for diazonium salts present a major drawback of this approach (up to several days until completion of the sidewall functionalization), but can be enhanced upon irradiation with visible light.[275–277] As excess diazonium salt often remains adsorbed on the SWCNT surface and leads to PL quenching,[13,181,230] removal by surfactant transfer or filtration is usually required. A one-pot procedure was implemented based on *in situ* diazotation of aromatic amines in water, by which sp^3-functionalized SWCNTs can be obtained on the milligram scale.[258] Less reactive compounds such as aryl halides can be used to create luminescent sp^3 defects under ultraviolet (UV) irradiation,[259,260] an approach that is also applicable to air-suspended SWCNTs in the gas phase.[228]

Among the earliest reported functionalization methods to introduce luminescent alkyl sp^3 defects was the Billups-Birch reduction,[278] which was primarily investigated for its ability to improve nanotube debundling and solubility.[279,280] In this approach, SWCNTs reduced by solvated electrons obtained from addition of Li or Na to liquid NH_3 are functionalized by adding alkyl iodides, which form the corresponding alkyl radicals upon SWCNT electron transfer and dehalogenation.[281] The ensuing alkylation reaction follows a cascade-like behavior and propagates along the nanotube lattice due to the increased electron density in already defective areas.[282] In a similar approach, Kwon *et al.* functionalized SWCNTs with a variety of alkyl iodides by using the mild reducing agent sodium dithionite in conjunction with sodium bicarbonate, and demonstrated the generation of divalent defects by employing diiodide compounds.[240] Divalent enone defects can also be created in photo-induced [2+2] cycloadditions.[262] By using thermal treatment under inert atmosphere after reductive alkylation, Maeda *et al.* reported increased alkyl defect emission brightness, presumably due to a reduction in detrimental alkyl defect clusters.[227,261] Additionally, they demonstrated that the large inductive effects of cyclic perfluoroalkyl compounds enable a high degree of control over the defect emission red-shift in different SWCNT species.[283]

In comparison to the rich functionalization chemistry developed for aqueous dispersion, only few methods have been developed for polymer-wrapped SWCNTs dispersed in organic solvents. However, film deposition methods employed for the fabrication of nanocavities, photonic circuits and light-emitting devices typically use organic solvents due to their higher vapor pressure and lower surface tension. Thus, in combination with the high purity of semiconducting SWCNTs attainable with polymer wrapping, functionalization methods which proceed in organic dispersion solvents are desirable. Berger *et al.* employed a phase-transfer agent and a polar solvent system in order to sufficiently increase the reactivity of diazonium salts to perform sp^3 functionalization.[230] Luminescent defects were also reported to arise when benzoyl radicals are created *in situ* from thermal decomposition of benzoyl peroxides.[252] The selective introduction of defects with $E_{11}{}^{*-}$ binding configuration *via* nucleophilic addition was demonstrated by Settele *et al.*, who combined strong organic bases and aniline derivatives in organic solvents.[221]

Lastly, it should be noted that several nanotube functionalization methods exist that do not lead to the discussed defect emission feature or have been developed with the aim to preserve the π-conjugation of the SWCNT lattice. Setaro *et al.* used a [2+1] cycloadditon reaction to couple azidodichlorotriazine units to nanotube sidewalls at high defect densities ($\approx$ 4% of the carbon lattice).[284] However, other aryl azides appear to induce sufficient sp^3 character in the SWCNT structure to result in $E_{11}{}^*$ defect emission.[243] Reaction of ssDNA-coated SWCNTs with guanine nucleotides in the presence of singlet oxygen led to equidistantly spaced lattice defects, as guided by the DNA wrapping structure.[285] The defects constitute only very shallow exciton traps and consequently lead to a red-shift of the intrinsic E_{11} emission up to $\approx$ 60 nm. Theoretical studies indicate that the functional group structure likely corresponds to a 4,5-guanine peroxide in $ortho^-/L_{-30}$ orientation (opposite to the $ortho^+/L_{30}$ position, compare Figure 2.11a).[286]

2.2.4 Oxygen defects

Although sp^3 functionalization with organic compounds has become the most widely adapted method for the introduction of luminescent defects due to its versatility, the very first observation of defect-related NIR emission was achieved with ozone-treated carbon nanotubes. Ghosh *et al.* subjected dispersions of SWCNTs to ozonolysis by slow addition of ozonated water, followed by irradiation with visible light for several hours (presumably leading to rearrangement of ozonide intermediates).[12] PL spectra of correspondingly treated SWCNT dispersions exhibited new, red-shifted emission features (at $\approx$ 1120 nm for (6,5) SWCNTs). Further

experiments suggested that the use of less aggressive reaction conditions can produce significantly brighter oxygen defects, as shown by Lin *et al.* with hypochlorite under UV irradiation and by Settele *et al.* employing a copper-catalyzed Fenton-type reaction.[222,287] Autoxidation of polyunsaturated fatty acids can produce oxygen-centered radicals that form luminescent defects on the nanotube surface under optical excitation of SWCNTs at the respective E_{22} transition (compare Figure 2.13a).[288]

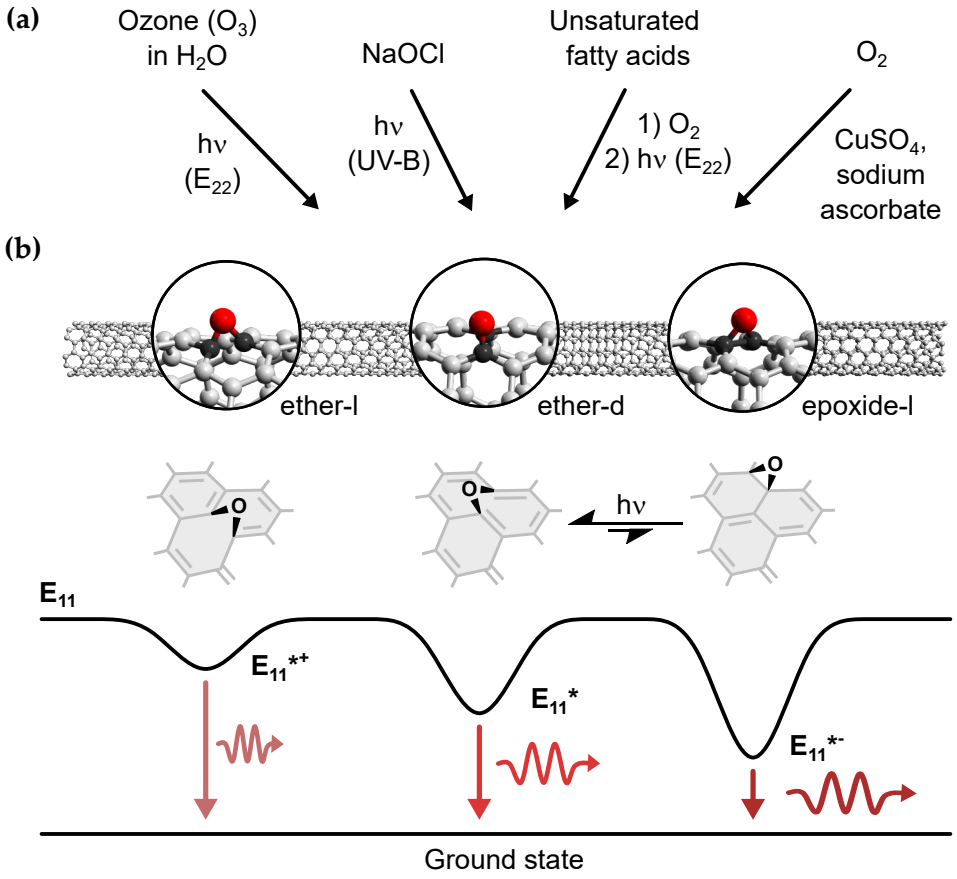

Figure 2.13: (a) Synthetic approaches to create luminescent oxygen defects in SWCNTs (from left to right): Ozonolysis (with ozonated water) and subsequent optical excitation with visible light (SWCNT excitation at E_{22} absorption),[12] photo-induced cleavage of hypochlorite ions to create reactive oxygen species (ROS),[287] autoxidation of polyunsaturated fatty acids followed by E_{22} excitation,[288] Fenton-like reaction with oxygen, copper(II)sulfate and sodium ascorbate.[222] **(b)** Distinct structural configurations of luminescent oxygen defects identified by DFT calculations in conjunction with low-temperature single-nanotube PL spectroscopy: ether-l, ether-d, and epoxide-l binding motifs lead to E_{11}^{*+}, E_{11}^{*}, and E_{11}^{*-} emission peaks, respectively.[219] Oxygen atoms bound in an epoxide-l configuration can rearrange to more stable ether-d defects under irradiation with visible light.[222]

The underlying reaction mechanisms involving ROS are complex, and the outcome of functionalization reactions depend strongly on pH and the concentration of dis-

solved oxygen and radical scavengers.[289] In the solid state, electron beam deposition of oxides (*e.g.*, Al_2O_3, SiO_2) or irradiation of nanotube films on reactive substrates under inert atmosphere also gave rise to oxygen defect emission.[290,291] This type of processing enabled the first observation of room-temperature SPE from carbon nanotubes by incorporation of otherwise untreated (6,5) SWCNTs in SiO_2 matrices.[216]

While luminescent oxygen defects share many optical properties with sp^3 aryl defects, their structural configuration differs significantly. In (6,5) SWCNTs, luminescent oxygen defects lead to additional NIR emission bands at $\approx$ 1120 nm and $\approx$ 1240 nm, which share the nomenclature of sp^3 defects (E_{11}^* and E_{11}^{*-}, respectively). DFT calculations suggest that the E_{11}^* peak can be attributed to an ether-d binding motif (with circumferential orientation of the C-O-C bonds), whereas the E_{11}^{*-} peak is commonly assigned to an epoxide-l structure oriented along the nanotube axis (see Figure 2.13b).[219] Upon irradiation with visible light, epoxide-l defects were shown to partially rearrange to the thermodynamically more stable ether-d configuration,[222] as predicted theoretically.[292] Less red-shifted defect emission peaks at $\approx$ 1050 nm can be identified in PL spectroscopy of functionalized SWCNTs at low temperature (labeled E_{11}^{*+}) and were assigned to ether-l defects with bonds oriented in parallel to the SWCNT axis.[219,290] This assignment is supported by observations of defect state emission at similar wavelengths in thin films of SWCNTs upon annealing on SiO_2 substrates, which should favor the creation of longitudinally oriented C-O-C bonds.[163] The absence of E_{11}^{*+} emission features in liquid-phase samples at room temperature can be rationalized by the low trap depth (resulting in higher thermal detrapping rates) and the selectivity of available methods towards the E_{11}^* binding configuration.

Luminescent oxygen defects were long considered to possess intrinsically lower emission efficiencies compared to sp^3 defects, as the ordering of bright and dark excitonic trap states was theoretically predicted to be reversed (*i.e.*, the energetically lowest exciton of the defect manifold does not correspond to an optically bright state).[210,218] However, recent studies suggest that strong brightening effects, comparable to sp^3 aryl defects, can be observed for oxygen-functionalized SWCNTs as well.[222,293] Previously reported protocols for functionalization with luminescent oxygen defects used fairly harsh reaction conditions, which could have promoted clustering or excessive oxidation of the carbon lattice to form carboxyl or ketone defects lacking luminescent properties.[294–296] In addition to that, the radical reaction pathways leading to the formation of oxygen defects are highly complex and particularly sensitive to pH and the presence of radical scavengers.[289] These findings suggest that more importantly than the possible intrinsic limitation by population of dark states, precise control

over reaction conditions is necessary to produce uniformly distributed and brightly luminescent oxygen defects.

2.3 Raman spectroscopy of SWCNTs

A fundamental understanding of the electronic and vibrational (phonon) structure of low-dimensional materials is crucial to rationally modify their optoelectronic properties. In this regard, Raman spectroscopy is a key experimental technique for the characterization of geometrical structure, chemical composition, lattice defects and doping of nanoscale semiconductors.[297–299] While the inelastic scattering of photons responsible for the Raman effect is intrinsically inefficient (with about one of 10^6 photons undergoing inelastic scattering), the obtained spectra can be remarkably complex and reveal extensive information of the phonon structure and electron-phonon interactions with high resolution. For the investigation of carbon nanotubes, Raman spectroscopy has proven to be particularly powerful by leveraging selective resonance enhancement at the E_{ii} optical transitions,[300] which even enables the spectroscopic characterization of individual SWCNTs.[301,302]

This Chapter provides a brief introduction to the theoretical concepts relevant for Raman scattering processes in SWCNTs, outlines the physical origin of related vibrational modes, and concludes with a section on the characterization and quantification of sp^3 defects with Raman spectroscopy.

2.3.1 Phonon structure

In condensed matter systems, phonons – the quantized collective vibrational excitations of the crystal lattice – strongly influence thermal and charge transport characteristics. Similar to their electronic structure, the phonon dispersion of SWCNTs can be inferred *via* the zone-folding approach from 2D graphene, in which the two carbon atoms of the unit cell give rise to six phonon branches. Three of them are acoustic (A) branches, while the other three are optical (O) phonon branches.[303] One acoustic and one optical phonon branch correspond to atomic vibrations perpendicular to the 2D plane, which constitute the out-of-plane (o) phonon modes. The other acoustic and optical phonon branches are associated with in-plane (i) vibrational motions. All phonons can be further divided into longitudinal (L) or transverse (T) modes depending on the direction of displacement relative to the propagating wave as determined by the wave vector k. Accordingly, the six phonon branches correspond to the longitudinal acoustic (LA), longitudinal optical (LO), in-plane transverse acoustic (iTA), in-plane transverse optical (iTO), out-of-plane transverse acoustic (oTA) and out-of-plane transverse optical (oTO) modes. The LA and LO modes are normal

to the iTA and iTO modes, and all four in-plane vibrations are normal to the out-of-plane (oTA, oTO) motions. A visualization of the atom displacements associated with the six phonon modes of graphene at the high-symmetry Γ and K points is provided in Figure 2.14. At the Γ point, the LO and iTO modes are Raman-active as they possess E_{2g} symmetry, whereas the other modes are Raman-inactive. As graphene is a non-ionic crystal, the LO and iTO modes are degenerate at the Γ point. This degeneracy is lifted by applying strain to the graphene sheet, or intrinsically in SWCNTs due to the lattice curvature.[303,304] While at the K point (where $k \neq 0$), all six phonon branches are, in principle, Raman-active, their intensity critically depends on the magnitude of electron-phonon coupling and the efficiency of the underlying double-resonant scattering processes.

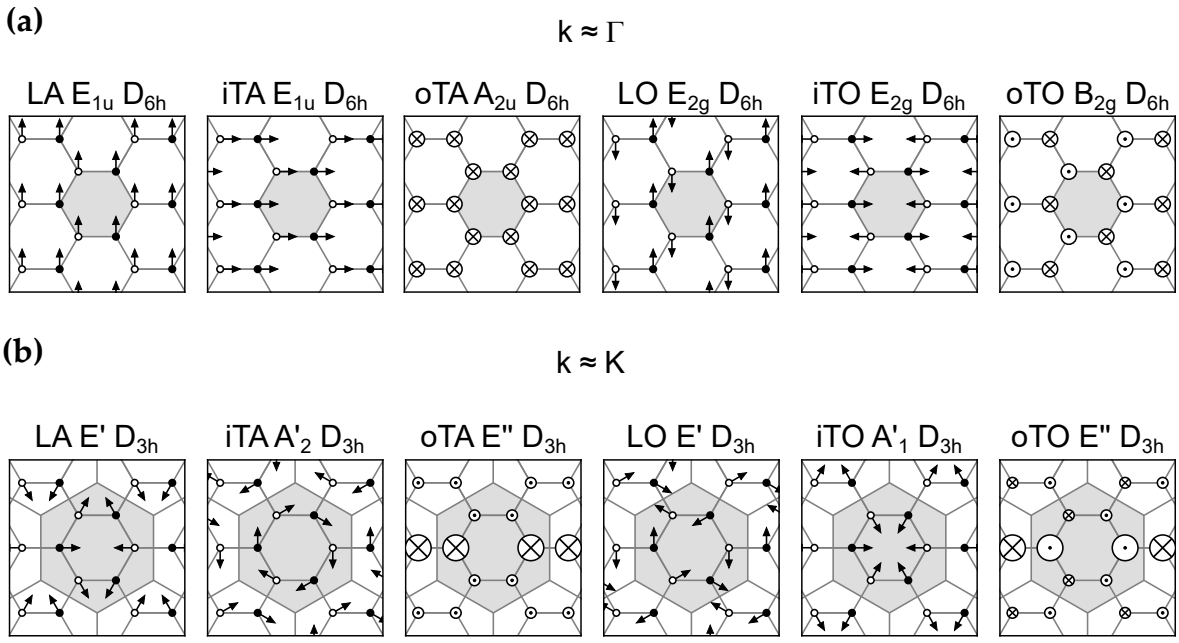

Figure 2.14: Illustration of atomic displacements corresponding to the phonon eigenvectors in graphene at the high-symmetry points Γ **(a)** and K **(b)**. The respective symmetry of the wave vector and space group in Mullikan notation are indicated for each phonon mode.[305]

2.3.2 Raman scattering processes

Raman scattering refers to the emission or absorption of phonons (scattering events) by an electron which has been excited to the conduction band, followed by relaxation of the electron to the valence band under emission of a photon with different energy depending on the phonon contribution. In a Raman spectrum, the intensity of the

scattered light I_s is plotted as a function of the change in energy relative to the incident excitation light, which is commonly referred to as the Raman shift

$$\Delta(1/\lambda_{i,s}) = \frac{10^7}{\lambda_s} - \frac{10^7}{\lambda_i}, \tag{2.13}$$

where λ_i and λ_s denote the wavelength of the incident and scattered light (in nm), respectively, and $\Delta(1/\lambda_{i,s})$ is usually given in units of cm^{-1}.[300] While Raman spectra enable the accurate determination of phonon frequencies, a quantitative interpretation of the corresponding signal intensity I_s requires exact knowledge of the scattering cross section for a given mode. In this regard, full-spectrum Raman excitation mapping (REM) could provide a pathway towards a more quantitative evaluation of peak intensities and Raman scattering cross sections.[306]

With regard to the initial photon absorption and corresponding electronic excitation, resonant and non-resonant excitation can be distinguished. In the case of resonant excitation, the energy of the incident light corresponds to an electronic excitation to a real state in the conduction band of graphene or SWCNTs. If this condition is not met, non-resonant excitation to a virtual state occurs, which is associated with signal intensities three orders of magnitude lower in comparison to resonant excitation. Furthermore, in resonant Raman processes, incident and scattered resonance can be distinguished. The former occurs if the energy separation between the ground and excited electronic state corresponds to the energy carried by the incident photon ($E_L = \Delta E$). Scattered resonance occurs when the energy of the excitation light matches the energy of the outgoing photon after interaction with a phonon of energy E_q ($E_L = \Delta E + E_q$). For SWCNTs, this resonance enhancement is particularly strong due to the vH singularities in the DOS, which forms the basis for efficient detection of (n, m) species in the presence of other, off-resonance SWCNTs.[297]

The vibrational relaxation following excitation of an electron to the conduction band can proceed *via* a one-, two-, or multi-phonon emission process. In such a series, the order of a particular scattering event is defined by the position of the event in the overall sequence. Due to the requirement of momentum conservation for photon absorption and emission, recombination of excited electrons and holes only occurs if the difference between the scattered state is smaller than twice the value of the photon wave vector. As photon wave vectors are considerably smaller than electron crystal momenta, zero-center (Γ point) phonon modes, which correspond to a first-order scattering process, can be observed in Raman spectroscopy. Second-order Raman scattering involves either inelastic scattering by two phonons, or a combination of one inelastic scattering event and elastic scattering at lattice

defects or crystal edges.[297] A summary of Raman scattering processes categorized by resonance type (incident or scattered), order, and number of involved phonons is given in Figure 2.15.

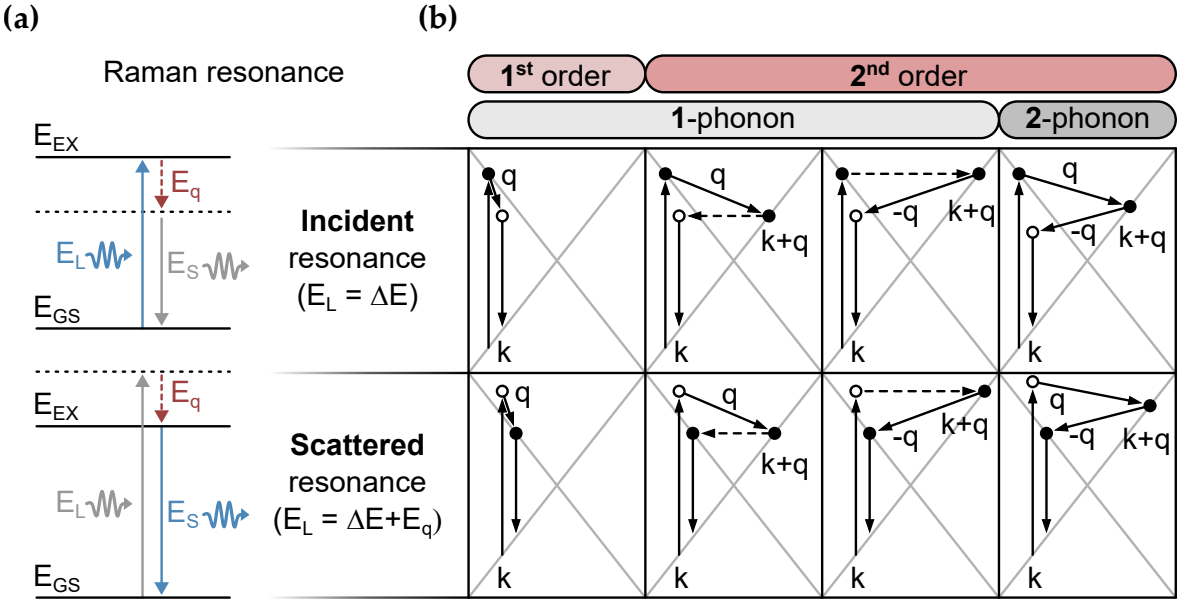

Figure 2.15: Schematic of Raman scattering processes in graphene and SWCNTs. **(a)** Excitation light (E_L) can be resonant with the energy separation between the ground (E_{GS}) and excited (E_{EX}) state, which gives incident resonance. In contrast, scattered resonance occurs if the difference between E_{GS} and E_{EX} corresponds to the energy of the outgoing photon (E_S) after scattering with a phonon of energy E_q. **(b)** Classification of incident and scattered resonance by order (1st order, 2nd order) and number of involved phonons. Resonance points in the electronic structure are indicated by filled circles, and horizontal dashed lines indicate elastic scattering (*e.g.*, at lattice defects).

The complexity of the phonon structure and variety of potential scattering processes in SWCNTs gives rise to numerous Raman modes, which exhibit distinct dependencies on nanotube diameter, excitation wavelength, and the presence of lattice defects. The following section provides an overview over the most prominent modes in SWCNTs, their physical origin, and the information which can be extracted from these features in Raman spectra recorded under different conditions (for a representative Raman spectrum of (6,5) SWCNTs, see Figure 2.16).

G-mode

The G-mode is present in all sp^2-hybridized carbon materials and results from an in-plane vibrational stretching motion of carbon-carbon bonds. It is associated with a first-order phonon scattering process, and its line shape closely follows that of a single Lorentzian peak in graphene.[307,308] In SWCNTs, the G-mode splits into several peaks

due to the circumferential confinement of phonon modes and curvature-induced bond strain, and the frequencies of circumferentially oriented phonon modes are lowered.[309] In total, six peaks can be observed in SWCNT Raman spectra, split into two sets of three with A_1, E_1, and E_2 symmetry. The most prominent modes are labeled G^+ ($\approx 1595\,cm^{-1}$) and G^- ($\approx 1570\,cm^{-1}$), and belong to A_1 and E_1 symmetry, respectively. Frequently observed peaks of lower intensity were identified as G-modes with E_2 symmetry in polarization-sensitive Raman experiments.[310] As the G^--mode corresponds to a circumferentially oriented iTO phonon, its frequency exhibits a dependence on nanotube diameter d_t, which can be determined on the level of individual SWCNTs.[301,307,311] In contrast, the G^+-mode is associated with a LO phonon mode (compare Figure 2.14a) and practically independent of d_t. The profile of the G^--mode can be used to determine whether a given SWCNT is metallic (Breit-Wigner-Fano line shape) or semiconducting (Lorentzian line shape).[312,313] The sensitivity of the G-modes on the electronic states in SWCNTs is also reflected in changes which occur upon chemical or electrical doping. For p-doping of SWCNTs, up-shifts of ω_{G^+} were reported due to reduced electron-phonon coupling, whereas n-doping leads to a decrease in ω_{G^+}.[297,314,315]

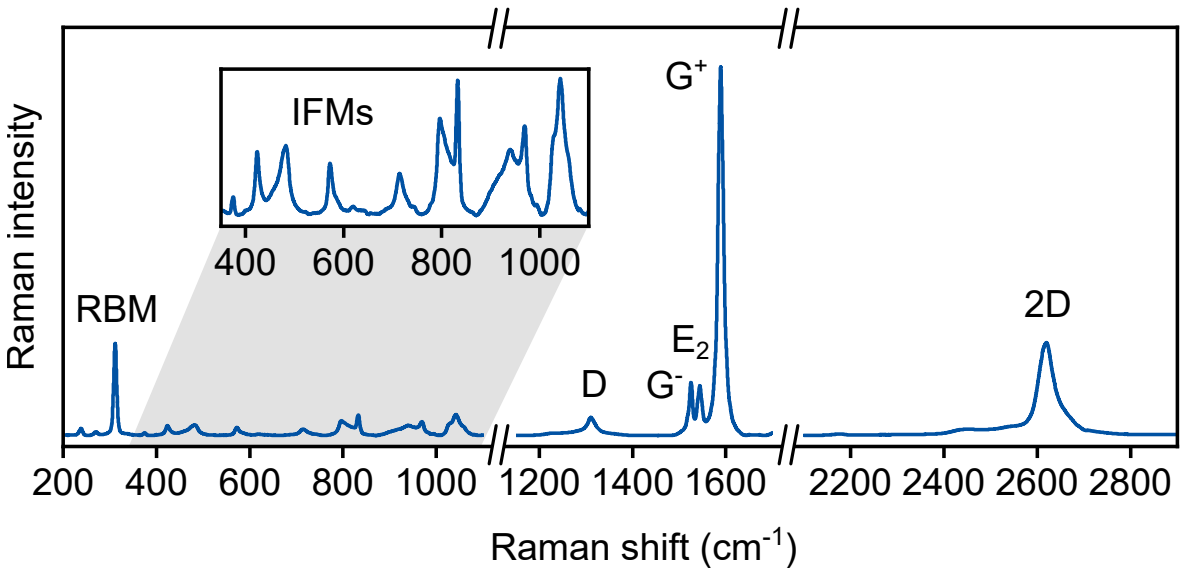

Figure 2.16: Resonant Raman spectrum of (6,5) SWCNTs and assignment of RBM, D-mode, G^--mode, G-mode-associated peak with E_2 symmetry, G^+-mode and 2D-mode, with detail of the IFM region (inset).

Radial breathing mode

The radial breathing mode (RBM) is a phonon mode exclusively observed in SWCNTs, and occurs in the range from $\approx 120 - 350\,cm^{-1}$ for nanotubes with diameters of $0.7 - 2.0\,nm$.[297,316,317] The RBM results from the cylindrical shape of SWCNTs and corresponds to a radial oscillation of the SWCNT lattice. It is a first-order pro-

cess and emerges from the oTA phonon branch at the Γ point in graphene (compare Figure 2.14a). The intensity of the RBM is closely related to the SWCNT curvature and becomes extremely weak for larger-diameter nanotubes ($d_t > 2.0\,nm$). This is in accordance with theoretical descriptions of the RBM which indicate a vanishing frequency and intensity for the oTA phonon branch in the limit of a flat graphene sheet ($d_t \rightarrow \infty$).[318] The RBM frequency ω_{RBM} is inversely proportional to the nanotube diameter according to

$$\omega_{RBM} = \frac{227}{d_t}\sqrt{1 + C_e \cdot d_t^2}, \tag{2.14}$$

where C_e denotes an empirical factor which quantifies the interaction of SWCNTs with the environment. For surfactant-dispersed SWCNTs or nanotube bundles, values of $C_e = 0.056$ closely model the relation between d_t and the RBM frequency.[319–321] In combination with the Raman resonance effect for nanotube excitation at the respective E_{ii} optical transition, the dependence of ω_{RBM} on nanotube diameter enables the assignment of (n, m) species in resonant Raman experiments.[301] This relation has found widespread use for SWCNT identification *via* (near-)resonant Raman spectroscopy.[316] Notably, the intensity ratio of the RBM and G^+-mode varies considerably for different nanotube species, as electron-phonon coupling in SWCNTs is highly dependent on chiral angle and SWCNT family (where $(n - m) \bmod 3 = 1 \text{ or } 2$ are distinguished).[322]

2D-mode

Similar to the G-mode, the 2D-mode is present in all sp^2-hybridized carbon materials in the range from $2500 - 2800\,cm^{-1}$.[297] It corresponds to a breathing-like in-plane vibrational motion of the carbon atoms contained in one hexagon (*i.e.*, the iTO phonon mode at the K point, compare Figure 2.14b). This process is not Raman-active in first-order scattering and only observed as an overtone.[300] The Raman D-mode, which is discussed below, can be identified at approximately half the frequency of the 2D-mode, and both modes share the same symmetry with regard to the underlying vibrational motion of the carbon atoms. Note that in some early publications, the 2D-mode is referred to as G'-mode. In pristine graphene, the 2D-mode line shape corresponds to a single Lorentzian, but experiences some deformation in other sp^2 carbon materials.[323–326] In contrast to the previously discussed RBM and G-mode, the 2D-mode results from a second-order two-phonon scattering process near the K point.[321,327] In second-order Raman scattering, the electron can return to its initial position k after interaction with two phonons with momentum q and -q (compare Figure 2.15b). As the resonance vector k diverges from the K point with increasing excitation energy E_L, the involved phonons modes change their energy, and the cor-

responding frequency changes with E_L (referred to as dispersive behavior).[297] The high absolute frequency of the 2D-mode makes it particularly sensitive towards small relative changes in nanotube geometry or electronic structure. For this reason, the 2D-mode has been at the center of Raman studies focusing on strain characterization[328] and SWCNT doping.[329]

D-mode

The presence of defects in the sp^2-hybridized SWCNT lattice can substantially change the appearance of corresponding Raman spectra. At a defect site, elastic scattering of an electron in combination with the first-order component of the hexagon breathing mode leads to the activation of a double-resonance peak centered at $\approx 1320\,cm^{-1}$.[330,331] This feature is referred to as the D-mode and associated with an in-plane optical phonon mode.[297] The D-mode shows dispersive behavior[332,333] and exhibits an inverse correlation between Raman shift and nanotube diameter.[334–336] More detailed analyses indicated that the fine structure of the D-mode actually consists of multiple peaks, which was attributed to the phonon dispersion anisotropy around the K point and resonance effects due to vH singularities.[330,333,337] In practice, the D-mode is particularly important for the identification and assessment of defects and structural modifications in sp^2-hybridized carbon materials,[300] which will be the focus of Chapter 2.3.3.

Intermediate frequency modes

Intermediate frequency modes (IFMs) are low-intensity Raman-active modes observed in the spectral region from 400 to $1100\,cm^{-1}$, between the RBM and D-mode.[300] These modes are associated with double-resonance Raman scattering processes and combination modes, but their precise origin and assignment has been a subject of debate.[338] In the IFM region, modes with dispersive and non-dispersive behavior were identified, and some were classified as defect-induced, whereas others were related to two-phonon processes or rationalized as being activated due to the finite length of SWCNTs.[339–345] Some of the observed features were assigned to the out-of-plane ZA phonon branch (also referred to as oTA,[321] at $\approx$ $400\,cm^{-1}$), the ZA overtone (2ZA, at $\approx$ $800\,cm^{-1}$), an oTO phonon mode (at $\approx$ $850\,cm^{-1}$), and a combination mode of the ZA and iTO phonon (iTO-ZA, at $\approx 900\,cm^{-1}$).[338,345] Despite the complex patterns and low signal intensities of IFMs, the involvement of second-order, one- and two-phonon scattering processes could open up new opportunities for defect characterization in highly pure SWCNT samples.

2.3.3 Defect characterization and quantification

Raman scattering processes are highly sensitive towards defects and structural modifications of the pristine sp^2-hybridized carbon lattice. For this reason and due to its non-invasive nature, Raman spectroscopy has become a standard technique to probe the defectiveness and degree of functionalization in graphene[346–354] and SWCNTs.[355–361] This includes atom substitutions, the replacement of hexagon structures by 5-7 ring defects, grain boundaries, presence of amorphous carbon, tube ends, and sp^3 defects.[300] The presence of these and related structural defects is typically accompanied by an increase in the intensity of the Raman D-mode. For point defects, assuming that their number remains small compared to the absolute number of lattice carbon atoms, the ratio of the Raman D- to $G^{(+)}$-mode intensity is expected to be proportional to the ratio of sp^3-to-sp^2-hybridized carbon atoms. Thus, the Raman $D/G^{(+)}$ ratio can be used as a metric for the relative determination of the lattice defect density.

For graphene, Cançado *et al.* expanded this approach to an absolute method by correlating Raman D/G ratios with defect densities determined by scanning tunneling microscopy of Ar^+-bombarded graphene samples.[347] The resulting empirical expression can be used to estimate the average defect distance L_d from the measured Raman D- and G-mode intensity ratio I_D/I_G:

$$L_d^2 = (1.8 \pm 0.5) \cdot 10^{-9} \lambda_L^4 \left(\frac{I_D}{I_G} \right)^{-1} . \tag{2.15}$$

By including the dependence of Raman D/G ratios on the excitation laser wavelength λ_L, Equation 2.15 enables the direct quantification of graphene lattice defects for arbitrary excitation energy.[347] A fundamental prerequisite for this benchmark study was the availability of high-quality graphene obtained from mechanical exfoliation. In the case of SWCNTs, a similar equation was not available until recently.

The following section briefly summarizes an absolute method for the quantification of luminescent sp^3 defects in SWCNTs, which was developed prior to and in the early phase of the work presented in this thesis. It was published in Sebastian *et al.*, *J. Phys. Chem. Lett.* **13**, 3542-3548 (2022).[19] Modified versions of previously published Figures are presented with permission of the American Chemical Society.

To establish an absolute quantitative expression for defect densities in SWCNTs, experimentally obtained Raman D/G^+ ratios need to be correlated to defect densities determined in real-space measurements. However, statistical analysis of single

defect sites in SWCNTs with electron microscopy still presents a significant challenge due to insufficient resolution, the cylindrical geometry of SWCNTs, and their tendency to form bundles. This limitation can be circumvented by a theoretical model which enables the calculation of the absolute defect density from the reduction of experimentally determined E_{11} PLQYs upon functionalization. The underlying model, referred to as diffusion-limited contact quenching (DLCQ),[167] enables an estimation of defect densities with the assumption that quenching sites and luminescent defects present local trap states and compete with the radiative decay of highly mobile E_{11} excitons (see Figure 2.17a). For pristine SWCNTs, the E_{11} PLQY can be expressed as[167,210]

$$\eta = \frac{\pi}{2\, n_q^2\, D\, \tau_{rad}}, \tag{2.16}$$

where n_q denotes the density of non-radiative defects (*e.g.*, defects introduced by liquid-phase processing, sonication, and tube ends). For the E_{11} exciton diffusion constant D and intrinsic radiative lifetime τ_{rad}, values of $(10.7 \pm 0.4)\,cm^2\,s^{-1}$ and $(3.35 \pm 0.41)\,ns$ are taken from experimental studies.[167,362] Upon introduction of luminescent defects (with unknown density n_d), the PLQY associated with the E_{11} state η^* in functionalized SWCNTs is given by

$$\eta^* = \frac{\pi}{2\,(n_q + n_d)^2\, D\, \tau_{rad}}. \tag{2.17}$$

The combination of Equations 2.16 and 2.17 readily provides an expression for the absolute density of luminescent defects:

$$n_d = n_q \left(\sqrt{\frac{\eta}{\eta^*}} - 1\right) = \sqrt{\frac{\pi}{2\,\eta\, D\, \tau_{rad}}} \left(\sqrt{\frac{\eta}{\eta^*}} - 1\right). \tag{2.18}$$

The application of Equation 2.18 to spectrally-resolved PLQY values for the E_{11} emission of pristine and functionalized SWCNTs yields absolute defect densities n_d, to which other nanotube properties such as charge transport characteristics can be related.[363] Notably, a linear relation

$$n_d = (414 \pm 11)\,\mu m^{-1} \cdot \Delta\left(\frac{I_D}{I_{G^+}}\right) \tag{2.19}$$

is obtained between the change of integrated Raman D/G^+ ratios and calculated defect densities for (6,5) SWCNTs at an excitation laser wavelength of 532 nm (see Figure 2.17b-e).

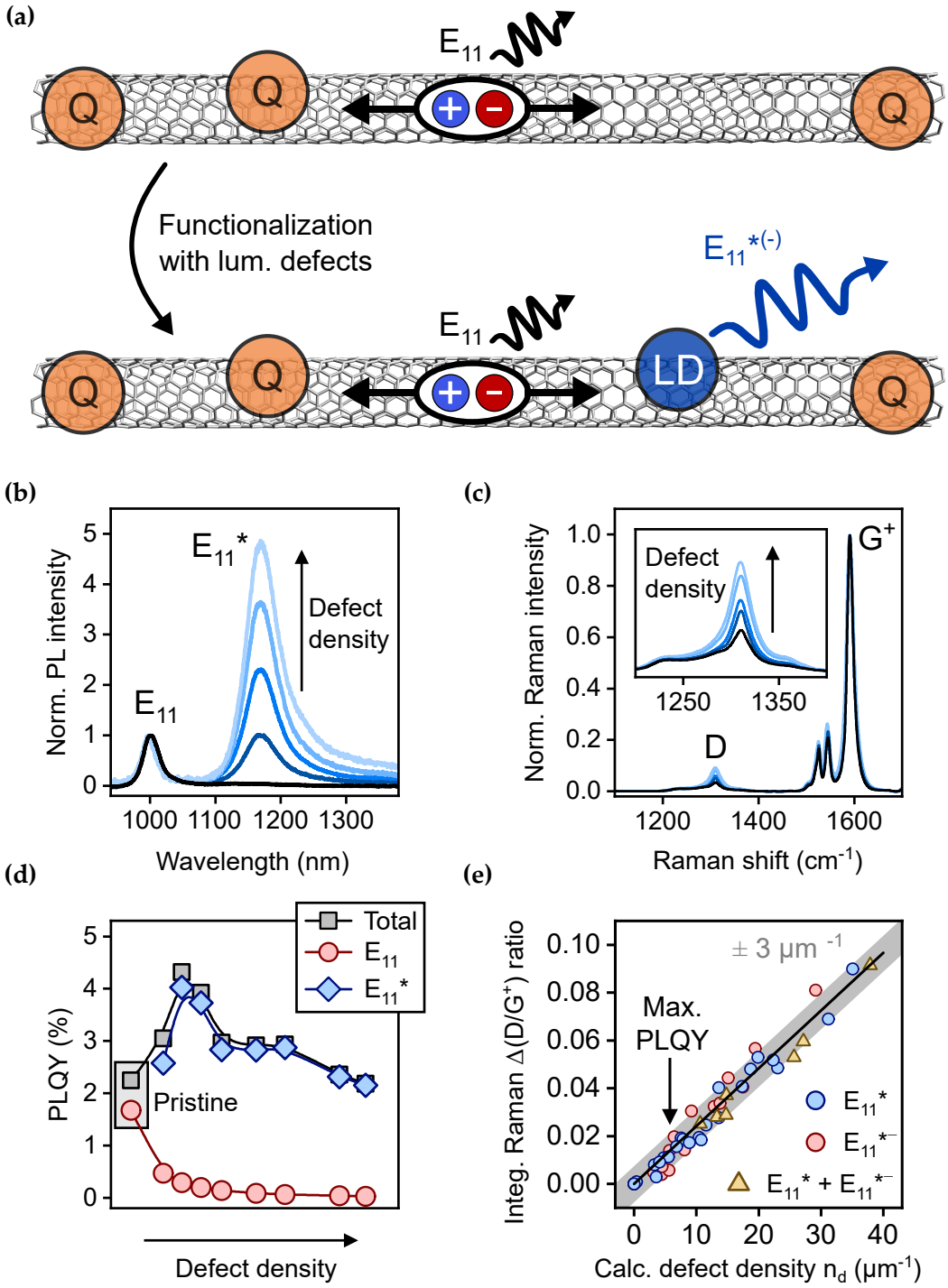

Figure 2.17: Absolute quantification of luminescent sp^3 defects in (6,5) SWCNTs.[19] **(a)** Diffusion-limited contact quenching of E_{11} excitons in SWCNTs, where the functionalization with luminescent sp^3 defects creates a new exciton decay pathway that leads to a reduction of the intrinsic E_{11} PLQY. **(b)** Normalized PL spectra of pristine and sp^3-functionalized (6,5) SWCNTs at different relative defect densities (E_{11}^* binding configuration). **(c)** Normalized Raman spectra of pristine and functionalized (6,5) SWCNTs (inset with detail of the Raman D-mode) at different defect densities. **(d)** Change of spectrally resolved PLQYs for (6,5) SWCNTs with increasing levels of luminescent sp^3 defects. **(e)** Plot of integrated Raman $\Delta(D/G^+)$ ratio *vs* defect densities n_d as calculated from E_{11} PLQYs according to Equation 2.18. A linear fit to the data (solid line) yields the corresponding calibration curve (see Equation 2.19).

Here, I_{D/G^+} denotes the integrated intensity ratio of the respective Raman modes. Note that the differential $\Delta(D/G^+)$ ratio is used instead of absolute values to ensure comparability between various nanotube raw materials and processing techniques, which typically result in different D/G^+ ratios for pristine SWCNTs (prior to sp^3 functionalization). Consequently, the calibration curve expressed by Equation 2.19 enables the absolute quantification of additionally introduced luminescent defects in (6,5) SWCNTs. The method is applicable to both E_{11}^* and E_{11}^{*-} defect binding configurations, as well as to SWCNTs functionalized in aqueous dispersions.[19]

While the outlined method for the absolute quantification of luminescent defects has become a useful tool for the characterization of functionalized SWCNTs,[266,267,363–365] it is limited to (6,5) SWCNTs at a Raman laser excitation wavelength of 532 nm. A more versatile quantification method that is applicable to different SWCNT species at arbitrary excitation wavelengths is highly desirable. However, the Raman intensity associated with a single SWCNT species changes dramatically with excitation energy due to the 1D nature of electronic states and phonon modes.[306,366] Thus, highly purified and nearly monochiral samples are required to unambiguously identify a relation between the Raman D/G^+ ratio and laser excitation energy for different nanotube species with distinct optical resonances. With recent progress in nanotube sorting and purification techniques, the opportunity for such a systematic evaluation has arrived, as Chapter 3 will demonstrate.

3 Unified quantification of luminescent defects in SWCNTs

This Chapter includes a publication which details the development of a method for the absolute quantification of luminescent defects in small-diameter SWCNTs based on Raman spectroscopy at arbitrary excitation energy.

For the original publication, refer to Sebastian *et al.*, *ACS Nano* **17**, 21771-21781 (2023).

Formblatt Kumulative Dissertation

1. Publikation/*Publication:*

Vollständige bibliographische Referenz/*Complete bibliographic reference:*

Finn L. Sebastian, Felicitas Becker, Yohei Yomogida, Yuuya Hosokawa, Simon Settele, Sebastian Lindenthal, Kazuhiro Yanagi, and Jana Zaumseil. *Unified quantification of quantum defects in small-diameter single-walled carbon nanotubes by Raman spectroscopy*. *ACS Nano* **17**, 21771-21781 (2023),
DOI: 10.1021/acsnano.3c07668.

2. Erstautorenschaft/*First authorship:* **Ja/*Yes***

3. Veröffentlicht/*Published:* **Ja/*Yes***

4. Beteiligungen/*Contributions (according to Contributor Role Taxonomy, CRediT):*

Contributor role	Doctoral student
Last name, first name	Sebastian, Finn Luca
Methodology	×
Software	
Validation	×
Formal analysis	×
Investigation	×
Resources	
Data curation	×
Writing - original draft	×
Writing - review and editing	×
Visualization	×
Supervision	×
Project administration	
Funding acquisition	

Hiermit bestätige ich, dass alle obigen Angaben korrekt sind.
I confirm that all declarations made above are correct.



Finn Luca Sebastian
Doktorand/*Doctoral student*

Betreuungsperson/*Supervisor:*
Hiermit bestätige ich, dass alle obigen Angaben korrekt sind und dass die selbstständigen Arbeitsanteile des Doktoranden an der aufgeführten Publikation hinreichend und signifikant sind.
I confirm that all declarations made above are correct and that the doctoral student's independent contribution to this publication is significant and sufficient to be considered for the cumulative dissertation.



04.08.2025

Prof. Dr. Jana Zaumseil

Datum/*Date*

ACS NANO

Open Access

This article is licensed under CC-BY-NC-ND 4.0

www.acsnano.org

ARTICLE

Unified Quantification of Quantum Defects in Small-Diameter Single-Walled Carbon Nanotubes by Raman Spectroscopy

Finn L. Sebastian, Felicitas Becker, Yohei Yomogida, Yuuya Hosokawa, Simon Settele, Sebastian Lindenthal, Kazuhiro Yanagi, and Jana Zaumseil*

Cite This: *ACS Nano* 2023, 17, 21771–21781

Read Online

ACCESS | Metrics & More | Article Recommendations | Supporting Information

ABSTRACT: **The covalent functionalization of single-walled carbon nanotubes (SWCNTs) with luminescent quantum defects enables their application as near-infrared single-photon sources, as optical sensors, and for *in vivo* tissue imaging. Tuning the emission wavelength and defect density is crucial for these applications. While the former can be controlled by different synthetic protocols and is easily measured, defect densities are still determined as relative rather than absolute values, limiting the comparability between different nanotube batches and chiralities. Here, we present an absolute and unified quantification metric for the defect density in SWCNT samples based on Raman spectroscopy. It is applicable to a range of small-diameter semiconducting nanotubes and for arbitrary laser wavelengths. We observe a clear inverse correlation of the D/G$^+$ ratio increase with nanotube diameter, indicating that curvature effects contribute significantly to the defect activation of Raman modes. Correlation of intermediate frequency modes with defect densities further corroborates their activation by defects and provides additional quantitative metrics for the characterization of functionalized SWCNTs.**

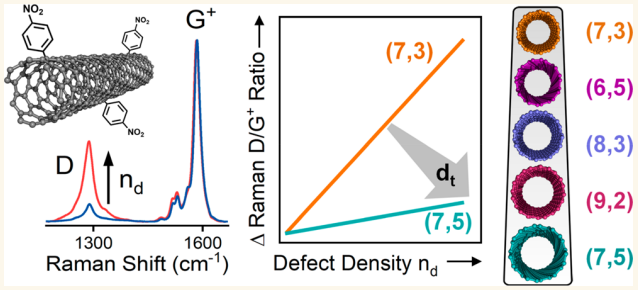

KEYWORDS: *single-walled carbon nanotubes, luminescent sp^3 defects, defect quantification, Raman spectroscopy, D/G ratio, diameter dependence*

Semiconducting single-walled carbon nanotubes (SWCNTs) with luminescent defects introduced by sp^3 functionalization have become an attractive material platform for bioimaging,[1,2] optical sensing,[3−5] electroluminescent devices,[6,7] and single-photon sources[8,9] in the near-infrared (nIR), especially beyond 1000 nm. These quantum defects are typically created by covalent functionalization of the sp^2-hybridized carbon lattice of SWCNTs with aryl or alkyl groups resulting in few sp^3 carbon atoms along the nanotube and corresponding changes in the local electronic structure.[10] The defects form energetically lower lying emissive states that act as zero-dimensional traps for mobile excitons, leading to further red-shifted narrow-band photoluminescence (PL) compared to pristine nanotubes and PL lifetimes of hundreds of picoseconds.[11,12] Due to the localization of previously mobile excitons, the overall PL quantum yield (PLQY) can increase substantially[13] and room-temperature single-photon emission can be observed.[8,9]

The emission wavelength of luminescent sp^3 defects is largely determined by the nanotube (n,m) chirality and the binding configuration of the defect on the nanotube lattice.[11,14] The latter can be selected by the choice of the functionalization method.[9,15,16] The degree of functionalization and hence the number of defects per nanotube length can be tuned by the reaction time or concentration of reactants and must be adjusted depending on the intended application. With ongoing efforts to utilize sp^3-functionalized SWCNTs for a variety of applications ranging from cancer detection to quantum information processing,[4,17] the ability to reliably and easily determine the precise density of sp^3 defects in a nanotube sample has become crucial to characterize and control their impact on the optical and electronic properties of SWCNTs.

For graphene, a method to determine the number density of point-like structural defects is well-established and has even

Received: August 15, 2023
Accepted: October 13, 2023
Published: October 19, 2023



ACS Publications

© 2023 The Authors. Published by American Chemical Society

https://doi.org/10.1021/acsnano.3c07668
ACS Nano 2023, 17, 21771–21781

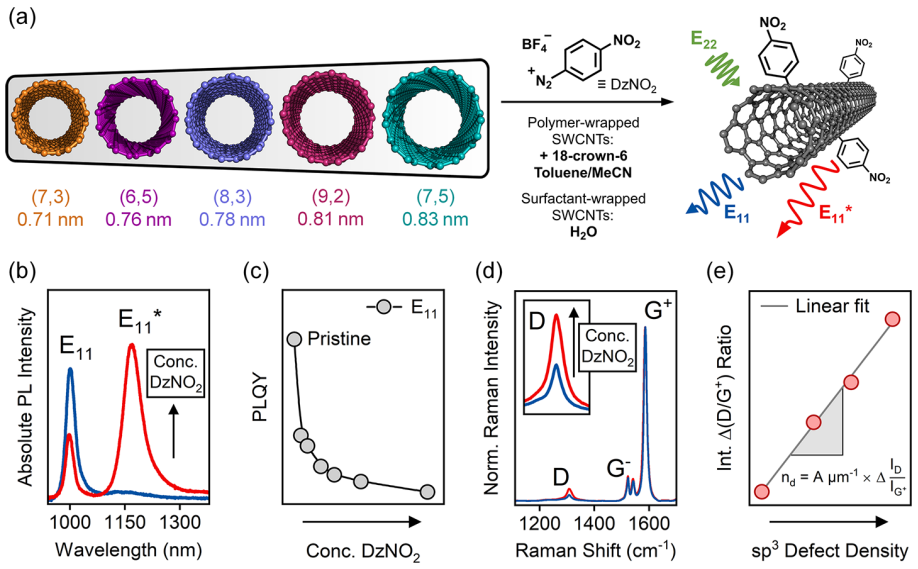

Figure 1. (a) Investigated SWCNT chiralities with different diameters and the reaction scheme for sp^3 functionalization using 4-nitrobenzenediazonium tetrafluoroborate ($DzNO_2$) in different solvent systems. Luminescent sp^3 defects act as trapping sites for mobile excitons created by E_{22} excitation, giving rise to red-shifted E_{11}* emission in addition to E_{11} emission. (b) Exemplary PL spectra of sp^3-functionalized (6,5) SWCNTs (red) showing E_{11}* emission compared to pristine nanotubes (blue). (c) PLQY of only the E_{11} emission for pristine and sp^3-functionalized (6,5) SWCNTs. The line is a guide for the eye. (d) Normalized average Raman spectra of pristine and sp^3-functionalized (6,5) SWCNTs and assignment of characteristic D, G^-, and G^+ modes, with the inset showing the D-mode. (e) Correlation of integrated differential Raman $\Delta(D/G^+)$ ratios with sp^3 defect densities calculated from E_{11} PLQY and a linear fit to the data.

been expanded to line defects.[18,19] It is based on Raman spectroscopy, which is highly sensitive to structural deformations of the carbon lattice. To obtain a quantitative model, Raman spectra were cross-correlated with the number of defects introduced by ion bombardment as determined by scanning tunneling microscopy.[20] A higher defect density was accompanied by a larger D-mode intensity (originating from second-order Raman scattering processes involving one phonon and elastic scattering at a defect site) relative to the G-mode intensity (proportional to the number of sp^2-hybridized carbon atoms). The resulting empirical expression for the average defect distance L_d in graphene also includes the dependence of the observed D/G intensity ratio (I_D/I_G) on the excitation laser wavelength λ_L:[18]

$$L_d^{\,2}\ (\mathrm{nm}^{-2}) = (1.8 \pm 0.5) \times 10^{-9} \lambda_L^{\,4} \cdot \left(\frac{I_D}{I_G}\right)^{-1} \quad (1)$$

This simple metric enables the absolute quantification of defects in graphene and has been used frequently to determine not only the quality after exfoliation[21] but also the degree of covalent functionalization.[22]

In contrast to that, the development of a universal metric to quantify the number of defects in SWCNTs has proven difficult. Similar to graphene, second-order Raman scattering processes at defect sites give rise to a D-mode around 1320 cm^{-1}. Its intensity relative to the G^+ optical phonon mode of the sp^2-hybridized carbon lattice is commonly used as a relative indicator for the presence of defects.[23,24] The wavenumber of the D-mode in SWCNTs also shows a dependence on excitation laser energy and nanotube diameter.[25−27] Although it was speculated that the quantification metric developed for graphene might also be applicable to other sp^2-hybridized carbon materials,[28] only a few attempts were made to systematically correlate D/G^+ ratios from Raman spectra of SWCNTs with defect densities obtained by independent measurements.[29−31] Compared to the atomically defined monolayers of graphene produced by chemical vapor deposition or mechanical exfoliation, the controlled introduction and direct real-space evaluation of structural defects in SWCNTs are difficult due to their cylindrical geometry and bundling effects in bulk samples. Furthermore, the purification of SWCNT raw material is usually carried out in the liquid phase and yields a distribution of different chiralities, diameters, and lengths depending on the specific protocol,[32,33] which have additional effects on the measured Raman modes.

Recently, we have shown that a linear correlation between the integrated Raman D/G^+ mode ratio at a fixed excitation wavelength and defect densities obtained from absolute PLQY measurements of pristine and covalently functionalized SWCNTs can be used to directly quantify the number of introduced sp^3 defects in (6,5) SWCNTs.[34] While this quantification method was shown to be reliable for (6,5) nanotubes in different types of dispersions (organic solvent or aqueous), for different lengths of nanotubes, and even for different types of sp^3 defects, it remained unclear if it could also be applied to other SWCNT chiralities and diameters as well as for different Raman excitation wavelengths similar to graphene.

Here, we introduce a unified empirical expression for the quantification of sp^3 defects in small-diameter (<1 nm) semiconducting SWCNTs using the D/G^+ ratios obtained from Raman spectra collected at arbitrary excitation wavelengths. We find a dependence of the linear calibration factor on the nanotube diameter, which indicates a strong impact of the curvature and strain on defect-activated Raman modes. This generalized approach provides a noninvasive and fast way to quantify the absolute number of sp^3 defects in various SWCNTs using only Raman spectroscopy. In addition to the familiar D-mode, we also consider other defect-activated Raman modes in the intermediate frequency range of

https://doi.org/10.1021/acsnano.3c07668
ACS Nano 2023, 17, 21771−21781

SWCNTs as quantitative metrics for the sp^3 functionalization of nanotubes.

RESULTS AND DISCUSSION

SWCNT Functionalization and Quantification of sp^3 Defects. Monochiral dispersions of small-diameter, semiconducting SWCNTs were prepared either by selective polymer-wrapping in toluene or by gel-chromatography of SWCNTs stabilized by surfactants in water. To prepare dispersions of (6,5) and (7,5) SWCNTs, CoMoCAT raw material was dispersed by shear force mixing in toluene solutions of different polyfluorene-based polymers.[35] Aqueous dispersions of (7,3), (8,3), and (9,2) SWCNTs were obtained from HiPco raw material employing a previously reported procedure based on a high-performance liquid chromatography (HPLC) system (for details, see Experimental Methods).[36] Prior to sp^3 functionalization, the purity of the pristine SWCNT dispersions was assessed by UV−vis−nIR absorption spectroscopy, PL excitation−emission mapping, and Raman spectroscopy. Absorption spectra of pristine SWCNT dispersions (see Figure S1 in the Supporting Information) show the characteristic E_{11} and E_{22} optical transitions along with the respective phonon side bands but essentially no indication of any other SWCNT chiralities except for residual (7,6) SWCNTs in the (7,5) nanotube dispersion. The PL excitation−emission maps in Figure S2 in the Supporting Information show the characteristic E_{11} emission at E_{22} excitation for each purified nanotube chirality and no additional semiconducting SWCNT species. The (n,m) chiral index assignment and absence of metallic carbon nanotubes was further confirmed using averaged Raman spectra in the region of the radial breathing modes (RBM) at excitation wavelengths of 532, 633, and 785 nm (see Figure S3 in the Supporting Information).[37,38] Lorentzian fits of Raman peaks in the region from 1500 to 1700 cm^{-1} (see Figure S4 in the Supporting Information) reveal the characteristic diameter dependence of the G^+ and G^- mode frequencies in agreement with the model by Telg et al.[39]

The different pristine SWCNTs were covalently functionalized with luminescent sp^3 defects using 4-nitrobenzenediazonium tetrafluoroborate ($DzNO_2$) as shown in Figure 1a, and the degree of sp^3 functionalization was tuned by adjusting the diazonium salt concentration. The functionalization of SWCNT dispersions in water was achieved by simply adding an aqueous solution of $DzNO_2$,[13] whereas the functionalization of polymer-wrapped nanotubes in toluene was aided by 18-crown-6 as a phase-transfer reagent.[40] The appearance of an additional red-shifted emission (E_{11}*) in the PL spectra of functionalized SWCNTs confirmed the introduction of luminescent sp^3 defects, as shown exemplarily for (6,5) SWCNTs in Figure 1b. While the total PLQY of the SWCNT dispersions at low-to-medium functionalization levels increased due to efficient trapping of highly mobile excitons at sp^3 defects and their radiative decay, the PLQY related only to the E_{11} emission always decreased (see Figure 1c). From this decrease of E_{11} PLQY compared to pristine nanotubes, the number density of luminescent sp^3 defects was calculated using the diffusion-limited contact quenching (DLCQ) model for excitons in SWCNTs.[41] Mobile excitons either decay radiatively through E_{11} emission or undergo nonradiative quenching at nanotube ends or lattice defects.[42,43] In the presence of luminescent sp^3 defects, the E_{11} PLQY is also reduced as excitons are trapped and recombine at the sp^3 defects, leading to the E_{11}* PL emission. An analytical expression for the density of introduced luminescent sp^3 defects (n_d in μm^{-1}) independent of the number of initial quenching sites can be derived based on the ratio of the E_{11} PLQY of pristine and sp^3-functionalized SWCNTs (η and η*, respectively; for details of the calculation and PLQY measurements see Experimental Methods).

The calculated sp^3 defect densities also depend on the chosen values for exciton diffusion constant D and E_{11} radiative lifetime τ_{rad}. Reported values for D are typically within a range of 2−10 $cm^2\ s^{-1}$,[43−45] whereas τ_{rad} was determined to be on the order of a few nanoseconds.[46,47] While there have only been a few studies on the effect of nanotube diameter and chirality on D and τ_{rad}, the available data consistently suggest no significant variations or clear trends in the investigated range of nanotube diameters.[47−49] Thus, D and τ_{rad} as determined for (6,5) SWCNTs in previous experimental studies[42,46] were employed for all calculations of sp^3 defect densities irrespective of nanotube chirality. Independent counting of defect emission peaks from single nanotubes at cryogenic temperatures for different batches of functionalized (6,5) nanotubes previously indicated that the defect densities obtained with the described DLCQ method were indeed very close to the average numbers within the nanotube ensemble.[34]

Raman Spectroscopy of Functionalized SWCNTs. The defect density in SWCNTs is also reflected in their Raman spectra, where an increase in the D/G^+ mode intensity ratio indicates more defects, as shown in Figure 1d. For purified samples and within the limit of moderate functionalization, i.e., without clustering of defects, the intensity of the Raman D-mode is proportional to the number of sp^3-hybridized carbon atoms.[50] As recently demonstrated for (6,5) SWCNTs, the difference of the integrated D/G^+ ratio between pristine and functionalized samples ($\Delta(D/G^+)$) can be used as an absolute metric for the number of introduced defects based on its linear correlation with the sp^3 defect densities obtained from E_{11} PLQY measurements (see Figure 1e).[34] It is independent of the initial number of defects in the raw material, the length of the nanotubes, or the dispersion medium.

To expand this approach to other SWCNT chiralities and to investigate its dependence on the Raman excitation wavelength and nanotube diameter, we characterized pristine and functionalized (7,3), (6,5), (8,3), (9,2), and (7,5) SWCNTs by PL and Raman spectroscopy. For all nanotube species, the sp^3 functionalization resulted in emission from E_{11}* defects as observed in the PL spectra of the SWCNT dispersions (see Figures S5a−S9a in the Supporting Information). Note that the relative PL intensities of defect and E_{11} emission are heavily influenced by the excitation power and the dielectric environment of the nanotubes (e.g., surfactant and solvent) and do not reflect the actual density of defects.[16] Spectrally resolved PLQY measurements reveal a sharp decrease of the absolute E_{11} PLQY with increasing sp^3 functionalization for all nanotube species and enable the direct calculation of defect densities based on the DLCQ model as outlined above (see Figures S5b−S9b in the Supporting Information).

For the correlation of the calculated sp^3 defect densities n_d and the D/G^+ intensity ratios, Raman maps of dropcast films of pristine and sp^3-functionalized SWCNTs were collected at excitation wavelengths of 532, 633, and 785 nm, and over 3000 individual spectra were averaged for each sample. The integrated D and G^+ mode intensities were obtained from Lorentzian fits to the averaged and baseline-corrected Raman

https://doi.org/10.1021/acsnano.3c07668
ACS Nano 2023, 17, 21771−21781

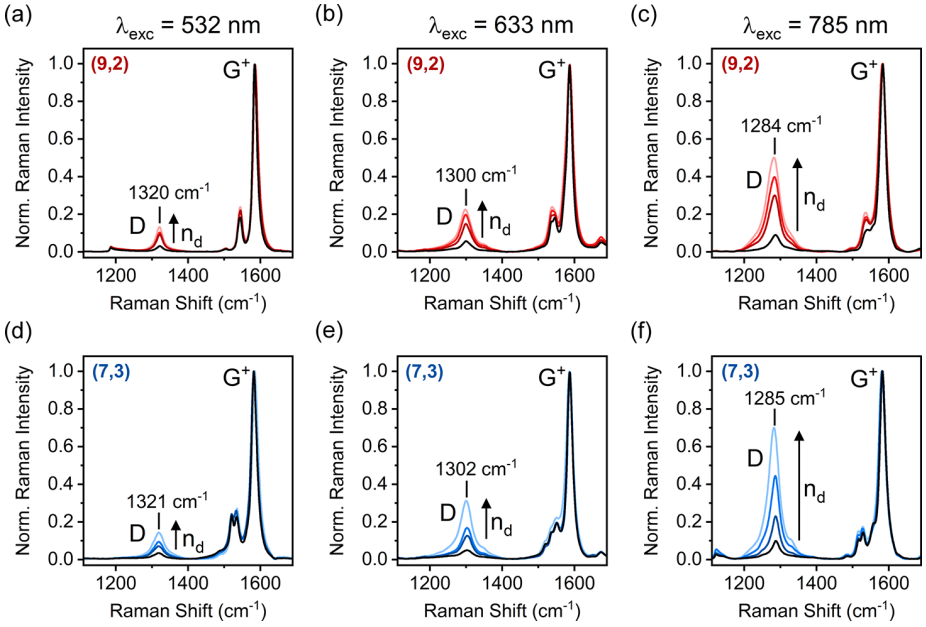

Figure 2. Averaged (>3000 spectra for each sample) and normalized Raman spectra of pristine and sp^3-functionalized (9,2) (a–c) and (7,3) SWCNTs (d–f), acquired at excitation laser wavelengths of 532 nm (E_L = 2.33 eV) (a, d), 633 nm (E_L = 1.96 eV) (b, e), and 785 nm (E_L = 1.58 eV) (c, f), demonstrating the red-shift of the Raman D-mode and higher D/G$^+$ intensity ratios with lower excitation energies (longer excitation wavelengths).

spectra. The results for (9,2) and (7,3) SWCNTs are shown exemplarily in Figure 2 (for other SWCNT chiralities, see Figure S10–S13 in the Supporting Information). The dispersive nature of the Raman D-mode[26] becomes evident for longer excitation wavelengths as the peak maximum shifts to lower wavenumbers. We observe no significant change in peak position or width of the G$^+$ mode for pristine and sp^3-functionalized SWCNTs, indicating that the perturbation of the sp^2-hybridized carbon lattice and the SWCNT band structure for moderate sp^3 functionalization is still negligible.

In addition to the expected increase in the Raman D/G$^+$ intensity ratio with the concentration of $DzNO_2$ during functionalization, the D/G$^+$ intensity ratio also shows a strong dependence on the excitation wavelength. For Raman spectra recorded with longer excitation wavelengths λ_L and thus lower excitation energies E_L, the D-mode becomes much more pronounced compared to the G$^+$ mode. This effect was initially observed and quantified in Raman studies of nanographites and graphene[18,51] and can be explained by the proportionality of the Raman cross section of the G-mode to the excitation energy E_L^4. In contrast to that, the cross section of the D-mode does not show any dependence on E_L. Systematic studies of this effect in SWCNTs were previously restricted to ion-bombarded double-walled nanotubes due to the limited availability of monochiral dispersions at the time. However, they indicated the same dependence.[28,52]

Laser-Wavelength-Independent Defect Quantification. To evaluate the transferability of the model derived for point-like defects in nanographites and graphene to SWCNTs, we correlate the Raman D/G$^+$ ratio with the calculated sp^3 defect density n_d from PLQY measurements for all investigated SWCNT chiralities and excitation wavelengths. For this quantitative analysis, the difference between the integrated D/G$^+$ ratios (i.e., the area ratios) instead of the intensity ratios is used, as it provides a more robust measure when only small perturbations of the pristine SWCNT lattice are present.[18] Furthermore, the integrated Raman D/G$^+$ ratio for the pristine SWCNTs is subtracted from all sp^3-functionalized samples, resulting in a differential value, the Δ(D/G$^+$) ratio. This differential value enables the application of this analysis to SWCNT samples with different initial defect densities and hence D-mode intensities before functionalization.

Figures 3a,b display the obtained plots of the integrated Δ(D/G$^+$) ratios vs calculated defect densities n_d for (9,2) and (8,3) SWCNTs, respectively (for data on other chiralities, see Figures S13a–S15a in the Supporting Information). In all cases, a linear correlation between the Δ(D/G$^+$) ratio and the sp^3 defect density n_d can be found but with very different slopes depending on the excitation wavelengths (532, 633, and 785 nm). Longer excitation wavelengths lead to greater slopes. The values for the slopes of Δ(D/G$^+$) vs n_d and the respective standard deviations obtained from linear fitting are reported in Table 1 for all investigated SWCNT chiralities.

In direct analogy to graphene,[18] a normalization of the slopes (here Δ(D/G$^+$) vs n_d) by the laser excitation wavelength λ_L^4 (or interchangeably to the excitation energy E_L^{-4}) leads to unified values with a substantially reduced relative standard deviation (RSD), as shown in Figure 3c,d (for other chiralities, see Figures S13b–S15b in the Supporting Information). The wavelength-corrected slopes for Δ(D/G$^+$) vs n_d can be averaged to yield a universal empirical expression for the sp^3 defect density (with λ_L in nanometers):

$$n_d\ (\mu m^{-1}) = \frac{A(d_t)\cdot 10^{13}}{\lambda_L^4}\cdot\Delta\left(\frac{I_D}{I_{G^+}}\right) \quad (2)$$

The resulting values for calibration factor A are reported in Table 1 for each SWCNT chirality. Equation 2 is applicable to SWCNT chiralities within the diameter range investigated here (0.7–0.85 nm) and for sp^3 defect densities in the range of ~5–80 μm^{-1} with an estimated accuracy of ±15%. Note that maximum PLQYs and highest defect-to-E_{11} PL intensities of

https://doi.org/10.1021/acsnano.3c07668
ACS Nano 2023, 17, 21771–21781

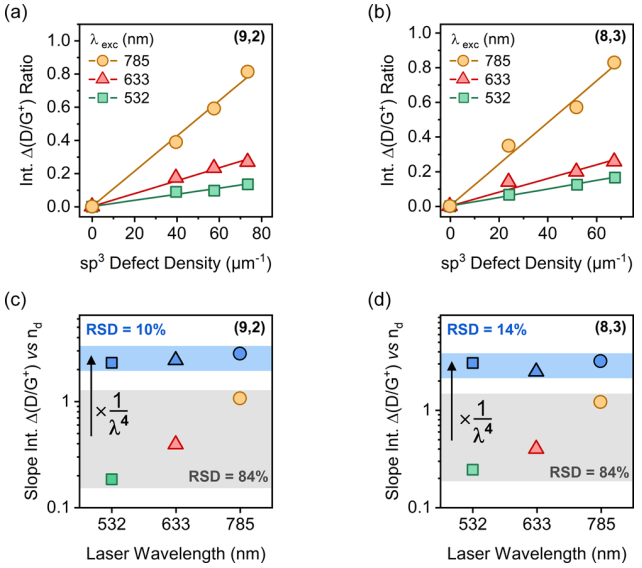

Figure 3. Integrated Raman $\Delta(D/G^+)$ ratio vs calculated sp^3 defect density n_d for pristine and sp^3-functionalized (9,2) (a) and (8,3) SWCNTs (b) at laser wavelengths of 532 nm (E_L = 2.33 eV), 633 nm (E_L = 1.96 eV), and 785 nm (E_L = 1.58 eV), including linear fits to the data (R^2(532 nm) = 0.99, R^2(633 nm) = 0.99, R^2(785 nm) = 0.99). (b) Slopes of linear fits in (a) and (b) for different excitation wavelengths (i.e., excitation energy E_L) and their normalization with E_L^4 or $1/\lambda^4$ for (c) (9,2) and (d) (8,3) SWCNTs including the relative standard deviation (RSD in %) before and after normalization.

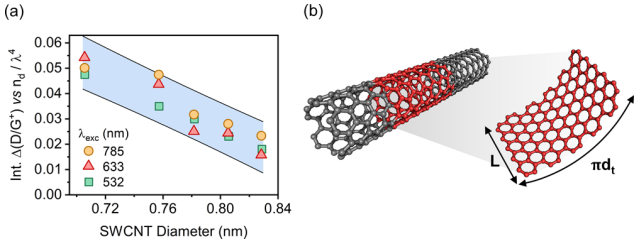

Figure 4. (a) Integrated Raman $\Delta(D/G^+)$ vs n_d ratios for different diameters of SWCNTs, normalized to the excitation laser wavelength λ_L^4. (b) Schematic illustration of the conceptual unfolding of the nanotube lattice for the normalization of the D/G$^+$ ratio to the SWCNT area ($L{\cdot}\pi d_t$), where L denotes the length of the nanotube segment and d_t is the tube diameter.

functionalized nanotubes are typically obtained at ~6−10 luminescent sp^3 defects per μm of SWCNT.[40] Thus, the presented quantification method can be used to guide the selection of suitable samples with optimum E_{11}* defect emission in optoelectronic devices or nanotube-based sensors based on simple Raman spectroscopy. It could further ensure comparability between different batches and sources of carbon nanotubes. Here we used both CoMoCat and HiPco nanotubes as well as different types of dispersion (polymer-wrapped in organic solvents and surfactant-stabilized in aqueous environments, see Experimental Methods) and still obtained a continuous linear correlation.

Dependence of D/G$^+$ Ratios on Nanotube Diameter. A closer look at the calibration factor A for the different SWCNT chiralities reveals a clear dependence on nanotube diameter (d_t) as shown in Figure 4a. For example, at identical calculated defect densities, the D/G$^+$ ratio for (7,3) SWCNTs (d_t = 0.71 nm) is larger by a factor of ~2.5 compared to (7,5) SWCNTs (d_t = 0.83 nm). At first glance, this deviation could be explained by a larger relative impact of individual sp^3 defects on the D-mode of SWCNTs with smaller diameters. To rationalize this argument, we adopt the model of D-mode activation in the lattice area directly around point-like defects, as developed for graphene.[20] Within this picture, a single sp^3 defect may result in a larger relative increase of the D-mode intensity when the number of sp^2-hybridized carbon atoms contributing to the G$^+$ mode is lower. This would be the case for SWCNTs with smaller diameters and hence circumferences but identical length. This effect can be quantified by unfolding the carbon nanotube lattice to obtain a two-dimensional graphene sheet with a defined area, as schematically depicted in Figure 4b. The number of carbon atoms per unit length of each nanotube chirality can thus be used to normalize the calibration factors A (see Table S1 and Figure S16 in the Supporting Information). While this normalization reduces the deviation between different SWCNT chiralities, nanotubes with smaller diameters still show significantly higher D/G$^+$ ratios for the same sp^3 defect density (i.e., smaller A) compared to those of SWCNTs with larger diameters. Evidently, for the investigated nanotube diameters the number of carbon atoms per μm for different nanotubes cannot fully explain the diameter dependence of A.

In addition to the pronounced diameter dependence of the D/G$^+$ ratio, other possible correlations were tested. As each sp^3 defect involves two sp^3 carbons in different ortho or para configurations,[14] their alignment with respect to the nanotube axis might also be reflected in the D/G$^+$ ratio, although at least for (6,5) nanotubes no dependence on the binding configuration was observed.[34] Among the investigated SWCNT chiralities, we find no distinct correlation with chiral angle or mod family (mod(2n+m, 3) = 1 or 2) as shown in Figure S17 in the Supporting Information. However, at similar chiral angles, a lower slope of ΔD/G$^+$ versus n_d is observed for mod family 2 compared to mod family 1 nanotubes. A comprehensive study of a broader range of SWCNTs with

Table 1. Slopes (Standard Deviations in Parentheses) of the Integrated $\Delta(D/G^+)$ Ratios vs the Calculated Defect Density n_D for All Investigated (n,m) Chiralities of SWCNTs at Three Different Raman Laser Excitation Wavelengths, Nanotube Diameters d_T, and Calibration Factors $A(d_t)$ (Standard Deviation) for Each SWCNT Chirality as Used in eq 2

laser wavelength (nm)	(7,3)	(6,5)	(8,3)	(9,2)	(7,5)
532	0.0038(0.0004)	0.0028(0.0002)	0.0025(0.0001)	0.0019(0.0002)	0.0014(0.0002)
633	0.0087(0.0006)	0.0073(0.0003)	0.0040(0.0003)	0.0039(0.0003)	0.0025(0.0001)
785	0.019(0.002)	0.0186(0.0007)	0.0120(0.0006)	0.0106(0.0003)	0.0088(0.0003)
d_t (nm)	0.71	0.76	0.78	0.81	0.83
$A(d_t)$	2.0(0.2)	2.4(0.4)	3.5(0.5)	4.0(0.4)	5.4(1.1)

https://doi.org/10.1021/acsnano.3c07668
ACS Nano 2023, 17, 21771−21781

similar diameters but different chiral angles or belonging to different mod families could resolve possible dependencies, but this is beyond the scope of this work.

Based on the available data, curvature effects appear to play a major role in highly strained SWCNTs with diameters below 1 nm. For the wavenumber of the D-mode in SWCNTs, an inverse dependence on nanotube diameter was determined experimentally and supported by numerical simulations.[26,27] In particular, strong deviations from the tight-binding and zone-folding model emerge in the dispersion of the transverse optical (TO) phonons at the K point of the Brillouin zone in small-diameter SWCNTs.[25,53] A point-defect in a highly strained lattice might be expected to have a larger impact than in a less strained or flat sp^2 carbon lattice despite the fact that there is already a higher sp^3 character in pristine nanotubes with small diameters than in large-diameter nanotubes.[54]

If the diameter dependence of the relative increase of the D/G^+ ratio versus defect density is related to curvature effects in SWCNTs, an expansion of the one-dimensional nanotube to a two-dimensional graphene sheet (equivalent to $d_t \rightarrow \infty$) may result in correlations similar to those of graphene. By representing the average defect density in nanometers via L_d (nm) = 1000 nm/n_d (μm^{-1}), a direct comparison between the empirical expressions obtained for graphene (eq 1) and SWCNTs (eq 2) can be drawn. We find that the D/G^+ ratios for a given defect density below ~20 μm^{-1} as calculated with eq 1 are on the same order of magnitude as those determined experimentally for the different nanotube chiralities (see Figure S18 and Table S2 in the Supporting Information). The investigated nanotubes with larger diameters (i.e., (9,2) and (7,5)) are closer to the values calculated for graphene. But smaller diameter nanotubes show higher D/G^+ ratios for the same low defect density. However, for very high defect densities (>30 μm^{-1}) the D/G^+ ratios for graphene deviate substantially and become consistently higher than the experimental values for nanotubes. It is not clear how these numbers can be reconciled. Clearly, rolling-up planar graphene sheets into small-diameter, highly strained SWCNTs exerts a strong influence on the relative ratio of the Raman D and G^+ modes for a given number of defects and the empirical expression for graphene cannot be applied to quantify defects in carbon nanotubes.

Although no conclusive quantitative relation between the nanotube diameter and changes in the D/G^+ ratios with defect density can be drawn from the limited range of five small-diameter SWCNTs, the available data strongly indicate that caution has to be taken when comparing defect densities of different carbon nanotube chiralities. Samples with different diameter distributions will give rather different D/G^+ ratios for the same or similar defect densities (initial or introduced), in addition to a strong dependence on the Raman laser wavelength. Future defect density analyses would profit greatly from more detailed theoretical studies on the impact of nanotube geometry, as well as defect configuration on Raman D and G^+ modes in functionalized or defective SWCNTs.

Activation of Intermediate Frequency Modes by sp^3 Defects. So far, we have considered only the impact of sp^3 defects on the D-mode of SWCNTs, which is arguably the most prominent indication of defects. However, additional defect-induced Raman features can be found in the spectral range between the RBM and D-mode, which are consequently named intermediate frequency modes (IFMs).[55] These IFMs typically exhibit much lower intensities than the D-mode and are most pronounced in Raman spectra of individual aligned SWCNTs.[56] Among the different IFMs, the signature of the ZA-derived phonon branch of graphene occurs in the range between 450 and 500 cm^{-1} and was found to increase with higher levels of defects.[56−60] As expected for a defect-related double-resonant process, the ZA-derived mode exhibits dispersive characteristics.[61] Its intensity also increases with longer excitation wavelengths. An additional Raman signal at ~600 cm^{-1} was also proposed to originate from a defect-induced double-resonant process involving the ZO-derived phonon branch.[56] Recent theoretical studies based on excitation close to E_{11} have further indicated the possible presence of defect-related modes in the IFM region.[62]

To clarify the nature of IFM features and their correlation with sp^3 defect densities of small-diameter nanotubes, we collected averaged Raman spectra in the IFM region (excitation wavelength 785 nm) for all pristine and sp^3-functionalized SWCNT samples. The Raman spectra for (6,5) SWCNTs normalized to the nearby RBM peak are shown in Figure 5a (for additional chiralities see Figures S19a−S22a in the Supporting Information). ZA- and ZO-derived phonon modes at 480 and 570 cm^{-1}, respectively, are evident and increase in intensity relative to the RBM signal with sp^3 defect density. Hence, they could be used in the same way as the D/G^+ ratio for defect quantification, as discussed above. We determined the integrated differential ratio Δ(IFM/RBM) from pristine and functionalized SWCNTs and found a linear correlation with the sp^3 defect density n_d for both IFMs (see Figure 5b and Figures S19b−S22b in the Supporting Information). Due to the highly selective and systematic introduction of sp^3 defects, we can conclude that both the ZA- and the ZO-derived phonon modes are indeed the result of

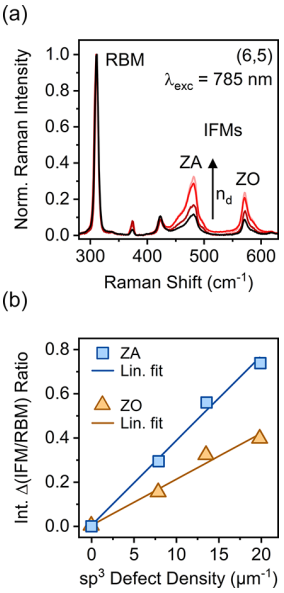

Figure 5. (a) Averaged and normalized (to RBM) Raman spectra (λ_{exc} = 785 nm) of pristine and sp^3-functionalized (6,5) SWCNTs in the intermediate frequency mode (IFM) region. (b) Integrated Δ(IFM/RBM) intensity ratio for the IFMs depicted in (a) and linear fits to the data (R^2 = 0.99 for ZA mode and R^2 = 0.99 for ZO mode).

https://doi.org/10.1021/acsnano.3c07668
ACS Nano 2023, 17, 21771−21781

defect-activated, double-resonant scattering processes as previously suggested.[56]

The slopes and respective standard deviations for linear fits of Δ(IFM/RBM) vs n_d are reported in Table S3 in the Supporting Information. They show strong variations with SWCNT species, which is most likely the result of the complex chirality and mod family dependence of the RBM to G^+ mode intensities, as reported previously for a variety of SWCNT chiralities.[63] In addition, the analysis of the IFM region is often complicated by traces of other SWCNT chiralities that also contribute to Raman features in the investigated spectral region, resulting in larger errors of the linear fits for (7,3) and (9,2) SWCNTs. Nevertheless, our findings indicate that for highly pure SWCNT samples, defect-related IFM features can also be used for the absolute quantification of sp^3 defects and hence offer an additional metric for covalent nanotube functionalization.

CONCLUSION

We have demonstrated a combined analysis of Raman spectra and PLQY measurements of functionalized SWCNTs for the absolute quantification of sp^3 quantum defects across different nanotube chiralities and diameters. Covalently functionalized (7,3), (6,5), (8,3), (9,2), and (7,5) SWCNTs with low to intermediate levels of sp^3 defects showed a linear correlation of the defect densities obtained from E_{11} PLQY measurements with the differential increase of the integrated Raman D/G^+ intensity ratios. A normalization of the resulting slopes to the Raman excitation wavelength λ_L^4 leads to a simple, excitation-energy-independent linear expression for the defect density in SWCNTs and thus enables a straightforward quantification of the number of introduced defects in nanotubes from Raman spectra alone. An inverse correlation between the integrated D/G^+ ratio increase and the nanotube diameter d_t indicates that curvature effects and strain exert a strong influence on defect-activated Raman modes in SWCNTs. This fairly strong diameter dependence of the D/G^+ ratio for different nanotube diameters also demonstrates that simple comparisons between different nanotube batches should be applied with caution. In addition to the characteristic increase of the D-mode intensity, sp^3-functionalization is also reflected in the intermediate frequency Raman modes of SWCNTs. Both the ZA- and ZO-derived phonon modes can be clearly assigned as defect-activated as their relative intensities scale linearly with defect density. They could be used as an additional and complementary metric for the degree of nanotube functionalization.

These unified defect characterization and quantification methods based on simple Raman spectroscopy should enable a more systematic evaluation of the efficiency of SWCNT functionalization methods as well as quality control for a range of nanotubes with sp^3 defects that find applications in biosensing and optoelectronics. They should also incite further systematic studies of a broader range of nanotube chiralities with different types of lattice defects, including, for example, oxygen defects. Finally, the development of further theoretical descriptions is required to arrive at a comprehensive picture and quantitative model for defect-related effects in the SWCNT Raman spectra.

EXPERIMENTAL METHODS

Preparation of Monochiral SWCNT Dispersions. *(6,5) and (7,5) SWCNTs.* Dispersions of (6,5) SWCNTs were obtained by shear force mixing (SFM, Silverson L2/Air, 10230 rpm, 20 °C, 72 h) of CoMoCAT raw material (Sigma-Aldrich, Charge No. MKCJ7287) in a solution of poly[(9,9-dioctylfluorenyl-2,7-diyl)-*alt*-(6,6′-(2,2′-bipyridine))] (PFO-BPy, American Dye Source, M_W = 40 kg mol^{-1}, 0.5 g L^{-1}) in toluene as reported previously.[35] (7,5) SWCNTs were likewise dispersed by shear force mixing in a solution of poly[(9,9-dioctylfluorenyl-2,7-diyl)] (PFO, Sigma-Aldrich, M_W > 20 kg mol^{-1}, 0.9 g L^{-1}) in toluene. Unexfoliated material was removed by centrifugation (Beckman Coulter Avanti J26XP centrifuge) at 60000*g* for 1 h and filtration of the supernatant through a poly(tetrafluoroethylene) (PTFE) syringe filter (pore size 5 μm). Vacuum filtration through PTFE membrane filters (Merck Millipore JVWP, pore size 0.1 μm) and washing of the resulting filter cakes with hot toluene (80 °C, 10 min) were performed to remove excess polymer, followed by redispersion of the polymer-wrapped nanotubes in fresh toluene via bath sonication.

(7,3), (8,3), and (9,2) SWCNTs. Monochiral (7,3), (8,3), and (9,2) SWCNTs were obtained by gel chromatography employing a mixed surfactant system following a previously reported protocol.[36,64] Initially, HiPco SWCNT raw material (NanoIntegris, Inc., diameter distribution 1.0 ± 0.3 nm) was dispersed in an aqueous solution of sodium cholate (SC, 0.8 w/vol %, >99%, Sigma-Aldrich) by ultrasonication (Branson Sonifier 250D) with 30% output power for 1−2 h. After ultracentrifugation at 210000*g* for 2 h, the collected supernatant was mixed with aqueous solutions of sodium dodecyl sulfate (SDS, >99%, Sigma-Aldrich) and SC to adjust the surfactant concentration depending on the (*n*,*m*) chirality. The separation was carried out with a high-performance liquid chromatography system (Cytiva AKTAexplorer 10S) and columns (Cytiva HiScale 26/20) filled with gel beads (Cytiva Sephacryl S-200 HR) at a temperature of 17 °C. The surfactant concentration of the SWCNT dispersion was adjusted to 0.6% SDS + 0.4% SC. After equilibration of the column with 0.6% SDS + 0.4% SC and loading with the SWCNT dispersion, adsorbed SWCNTs were eluted using a mixed surfactant solution of 0.6% SDS + 0.4% SC + *x*% sodium lithocholate (LC, >98%, Tokyo Chemical Industry Co., Ltd.). The concentration *x*% of LC was adjusted to 0.03%, 0.056%, and 0.065% to obtain (7,3), (8,3), and (9,2) SWCNT fractions, respectively. The obtained aqueous dispersions of SWCNTs were concentrated by centrifugal filtration at 3000*g* for 45 min (Hettich Mikro 220R centrifuge, Universal 320R 1615 rotor) using centrifugal filters with a 100 kDa molecular weight cutoff (Merck Amicon Ultra-4). The remaining SWCNT dispersion was transferred into an aqueous solution of SDS (0.33 w/vol %) and adjusted to an optical density (OD) of 0.2 cm^{-1} at the E_{11} transition.

Functionalization of SWCNTs with sp^3 Defects. *(6,5) and (7,5) SWCNTs.* PFO-BPy-wrapped (6,5) SWCNTs were functionalized in a 80:20 (vol %) mixture of toluene/acetonitrile (MeCN) according to a procedure introduced previously by Berger et al.[40] To prevent the aggregation of SWCNTs, their concentration was always adjusted to 0.36 mg L^{-1} in the final reaction mixture (corresponding to an OD of 0.2 cm^{-1}). Initially, a solution of 18-crown-6 in toluene was added to a dispersion of SWCNTs such that the final concentration of 18-crown-6 was 7.6 mmol L^{-1} after the addition of the remaining reactants. To achieve a ratio of 80:20 vol % of toluene/MeCN, the respective volume of MeCN was then added to the reaction mixture. Appropriate amounts of a stock solution (5 g L^{-1}) of 4-nitrobenzenediazonium tetrafluoroborate ($DzNO_2$) in MeCN were added to achieve concentrations between 20 and 1000 mg L^{-1}. After storage in the dark at room temperature for 16 h, the reaction mixture was filtered through a PTFE membrane filter (Merck Millipore JVWP, pore size 0.1 μm). The filter cake was washed with MeCN (10 mL) and toluene (5 mL) to remove the remaining diazonium salt and excess polymer. Redispersion of the sp^3-functionalized SWCNTs was performed by bath sonication in fresh toluene. For PFO-wrapped (7,5) SWCNTs, the preparation and workup of the reaction mixture were similar; however, a fixed concentration of 2000 mg L^{-1} of $DzNO_2$ was used and reaction times were varied between 10 and 200 h to achieve different degrees of functionalization.

(7,3), (8,3), and (9,2) SWCNTs. Aqueous dispersions of SWCNTs in 0.33 w/vol % SDS were combined with the appropriate volume of

https://doi.org/10.1021/acsnano.3c07668
ACS Nano 2023, 17, 21771−21781

an aqueous solution of $DzNO_2$ such that final $DzNO_2$ concentrations between 5×10^{-5} and 5×10^{-3} mg mL^{-1} were achieved depending on the reactivity of the SWCNT species. The reaction mixture was stored at room temperature in the dark for at least 4 days to ensure the completion of the functionalization reaction.

Characterization. Baseline-corrected UV−vis−nIR absorption spectra were collected with a Varian Cary 6000i UV−vis−nIR absorption spectrometer. All acquired spectra were corrected with a scattering background $S(\lambda) = S_0 e^{-b\lambda}$ according to a literature procedure.[65,66] Raman spectroscopy was carried out with a Renishaw inVia Reflex confocal Raman microscope in a backscattering configuration equipped with an ×50 long-working distance objective (Olympus, N.A. 0.5). Samples were prepared by drop-casting the dispersion on glass substrates (Schott AF32eco), followed by thorough washing with tetrahydrofuran and 2-propanol for dispersions of polymer-wrapped SWCNTs or with deionized water in the case of aqueous SWCNT dispersions. Raman spectra were recorded using three different lasers operating at wavelengths of 532 nm (2.33 eV), 633 nm (1.96 eV), and 785 nm (1.58 eV). Over 3000 individual Raman spectra were collected from an area of $60 \times 60\ \mu m^2$, averaged and baseline-corrected for each sample. Raman modes of SWCNTs were analyzed using Lorentzian fits.[23] Photoluminescence excitation−emission maps were recorded with a Fluorolog-3 spectrometer (Horiba Jobin-Yvon) equipped with a xenon arc-discharge lamp (450 W), an excitation double monochromator, and a liquid-nitrogen-cooled linear InGaAs array (Symphony II).

Photoluminescence Spectroscopy. For photoluminescence measurements, the output of a picosecond-pulsed supercontinuum laser (NKT Photonics SuperK Extreme) was wavelength-filtered corresponding to the SWCNT E_{22} transition and focused on the nanotube dispersion inside a quartz glass cuvette using an nIR-optimized ×50 objective (Olympus, N.A. 0.65). Emitted light was collected through the same objective and PL spectra were recorded using a grating spectrograph (Princeton Instruments Acton SpectraPro SP2358, grating 150 lines/mm) in combination with a liquid-nitrogen-cooled InGaAs line camera (Princeton Instruments OMA V:1024 1.7 LN).

Photoluminescence Quantum Yield Measurements. Photoluminescence quantum yields (PLQYs) of SWCNT dispersions were determined by an absolute method as described previously.[35] A quartz glass cuvette was filled with 1 mL of a SWCNT dispersion (OD = 0.2 cm^{-1} at E_{11}) and placed inside an integrating sphere (LabSphere with Spectralon coating). The light exiting the integrating sphere was guided to the spectrometer and detector (see above) with an optical fiber. The PLQY (η) of each sample was determined as the fraction of emitted (N_{em}) to absorbed photons (N_{abs}) according to

$$\eta = \frac{N_{em}}{N_{abs}} \tag{3}$$

To obtain a value proportional to N_{em}, the recorded signal for a solvent reference and the SWCNT dispersion were each multiplied with the wavelength, integrated, and subtracted. An identical analysis was performed with the attenuated laser intensity at the E_{22} transition for the SWCNT sample and a solvent reference to calculate N_{abs} and subsequently the PLQY according to eq 3. The absorption characteristics of optics in the detection path and wavelength-dependent detector efficiency were accounted for by a collection of calibration spectra using a broad-band light source (SLS201/M, Thorlabs).

Calculation of sp^3 Defect Densities. The calculation of luminescent sp^3 defect density is based on the model of diffusion-limited contact quenching (DLCQ) as reported previously,[34] which assumes competition between radiative decay of mobile excitons via E_{11} or E_{11}* emission and nonradiative decay at quenching sites, for example, nanotube ends.[41] In pristine SWCNTs, the E_{11} PLQY can be calculated according to

$$\eta = \frac{\pi}{2 \cdot n_q^2 \cdot D \cdot \tau_{rad}} \tag{4}$$

Here, n_q denotes the number of innate quenching sites per μm of nanotube, D the diffusion constant, and τ_{rad} the radiative lifetime of mobile excitons in the E_{11} state. The last two are independent of the nanotube length and the density of emissive defects or nonradiative quenching sites. In this work, we use values of $D = 10.7 \pm 0.4$ cm^2 s^{-1} and $\tau_{rad} = 3.35 \pm 0.41$ ns for all investigated SWCNT species, although these were determined in previous experimental studies only for (6,5) SWCNTs.[42,46]

For functionalized SWCNTs, additional traps for excitons in the form of luminescent sp^3 defects are introduced. This reduces the probability for the radiative E_{11} decay of excitons which is reflected in the expression for the E_{11} PLQY of functionalized SWCNTs (η*):

$$\eta^* = \frac{\pi}{2 \cdot (n_q + n_d)^2 \cdot D \cdot \tau_{rad}} \tag{5}$$

An expression for the density of sp^3 defects n_d is obtained by combining eqs 4 and 5:

$$n_d = n_q \left(\sqrt{\frac{\eta}{\eta^*}} - 1 \right) = \sqrt{\frac{\pi}{2 \cdot \eta \cdot D \cdot \tau_{rad}}} \left(\sqrt{\frac{\eta}{\eta^*}} - 1 \right) \tag{6}$$

From the margins of error for the exciton diffusion constant, the exciton radiative lifetime, and the PLQY determination, an overall error of ±15% can be assumed for the extracted values of n_d.

ASSOCIATED CONTENT

Supporting Information

The Supporting Information is available free of charge at https://pubs.acs.org/doi/10.1021/acsnano.3c07668.

UV−vis−nIR absorption spectra, PLE maps, RBM Raman spectra, PL spectra and PLQY measurements, Raman spectra at different excitation wavelengths, diameter dependence of G^+ and G^- Raman modes, linear fitting of D/G^+ ratios vs defect density, normalization of D/G^+ ratios vs defect density slopes to the number of carbon atoms per micrometer of nanotube, correlation of D/G^+ ratios with SWCNT chiral angle and mod family, IFM Raman spectra, and linear fits of integrated IFM/RBM intensities vs defect density (PDF)

AUTHOR INFORMATION

Corresponding Author

Jana Zaumseil − *Institute for Physical Chemistry, Universität Heidelberg, D-69120 Heidelberg, Germany;* orcid.org/0000-0002-2048-217X; Email: zaumseil@uni-heidelberg.de

Authors

Finn L. Sebastian − *Institute for Physical Chemistry, Universität Heidelberg, D-69120 Heidelberg, Germany;* orcid.org/0000-0003-1161-633X

Felicitas Becker − *Institute for Physical Chemistry, Universität Heidelberg, D-69120 Heidelberg, Germany*

Yohei Yomogida − *Department of Physics, Tokyo Metropolitan University, Tokyo 192-0397, Japan;* orcid.org/0000-0002-8569-6179

Yuuya Hosokawa − *Department of Physics, Tokyo Metropolitan University, Tokyo 192-0397, Japan*

Simon Settele − *Institute for Physical Chemistry, Universität Heidelberg, D-69120 Heidelberg, Germany;* orcid.org/0000-0002-0082-2587

Sebastian Lindenthal − *Institute for Physical Chemistry, Universität Heidelberg, D-69120 Heidelberg, Germany*

Kazuhiro Yanagi − *Department of Physics, Tokyo Metropolitan University, Tokyo 192-0397, Japan;* orcid.org/0000-0002-7609-1493

Complete contact information is available at: https://pubs.acs.org/10.1021/acsnano.3c07668

Notes

The authors declare no competing financial interest.

ACKNOWLEDGMENTS

This project has received funding from the European Research Council (ERC) under the European Union's Horizon 2020 research and innovation programme (Grant agreement No. 817494, "TRIFECTs"). This study was partially supported by JST CREST (JPMJCR17I5) and JSPS KAKENHI (JP22H01911, JP22H05468, JP22H05469, JP20H02573, JP21H05017, JP23H00259).

REFERENCES

(1) Mandal, A. K.; Wu, X.; Ferreira, J. S.; Kim, M.; Powell, L. R.; Kwon, H.; Groc, L.; Wang, Y.; Cognet, L. Fluorescent sp^3 Defect-Tailored Carbon Nanotubes Enable NIR-II Single Particle Imaging in Live Brain Slices at Ultra-Low Excitation Doses. *Sci. Rep.* **2020**, *10*, 5286.

(2) Lin, C.-W.; Bachilo, S. M.; Zheng, Y.; Tsedev, U.; Huang, S.; Weisman, R. B.; Belcher, A. M. Creating Fluorescent Quantum Defects in Carbon Nanotubes using Hypochlorite and Light. *Nat. Commun.* **2019**, *10*, 2874.

(3) Kwon, H.; Kim, M.; Meany, B.; Piao, Y.; Powell, L. R.; Wang, Y. Optical Probing of Local pH and Temperature in Complex Fluids with Covalently Functionalized, Semiconducting Carbon Nanotubes. *J. Phys. Chem. C* **2015**, *119*, 3733−3739.

(4) Kim, M.; Chen, C.; Wang, P.; Mulvey, J. J.; Yang, Y.; Wun, C.; Antman-Passig, M.; Luo, H.-B.; Cho, S.; Long-Roche, K.; Ramanathan, L. V.; Jagota, A.; Zheng, M.; Wang, Y.; Heller, D. A. Detection of Ovarian Cancer via the Spectral Fingerprinting of Quantum-defect-modified Carbon Nanotubes in Serum by Machine Learning. *Nat. Biomed. Eng.* **2022**, *6*, 267−275.

(5) Spreinat, A.; Dohmen, M. M.; Lüttgens, J.; Herrmann, N.; Klepzig, L. F.; Nißler, R.; Weber, S.; Mann, F. A.; Lauth, J.; Kruss, S. Quantum Defects in Fluorescent Carbon Nanotubes for Sensing and Mechanistic Studies. *J. Phys. Chem. C* **2021**, *125*, 18341−18351.

(6) Zorn, N. F.; Berger, F. J.; Zaumseil, J. Charge Transport in and Electroluminescence from sp^3-Functionalized Carbon Nanotube Networks. *ACS Nano* **2021**, *15*, 10451−10463.

(7) Li, M.-K.; Riaz, A.; Wederhake, M.; Fink, K.; Saha, A.; Dehm, S.; He, X.; Schöppler, F.; Kappes, M. M.; Htoon, H.; Popov, V. N.; Doorn, S. K.; Hertel, T.; Hennrich, F.; Krupke, R. Electroluminescence from Single-Walled Carbon Nanotubes with Quantum Defects. *ACS Nano* **2022**, *16*, 11742−11754.

(8) He, X.; Htoon, H.; Doorn, S. K.; Pernice, W. H. P.; Pyatkov, F.; Krupke, R.; Jeantet, A.; Chassagneux, Y.; Voisin, C. Carbon Nanotubes as Emerging Quantum-light Sources. *Nat. Mater.* **2018**, *17*, 663−670.

(9) He, X.; Hartmann, N. F.; Ma, X.; Kim, Y.; Ihly, R.; Blackburn, J. L.; Gao, W.; Kono, J.; Yomogida, Y.; Hirano, A.; Tanaka, T.; Kataura, H.; Htoon, H.; Doorn, S. K. Tunable Room-Temperature Single-Photon Emission at Telecom Wavelengths from sp^3 Defects in Carbon Nanotubes. *Nat. Photonics* **2017**, *11*, 577−582.

(10) Brozena, A. H.; Kim, M.; Powell, L. R.; Wang, Y. Controlling the Optical Properties of Carbon Nanotubes with Organic Colour-Centre Quantum Defects. *Nat. Rev. Chem.* **2019**, *3*, 375−392.

(11) He, X.; Gifford, B. J.; Hartmann, N. F.; Ihly, R.; Ma, X.; Kilina, S. V.; Luo, Y.; Shayan, K.; Strauf, S.; Blackburn, J. L.; Tretiak, S.; Doorn, S. K.; Htoon, H. Low-Temperature Single Carbon Nanotube Spectroscopy of sp^3 Quantum Defects. *ACS Nano* **2017**, *11*, 10785−10796.

(12) Hartmann, N. F.; Velizhanin, K. A.; Haroz, E. H.; Kim, M.; Ma, X.; Wang, Y.; Htoon, H.; Doorn, S. K. Photoluminescence Dynamics of Aryl sp^3 Defect States in Single-Walled Carbon Nanotubes. *ACS Nano* **2016**, *10*, 8355−8365.

(13) Piao, Y.; Meany, B.; Powell, L. R.; Valley, N.; Kwon, H.; Schatz, G. C.; Wang, Y. Brightening of Carbon Nanotube Photoluminescence through the Incorporation of sp^3 Defects. *Nat. Chem.* **2013**, *5*, 840−845.

(14) Saha, A.; Gifford, B. J.; He, X.; Ao, G.; Zheng, M.; Kataura, H.; Htoon, H.; Kilina, S.; Tretiak, S.; Doorn, S. K. Narrow-Band Single-Photon Emission through Selective Aryl Functionalization of Zigzag Carbon Nanotubes. *Nat. Chem.* **2018**, *10*, 1089−1095.

(15) Kwon, H.; Furmanchuk, A.; Kim, M.; Meany, B.; Guo, Y.; Schatz, G. C.; Wang, Y. Molecularly Tunable Fluorescent Quantum Defects. *J. Am. Chem. Soc.* **2016**, *138*, 6878−6885.

(16) Settele, S.; Berger, F. J.; Lindenthal, S.; Zhao, S.; El Yumin, A. A.; Zorn, N. F.; Asyuda, A.; Zharnikov, M.; Högele, A.; Zaumseil, J. Synthetic Control over the Binding Configuration of Luminescent sp^3-Defects in Single-Walled Carbon Nanotubes. *Nat. Commun.* **2021**, *12*, 2119.

(17) Chen, J.-S.; Trerayapiwat, K. J.; Sun, L.; Krzyaniak, M. D.; Wasielewski, M. R.; Rajh, T.; Sharifzadeh, S.; Ma, X. Long-Lived Electronic Spin Qubits in Single-Walled Carbon Nanotubes. *Nat. Commun.* **2023**, *14*, 848.

(18) Cançado, L. G.; Jorio, A.; Martins Ferreira, E. H.; Stavale, F.; Achete, C. A.; Capaz, R. B.; Moutinho, M. V.; Lombardo, A.; Kulmala, T. S.; Ferrari, A. C. Quantifying Defects in Graphene via Raman Spectroscopy at Different Excitation Energies. *Nano Lett.* **2011**, *11*, 3190−3196.

(19) Cançado, L. G.; Gomes da Silva, M.; Martins Ferreira, E. H; Hof, F.; Kampioti, K.; Huang, K.; Penicaud, A.; Achete, C. A.; Capaz, R. B; Jorio, A. Disentangling Contributions of Point and Line Defects in the Raman Spectra of Graphene-Related Materials. *2D Mater.* **2017**, *4*, No. 025039.

(20) Lucchese, M. M.; Stavale, F.; Martins Ferreira, E. H.; Vilani, C.; Moutinho, M. V. O.; Capaz, R. B.; Achete, C. A.; Jorio, A. Quantifying Ion-Induced Defects and Raman Relaxation Length in Graphene. *Carbon* **2010**, *48*, 1592−1597.

(21) Turner, P.; Paton, K. R.; Legge, E. J.; de Luna Bugallo, A.; Rocha-Robledo, A. K. S.; Zahab, A.-A.; Centeno, A.; Sacco, A.; Pesquera, A.; Zurutuza, A.; Rossi, A. M.; Tran, D. N. H.; L Silva, D.; Losic, D.; Farivar, F.; Kerdoncuff, H.; Kwon, H.; Pirart, J.; Campos, J. L. E.; Subhedar, K. M.; Tay, L.-L.; Ren, L.; Cançado, L. G.; Paillet, M.; Finnie, P.; Yap, P. L.; Arenal, R.; Dhakate, S. R.; Wood, S.; Jiménez-Sandoval, S.; Batten, T.; Nagyte, V.; Yao, Y.; Hight Walker, A. R.; Martins Ferreira, E. H.; Casiraghi, C.; Pollard, A. J. International Interlaboratory Comparison of Raman Spectroscopic Analysis of CVD-Grown Graphene. *2D Mater.* **2022**, *9*, No. 035010.

(22) Englert, J. M.; Vecera, P.; Knirsch, K. C.; Schäfer, R. A.; Hauke, F.; Hirsch, A. Scanning-Raman-Microscopy for the Statistical Analysis of Covalently Functionalized Graphene. *ACS Nano* **2013**, *7*, 5472−5482.

(23) Dresselhaus, M. S.; Dresselhaus, G.; Saito, R.; Jorio, A. Raman Spectroscopy of Carbon Nanotubes. *Phys. Rep.* **2005**, *409*, 47−99.

(24) Dresselhaus, M. S.; Jorio, A.; Hofmann, M.; Dresselhaus, G.; Saito, R. Perspectives on Carbon Nanotubes and Graphene Raman Spectroscopy. *Nano Lett.* **2010**, *10*, 751−758.

(25) Herziger, F.; Vierck, A.; Laudenbach, J.; Maultzsch, J. Understanding Double-Resonant Raman Scattering in Chiral Carbon Nanotubes: Diameter and Energy Dependence of the *D* Mode. *Phys. Rev. B* **2015**, *92*, No. 235409.

(26) Laudenbach, J.; Hennrich, F.; Telg, H.; Kappes, M.; Maultzsch, J. Resonance Behavior of the Defect-Induced Raman Mode of Single-Chirality Enriched Carbon Nanotubes. *Phys. Rev. B* **2013**, *87*, No. 165423.

(27) Laudenbach, J.; Schmid, D.; Herziger, F.; Hennrich, F.; Kappes, M.; Muoth, M.; Haluska, M.; Hof, F.; Backes, C.; Hauke, F.; Hirsch, A.; Maultzsch, J. Diameter Dependence of the Defect-Induced Raman Modes in Functionalized Carbon Nanotubes. *Carbon* **2017**, *112*, 1−7.

(28) Dresselhaus, M. S.; Jorio, A.; Souza Filho, A. G.; Saito, R. Defect Characterization in Graphene and Carbon Nanotubes Using Raman Spectroscopy. *Philos. Trans. R Soc. A* **2010**, *368*, 5355−5377.
(29) Simmons, J. M.; Nichols, B. M.; Baker, S. E.; Marcus, M. S.; Castellini, O. M.; Lee, C. S.; Hamers, R. J.; Eriksson, M. A. Effect of Ozone Oxidation on Single-Walled Carbon Nanotubes. *J. Phys. Chem. B* **2006**, *110*, 7113−7118.
(30) Dillon, A. C.; Parilla, P. A.; Alleman, J. L.; Gennett, T.; Jones, K. M.; Heben, M. J. Systematic Inclusion of Defects in Pure Carbon Single-Wall Nanotubes and their Effect on the Raman D-Band. *Chem. Phys. Lett.* **2005**, *401*, 522−528.
(31) Ogrin, D.; Chattopadhyay, J.; Sadana, A. K.; Billups, W. E.; Barron, A. R. Epoxidation and Deoxygenation of Single-Walled Carbon Nanotubes: Quantification of Epoxide Defects. *J. Am. Chem. Soc.* **2006**, *128*, 11322−11323.
(32) Qiu, S.; Wu, K.; Gao, B.; Li, L.; Jin, H.; Li, Q. Solution-Processing of High-Purity Semiconducting Single-Walled Carbon Nanotubes for Electronics Devices. *Adv. Mater.* **2019**, *31*, No. 1800750.
(33) Huang, X.; McLean, R. S.; Zheng, M. High-Resolution Length Sorting and Purification of DNA-Wrapped Carbon Nanotubes by Size-Exclusion Chromatography. *Anal. Chem.* **2005**, *77*, 6225−6228.
(34) Sebastian, F. L.; Zorn, N. F.; Settele, S.; Lindenthal, S.; Berger, F. J.; Bendel, C.; Li, H.; Flavel, B. S.; Zaumseil, J. Absolute Quantification of sp^3 Defects in Semiconducting Single-Wall Carbon Nanotubes by Raman Spectroscopy. *J. Phys. Chem. Lett.* **2022**, *13*, 3542−3548.
(35) Graf, A.; Zakharko, Y.; Schießl, S. P.; Backes, C.; Pfohl, M.; Flavel, B. S.; Zaumseil, J. Large Scale, Selective Dispersion of Long Single-Walled Carbon Nanotubes with High Photoluminescence Quantum Yield by Shear Force Mixing. *Carbon* **2016**, *105*, 593−599.
(36) Yomogida, Y.; Tanaka, T.; Tsuzuki, M.; Wei, X.; Kataura, H. Automatic Sorting of Single-Chirality Single-Wall Carbon Nanotubes Using Hydrophobic Cholates: Implications for Multicolor Near-Infrared Optical Technologies. *ACS Appl. Nano Mater.* **2020**, *3*, 11289−11297.
(37) Grimm, S.; Schießl, S. P.; Zakharko, Y.; Rother, M.; Brohmann, M.; Zaumseil, J. Doping-Dependent G-Mode Shifts of Small Diameter Semiconducting Single-Walled Carbon Nanotubes. *Carbon* **2017**, *118*, 261−267.
(38) Maultzsch, J.; Telg, H.; Reich, S.; Thomsen, C. Radial Breathing mode of Single-Walled Carbon Nanotubes: Optical Transition Energies and Chiral-Index Assignment. *Phys. Rev. B* **2005**, *72*, No. 205438.
(39) Telg, H.; Duque, J. G.; Staiger, M.; Tu, X.; Hennrich, F.; Kappes, M. M.; Zheng, M.; Maultzsch, J.; Thomsen, C.; Doorn, S. K. Chiral Index Dependence of the G^+ and G^- Raman Modes in Semiconducting Carbon Nanotubes. *ACS Nano* **2012**, *6*, 904−911.
(40) Berger, F. J.; Lüttgens, J.; Nowack, T.; Kutsch, T.; Lindenthal, S.; Kistner, L.; Muller, C. C.; Bongartz, L. M.; Lumsargis, V. A.; Zakharko, Y.; Zaumseil, J. Brightening of Long, Polymer-Wrapped Carbon Nanotubes by sp^3 Functionalization in Organic Solvents. *ACS Nano* **2019**, *13*, 9259−9269.
(41) Miyauchi, Y.; Iwamura, M.; Mouri, S.; Kawazoe, T.; Ohtsu, M.; Matsuda, K. Brightening of Excitons in Carbon Nanotubes on Dimensionality Modification. *Nat. Photonics* **2013**, *7*, 715−719.
(42) Hertel, T.; Himmelein, S.; Ackermann, T.; Stich, D.; Crochet, J. Diffusion Limited Photoluminescence Quantum Yields in 1-D Semiconductors: Single-Wall Carbon Nanotubes. *ACS Nano* **2010**, *4*, 7161−7168.
(43) Liu, T.; Xiao, Z. Exact and Closed Form Solutions for the Quantum Yield, Exciton Diffusion Length, and Lifetime To Reveal the Universal Behaviors of the Photoluminescence of Defective Single-Walled Carbon Nanotubes. *J. Phys. Chem. C* **2011**, *115*, 16920−16927.
(44) Georgi, C.; Böhmler, M.; Qian, H.; Novotny, L.; Hartschuh, A. Probing Exciton Propagation and Quenching in Carbon Nanotubes with Near-Field Optical Microscopy. *Phys. Status solidi B* **2009**, *246*, 2683−2688.
(45) Crochet, J. J.; Duque, J. G.; Werner, J. H.; Lounis, B.; Cognet, L.; Doorn, S. K. Disorder Limited Exciton Transport in Colloidal Single-Wall Carbon Nanotubes. *Nano Lett.* **2012**, *12*, 5091−5096.
(46) Hofmann, M. S.; Glückert, J. T.; Noe, J.; Bourjau, C.; Dehmel, R.; Hogele, A. Bright, Long-Lived and Coherent Excitons in Carbon Nanotube Quantum Dots. *Nat. Nanotechnol.* **2013**, *8*, 502−505.
(47) Miyauchi, Y.; Hirori, H.; Matsuda, K.; Kanemitsu, Y. Radiative Lifetimes and Coherence Lengths of One-Dimensional Excitons in Single-Walled Carbon Nanotubes. *Phys. Rev. B* **2009**, *80*, No. 081410.
(48) Cognet, L.; Tsyboulski, D. A.; Rocha, J.-D. R.; Doyle, C. D.; Tour, J. M.; Weisman, R. B. Stepwise Quenching of Exciton Fluorescence in Carbon Nanotubes by Single-Molecule Reactions. *Science* **2007**, *316*, 1465−1468.
(49) Siitonen, A. J.; Tsyboulski, D. A.; Bachilo, S. M.; Weisman, R. B. Dependence of Exciton Mobility on Structure in Single-Walled Carbon Nanotubes. *J. Phys. Chem. Lett.* **2010**, *1*, 2189−2192.
(50) Strano, M. S.; Dyke, C. A.; Usrey, M. L.; Barone, P. W.; Allen, M. J.; Shan, H.; Kittrell, C.; Hauge, R. H.; Tour, J. M.; Smalley, R. E. Electronic Structure Control of Single-Walled Carbon Nanotube Functionalization. *Science* **2003**, *301*, 1519−1522.
(51) Cançado, L. G.; Jorio, A.; Pimenta, M. A. Measuring the Absolute Raman Cross Section of Nanographites As a Function of Laser Energy and Crystallite Size. *Phys. Rev. B* **2007**, *76*, No. 064304.
(52) Saraiva, G. D.; Souza Filho, A. G.; Braunstein, G.; Barros, E. B.; Mendes Filho, J.; Moreira, E. C.; Fagan, S. B.; Baptista, D. L.; Kim, Y. A.; Muramatsu, H.; Endo, M.; Dresselhaus, M. S. Resonance Raman Spectroscopy in Si and C Ion-Implanted Double-Wall Carbon Nanotubes. *Phys. Rev. B* **2009**, *80*, No. 155452.
(53) Jorio, A.; Fantini, C.; Pimenta, M. A.; Capaz, R. B.; Samsonidze, G. G.; Dresselhaus, G.; Dresselhaus, M. S.; Jiang, J.; Kobayashi, N.; Grüneis, A.; Saito, R. Resonance Raman Spectroscopy (n,m)-Dependent Effects in Small-Diameter Single-Wall Carbon Nanotubes. *Phys. Rev. B* **2005**, *71*, No. 075401.
(54) Kürti, J.; Zólyomi, V.; Kertesz, M.; Sun, G. The Geometry and the Radial Breathing Mode of Carbon Nanotubes: Beyond the Ideal Behaviour. *New J. Phys.* **2003**, *5*, 125.
(55) Rao, A. M.; Richter, E.; Bandow, S.; Chase, B.; Eklund, P. C.; Williams, K. A.; Fang, S.; Subbaswamy, K. R.; Menon, M.; Thess, A.; Smalley, R. E.; Dresselhaus, G.; Dresselhaus, M. S. Diameter-Selective Raman Scattering from Vibrational Modes in Carbon Nanotubes. *Science* **1997**, *275*, 187−191.
(56) Vierck, A.; Gannott, F.; Schweiger, M.; Zaumseil, J.; Maultzsch, J. ZA-Derived Phonons in the Raman Spectra of Single-Walled Carbon Nanotubes. *Carbon* **2017**, *117*, 360−366.
(57) Kalbac, M.; Kavan, L.; Zukalová, M.; Dunsch, L. The Intermediate Frequency Modes of Single- and Double-Walled Carbon Nanotubes: A Raman Spectroscopic and In Situ Raman Spectroelectrochemical Study. *Chem. Eur. J.* **2006**, *12*, 4451−4457.
(58) Inaba, T.; Tanaka, Y.; Konabe, S.; Homma, Y. Effects of Chirality and Defect Density on the Intermediate Frequency Raman Modes of Individually Suspended Single-Walled Carbon Nanotubes. *J. Phys. Chem. C* **2018**, *122*, 9184−9190.
(59) Skákalová, V.; Maultzsch, J.; Osváth, Z.; Biró, L. P.; Roth, S. Intermediate Frequency Modes in Raman Spectra of Ar+-Irradiated Single-Wall Carbon Nanotubes. *Phys. Status Solidi RRL* **2007**, *1*, 138−140.
(60) Lin, Z.; Beltrán, L. C.; De los Santos, Z. A.; Li, Y.; Adel, T.; Fagan, J. A.; Hight Walker, A. R.; Egelman, E. H.; Zheng, M. DNA-Guided Lattice Remodeling of Carbon Nanotubes. *Science* **2022**, *377*, 535−539.
(61) Fantini, C.; Jorio, A.; Souza, M.; Ladeira, L. O.; Souza Filho, A. G.; Saito, R.; Samsonidze, G. G.; Dresselhaus, G.; Dresselhaus, M. S.; Pimenta, M. A. One-Dimensional Character of Combination Modes in the Resonance Raman Scattering of Carbon Nanotubes. *Phys. Rev. Lett.* **2004**, *93*, No. 087401.
(62) Weight, B. M.; Zheng, M.; Tretiak, S. Signatures of Chemical Dopants in Simulated Resonance Raman Spectroscopy of Carbon Nanotubes. *J. Phys. Chem. Lett.* **2023**, *14*, 1182−1191.

https://doi.org/10.1021/acsnano.3c07668
ACS Nano 2023, 17, 21771−21781

(63) Piao, Y.; Simpson, J. R.; Streit, J. K.; Ao, G.; Zheng, M.; Fagan, J. A.; Hight Walker, A. R. Intensity Ratio of Resonant Raman Modes for (n,m) Enriched Semiconducting Carbon Nanotubes. *ACS Nano* **2016**, *10*, 5252−5259.
(64) Yomogida, Y.; Tanaka, T.; Zhang, M.; Yudasaka, M.; Wei, X.; Kataura, H. Industrial-scale Separation of High-Purity Single-Chirality Single-Wall Carbon Nanotubes for Biological Imaging. *Nat. Commun.* **2016**, *7*, 12056.
(65) Pfohl, M.; Tune, D. D.; Graf, A.; Zaumseil, J.; Krupke, R.; Flavel, B. S. Fitting Single-Walled Carbon Nanotube Optical Spectra. *ACS Omega* **2017**, *2*, 1163−1171.
(66) Naumov, A. V.; Ghosh, S.; Tsyboulski, D. A.; Bachilo, S. M.; Weisman, R. B. Analyzing Absorption Backgrounds in Single-Walled Carbon Nanotube Spectra. *ACS Nano* **2011**, *5*, 1639−1648.

https://doi.org/10.1021/acsnano.3c07668
ACS Nano 2023, 17, 21771−21781

Supporting Information

Unified Quantification of Quantum Defects in Small-Diameter Single-Walled Carbon Nanotubes by Raman Spectroscopy

Finn L. Sebastian[1], Felicitas Becker[1], Yohei Yomogida[2], Yuuya Hosokawa[2], Simon Settele[1], Sebastian Lindenthal[1], Kazuhiro Yanagi[2], Jana Zaumseil[1]*

[1]Institute for Physical Chemistry, Universität Heidelberg, D-69120 Heidelberg, Germany

[2]Department of Physics, Tokyo Metropolitan University, Tokyo 192-0397, Japan

Corresponding Author

*E-mail: zaumseil@uni-heidelberg.de

UV-Vis-nIR absorption spectra S-3
Photoluminescence excitation-emission maps S-4
Raman spectra of SWCNTs (RBM region) at different excitation wavelengths S-5
Diameter dependence of Raman G^+ and G^- mode wavenumber S-6
Photoluminescence spectra and PLQYs S-7
(7,3) SWCNTs S-7
(8,3) SWCNTs S-8
(9,2) SWCNTs S-8
(7,5) SWCNTs S-9
Raman spectra of SWCNTs at different excitation wavelengths S-10
(6,5) SWCNTs S-10
(8,3) SWCNTs S-10
(7,5) SWCNTs S-11
Linear fits of $\Delta(D/G^+)$ *vs* n_d at different excitation wavelengths S-12
(7,3) SWCNTs S-12
(6,5) SWCNTs S-12
(7,5) SWCNTs S-13
Normalization to the number of carbon atoms per micrometer S-14
Correlation with chiral angle and mod family S-14
Comparison of defect density in graphene and SWCNTs S-15
IFM Raman spectra S-16
(7,3) SWCNTs S-16
(8,3) SWCNTs S-16
(9,2) SWCNTs S-17
(7,5) SWCNTs S-17
Slopes of linear fits Δ(IFM/RBM) *vs* n_d S-18
REFERENCES S-18

Figures and Tables

UV-Vis-nIR absorption spectra

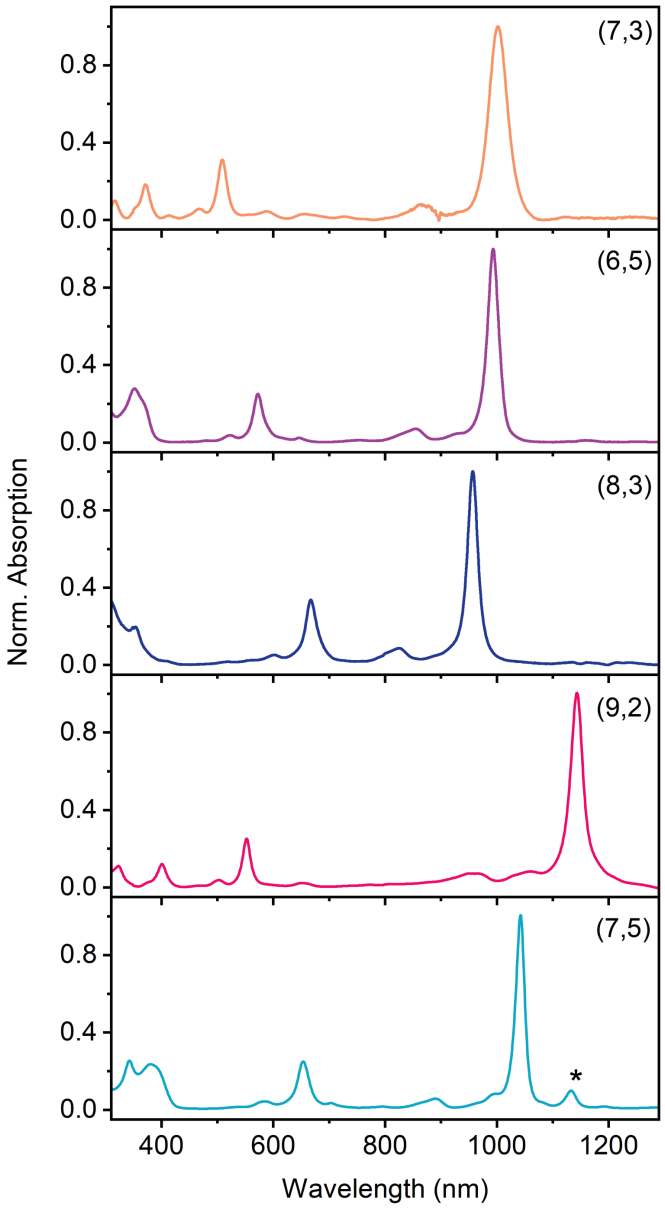

Figure S1. (a) Normalized UV-Vis-nIR absorption spectra of pristine (7,3), (6,5), (8,3), (9,2), and (7,5) SWCNTs (residual (7,6) SWCNTs are marked with an asterisk).

Photoluminescence excitation-emission maps

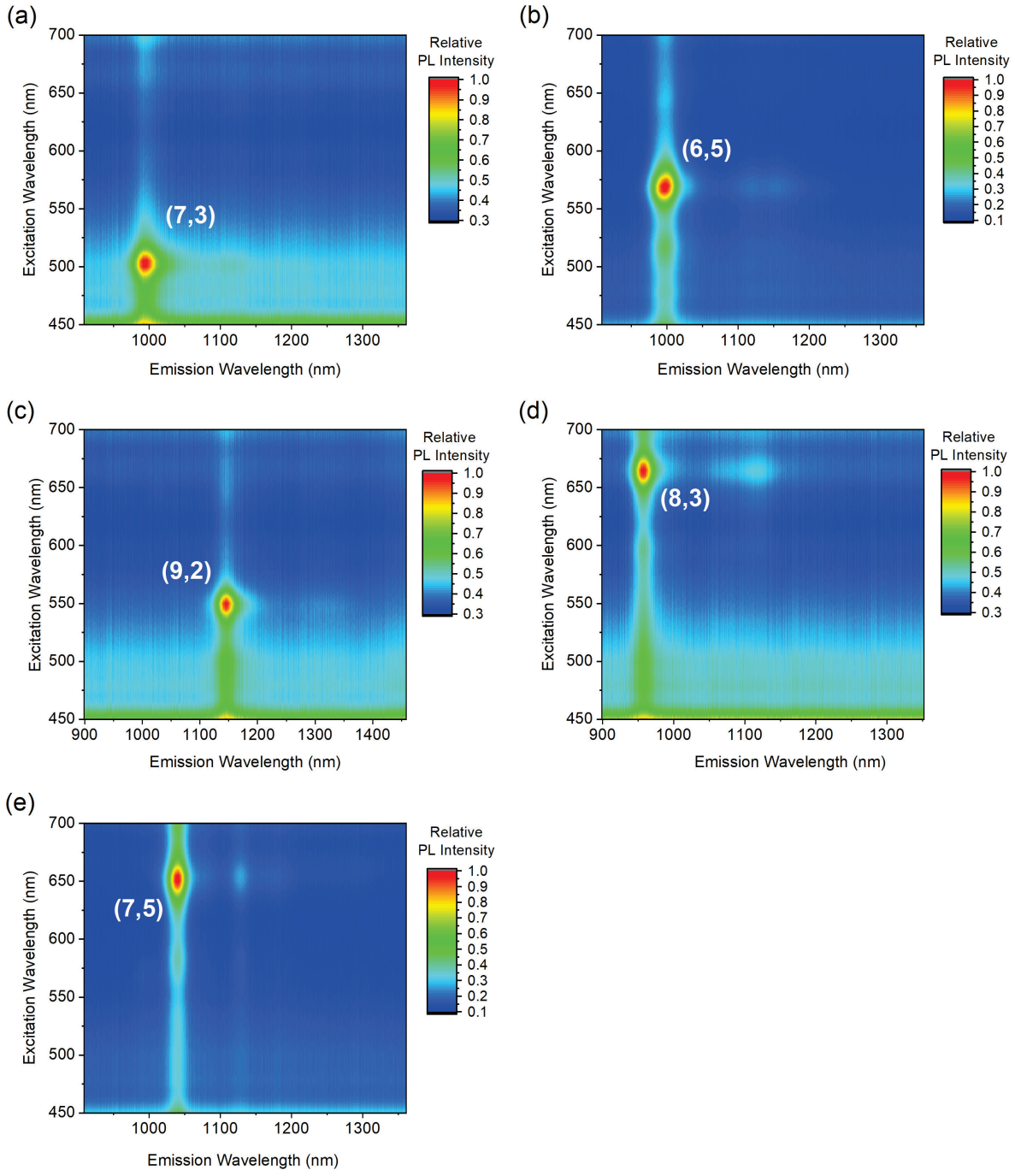

Figure S2. Photoluminescence excitation-emission maps of pristine (a) (7,3), (b) (6,5), (c) (8,3), (d) (9,2), and (e) (7,5) SWCNTs.

Raman spectra of SWCNTs (RBM region) at different excitation wavelengths

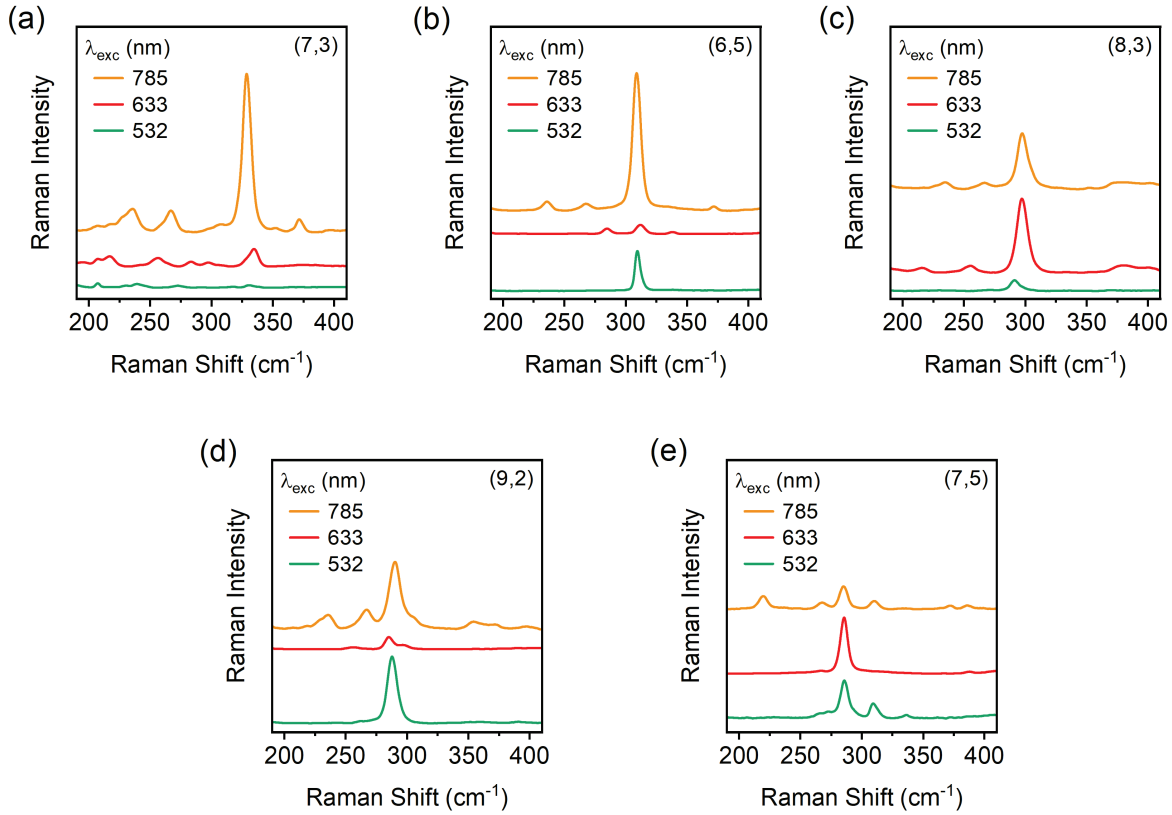

Figure S3. Averaged Raman spectra (from >2000 individual spots for each spectrum) of (a) (7,3), (b) (6,5), (c) (8,3), (d) (9,2), and (e) (7,5) SWCNTs in the RBM region, acquired at excitation wavelengths of 532 nm, 633 nm, and 785 nm.

Diameter dependence of Raman G^+ and G^- mode wavenumber

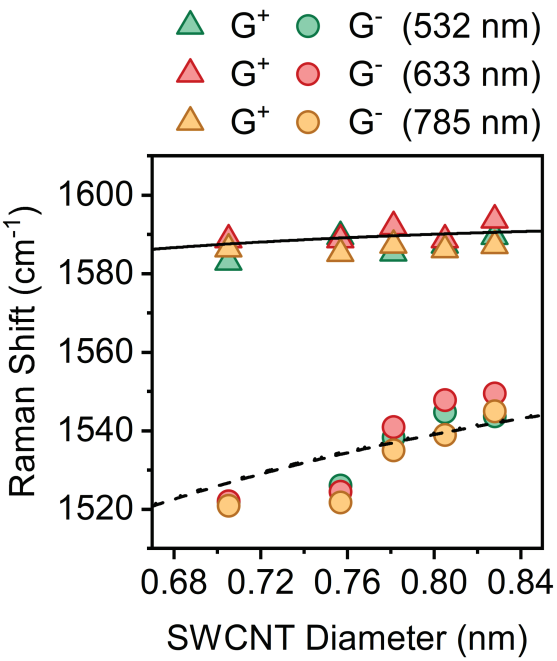

Figure S4. Wavenumbers of Raman G^+ and G^- modes obtained from Lorentzian fits to Raman spectra of pristine (7,3), (6,5), (8,3), (9,2), and (7,5) SWCNTs at excitation laser wavelengths of 532 nm, 633 nm, and 785 nm. The solid and dashed lines represent empirical expressions for the diameter dependence of G^+ and G^- modes as reported by Telg *et al.*[1]

Photoluminescence spectra and PLQYs

(7,3) SWCNTs

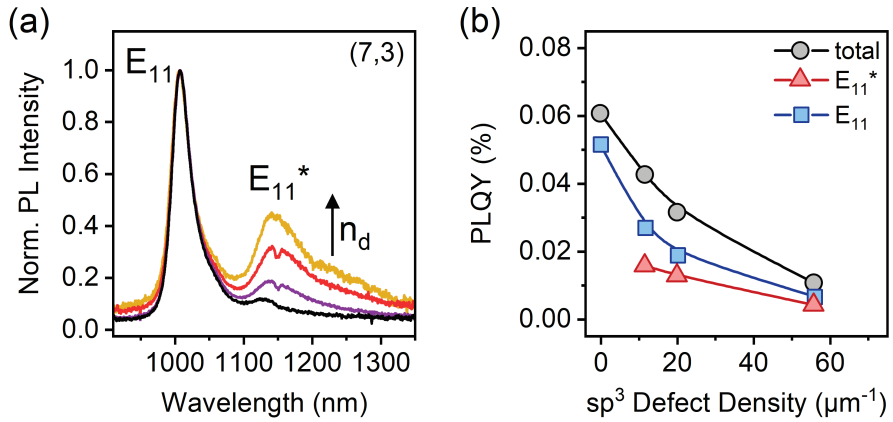

Figure S5. (a) Normalized PL spectra under resonant excitation at 509 nm and (b) PLQYs of pristine and sp^3-functionalized (7,3) SWCNTs dispersed by SDS in water. Solid lines are guides to the eye.

(6,5) SWCNTs

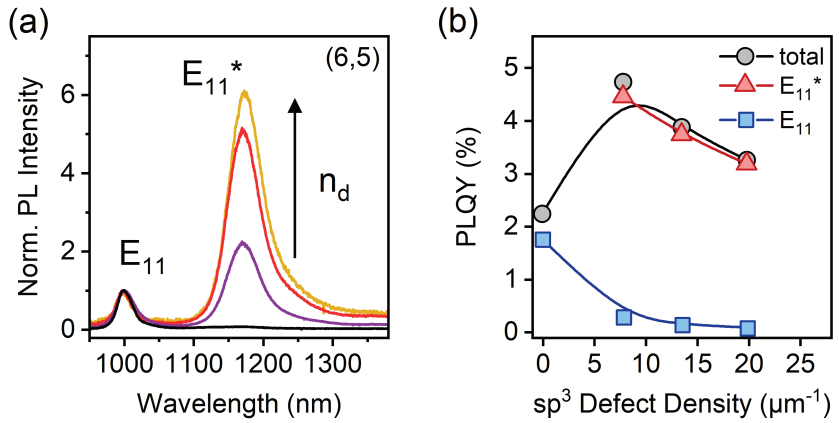

Figure S6. (a) Normalized PL spectra under resonant excitation at 575 nm and (b) PLQYs of pristine and sp^3-functionalized (6,5) SWCNTs dispersed by PFO-BPy in toluene. Solid lines are guides to the eye.

(8,3) SWCNTs

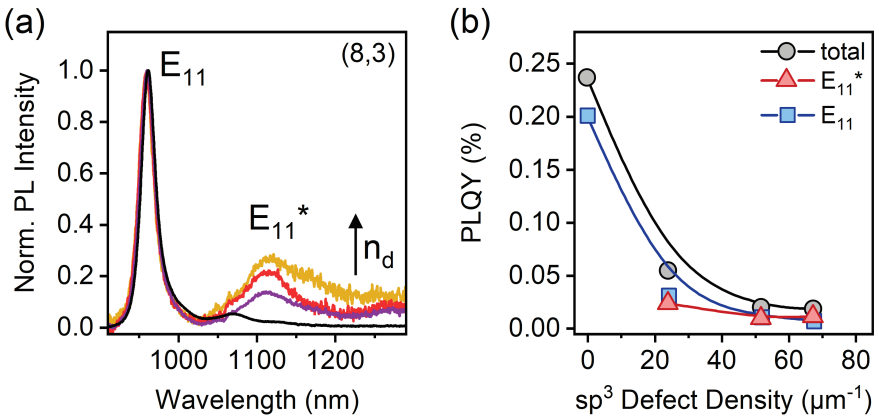

Figure S7. (a) Normalized PL spectra under resonant excitation at 668 nm and (b) PLQYs of pristine and sp^3-functionalized (8,3) SWCNTs dispersed by SDS in water. Solid lines are guides to the eye.

(9,2) SWCNTs

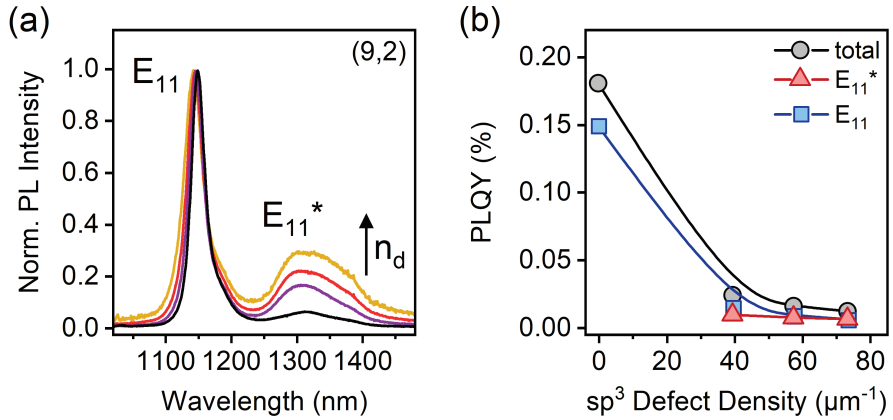

Figure S8. (a) Normalized PL spectra under resonant excitation at 553 nm and (b) PLQYs of pristine and sp^3-functionalized (9,2) SWCNTs dispersed by SDS in water. Solid lines are guides to the eye.

(7,5) SWCNTs

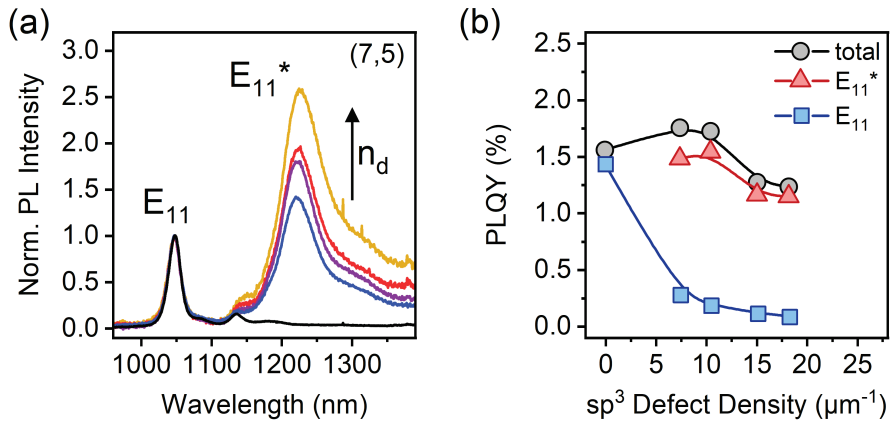

Figure S9. (a) Normalized PL spectra under resonant excitation at 652 nm and (b) PLQYs of pristine and sp^3-functionalized (7,5) SWCNTs dispersed by PFO in toluene. Solid lines are guides to the eye.

Raman spectra of SWCNTs at different excitation wavelengths

(6,5) SWCNTs

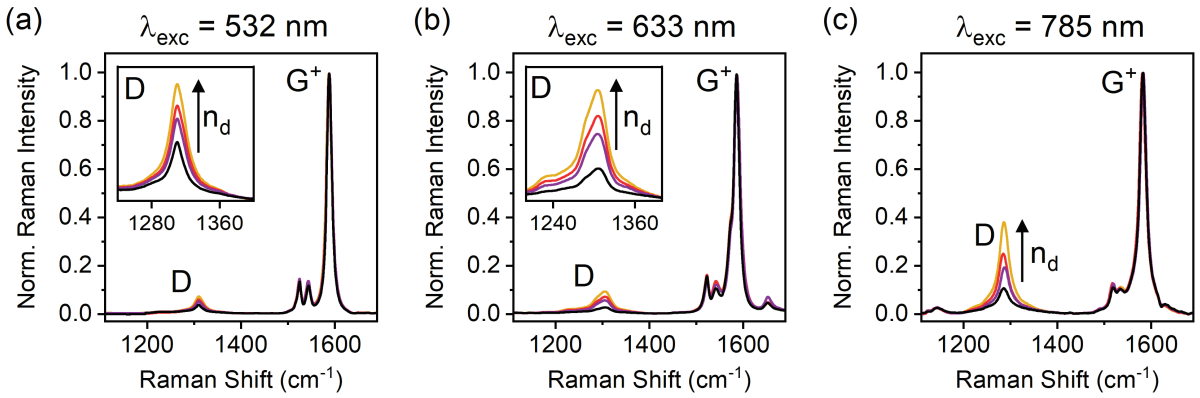

Figure S10. Normalized Raman spectra of pristine (black) and sp^3-functionalized (6,5) SWCNTs ($DzNO_2$) at different Raman excitation wavelengths of 532 nm (a), 633 nm (b), and 785 nm (c).

(8,3) SWCNTs

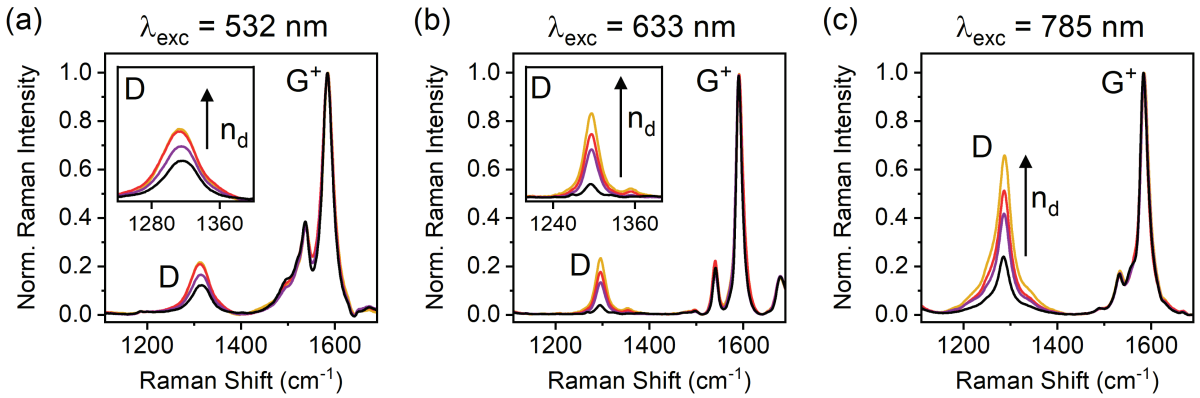

Figure S11. Normalized Raman spectra of pristine (black) and sp^3-functionalized (8,3) SWCNTs ($DzNO_2$) at different Raman excitation wavelengths of 532 nm (a), 633 nm (b), and 785 nm (c).

(7,5) SWCNTs

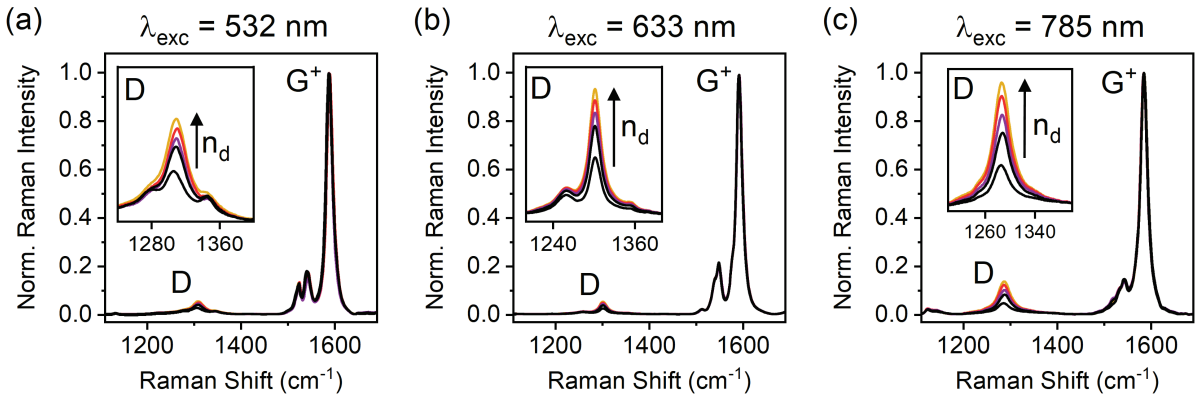

Figure S12. Normalized Raman spectra of pristine (black) and sp^3-functionalized (7,5) SWCNTs ($DzNO_2$) at different Raman excitation wavelengths of 532 nm (a), 633 nm (b), and 785 nm (c).

Linear fits of $\Delta(D/G^+)$ *vs* n_d at different excitation wavelengths

(7,3) SWCNTs

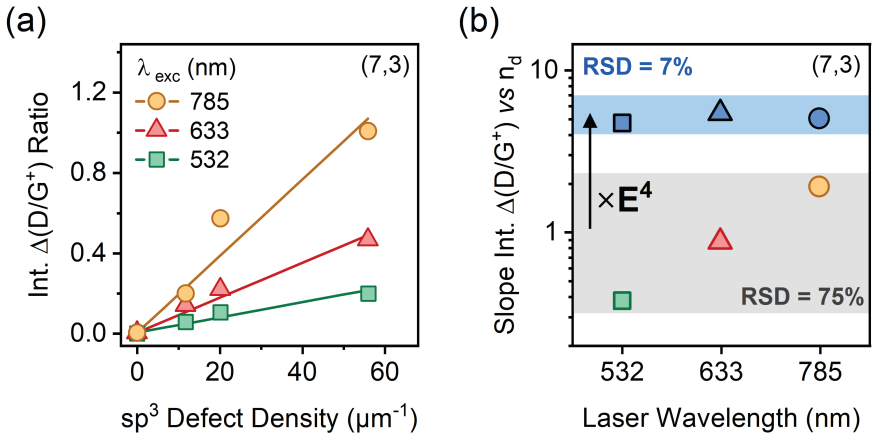

Figure S13. (a) Linear fits of integrated $\Delta(D/G^+)$ Raman mode ratio *vs* defect density from PLQY measurements for sp^3-functionalized (7,3) SWCNTs at excitation wavelengths of 532 nm ($R^2 = 0.98$), 633 nm ($R^2 = 0.99$), and 785 nm ($R^2 = 0.98$). (b) Slopes of linear fits in (a) for different excitation wavelengths (*i.e.*, excitation energy) and their normalization with excitation energy E_L^4 including relative standard deviation (RSD) in %.

(6,5) SWCNTs

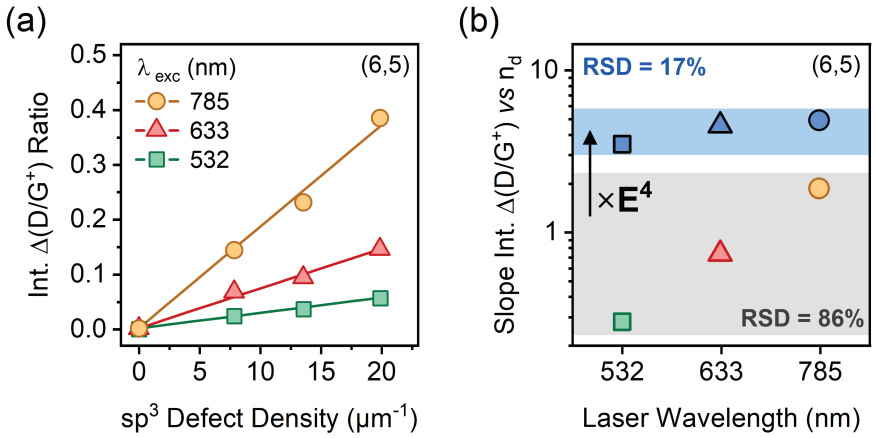

Figure S14. (a) Linear fits of integrated $\Delta(D/G^+)$ Raman mode ratio *vs* defect density from PLQY measurements for sp^3-functionalized (6,5) SWCNTs at excitation wavelengths of 532 nm ($R^2 = 0.99$), 633 nm ($R^2 = 0.99$), and 785 nm ($R^2 = 0.99$). (b) Slopes of linear fits in (a) for different excitation wavelengths (*i.e.*, excitation energy) and their normalization with excitation energy E_L^4 including relative standard deviation (RSD) in %.

(7,5) SWCNTs

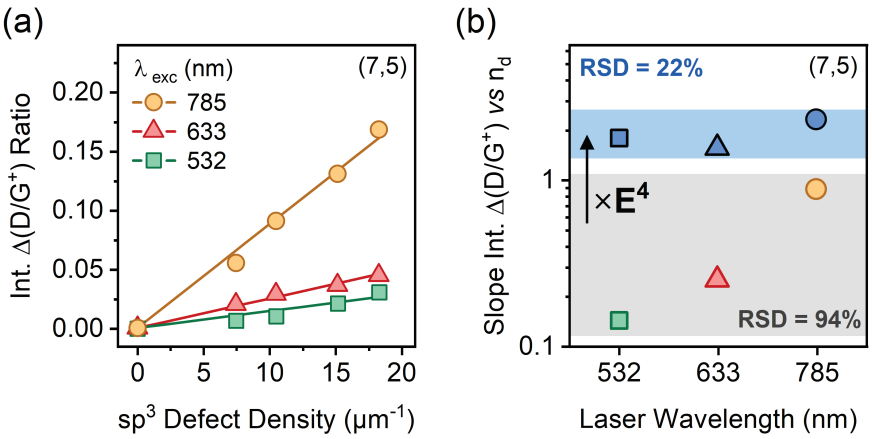

Figure S15. (a) Linear fits of integrated $\Delta(D/G^+)$ Raman mode ratio *vs* defect density from PLQY measurements for sp^3-functionalized (7,5) SWCNTs at excitation wavelengths of 532 nm ($R^2 = 0.98$), 633 nm ($R^2 = 0.99$), and 785 nm ($R^2 = 0.99$). (b) Slopes of linear fits in (a) for different excitation wavelengths (*i.e.*, excitation energy) and their normalization with excitation energy E_L^4 including relative standard deviation (RSD) in %.

Normalization to the number of carbon atoms per micrometer

Table S1. Number of carbon atoms and SWCNT lattice area per micrometer of carbon nanotube for the investigated chiralities.

Chirality	(7,3)	(6,5)	(8,3)	(9,2)	(7,5)
Number of carbon atoms (μm^{-1})	83441	89554	92458	95276	98012
Area (m^2)	2.23×10^{-15}	2.39×10^{-15}	2.45×10^{-15}	2.54×10^{-15}	2.61×10^{-15}

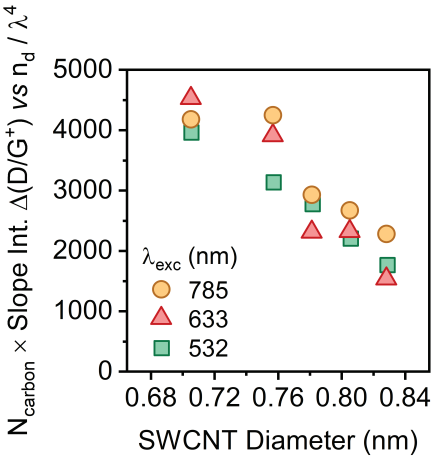

Figure S16. Slope of the integrated Raman $\Delta(D/G^+)$ ratio *vs* calculated defect density n_d multiplied with the number of carbon atoms per micrometer of the respective SWCNT chirality.

Correlation with chiral angle and mod family

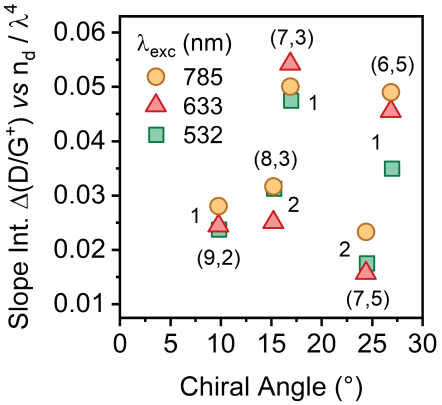

Figure S17. Slope of the integrated Raman $\Delta(D/G^+)$ ratio normalized to the excitation wavelength λ_L^{-4} *vs* chiral angle θ. (7,3), (6,5), and (9,2) SWCNTs belong to the mod 1 family, whereas (8,3) and (7,5) SWCNTs belong to the mod 2 family.

Comparison of defect density in graphene and SWCNTs

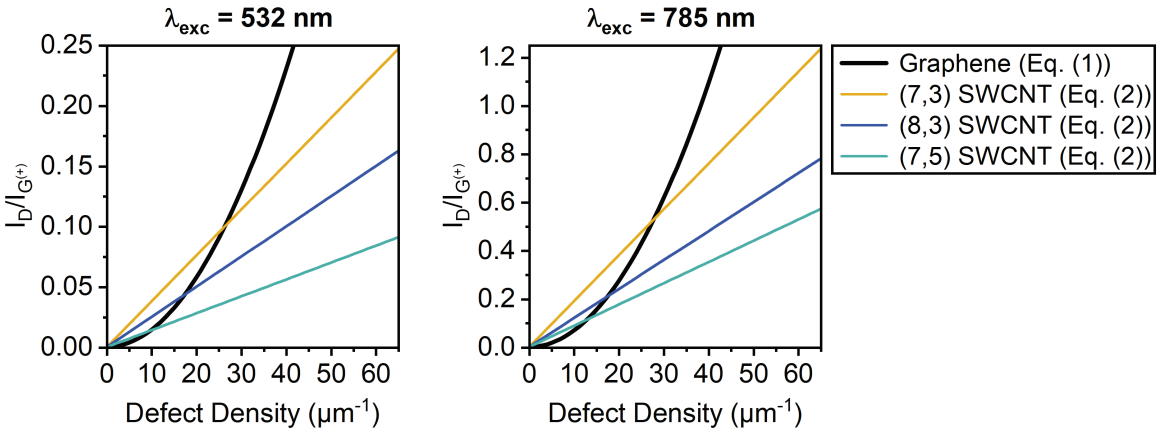

Figure S18. (a) Raman $I_D/I_{G^{(+)}}$ ratio *vs* calculated defect density n_d (μm^{-1}) at excitation wavelengths of 532 nm and 785 nm for graphene and different SWCNT species according to equations (1) and (2) in the main text, respectively.

Table S2. Raman $I_D/I_{G^{(+)}}$ ratios at specific calculated defect densities n_d (μm^{-1}) for all investigated SWCNT chiralities and graphene according to equations (1) and (2) in the main text (Raman excitation wavelength 532 nm).

n_d (μm^{-1})	**$I_D/I_{G^{(+)}}$ (n_d (μm^{-1}))**					
	(7,3)	**(6,5)**	**(8,3)**	**(9,2)**	**(7,5)**	**Graphene**
5	0.020	0.017	0.011	0.010	0.007	0.004
10	0.040	0.033	0.023	0.020	0.015	0.014
20	0.080	0.067	0.046	0.040	0.030	0.058
50	0.200	0.167	0.114	0.100	0.074	0.360

IFM Raman spectra

(7,3) SWCNTs

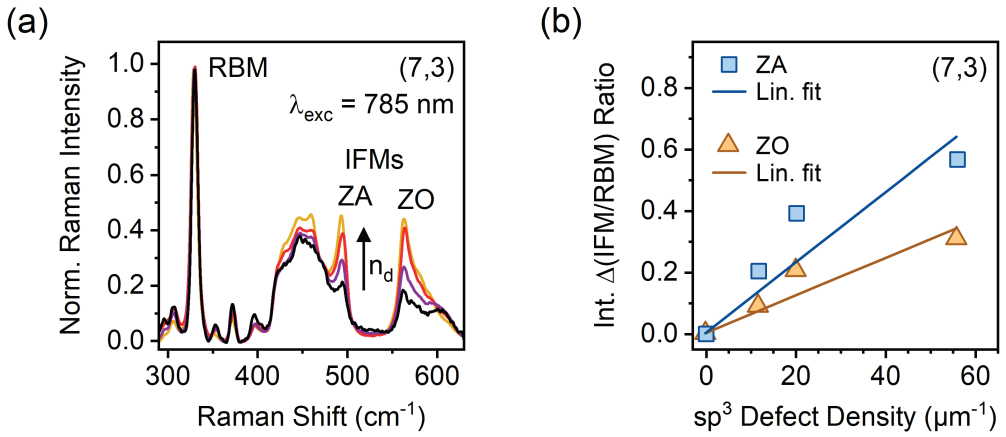

Figure S19. (a) Raman spectra of pristine and sp^3-functionalized (7,3) SWCNTs in the region of intermediate frequencies acquired at 785 nm excitation. (b) Linear fits of Δ(IFM/RBM) *vs* calculated sp^3 defect density n_d for both intermediate frequency modes I and II as marked in (a), R^2 (ZA) = 0.96, R^2 (ZO) = 0.97.

(8,3) SWCNTs

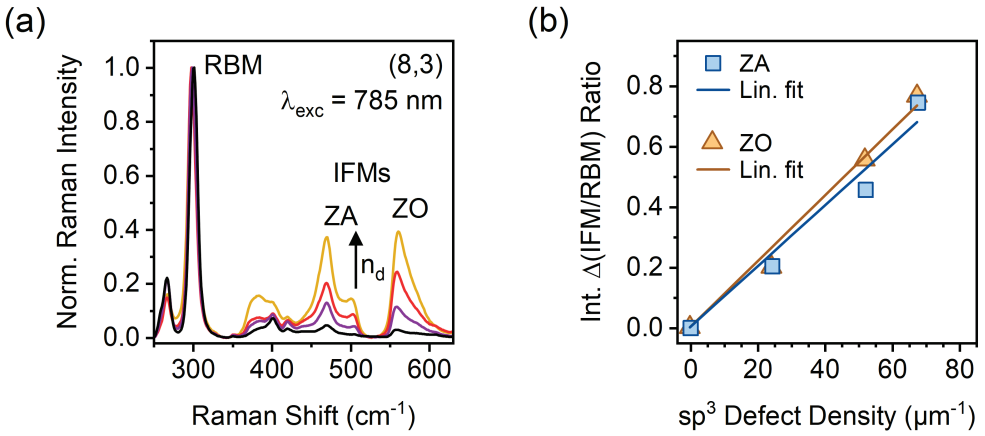

Figure S20. (a) Raman spectra of pristine and sp^3-functionalized (8,3) SWCNTs in the region of intermediate frequencies acquired at 785 nm excitation. (b) Linear fits of Δ(IFM/RBM) *vs* calculated sp^3 defect density n_d for both intermediate frequency modes I and II as marked in (a), R^2 (ZA) = 0.99, R^2 (ZO) = 0.99.

(9,2) SWCNTs

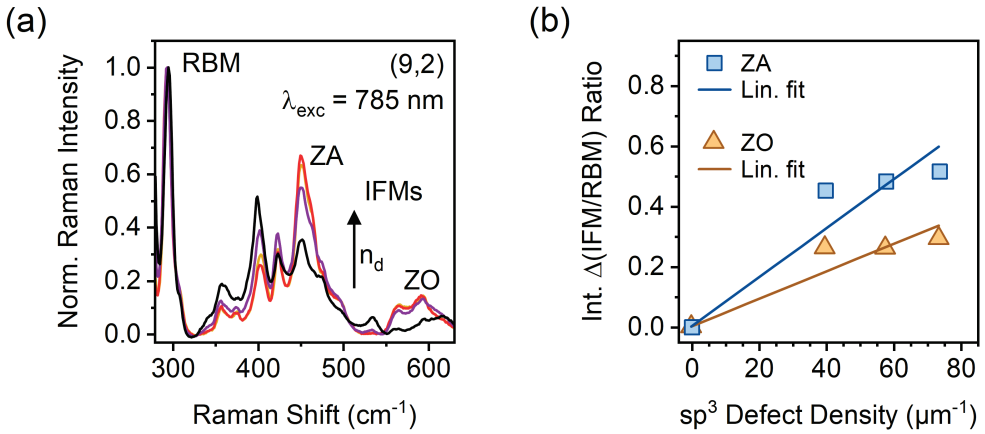

Figure S21. (a) Raman spectra of pristine and sp^3-functionalized (9,2) SWCNTs in the region of intermediate frequencies acquired at 785 nm excitation. (b) Linear fits of Δ(IFM/RBM) *vs* calculated sp^3 defect density n_d for both intermediate frequency modes I and II as marked in (a), R^2 (ZA) = 0.98, R^2 (ZO) = 0.98.

(7,5) SWCNTs

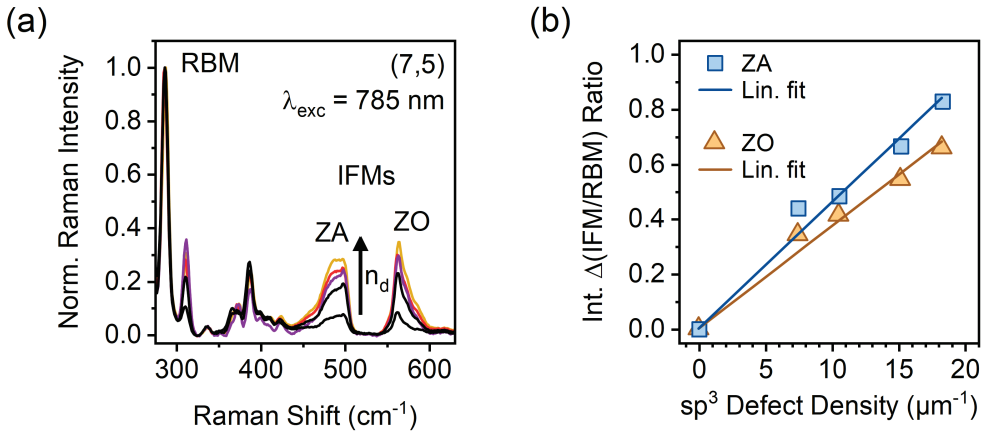

Figure S22. (a) Raman spectra of pristine and sp^3-functionalized (7,5) SWCNTs in the region of intermediate frequencies acquired at 785 nm excitation. (b) Linear fits of Δ(IFM/RBM) *vs* calculated sp^3 defect density n_d for both intermediate frequency modes I and II as marked in (a), R^2 (ZA) = 0.99, R^2 (ZO) = 0.99.

Slopes of linear fits Δ(IFM/RBM) *vs* n_d

Table S3. Slope (standard deviation) of Δ(IFM/RBM) ratio *vs* calculated sp^3 defect density n_d linear fit for different SWCNT chiralities from Raman spectra collected at an excitation wavelength of 785 nm.

Chirality	**(7,3)**	**(6,5)**	**(8,3)**	**(9,2)**	**(7,5)**
Slope Δ(ZA/RBM) *vs* n_d	0.001 (0.002)	0.038 (0.002)	0.010 (0.001)	0.008 (0.001)	0.046 (0.002)
Slope Δ(ZO/RBM) *vs* n_d	0.006 (0.001)	0.021 (0.002)	0.011 (0.001)	0.005 (0.001)	0.037 (0.002)

REFERENCES

(1) Telg, H.; Duque, J. G.; Staiger, M.; Tu, X.; Hennrich, F.; Kappes, M. M.; Zheng, M.; Maultzsch, J.; Thomsen, C.; Doorn, S. K. Chiral Index Dependence of the G^+ and G^- Raman Modes in Semiconducting Carbon Nanotubes. *ACS Nano* **2012,** *6*, 904-911.

4 Spectroscopic identification of defect clustering in SWCNTs

This Chapter consists of a publication in which clustering of luminescent defects is identified with a combined approach of Raman spectroscopy, photoluminescence quantum yield measurements, and photoluminescence spectroscopy of single SWCNTs at cryogenic temperature.

For the original publication, refer to Sebastian *et al.*, *Nanoscale Horiz.* **9**, 2286-2294 (2024).

Formblatt Kumulative Dissertation

1. Publikation/*Publication:*

Vollständige bibliographische Referenz/*Complete bibliographic reference:*

Finn L. Sebastian, Simon Settele, Han Li, Benjamin S. Flavel, and Jana Zaumseil. *How to recognize clustering of luminescent defects in single-wall carbon nanotubes*. *Nanoscale Horiz.* **9**, 2286-2294 (2024), DOI: 10.1039/D4NH00383G.

2. Erstautorenschaft/*First authorship:* **Ja/*Yes***

3. Veröffentlicht/*Published:* **Ja/*Yes***

4. Beteiligungen/*Contributions (according to Contributor Role Taxonomy, CRediT):*

Contributor role	Doctoral student
Last name, first name	Sebastian, Finn Luca
Methodology	×
Software	
Validation	×
Formal analysis	×
Investigation	×
Resources	
Data curation	×
Writing - original draft	×
Writing - review and editing	×
Visualization	×
Supervision	
Project administration	
Funding acquisition	

Hiermit bestätige ich, dass alle obigen Angaben korrekt sind.
I confirm that all declarations made above are correct.



Finn Luca Sebastian
Doktorand/*Doctoral student*

Betreuungsperson/*Supervisor:*
Hiermit bestätige ich, dass alle obigen Angaben korrekt sind und dass die selbstständigen Arbeitsanteile des Doktoranden an der aufgeführten Publikation hinreichend und signifikant sind.
I confirm that all declarations made above are correct and that the doctoral student's independent contribution to this publication is significant and sufficient to be considered for the cumulative dissertation.



04.08.2025

Prof. Dr. Jana Zaumseil

Datum/*Date*

Nanoscale Horizons

ROYAL SOCIETY OF CHEMISTRY

COMMUNICATION

View Article Online
View Journal | View Issue

Check for updates

Cite this: *Nanoscale Horiz.*, 2024, 9, 2286

Received 6th August 2024,
Accepted 3rd October 2024

DOI: 10.1039/d4nh00383g

rsc.li/nanoscale-horizons

How to recognize clustering of luminescent defects in single-wall carbon nanotubes†

Finn L. Sebastian, [a] Simon Settele, [a] Han Li, [bc] Benjamin S. Flavel [d] and Jana Zaumseil *[a]

Semiconducting single-wall carbon nanotubes (SWCNTs) are a promising material platform for near-infrared *in vivo* imaging, optical sensing, and single-photon emission at telecommunication wavelengths. The functionalization of SWCNTs with luminescent defects can lead to significantly enhanced photoluminescence (PL) properties due to efficient trapping of highly mobile excitons and red-shifted emission from these trap states. Among the most studied luminescent defect types are oxygen and aryl defects that have largely similar optical properties. So far, no direct comparison between SWCNTs functionalized with oxygen and aryl defects under identical conditions has been performed. Here, we employ a combination of spectroscopic techniques to quantify the number of defects, their distribution along the nanotubes and thus their exciton trapping efficiencies. The different slopes of Raman D/G$^+$ ratios *versus* calculated defect densities from PL quantum yield measurements indicate substantial dissimilarities between oxygen and aryl defects. Supported by statistical analysis of single-nanotube PL spectra at cryogenic temperatures they reveal clustering of oxygen defects. The clustering of 2–3 oxygen defects, which act as a single exciton trap, occurs irrespective of the functionalization method and thus enables the use of simple equations to determine the density of oxygen defects and defect clusters in SWCNTs based on standard Raman spectroscopy. The presented analytical approach is a versatile and sensitive tool to study defect distribution and clustering in SWCNTs and can be applied to any new functionalization method.

New concepts

A unique combination of spectroscopic techniques for the investigation of luminescent defects in single-wall carbon nanotubes (SWCNTs) reveals clustering of oxygen defects in contrast to aryl sp^3 defects. The presented approach utilizes Raman spectroscopy and photoluminescence quantum yield (PLQY) measurements to elucidate the lateral distribution of different types of lattice defects along functionalized carbon nanotubes and the related efficiency of exciton trapping (independently corroborated by statistical analysis of single-SWCNT photoluminescence spectra at cryogenic temperatures). The quantitative comparison of Raman Δ(D/G$^+$) ratios *versus* calculated defect densities from PLQY measurements enables the identification and characterization of defect clusters. This new method for the quantification of defect densities and defect distributions can be easily expanded to other functionalization methods. Thus, it is a powerful tool for the systematic investigation of luminescent defects in SWCNTs and for further optimization of their near-infrared emission.

Introduction

The covalent functionalization of single-wall carbon nanotubes (SWCNTs) with luminescent defects has emerged as a promising strategy to improve and tune their near-infrared luminescence properties for optical sensing,[1–4] high contrast *in vivo* imaging in the second biological window,[5,6] high-purity single-photon emission,[7–9] and optoelectronic devices operating at telecommunication wavelengths.[10–12] Regardless of their exact chemical composition or binding configuration, luminescent defects act as zero-dimensional trap sites for mobile E_{11} excitons diffusing along the SWCNT lattice.[13,14] Photoluminescence (PL) from these energetically lower states occurs at wavelengths even further red-shifted into the near-infrared (nIR) than E_{11} and with fluorescence lifetimes of hundreds of picoseconds. The energy difference between the mobile E_{11} exciton and defect emission (*i.e.*, optical trap depth, ΔE_{opt}) ranges from 100 to 300 meV. Luminescent defects are able to trap and localize excitons at room temperature and thus prevent non-radiative decay at quenching sites (*e.g.*, nanotube ends). The suppression of this non-radiative decay path

[a] *Institute for Physical Chemistry, Universität Heidelberg, D-69120 Heidelberg, Germany. E-mail: zaumseil@uni-heidelberg.de*
[b] *Department of Mechanical and Materials Engineering, University of Turku, FI-20014 Turku, Finland*
[c] *Turku Collegium for Science, Medicine and Technology, University of Turku, FI-20520 Turku, Finland*
[d] *Institute of Nanotechnology, Karlsruhe Institute of Technology, D-76131 Karlsruhe, Germany*

† Electronic supplementary information (ESI) available. See DOI: https://doi.org/10.1039/d4nh00383g

This journal is © The Royal Society of Chemistry 2024

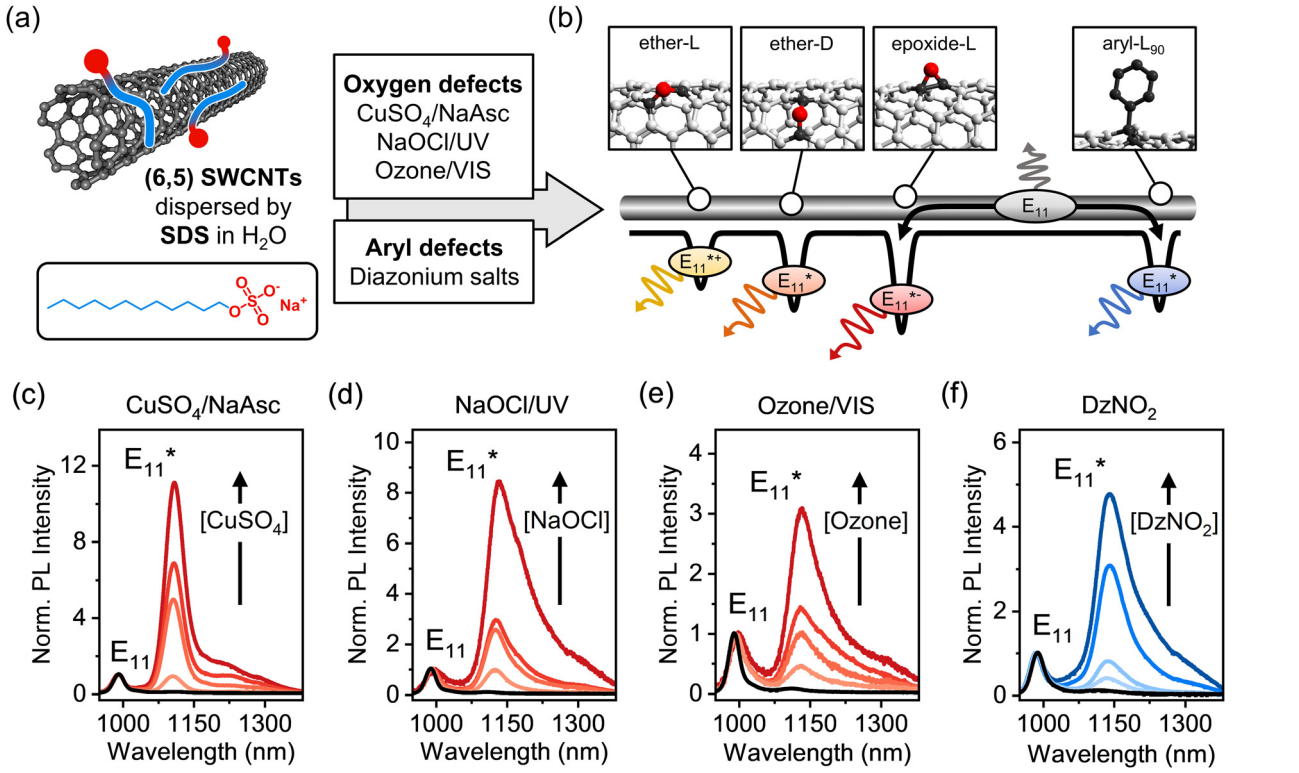

Fig. 1 (a) Covalent functionalization of (6,5) SWCNTs with luminescent defects in aqueous dispersion with surfactant SDS. Oxygen defects are created using $CuSO_4$/NaAsc, NaOCl/UV-light, or ozonation followed by SWCNT excitation with visible light. Treatment of SWCNTs with 4-nitrobenzenediazonium tetrafluoroborate ($DzNO_2$) introduces aryl sp^3 defects. (b) Schematic of different types of oxygen (ether-L, ether-D, and epoxide-L) and sp^3 defects (aryl-L_{90}) that act as trap sites with different depths for mobile E_{11} excitons. (c)–(f) Normalized (to E_{11}) PL spectra of pristine (black) and functionalized (6,5) SWCNTs in aqueous dispersion.

considerably enhances the photoluminescence quantum yields (PLQYs) of SWCNTs within a narrow window of optimal defect density.[15–18] Most commonly these defects are created, characterized and theoretically investigated in chiral (6,5) carbon nanotubes due to their abundance, easy purification and high reactivity.[19–21] Hence, we will focus on (6,5) SWCNTs from here on.

Among the various types of luminescent defects in (6,5) SWCNTs, oxygen and aryl defects have been the main focus of experimental and theoretical studies, as they are easily introduced using reactive oxygen species (ROS)[6,20,22,23] or aryldiazonium salts (Fig. 1a).[14,24–26] In both cases, the emission wavelength of the defect PL is mainly determined by the binding configuration of the introduced defect moieties on the SWCNT lattice. For oxygen defects, three thermodynamically stable binding configurations can be distinguished.[13] In one of them, the oxygen atom forms an epoxide, while the other two are ether-type configurations with different optical trap depths depending on the carbon–carbon bonds in either circumferential (ether-D) or longitudinal (ether-L) orientation with respect to the SWCNT axis, as shown schematically in Fig. 1b. Similar to that, two stable and experimentally observed configurations of sp^3 defects with distinct PL emission wavelengths are created upon binding of aryl groups to the nanotube lattice and formation of two sp^3 carbons in different *ortho* (*e.g.*, aryl-L_{90} see Fig. 1b) or *para* positions.[27–29]

Luminescent oxygen and aryl defects exhibit similar optical properties in addition to their equally red-shifted emission, such as nonlinear scaling of the defect emission intensity with excitation power[30] and a significant energy offset between the optical and thermal trap depths.[31] However, large deviations were found for the brightening factors for SWCNTs functionalized with oxygen or aryl sp^3 defects. The reported absolute values vary, but, typically oxygen defects lead to an increase in total PLQY by a factor of 2–3,[6,20] whereas aryl defects can cause a PLQY increase by a factor of >5, depending on the functional group and initial SWCNT length.[15,17,24] A reversed order of bright and dark exciton states for oxygen and aryl defects was considered as a possible explanation.[14,31] Additionally, the introduction of exciton quenching sites due to unintentional over-oxidation of SWCNTs under harsh conditions during functionalization with ROS may play a role.[6,20] The efficient capture of mobile E_{11} excitons followed by defect emission depends on the distribution and trap depth of different defects on the nanotubes lattice, which is usually assumed to be uniform. However, clustering of defects may occur depending on the functionalization method and should have a substantial impact on emission properties relevant for applications in sensing, imaging and optoelectronics.

To this end, we present a comparative study of oxygen- and aryl-functionalized (6,5) SWCNTs and demonstrate how

to recognize clustering of luminescent defects. We employ a combined analytical approach of Raman spectroscopy and spectrally-resolved PLQY measurements to quantify the absolute density of luminescent exciton quenching sites on the carbon nanotube lattice for different functionalization reactions. This method provides precise defect densities (per μm of nanotube) for aryl sp^3 defects in different SWCNT species and is independent of the Raman excitation laser wavelength as shown previously.[32,33] However, we find a striking difference in exciton trapping efficiency for SWCNTs with luminescent oxygen defects at identical levels of functionalization to aryl defects as corroborated by a statistical analysis of single-nanotube PL spectroscopy at cryogenic temperature. We attribute these findings to clustering of oxygen defects at length scales similar to or smaller than the mobile exciton size, whereas aryl defects act mostly as separate exciton traps. We propose the presented approach as a robust and powerful tool to identify and quantify inhomogeneities in defect distribution and defect clustering in functionalized SWCNTs.

Results and discussion

To quantify and directly compare different luminescent oxygen and aryl defects, purified dispersions of (6,5) SWCNTs stabilized in water by sodium dodecyl sulfate (SDS) were obtained through aqueous two-phase extraction as reported previously.[32] The nearly monochiral (6,5) SWCNT dispersions were characterized by UV-Vis-nIR absorption and PL excitation–emission spectroscopy (Fig. S1 and S2, ESI†). The functionalization of (6,5) SWCNTs with luminescent defects was performed using a variety of synthetic methods (see Fig. 1a). Oxygen defects were introduced *via* three previously reported procedures: ozonation of SWCNTs and subsequent photoconversion with visible light,[20] UV-light driven dissociation of sodium hypochlorite (NaOCl),[6] and with a Fenton-like reaction using copper(II) sulfate ($CuSO_4$) and sodium ascorbate (NaAsc)[23] (for details, see Experimental methods, ESI†). While oxygen functionalization was shown to initially introduce ether-L, ether-D and epoxide-L defects with different trap depths (Fig. 1b),[13] the epoxide defects mostly rearrange to the thermodynamically favored ether-D configuration upon exposure of SWCNTs to light.[23] The covalent functionalization with aryl defects was accomplished using 4-nitrobenzenediazonium tetrafluoroborate ($DzNO_2$), which forms radical species that attack the sp^2-hybridized nanotube lattice leading to sp^3 carbons with a predominantly aryl-L_{90} configuration.[28]

The degree of functionalization was tuned by varying the concentration of the respective reactants. In the case of SWCNT ozonation, the characteristic UV absorption peak of ozone at 260 nm was monitored to adjust its concentration in water prior to addition to the nanotube dispersion, as shown in Fig. S3, ESI.† Importantly, all functionalization reactions were performed on the same batch of SWCNTs and with the same surfactant (SDS) to ensure comparability of the subsequent characterization. The successful introduction of luminescent defects was confirmed by the emergence of defect-induced emission peaks at ~1120 nm (ether-D defect) and ~1140 nm (aryl-L_{90} defect) as shown in Fig. 1c–f (for absolute PL spectra, see Fig. S4, ESI†). These defect emission peaks are commonly labelled based on their spectral position with respect to the E_{11} emission and not their precise molecular origin. Hence, for both oxygen and aryl defects we refer to the main defect emission peaks as E_{11}*. For all functionalization methods, a linear increase of the E_{11}*/E_{11} PL intensity ratio with the reactant concentration was observed (Fig. S5, ESI†). Note that the Fenton-like reaction (Fig. 1c) leads to a narrower E_{11}* emission peak, which we attribute to the very mild reaction conditions with fewer possible side-reactions.

After functionalization, a surfactant exchange of the SWCNTs to 1% (w/v) sodium deoxycholate (DOC) was carried out *via* spin-filtration to remove reaction by-products and generate stable dispersions for further analysis. Drop-cast films of all dispersions were analyzed by resonant Raman spectroscopy (laser excitation wavelength λ_{exc} = 532 nm). Fig. 2a–d show averaged Raman spectra for all functionalization methods at different defect densities (corresponding to samples in Fig. 1c–f). The Raman D-mode intensity is proportional to the number of point defects in the SWCNT lattice, whereas the intensity of the G^+-mode originates from the longitudinal optical phonon of the sp^2-hybridized nanotube lattice.[34] Thus, the Raman D/G^+ ratio increases with functionalization and can be used as a relative metric to estimate the density of luminescent defects. For different sp^3 aryl defects in (6,5) SWCNTs – but not yet for oxygen defects – a quantitative correlation was established, *vide infra*.[32,33]

Treatment of nanotubes with oxidizing agents such as ozone, hypochlorite or $CuSO_4$/NaAsc, although at low concentrations, can lead to slight p-doping, which is also reflected in their Raman spectra and may complicate the analysis for defect quantification. Signatures of doping, *i.e.*, increased intensities of the E_2 mode as well as broadening of the G^+- and 2D-mode linewidth were observed for some oxygen-functionalized SWCNTs.[35,36] To separate these effects, films of pristine and functionalized (6,5) SWCNTs were intentionally p-doped by immersion in toluene solutions of the molecular oxidant F_4TCNQ (for details, see Experimental methods, ESI†).[37,38] While the typical signatures of p-doping are observed (Fig. S6, ESI†), no changes of the integrated Raman D/G^+ ratio occur (Fig. S7, ESI†), indicating that low-level p-doping does not interfere with the defect quantification for oxygen-functionalized SWCNTs by Raman spectroscopy.

Complementary to the relative defect densities obtained by Raman spectroscopy, absolute defect densities can be calculated within the framework of the diffusion-limited contact quenching (DLCQ) model. Within this model, exciton diffusion in SWCNTs is assumed to be governed exclusively by radiative decay of highly mobile E_{11} excitons or non-radiative decay at quenching sites, *e.g.* nanotube ends.[17,39] Covalent functionalization with luminescent defects introduces new loss channels for E_{11} excitons, leading to an additional decrease of the E_{11} PLQY. This enables the calculation of luminescent defect densities, provided that PLQYs can be determined reliably.

 This journal is © The Royal Society of Chemistry 2024

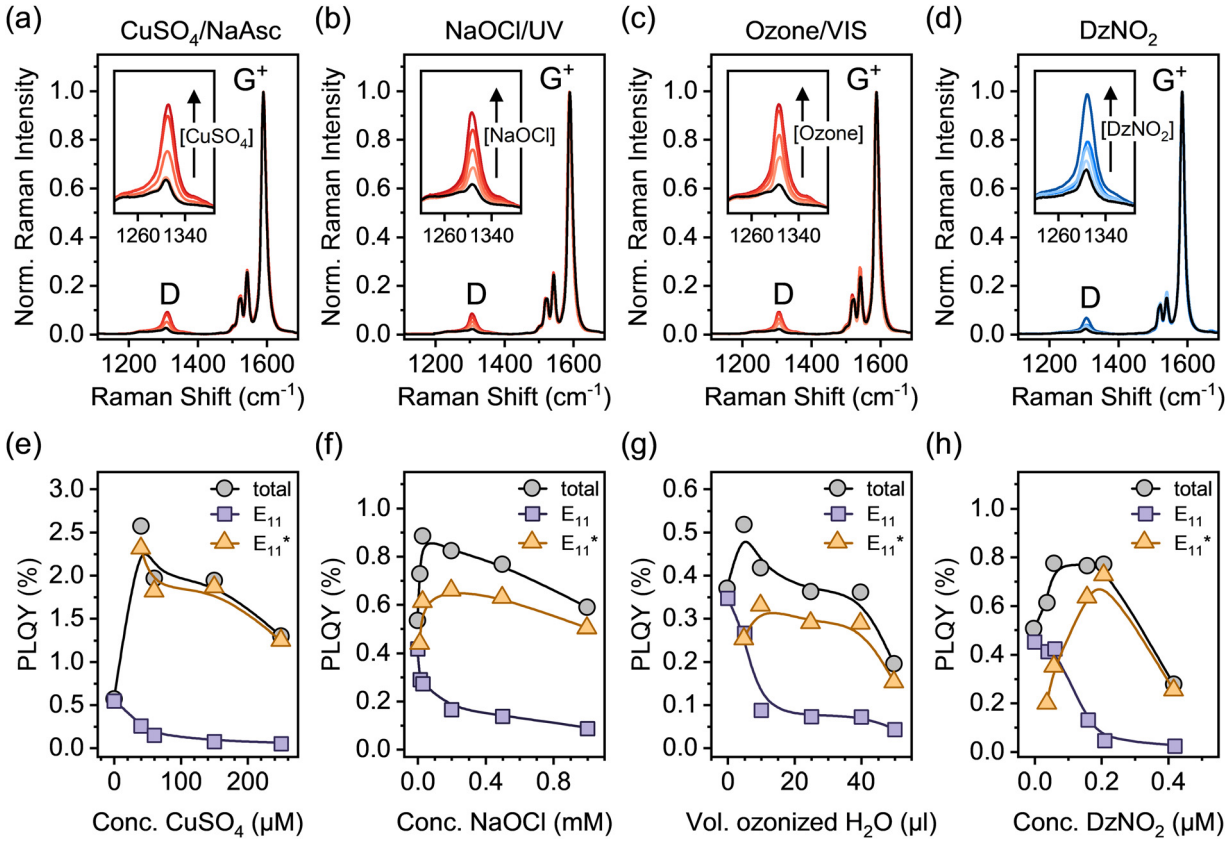

Fig. 2 (a)–(d) Normalized (to G^+ peak) averaged Raman spectra of pristine (black) and different functionalized (6,5) SWCNTs (λ_{exc} = 532 nm, >3600 individual spectra for each sample). The insets show the evolution of the defect-related D-mode with increasing degree of functionalization. (e)–(h) Corresponding total and spectrally resolved PLQYs for pristine and different functionalized (6,5) SWCNTs in aqueous dispersion depending on reactant concentration (after surfactant exchange to 1% (w/v) DOC).

The combination of relative Raman D/G^+ ratios and defect densities calculated from the spectrally resolved E_{11} PLQY of pristine and functionalized SWCNTs is a powerful tool to compare and investigate different types of luminescent defects as both techniques are highly sensitive to small changes in the electronic structure of nanotubes. For sp^3 aryl defects created by different synthetic routes this method was already shown to provide a robust correlation for defects densities up to $\sim 40\ \mu m^{-1}$ and thus enables facile quantification of the defect density by Raman spectroscopy alone.[32,33]

To compare and expand this correlation to oxygen defects, we determined the absolute PLQYs of (6,5) SWCNTs functionalized with oxygen and aryl defects and calculated the defect densities from the measured decrease in E_{11} PLQY (for details on PLQY measurements and defect density calculation see Experimental methods, ESI†). Spectrally resolved PLQYs for pristine and functionalized SWCNTs are presented in Fig. 2e–h. At low degrees of functionalization, an increase of the total PLQY is observed irrespective of the functionalization method. Efficient exciton trapping and radiative relaxation *via* E_{11}^* emission overcompensates for the simultaneous decrease in E_{11} emission. At medium to high levels of functionalization, the total PLQY decreases again, as the defects start to significantly disturb the electronic structure of the pristine SWCNT lattice.

In analogy to our previous studies on aryl defects,[32,33] the change of the integrated Raman D/G^+ ratios ($\Delta(D/G^+)$) was correlated with the calculated defect densities n_d from E_{11} PLQY measurements (see Fig. 3a). Using the $\Delta(D/G^+)$ ratio instead of the absolute values generally ensures higher comparability of the Raman data across different SWCNT batches and starting materials. In this work, the same batch of nanotube material was used for all samples. A linear dependence of the $\Delta(D/G^+)$ ratio on the calculated density of luminescent oxygen defects was obtained for all samples. For luminescent aryl defects, the slope was the same as previously reported for (6,5) SWCNTs.[32,33] In contrast to that, a strong deviation from this gradient is evident for all oxygen-functionalized nanotubes. Regardless of the functionalization method, all samples of (6,5) SWCNTs with luminescent oxygen defects exhibit a slope that is larger by a factor of ~2.3 than that for the aryl defects (see Fig. 3b; for individual linear fits see Fig. S8, ESI†). Similar differences are also observed for other defect-related Raman peaks, such as the intermediate frequency modes (IFMs)[33,40] presented in Fig. S9–S11, ESI.†

Clearly, despite very similar spectral signatures in PL and Raman spectroscopy, there must be a fundamental difference between luminescent oxygen and aryl defects in SWCNTs and their interaction with mobile excitons. Importantly, the

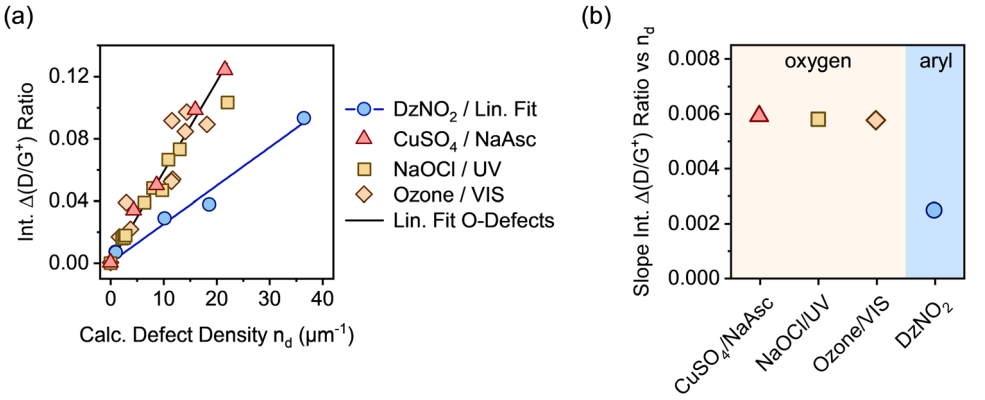

Fig. 3 (a) Integrated Raman $\Delta(D/G^+)$ ratios *versus* calculated defect densities (n_d) based on PLQY for (6,5) SWCNTs functionalized by different methods creating oxygen or aryl sp^3 defects. Linear fits for oxygen defects, combined (R^2 = 0.97) and aryl sp^3 defects (R^2 = 0.98). (b) Extracted slopes of the integrated $\Delta(D/G^+)$ ratio *versus* calculated defect density for each functionalization method.

calculation of defect densities based on the DLCQ model only considers the diffusion constant and radiative lifetime of the E_{11} exciton but no defect-specific photophysical processes.[17,41] Hence, it gives direct access to the E_{11} exciton quenching probability of local defects on the SWCNT lattice. However, the observed deviation of the slopes of the Raman D/G^+ ratios indicate either a different D-mode Raman cross-section or higher defect densities for oxygen-functionalized compared to aryl-functionalized nanotubes.

Previous work on defective carbon-based materials indicated that the intensity of the disorder-related Raman D-mode is not particularly sensitive to the actual structure (functional group or hybridization) of point-like lattice defects.[34,42] As all types of oxygen and aryl defects involve binding to exactly two carbon atoms, the defect size and thus the probability of second-order scattering processes (*i.e.*, Raman D-mode cross-section) should be equally insensitive to the precise chemical nature of the point-like defects. This assumption only leaves a higher number of structural defects than calculated from PLQY measurements as a possible explanation, which could be caused by clustering of the oxygen defects. The possibility of clustering of defects during covalent functionalization of carbon nanotubes was considered before,[43] but only shown to occur in additional alkylation reactions on already functionalized SWCNTs.[44] Furthermore, theoretical studies on SWCNT shortening by chemical oxidation with hydrogen peroxide suggest that ROS preferentially attack the carbon nanotube lattice at already defective areas, which may promote clustering.[45]

For a cluster of defects with an average spacing similar to or smaller than the size of the exciton (*i.e.*, few nanometers[17,46]), several defects may act as a single quenching site for the mobile excitons in the DLCQ model. Furthermore, collective exciton states of coupled defects were proposed for closely spaced luminescent defects.[47–50] Irrespective of the actual local electronic structure, the exciton trapping efficiency probably does not simply scale linearly with the absolute number of individual luminescent defects. Their precise distribution along the SWCNT lattice will strongly influence the correlation between lattice defects as determined from the Raman D/G^+ ratio and the calculated defect density from E_{11} PLQY measurements.

To directly assess the possibility of defect clustering for oxygen defects, we performed PL spectroscopy on individual oxygen-functionalized SWCNTs embedded in a polymer matrix at cryogenic temperatures (4.7 K). Under these conditions SWCNTs show strong localization of even the E_{11} excitons due to slight variations in the local dielectric environment.[51,52] Luminescent defects are similarly influenced by dielectric fluctuations of the environment. Thus, the defect emission energies even of luminescent defects with identical binding configuration vary slightly. These differences can be resolved at cryogenic temperatures due to the strongly reduced linewidths. Hence, it is possible to quantify the number of luminescent defects on a single nanotube by simply counting the different peaks, as demonstrated previously for aryl defects in polymer-wrapped SWCNTs.[32] The statistical analysis of the number of defect emission peaks provides direct access to the average number of individual emissive sites per nanotube. Together with atomic force microscopy (AFM) to determine the average nanotube length, the density of luminescent defects per μm can be obtained and compared to the results obtained from PLQY measurements and the DLCQ model.

To perform this analysis, oxygen-functionalized (6,5) SWCNTs were transferred to toluene solutions of the fluorene–bipyridine copolymer PFO-BPy, which exhibits a high dispersion efficiency for (6,5) SWCNTs.[21] After transfer of highly dilute nanotube dispersions into a polystyrene matrix, single-nanotube PL spectra were acquired at 4.7 K in an optical cryostat (for details see Experimental methods, ESI†). Representative PL spectra for individual (6,5) SWCNTs with E_{11}^* oxygen defects are displayed in Fig. 4a–d. Single defects can be identified as narrow peaks in the respective spectral region characteristic for a certain binding configuration (1030–1100 nm for E_{11}^{*+}, 1100–1200 nm for E_{11}^*, 1200–1300 nm for E_{11}^{*-}). Fig. S12 and S13 (ESI†) show additional single-SWCNT PL spectra.

About 30% of the measured SWCNTs exhibited defect PL emission in the E_{11}^{*+} and E_{11}^{*-} spectral region (Fig. 4e–g). The E_{11}^{*+} emission likely occurs from longitudinally oriented ether-type

 This journal is © The Royal Society of Chemistry 2024

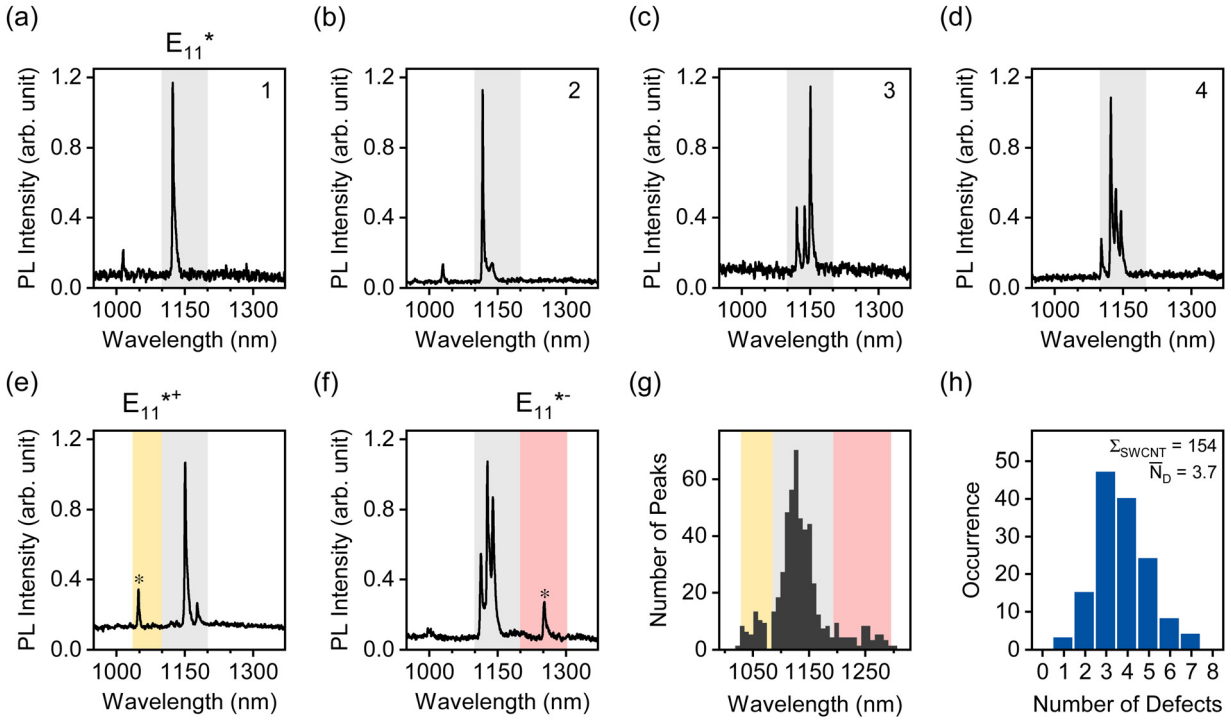

Fig. 4 (a)–(d) Low-temperature (4.7 K) PL spectra of individual (6,5) SWCNTs functionalized with $CuSO_4$/NaAsc, embedded in a polystyrene matrix. The number of oxygen defect sites per nanotube (top right corner) was determined as the number of peaks in the spectral region of the E_{11}* emission (grey area). (e) and (f) Representative low-temperature spectra where PL emission from the E_{11}*$^+$ (yellow area) and E_{11}*$^-$ (pink area) defect configurations is observed. (g) Spectral distribution of all counted defect PL peaks. (h) Defect PL peak histogram of 154 individual (6,5) SWCNTs with an average defect density of 3.7 defects per nanotube.

defects (ether-L) with a shallower exciton trap depth ($\Delta E_{opt} \sim 50$ meV, compared to ~140 meV for E_{11}* and ~250 meV for E_{11}*$^-$).[13] This defect is also often referred to as the Y_1 band in PL spectra of SWCNTs and becomes more prominent in thin films of SWCNTs on substrates with polar surfaces (*e.g.*, SiO_2 or glass) upon annealing.[53] Emission from this shallow exciton trap state is low at room temperature but becomes significant under cryogenic conditions. It is plausible that thermal detrapping of excitons from these shallow traps back to the E_{11} level is dominant at room temperature.[31] Hence, E_{11}*$^+$ defects should not contribute to the decrease in E_{11} PLQY to the same degree as deeper exciton traps (E_{11}* and E_{11}*$^-$) while still leading to a higher Δ(D/G$^+$) ratio.

A full statistical analysis of over 150 single-SWCNT PL spectra gave an average value of 3.7 luminescent defects per nanotube, with a minimum of one and a maximum of seven defects per nanotube, as shown in Fig. 4h. AFM length statistics of the sample yielded an average nanotube length of 310 nm (compare Fig. S14, ESI†). Combining these values gives an average defect density of 11.9 μm^{-1} for oxygen-functionalized SWCNTs, which is 2.4 times larger than the calculated defect density of 4.9 μm^{-1} from the E_{11} PLQY of the same sample. When the same counting method was applied to sp^3 aryl defects in previous studies, the defect densities aligned remarkably well with the numbers extracted with the DLCQ model.[32] This ratio of real and expected defect density is also remarkably close to the factor of 2.3 by which the Δ(D/G$^+$) *vs.* n_d slope deviates for oxygen and aryl defects as shown in Fig. 3a.

Clearly, the correlation between the Raman Δ(D/G$^+$) ratio and the defect density – determined from E_{11} PLQYs or by counting the defects on individual SWCNTs – is strikingly different for oxygen and aryl sp^3 defects. As argued above, this deviation could be explained with the preferential formation of oxygen defect clusters by ROS-based functionalization methods. Assuming that 2 to 3 defects form a cluster smaller than the size of a mobile exciton, these excitons would interact with such clustered oxygen defects as one collective trap state at room temperature. This would result in an apparently lower trapping efficiency per structural defect as measured by the Raman D/G$^+$ ratio. Thus, higher E_{11} PLQYs and lower calculated defect densities would be observed for the same number of structural defects. Conversely, at cryogenic conditions even minor differences in the local dielectric environment of oxygen defect clusters due to inhomogeneities of the polymer matrix would distinguish these traps from each other and enable a direct quantification. At low temperatures, exciton detrapping is suppressed, and even individual defects with low exciton trapping probabilities within a larger cluster can be identified in single-nanotube PL spectra.

The remarkable agreement between data obtained independently by Raman/PLQY and cryo-PL/AFM measurements suggests that the quantification of the number of oxygen defect clusters can be performed by adapting the equation derived for aryl defects.[32] The number of collective exciton traps in the

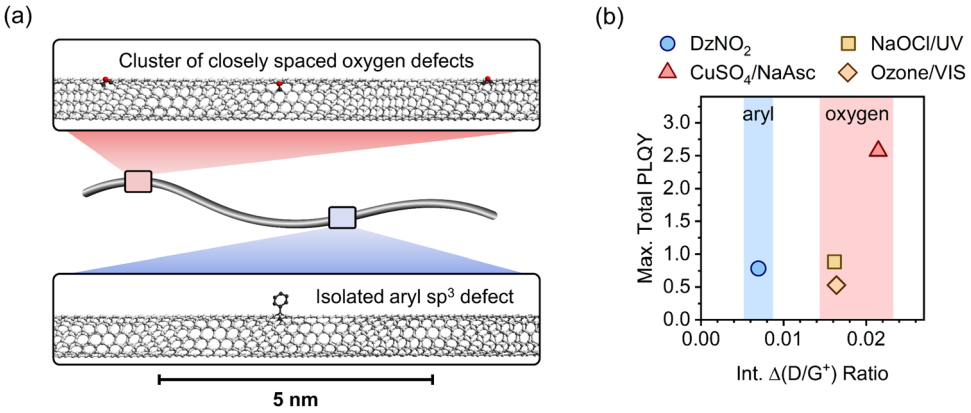

Fig. 5 (a) Schematic depiction of defect clustering in SWCNTs. Closely spaced (smaller than the size of a mobile exciton) luminescent oxygen defects act as one effective exciton trap compared to individual aryl sp^3 defects while contributing more to the Raman D/G^+ ratio. (b) Maximum total PLQYs *versus* integrated $\Delta(D/G^+)$ ratio for different functionalization methods. For all luminescent oxygen defects, the highest PLQYs are obtained for larger D/G^+ ratios compared to aryl sp^3 defects.

form of oxygen clusters is then

$$n_{\text{O-Cluster}}\left(\mu m^{-1}\right) = 172\ \mu m^{-1} \cdot \Delta\left(\frac{I_D}{I_{G^+}}\right), \quad (1)$$

where $\Delta(I_D/I_{G^+})$ represents the change of the integrated Raman D/G^+ ratio of the functionalized (6,5) SWCNT sample compared to the pristine samples (for resonant excitation at 532 nm). Consequently, the actual number of individual oxygen atom defects can be calculated with

$$n_{\text{O-Defect}}\left(\mu m^{-1}\right) = 405\ \mu m^{-1} \cdot \Delta\left(\frac{I_D}{I_{G^+}}\right), \quad (2)$$

which is – within the margin of experimental error – identical to the previously reported equation for individual aryl sp^3 defects.[32]

Fig. 5a gives a schematic representation of luminescent oxygen and aryl defects in SWCNTs. Corresponding to the deviation in Raman $\Delta(D/G^+)$ ratio *vs.* n_d slopes, one oxygen defect cluster should correspond to 2–3 individual oxygen defects. This structural model provides a straightforward tool to assess already developed, and in particular, new functionalization methods. If the correlation of Raman $\Delta(D/G^+)$ ratios and calculated defect densities results in values smaller than 172 μm^{-1} (compare eqn (1)), stronger clustering should be expected compared to oxygen defects. Likewise, larger values are an indicator for wider separation of individual structural defects.

For the application of functionalized SWCNTs as emitters the question arises whether defect clustering is desirable or detrimental for reaching the highest total PLQY. Hence, we correlated the maximum total PLQYs for the different functionalization methods with the corresponding Raman $\Delta(D/G^+)$ ratios (see Fig. 5b). Interestingly, the maximum PLQY for SWCNTs with aryl sp^3 defects occurs at significantly lower degrees of functionalization compared to oxygen defects. A higher degree of functionalization is required to obtain the brightest SWCNTs with oxygen defects. This might be attributed to the higher actual number of single oxygen defects necessary to achieve the optimal exciton trapping efficiency. The number of oxygen clusters at which maximum total PLQYs are observed are in good agreement with the density of luminescent exciton traps necessary to achieve optimal brightening for aryl-functionalized SWCNTs ($\sim$4–8 defects μm^{-1}). Interestingly, the maximum PLQY (2.5%) for SWCNTs functionalized with the Fenton-like reaction is substantially higher than those for all other methods (0.5–0.9%). This surprising difference, especially compared to the other oxygen functionalization methods, might be rationalized with the continuous production of low concentrations of ROS by the Fenton-like reaction (with $CuSO_4$/NaAsc) and thus a more controlled reaction with the nanotube lattice. In contrast to that, the harsh conditions of the other methods (*e.g.*, treatment with ozone, hypochlorite or other inorganic oxidizing agents) are more likely to create higher concentrations of ROS and thus may lead to over-functionalized areas that act only as quenching sites and may also cause the observed broadening of the defect emission peaks.[6,54]

Conclusion

In summary, we have shown that the combination of Raman spectroscopy, spectrally-resolved PLQY measurements, and low-temperature single-nanotube PL spectroscopy can be used to recognize and quantify clustering of luminescent oxygen defects in functionalized (6,5) SWCNTs in comparison to typical aryl sp^3 defects. One oxygen defect cluster contains about 2–3 individual defects that act as one exciton trap. Since clustering of oxygen defects occurs irrespective of the method of functionalization, we can provide simple and general equations for the precise quantification of oxygen defects and oxygen defect clusters in (6,5) SWCNTs based on standard resonant Raman spectroscopy alone. We show that the comparison of the slopes of the Raman $\Delta(D/G^+)$ ratios vs calculated defect densities from PLQY measurements can serve as a direct measure for clustering. This quantification method can be

 This journal is © The Royal Society of Chemistry 2024

expanded easily to other functionalization protocols and gives indirect information about the local distribution of exciton trapping sites and individual defects. Hence, this comparative study provides a blueprint for the characterization of new synthetic methods for the introduction of luminescent defects. For example, the functionalization of SWCNTs with bidentate reactants such as bisdiazonium compounds[25] or divalent functional groups[55] could be investigated in more detail based on this approach. A comparison with the reference slopes presented here should enable a quick and reliable assessment of possible defect clustering. Overall, the absolute quantification of defect densities by combining Raman spectroscopy and PLQY measurements is a valuable tool for the systematic and reproducible investigation of luminescent defects in SWCNTs.

Author contributions

F. L. S. fabricated and measured all samples and analyzed the data. S. S. contributed to sample preparation and characterization. H. L. and B. S. F. provided ATPE-sorted (6,5) SWCNTs. J. Z. conceived and supervised the project. F. L. S. and J. Z. wrote the manuscript with input from all authors.

Data availability

The data generated and analyzed for this article are available in the heiDATA repository at **https://doi.org/10.11588/data/TS6XA6**.

Conflicts of interest

The authors declare no competing interests.

Acknowledgements

This project has received funding from the European Research Council (ERC) under the European Union's Horizon 2020 research and innovation programme (Grant Agreement No. 817494 "TRIFECTS"). B. S. F. and H. L. gratefully acknowledge support by the DFG under grant numbers FL 834/5-1, FL 834/9-1 and FL 834/12-1. H. L. acknowledges financial support from the Turku Collegium for Science, Medicine and Technology (TCSMT). The authors thank Kerstin Brödner and Marcus Dodds for their technical support during initial tests of the ozone functionalization reaction.

References

1 J. Ackermann, J. T. Metternich, S. Herbertz and S. Kruss, *Angew. Chem., Int. Ed.*, 2022, **61**, e202112372.
2 P. Galonska, J. M. Mohr, C. A. Schrage, L. Schnitzler and S. Kruss, *J. Phys. Chem. Lett.*, 2023, **14**, 3483–3490.
3 S. Settele, C. A. Schrage, S. Jung, E. Michel, H. Li, B. S. Flavel, A. S. K. Hashmi, S. Kruss and J. Zaumseil, *Nat. Commun.*, 2024, **15**, 706.
4 H. Kwon, M. Kim, B. Meany, Y. M. Piao, L. R. Powell and Y. H. Wang, *J. Phys. Chem. C*, 2015, **119**, 3733–3739.
5 A. K. Mandal, X. Wu, J. S. Ferreira, M. Kim, L. R. Powell, H. Kwon, L. Groc, Y. Wang and L. Cognet, *Sci. Rep.*, 2020, **10**, 5286.
6 C.-W. Lin, S. M. Bachilo, Y. Zheng, U. Tsedev, S. Huang, R. B. Weisman and A. M. Belcher, *Nat. Commun.*, 2019, **10**, 2874.
7 X. Ma, N. F. Hartmann, J. K. S. Baldwin, S. K. Doorn and H. Htoon, *Nat. Nanotechnol.*, 2015, **10**, 671–675.
8 X. He, N. F. Hartmann, X. Ma, Y. Kim, R. Ihly, J. L. Blackburn, W. Gao, J. Kono, Y. Yomogida, A. Hirano, T. Tanaka, H. Kataura, H. Htoon and S. K. Doorn, *Nat. Photonics*, 2017, **11**, 577–582.
9 M.-K. Li, S. Dehm, M. M. Kappes, F. Hennrich and R. Krupke, *ACS Nano*, 2024, **18**, 9525–9534.
10 N. F. Zorn, S. Settele, F. L. Sebastian, S. Lindenthal and J. Zaumseil, *ACS Appl. Opt. Mater.*, 2023, **1**, 1706–1714.
11 M.-K. Li, A. Riaz, M. Wederhake, K. Fink, A. Saha, S. Dehm, X. He, F. Schöppler, M. M. Kappes, H. Htoon, V. N. Popov, S. K. Doorn, T. Hertel, F. Hennrich and R. Krupke, *ACS Nano*, 2022, **16**, 11742–11754.
12 N. F. Zorn, F. J. Berger and J. Zaumseil, *ACS Nano*, 2021, **15**, 10451–10463.
13 X. Ma, L. Adamska, H. Yamaguchi, S. E. Yalcin, S. Tretiak, S. K. Doorn and H. Htoon, *ACS Nano*, 2014, **8**, 10782–10789.
14 N. F. Hartmann, K. A. Velizhanin, E. H. Haroz, M. Kim, X. Ma, Y. Wang, H. Htoon and S. K. Doorn, *ACS Nano*, 2016, **10**, 8355–8365.
15 F. J. Berger, J. Lüttgens, T. Nowack, T. Kutsch, S. Lindenthal, L. Kistner, C. C. Muller, L. M. Bongartz, V. A. Lumsargis, Y. Zakharko and J. Zaumseil, *ACS Nano*, 2019, **13**, 9259–9269.
16 S. Settele, F. J. Berger, S. Lindenthal, S. Zhao, A. A. El Yumin, N. F. Zorn, A. Asyuda, M. Zharnikov, A. Högele and J. Zaumseil, *Nat. Commun.*, 2021, 12.
17 Y. Miyauchi, M. Iwamura, S. Mouri, T. Kawazoe, M. Ohtsu and K. Matsuda, *Nat. Photonics*, 2013, **7**, 715–719.
18 J. Zaumseil, *Adv. Opt. Mater.*, 2022, **10**, 2101576.
19 D. Janas, *Mater. Horiz.*, 2020, **7**, 2860–2881.
20 S. Ghosh, S. M. Bachilo, R. A. Simonette, K. M. Beckingham and R. B. Weisman, *Science*, 2010, **330**, 1656–1659.
21 A. Graf, Y. Zakharko, S. P. Schießl, C. Backes, M. Pfohl, B. S. Flavel and J. Zaumseil, *Carbon*, 2016, **105**, 593–599.
22 C. F. Chiu, W. A. Saidi, V. E. Kagan and A. Star, *J. Phys. Chem. Lett.*, 2017, **139**, 4859–4865.
23 S. Settele, F. Stammer, F. L. Sebastian, S. Lindenthal, S. R. Wald, H. Li, B. S. Flavel and J. Zaumseil, *ACS Nano*, 2024, **18**, 20667–20678.
24 Y. Piao, B. Meany, L. R. Powell, N. Valley, H. Kwon, G. C. Schatz and Y. Wang, *Nat. Chem.*, 2013, **5**, 840–845.
25 T. Shiraki, T. Shiraishi, G. Juhasz and N. Nakashima, *Sci. Rep.*, 2016, **6**, 28393.
26 A. Saha, B. J. Gifford, X. He, G. Ao, M. Zheng, H. Kataura, H. Htoon, S. Kilina, S. Tretiak and S. K. Doorn, *Nat. Chem.*, 2018, **10**, 1089–1095.

27 X. He, B. J. Gifford, N. F. Hartmann, R. Ihly, X. Ma, S. V. Kilina, Y. Luo, K. Shayan, S. Strauf, J. L. Blackburn, S. Tretiak, S. K. Doorn and H. Htoon, *ACS Nano*, 2017, **11**, 10785–10796.
28 P. Wang, J. Fortner, H. Luo, J. Kłos, X. Wu, H. Qu, F. Chen, Y. Li and Y. Wang, *J. Phys. Chem. Lett.*, 2022, **144**, 13234–13241.
29 H. Kwon, A. Furmanchuk, M. Kim, B. Meany, Y. Guo, G. C. Schatz and Y. Wang, *J. Am. Chem. Soc.*, 2016, **138**, 6878–6885.
30 M. Iwamura, N. Akizuki, Y. Miyauchi, S. Mouri, J. Shaver, Z. Gao, L. Cognet, B. Lounis and K. Matsuda, *ACS Nano*, 2014, **8**, 11254–11260.
31 M. Kim, L. Adamska, N. F. Hartmann, H. Kwon, J. Liu, K. A. Velizhanin, Y. Piao, L. R. Powell, B. Meany, S. K. Doorn, S. Tretiak and Y. Wang, *J. Phys. Chem. C*, 2016, **120**, 11268–11276.
32 F. L. Sebastian, N. F. Zorn, S. Settele, S. Lindenthal, F. J. Berger, C. Bendel, H. Li, B. S. Flavel and J. Zaumseil, *J. Phys. Chem. Lett.*, 2022, **13**, 3542–3548.
33 F. L. Sebastian, F. Becker, Y. Yomogida, Y. Hosokawa, S. Settele, S. Lindenthal, K. Yanagi and J. Zaumseil, *ACS Nano*, 2023, **17**, 21771–21781.
34 M. S. Dresselhaus, A. Jorio, A. G. Souza Filho and R. Saito, *Philos. Trans. R. Soc., A*, 2010, **368**, 5355–5377.
35 S. Grimm, S. P. Schießl, Y. Zakharko, M. Rother, M. Brohmann and J. Zaumseil, *Carbon*, 2017, **118**, 261–267.
36 A. Jorio and R. Saito, *J. Appl. Phys.*, 2021, 129.
37 N. J. Stanton, R. Ihly, B. Norton-Baker, A. J. Ferguson and J. L. Blackburn, *Appl. Phys. Lett.*, 2021, 119.
38 Y. Nosho, Y. Ohno, S. Kishimoto and T. Mizutani, *Nanotechnology*, 2007, **18**, 415202.
39 T. Hertel, S. Himmelein, T. Ackermann, D. Stich and J. Crochet, *ACS Nano*, 2010, **4**, 7161–7168.
40 A. Vierck, F. Gannott, M. Schweiger, J. Zaumseil and J. Maultzsch, *Carbon*, 2017, **117**, 360–366.
41 M. S. Hofmann, J. T. Gluckert, J. Noe, C. Bourjau, R. Dehmel and A. Hogele, *Nat. Nanotechnol.*, 2013, **8**, 502–505.
42 I. O. Maciel, N. Anderson, M. A. Pimenta, A. Hartschuh, H. Qian, M. Terrones, H. Terrones, J. Campos-Delgado, A. M. Rao, L. Novotny and A. Jorio, *Nat. Mater.*, 2008, **7**, 878–883.
43 A. H. Brozena, M. Kim, L. R. Powell and Y. Wang, *Nat. Rev. Chem.*, 2019, **3**, 375–392.
44 S. Deng, Y. Zhang, A. H. Brozena, M. L. Mayes, P. Banerjee, W.-A. Chiou, G. W. Rubloff, G. C. Schatz and Y. Wang, *Nat. Commun.*, 2011, **2**, 382.
45 Y. Li, X. Wu, M. Kim, J. Fortner, H. Qu and Y. Wang, *Chem. Mater.*, 2019, **31**, 4536–4544.
46 L. Lüer, S. Hoseinkhani, D. Polli, J. Crochet, T. Hertel and G. Lanzani, *Nat. Phys.*, 2009, **5**, 54–58.
47 J. Fortner and Y. Wang, *J. Phys. Chem. Lett.*, 2022, **13**, 8908–8913.
48 Y. Zheng, Y. Kim, A. C. Jones, G. Olinger, E. R. Bittner, S. M. Bachilo, S. K. Doorn, R. B. Weisman, A. Piryatinski and H. Htoon, *ACS Nano*, 2021, **15**, 10406–10414.
49 B. M. Weight, A. E. Sifain, B. J. Gifford, D. Kilin, S. Kilina and S. Tretiak, *J. Phys. Chem. Lett.*, 2021, **12**, 7846–7853.
50 A. Borel, F. Rapisarda, S. K. Doorn, C. Voisin and Y. Chassagneux, *Nano Lett.*, 2024, **24**, 3456–3461.
51 M. S. Hofmann, J. Noe, A. Kneer, J. J. Crochet and A. Hogele, *Nano Lett.*, 2016, **16**, 2958–2962.
52 C. Raynaud, T. Claude, A. Borel, M. R. Amara, A. Graf, J. Zaumseil, J. S. Lauret, Y. Chassagneux and C. Voisin, *Nano Lett.*, 2019, **19**, 7210–7216.
53 N. F. Zorn, S. Settele, S. Zhao, S. Lindenthal, A. A. El Yumin, T. Wedl, H. Li, B. S. Flavel, A. Högele and J. Zaumseil, *Adv. Opt. Mater.*, 2023, **11**, 2300236.
54 M. Yang, Y. Iizumi, L. Chen, T. Okazaki, D. Futaba and M. Zhang, *Carbon*, 2023, **208**, 238–246.
55 B. J. Gifford, X. He, M. Kim, H. Kwon, A. Saha, A. E. Sifain, Y. Wang, H. Htoon, S. Kilina, S. K. Doorn and S. Tretiak, *Chem. Mater.*, 2019, **31**, 6950–6961.

This journal is © The Royal Society of Chemistry 2024

Electronic Supplementary Information (ESI)

How to Recognize Clustering of Luminescent Defects in Single-Wall Carbon Nanotubes

Finn L. Sebastian[1], Simon Settele[1], Han Li[2,3], Benjamin S. Flavel[4], and Jana Zaumseil[1,*]

[1]Institute for Physical Chemistry, Universität Heidelberg, D-69120 Heidelberg, Germany

[2]Department of Mechanical and Materials Engineering, University of Turku, FI-20014 Turku, Finland

[3]Turku Collegium for Science, Medicine and Technology, University of Turku, FI-20520 Turku, Finland

[4]Institute of Nanotechnology, Karlsruhe Institute of Technology, D-76131 Karlsruhe, Germany

Corresponding Author

*E-mail: zaumseil@uni-heidelberg.de

Experimental Methods S-3
Dispersion and selection of (6,5) SWCNTs S-3
Functionalization of (6,5) SWCNTs with oxygen and 4-nitroaryl defects S-3
Chemical doping of (6,5) SWCNTs films S-4
Transfer of aqueous (6,5) SWCNT dispersions to toluene S-4
Characterization S-5
Photoluminescence quantum yields S-5
Calculation of luminescent defect density S-6
Single-SWCNT PL spectroscopy at cryogenic temperatures S-7
Additional spectra S-8
UV-Vis-nIR absorption spectrum of pristine (6,5) SWCNTs S-8
Photoluminescence excitation-emission map of pristine (6,5) SWCNTs S-8
UV-Vis absorption spectrum of ozonated water S-9
Absolute PL spectra for different functionalization methods S-10
E_{11}*/E_{11} PL intensity ratios for different functionalization methods S-11
Raman spectra of p-doped pristine and functionalized SWCNTs S-12
Raman $\Delta(D/G^+)$ *vs* calculated defect density n_d for different functionalization methods S-14
Raman spectroscopy of pristine and functionalized SWCNTs (RBM and IFM region) S-15
Raman Δ(IFM/RBM) *vs* calculated defect density n_d for different functionalization methods S-17
Extracted Raman Δ(IFM/RBM) *vs* n_d slopes S-18
Additional low-temperature single-SWCNT PL spectra S-19
AFM length statistics of functionalized SWCNTs S-21
References S-22

Experimental Methods

Dispersion and selection of (6,5) SWCNTs

(6,5) SWCNTs were selected from CoMoCAT raw material (CHASM SG65i-L58) by aqueous two-phase extraction (ATPE) as reported previously.[1] The raw material was dispersed in deoxycholate (DOC, BioXtra) and transferred to a two-phase system of dextran (M_W = 70 kDa, TCI Chemicals) and poly(ethylene glycol) (PEG, M_W = 6 kDa, Alfa Aesar). For separation of (6,5) SWCNTs, a diameter sorting protocol based on addition of sodium dodecyl sulfate (SDS, Sigma-Aldrich) was employed. The concentration of SDS was increased to 1.1% (w/v) at a fixed DOC concentration of 0.04% (w/v) for removal of large diameter SWCNTs from the top phase. (6,5) SWCNT-enriched fractions were collected between SDS concentration of 1.2% to 1.5% (w/v). Semiconducting and metallic SWCNTs were separated by addition of sodium cholate (SC, Sigma-Aldrich) and sodium hypochlorite (NaOCl, Sigma-Aldrich) as an oxidant. The selected (6,5) SWCNTs in DOC were concentrated by filtration in a pressurized ultrafiltration stirred cell (Millipore) with a M_W = 300 kDa cut-off membrane, and 1% (w/v) SDS was added before further use.

Functionalization of (6,5) SWCNTs with oxygen and 4-nitroaryl defects

For the functionalization of (6,5) SWCNTs with oxygen defects, three different methods were used. The first method employed a Fenton-like reaction based on the addition of copper(II) sulfate pentahydrate ($CuSO_4(H_2O)_5$, Sigma-Aldrich, ≥99.9% trace-metal basis) and sodium-L-ascorbate (NaAsc, Sigma-Aldrich, ≥99%) according to a procedure by Settele *et al.*[2] In short, aqueous dispersions of (6,5) SWCNT were adjusted to an optical density (OD) of 0.33 cm^{-1} at the E_{11} absorption peak with ultra-pure water (total volume 1 ml), and a final surfactant concentration of 0.33% (w/v) SDS. Aliquots of aqueous solutions of $CuSO_4$ and NaAsc were added to (6,5) SWCNT dispersions to achieve final concentrations of $CuSO_4$ between 25 and 250 µM and a molar ratio of 1:12 ($CuSO_4$:NaAsc) in the reaction mixture. After storage in the dark for 16 h, the reaction was stopped by addition of Na_4EDTA (10 µl, 1.4 M, Sigma-Aldrich, 98%) and 10% (w/v) DOC (20 µl), followed by irradiation with UV-light for 2 h (365 nm, SOLIS-365C, Thorlabs, 1.9 $mW \cdot mm^{-2}$) to promote the reorganization of oxygen defects.

The second functionalization method was adapted from a protocol reported by Lin *et al.*[3] ATPE-sorted dispersions of (6,5) SWCNTs in 1% (w/v) SDS were diluted to an OD of 0.1 cm^{-1} (total volume 3 ml) and a final SDS concentration of 0.1% (w/v). NaOCl (12% available chloride, Carl Roth) was added to achieve final concentrations between 0.015 and 1 mM in the reaction

mixture. After irradiation with UV-C-light (254 nm, VL-215.LC, Vilber Lourmat, 15 W) for 30 min, the reaction was stopped by addition of 20 µl of 10% (w/v) aqueous DOC solution.

The third functionalization method was adapted from Ghosh *et al.*[4] Ozone (Ozone Generator, Cambridge NanoTech Inc.) was bubbled through 7 ml of ultra-pure water in a Schlenk tube for 10 min, followed by dilution to an OD of 0.3 cm^{-1} at the ozone UV absorption peak (260 nm). ATPE-sorted dispersions of (6,5) SWCNTs were adjusted to an OD of 0.2 cm^{-1} (total volume 1.5 ml) and a final SDS concentration of 0.2 cm^{-1}. Depending on the intended degree of functionalization, between 5 and 50 µl of the ozonated ultra-pure water were slowly added while stirring. Photoconversion of the reaction product was achieved by irradiation with a green light-emitting diode (525 nm, SOLIS-525C, Thorlabs, 1.5 $mW \cdot mm^{-2}$) until no further changes of the PL spectrum were observed (~ 60-90 min).

For functionalization of SWCNTs with 4-nitroaryl defects, ATPE-sorted (6,5) SWCNTs were diluted to an OD of 0.33 cm^{-1} at the E_{11} absorption peak (total volume 1 ml) and an SDS concentration of 0.33 cm^{-1}. Aliquots of aqueous solutions of 4-nitrobenzenediazonium tetrafluoroborate ($DzNO_2$, TCI Chemicals, >98%) were added to achieve concentrations between 0.04 and 0.42 µM in the reaction mixture. After storage in the dark for 7 days to ensure complete decomposition of the diazonium salt, 20 µl of 10% (w/v) aqueous DOC solution were added to the reaction mixture.

Independent of the functionalization method, SWCNT dispersions were spin-filtrated (Amicon Ultra-4, 100 kDa cut-off) immediately after completion of the reaction and transferred to 1% (w/v) aqueous DOC before further characterization.

Chemical doping of (6,5) SWCNTs films

Drop-cast films of (6,5) SWCNTs on glass (Schott AF32eco) were immersed in solutions of the molecular p-type dopant 2,3,5,6-tetrafluoro-7,7,8,8-tetracyanoquinodimethane (F_4TCNQ, TCI Chemicals, >98%) in toluene (200 $\mu g \cdot ml^{-1}$) for different periods of time. The films were rinsed with toluene and blow-dried with nitrogen before further characterization.

Transfer of aqueous (6,5) SWCNT dispersions to toluene

A volume of 5 ml of functionalized (6,5) SWCNTs in 0.33% (w/v) aqueous SDS solution were filtered through PTFE membranes (Merck Millipore JVWP, pore size 0.1 µm) and washed thoroughly with ultra-pure water to remove the surfactant. The filter was then subjected to bath sonication for 30 min in a solution of poly[(9,9-dioctylfluorenyl-2,7-diyl)-*alt*-(6,6′-(2,2′-bipyridine))] (PFO-BPy, American Dye Source, M_W = 40 kDa, 0.5 $g \cdot L^{-1}$) in toluene (5 ml, Sigma-

Aldrich, ≥99.5%). Unexfoliated material was removed by centrifugation of the stock dispersion, followed by centrifugation of the supernatant (each step at 60000 *g* for 45 min, Beckman Coulter Avanti J26XP centrifuge). The supernatant obtained after the second step was used to prepare samples for AFM and low-temperature PL spectroscopy.

Characterization

Baseline-corrected UV-Vis-nIR absorption spectra were recorded with a Cary 6000i absorption spectrometer (Varian, Inc.). A scattering background $S(\lambda) = S_0 e^{-b\lambda}$ was subtracted from the acquired spectra.[5]

Atomic force microscopy (AFM) was performed under ambient conditions with a Bruker Dimension Icon atomic force microscope in ScanAsyst mode. The SWCNTs were spin-coated (2000 rpm, 60 s) onto cleaned native silicon wafers from dispersions obtained after transfer of SDS-dispersed SWCNTs to toluene/PFO-BPy, followed by rinsing with tetrahydrofuran (THF) and isopropanol (IPA). Gwyddion 2.64 was used for nanotube length distribution analysis.

Raman spectra of pristine and functionalized (6,5) SWCNTs were acquired with a Renishaw InVia Reflex confocal Raman microscope in backscattering configuration (50× long working distance objective, Olympus, N.A. 0.5) under near-resonant excitation with a 532 nm laser. Dispersions of SWCNTs were drop-cast onto glass substrates (Schott AF32eco), and gently rinsed with water. Over 3600 spectra were collected and averaged for each sample. Integrated Raman $\Delta(D/G^+)$ ratios were determined by integration of the average normalized Raman spectra from 1200 – 1400 cm^{-1} (D-mode) and 1560 – 1650 cm^{-1} (G^+-mode).

Room-temperature photoluminescence (PL) spectroscopy and emission-excitation (PLE) mapping was performed with a Fluorolog-3 spectrometer (Horiba Jobin-Yvon). A xenon arc-discharge lamp (450 W) coupled to a double grating monochromator was employed as the excitation light source. Light emitted from the SWCNT dispersions was passed through a long-pass filter (850 nm), Czerny-Turner imaging spectrograph and recorded with a liquid nitrogen cooled InGaAs line camera (Symphony II).

Photoluminescence quantum yields

Absolute photoluminescence quantum yields (PLQYs) of pristine and functionalized dispersions were determined with an integrating sphere as the ratio of emitted (N_{em}) and absorbed photons (N_{abs}) in accordance with previously reported procedures:[6, 7]

$$\eta = \frac{N_{em}}{N_{abs}} \quad (1)$$

SWCNT dispersions were diluted to an OD of 0.15 to 0.2 cm^{-1} at the E_{11} transition to minimize re-absorption. A quartz glass cuvette (Hellma Analytics QX) with 1 ml of dispersion was placed in an integrating sphere (LabSphere, Spectralon coating). The spectrally filtered output of a picosecond-pulsed supercontinuum laser (NKT Photonics SuperK Extreme) was used for resonant excitation of SWCNTs at the E_{22} transition (570 nm), and the light exiting the integrating sphere was coupled into the spectrometer (Acton SpectraPro SP2358) with an optical fiber. The PL of the sample in the near-infrared (nIR) and the attenuated laser signal at the excitation wavelength were recorded with a liquid nitrogen-cooled InGaAs line camera (Princeton Instruments OMA V:1024). Identical measurements were performed with 1% (w/v) aqueous DOC to correct for light absorption and scattering of the solvent. Integration of the sample emission yields a value proportional to the number of emitted photons. Similarly, the integrated attenuated laser signal for each sample is subtracted from the value obtained for the solvent reference to determine the number of absorbed photons. To account for the wavelength-dependent sensitivity of the detector and the absorption of optical components, a stabilized broadband light source (Thorlabs SLS201/M, 300-2600 nm) with known spectral output was used to collect calibration lamp spectra.

Calculation of luminescent defect density

Luminescent defect densities were calculated based on the model of diffusion-limited contact quenching (DLCQ) of excitons in SWCNTs as reported previously.[1] The DLCQ model assumes that E_{11} excitons undergo either nonradiative quenching at quenching sites, *e.g.*, nanotube ends, or decay *via* radiative E_{11} PL emission. The PLQY of the E_{11} emission in pristine SWCNT can be calculated as

$$\eta = \frac{\pi}{2 \cdot n_q^2 \cdot D \cdot \tau_{rad}}\ , \quad (2)$$

where n_q represents the number of quenching sites per µm of nanotube, D is the exciton diffusion constant and τ_{rad} the radiative lifetime of the E_{11} exciton. Here, values of D = 10.7 ± 0.4 $cm^2 \cdot s^{-1}$ and τ_{rad} = 3.35 ± 0.41 ns are used as reported in previous experimental studies.[8, 9] The introduction of luminescent defects (n_d) leads to additional radiative decay pathways resulting in a reduction of the E_{11} PLQY η^* of functionalized SWCNTs:

$$\eta^* = \frac{\pi}{2 \cdot (n_q + n_d)^2 \cdot D \cdot \tau_{rad}} \quad (3)$$

The combination of equations (2) and (3) yields an expression for the number density (μm^{-1}) of luminescent defects:

$$n_d = n_q\left(\sqrt{\frac{\eta}{\eta^*}} - 1\right) = \sqrt{\frac{\pi}{2 \cdot \eta \cdot D \cdot \tau_{rad}}}\left(\sqrt{\frac{\eta}{\eta^*}} - 1\right) \quad (4)$$

Single-SWCNT PL spectroscopy at cryogenic temperatures

Dispersions obtained after transfer of SDS-dispersed SWCNTs to toluene/PFO-BPy were diluted to an OD of 0.005 cm^{-1} at the E_{11} absorption peak and mixed with a solution of polystyrene (Polymer Source Inc., M_W = 230 kDa) in toluene (40 $g \cdot L^{-1}$) in equal volumes. Spin-coating (2000 rpm, 60 s) of the obtained mixture (30 µl) onto gold-coated (150 nm) glass substrates completed the sample preparation.

A closed-cycle liquid helium cooled optical cryostat (Montana Instruments, Cryostation s50) was employed to perform low-temperature single-SWCNT PL spectroscopy at 4.7 K. To this end, a nIR-optimized ×50 long-working distance objective (Mitutoyo, N.A. 0.42) was used to focus the output of a continuous wave laser diode (Coherent, Inc. OBIS 640 nm, 1 mW) onto the sample. Emitted light was collected and projected through a long-pass filter (850 nm) onto a grating spectrograph (Princeton Instruments, IsoPlane SCT-320) equipped with a 1200 nm blaze grating (85 lines per mm). PL spectra were recorded with a thermoelectrically cooled two-dimensional InGaAs camera array (Princeton Instruments, NIRvana 640ST). The data collection was automated using a custom script to control a piezo-based nanopositioning system (Attocube ANC350, ANPx101 and ANPz102 nanopositioners). A small number of PL spectra probably originating from bundled or aggregated SWCNTs were identified by the presence of broad and ill-defined E_{11} PL emission in accordance with literature reports.[1,10,11] These spectra were disregarded in the subsequent statistical analysis.

Additional spectra

UV-Vis-nIR absorption spectrum of pristine (6,5) SWCNTs

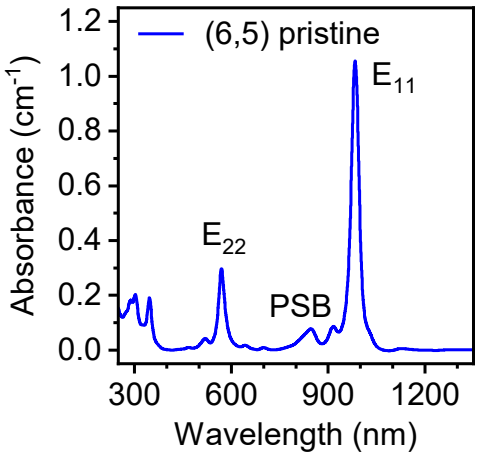

Figure S1. Baseline-corrected UV-Vis-nIR absorption spectrum of pristine (6,5) SWCNTs in aqueous dispersion (1% (w/v) SDS), with assignment of the E_{22}, E_{11}, and E_{11} phonon sideband (PSB) optical transitions.

Photoluminescence excitation-emission map of pristine (6,5) SWCNTs

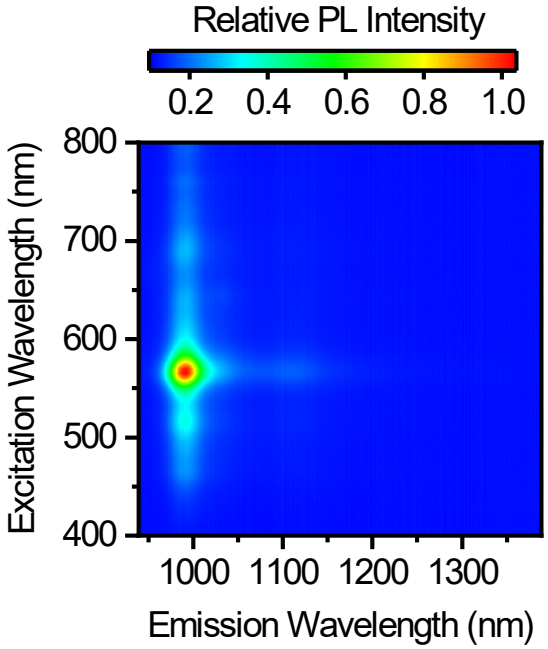

Figure S2. Photoluminescence excitation-emission map of pristine (6,5) SWCNTs in aqueous dispersion (0.3% (w/v) SDS).

UV-Vis absorption spectrum of ozonated water

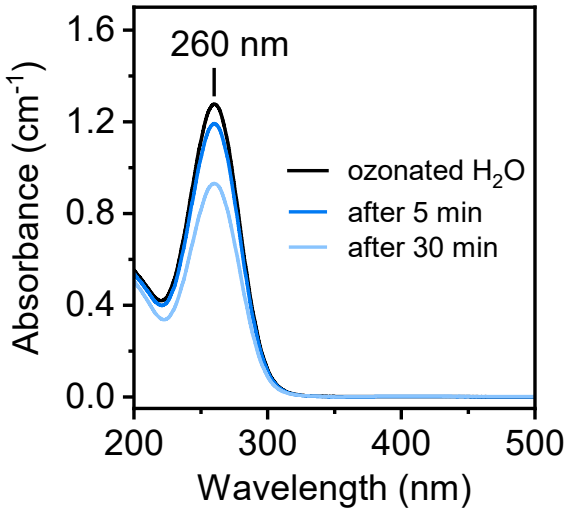

Figure S3. UV-Vis-nIR absorption spectra of water after ozonation, demonstrating the evolution of the ozone absorption peak (260 nm) 5 min and 30 min after ozonation.

Absolute PL spectra for different functionalization methods

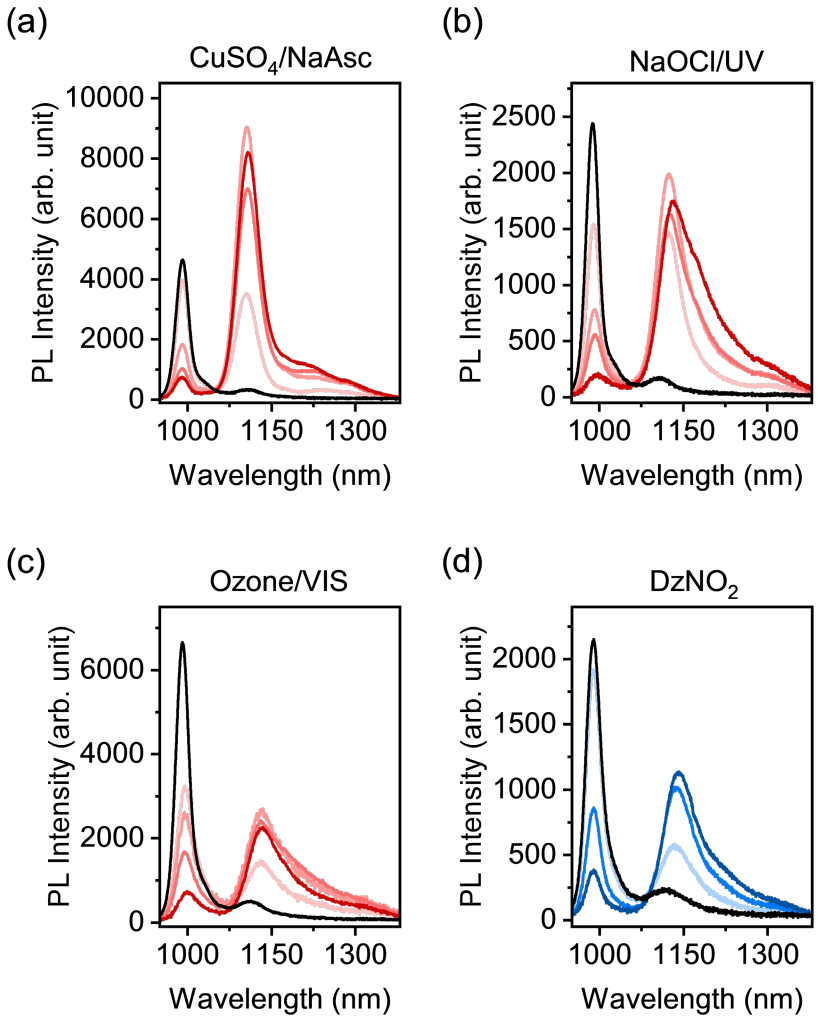

Figure S4. Absolute PL spectra of (6,5) SWCNTs functionalized with luminescent oxygen and aryl defects by different synthetic methods (**(a)** $CuSO_4$/NaAsc, **(b)** NaOCl/UV-light, **(c)** ozone/visible light, **(d)** $DzNO_2$).

E_{11}*/E_{11} PL intensity ratios for different functionalization methods

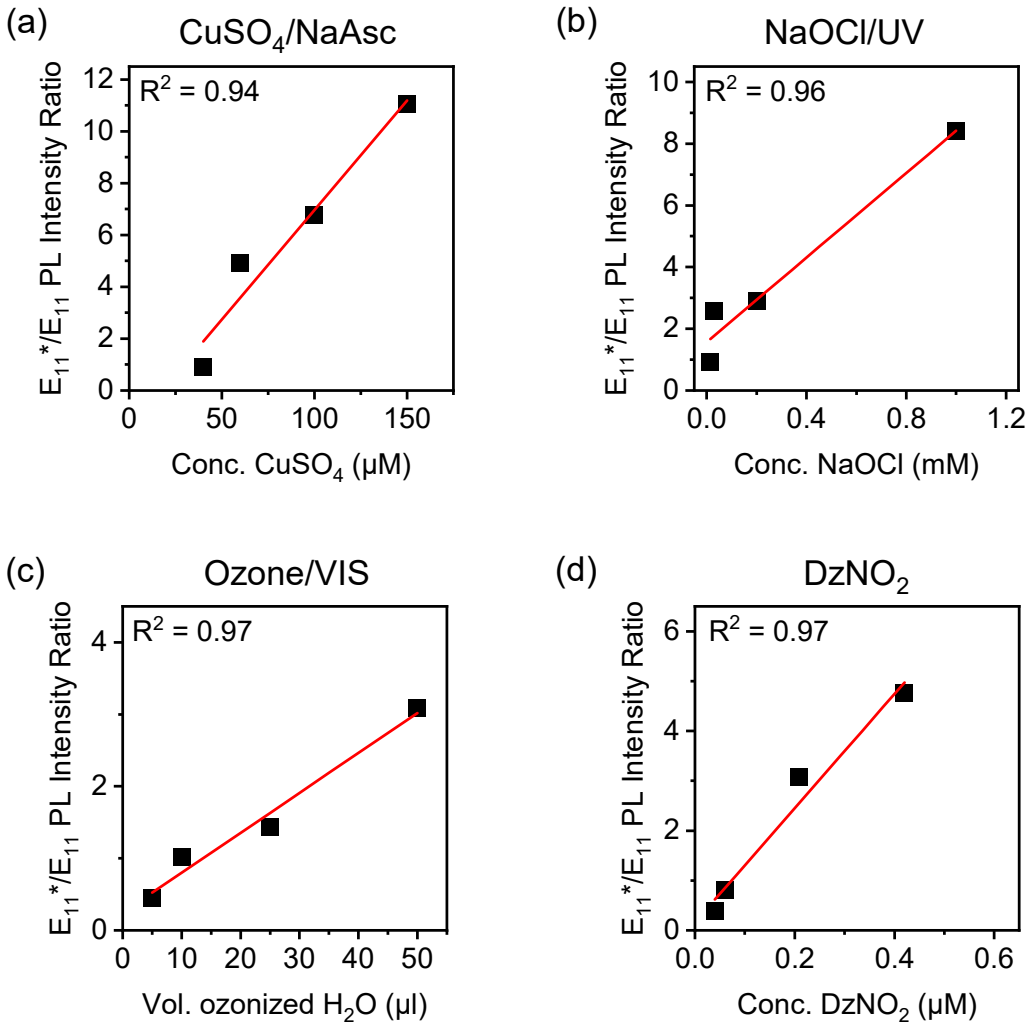

Figure S5. Dependence of the E_{11}*/E_{11} PL intensity ratios on the reactant concentration for (6,5) SWCNTs functionalized with luminescent oxygen and aryl defects by different synthetic methods (**(a)** $CuSO_4$/NaAsc, **(b)** NaOCl/UV-light, **(c)** ozone/visible light, **(d)** $DzNO_2$). Red lines are linear fits to the data (respective R^2 values are noted in the graphs).

Raman spectra of p-doped pristine and functionalized SWCNTs

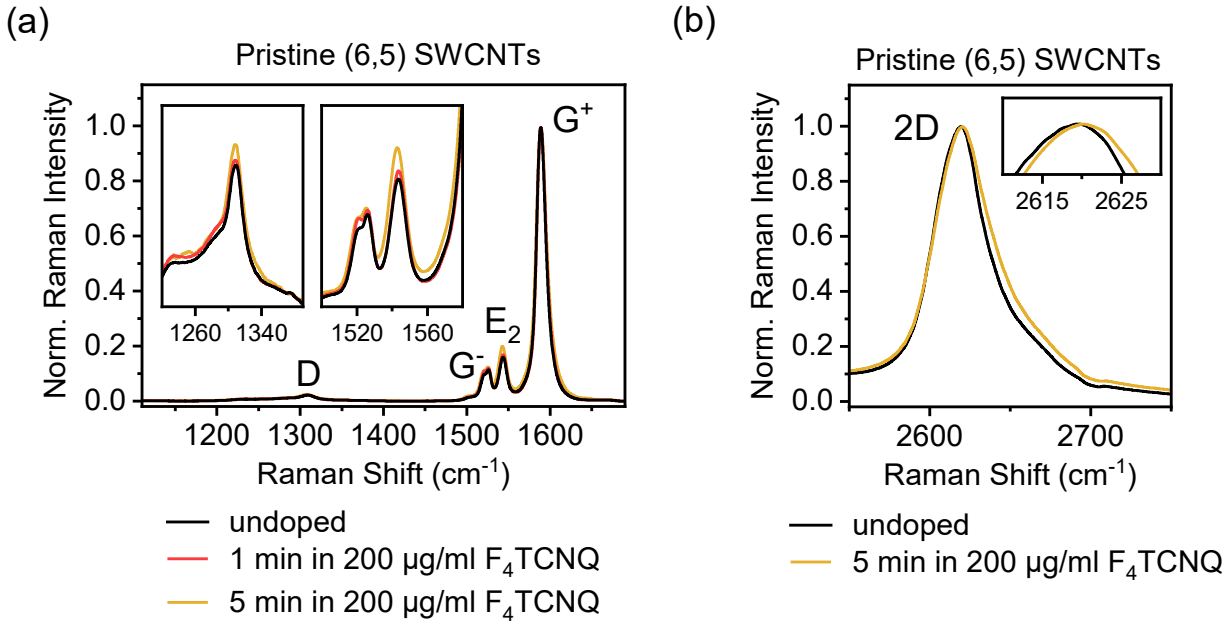

Figure S6. Influence of chemical doping on Raman spectra of (6,5) SWCNTs. **(a)** Averaged and normalized (to G^+-mode) Raman spectra of pristine (6,5) SWCNTs (drop cast film) without treatment and after 1 min and 5 min of immersion in a solution of the p-type dopant F_4TCNQ (solution in toluene, 200 µg/ml). **(b)** Averaged and normalized Raman spectra of the 2D-mode of pristine (6,5) SWCNTs before and after doping.

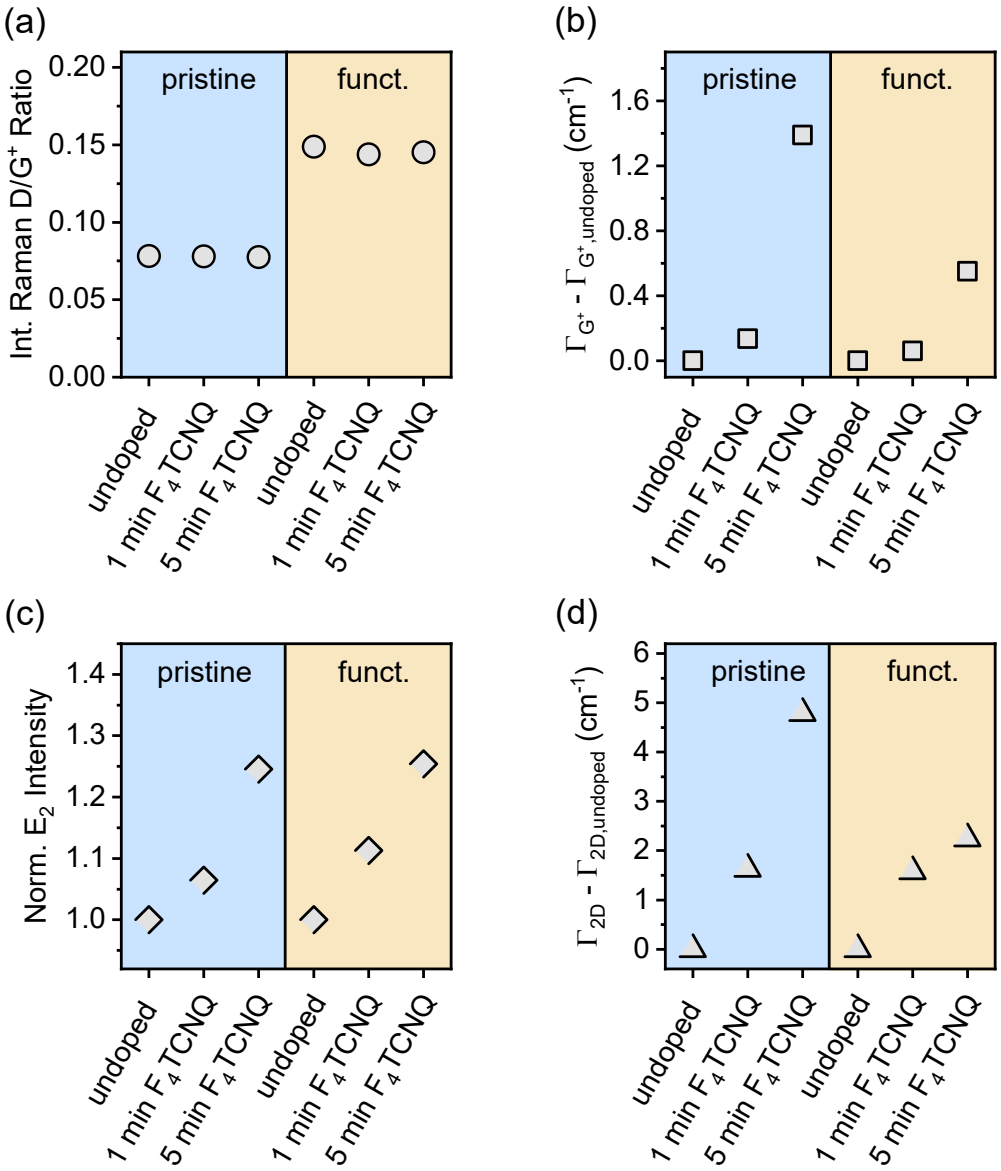

Figure S7. **(a)** Integrated Raman D/G$^+$ ratios for undoped/doped SWCNTs (pristine and functionalized with $CuSO_4$/NaAsc). **(b)** Raman G$^+$-mode linewidth (Γ_{D+}, full width at half maximum) for doped SWCNTs relative to the initial linewidth of the undoped sample. **(c)** Normalized intensity of the Raman E_2-mode for undoped/doped SWCNTs. **(d)** Linewidth of Raman 2D-mode (Γ_{2D}) for doped SWCNTs relative to the initial linewidth of the undoped sample.

Raman Δ(D/G$^+$) *vs* calculated defect density n_d for different functionalization methods

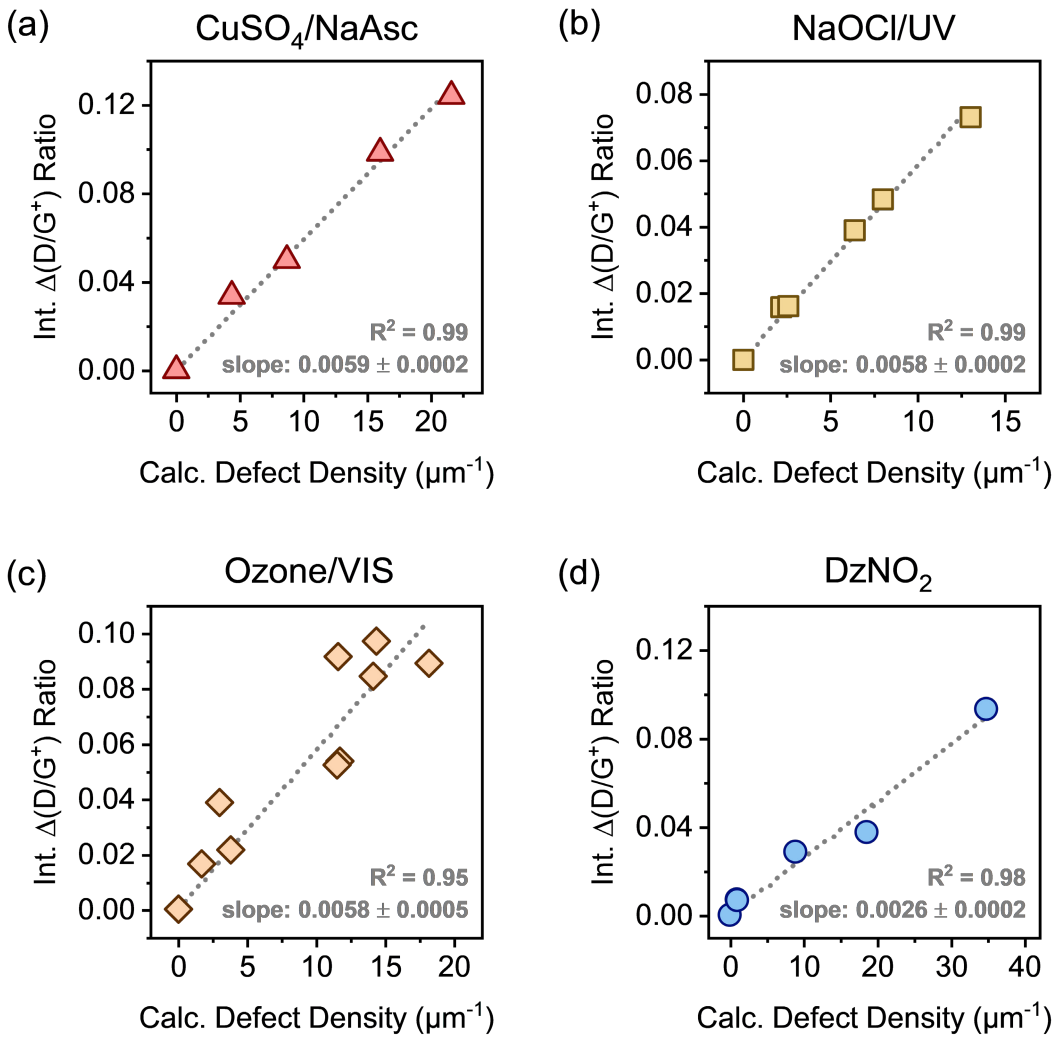

Figure S8. Integrated Raman Δ(D/G$^+$) ratios versus calculated defect density n_d (µm^{-1}) from PLQY measurements for (6,5) SWCNTs functionalized with luminescent oxygen and aryl defects via different synthetic methods (**(a)** $CuSO_4$/NaAsc, **(b)** NaOCl/UV-light, **(c)** ozone/visible light, **(d)** $DzNO_2$). Dashed grey lines are linear fits to the data (slope of the fit and respective R^2 values are noted in the graphs).

Raman spectroscopy of pristine and functionalized SWCNTs (RBM and IFM region)

The impact of luminescent oxygen and aryl defects on Raman modes other than the D- and G^+-mode should also be evaluated. In the spectral region between the radial breathing mode (RBM) and D-mode of SWCNTs, so-called intermediate frequency modes (IFMs) with weaker absolute signal intensities can be identified. For some IFMs dispersive characteristics in accordance with the involvement of double-resonant scattering processes were reported that are indicative of a defect-related origin.[12] Recently, we have demonstrated that the intensities of those IFMs, which can be derived from the ZA and ZO phonon branches in graphene, increase linearly with the defect density calculated from the E_{11} PLQY. This relation provides an additional method for the absolute quantification of luminescent defects in SWCNTs.[13] Furthermore, due to their chirality-dependent frequency, defect-related IFMs can also be applied for a relative quantification of the defect density in SWCNT mixtures.[14]

We recorded Raman spectra of drop-cast films of oxygen- and aryl-functionalized (6,5) SWCNTs in the IFM region using a 785 nm excitation laser. Averaged Raman spectra for all functionalization methods are shown in **Figure S9**. In all spectra the ZA-derived IFM can be identified at ~480 cm^{-1} whereas the ZO-derived IFM appears at ~580 cm^{-1}. For a quantitative evaluation the integrated IFM intensities were divided by the integrated intensity of the RBM of (6,5) SWCNTs (308 cm^{-1}) and the change of the integrated ratio, Δ(IFM/RBM), was correlated with the calculated defect density n_d. Irrespective of the functionalization method, a linear relation between Δ(IFM/RBM) and n_d was found although with significantly steeper slopes for oxygen defects compared to aryl defects, similar to the results reported for the D/G^+ ratios (Figure 3a). Individual slopes of Δ(IFM/RBM) *vs* n_d are presented in **Figure S10**. The low absolute Raman intensities of IFMs lead to some deviations of the Δ(IFM/RBM) *vs* n_d slopes for different methods of oxygen defect functionalization. However, the overall trend clearly supports the findings for the Raman $\Delta(D/G^+)$ ratio. For both the slope of Δ(ZA/RBM) and Δ(ZO/RBM) *vs* n_d, the values are larger by a factor of 1.9 for oxygen defects compared to aryl defects (see **Figure S11**).

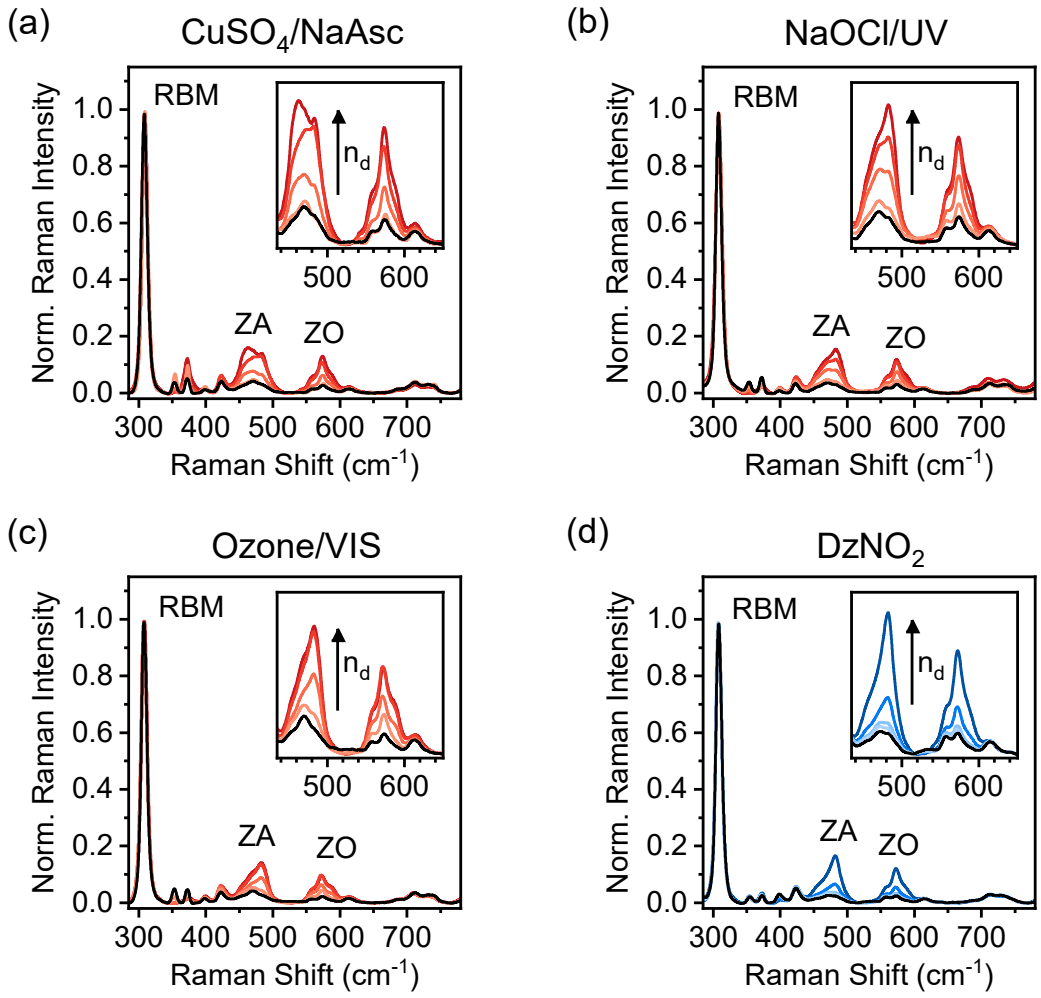

Figure S9. Averaged and normalized (to RBM at 308 cm^{-1}) Raman spectra of pristine and functionalized (6,5) SWCNTs for all functionalization methods; **(a)** $CuSO_4$/NaAsc, **(b)** NaOCl/UV-light, **(c)** ozone/visible light, **(d)** $DzNO_2$, λ_{exc} = 785 nm, >3600 individual spectra per sample. Insets display the evolution of the intermediate frequency modes (IFMs) for increasing degree of functionalization.

Raman Δ(IFM/RBM) *vs* calculated defect density n_d for different functionalization methods

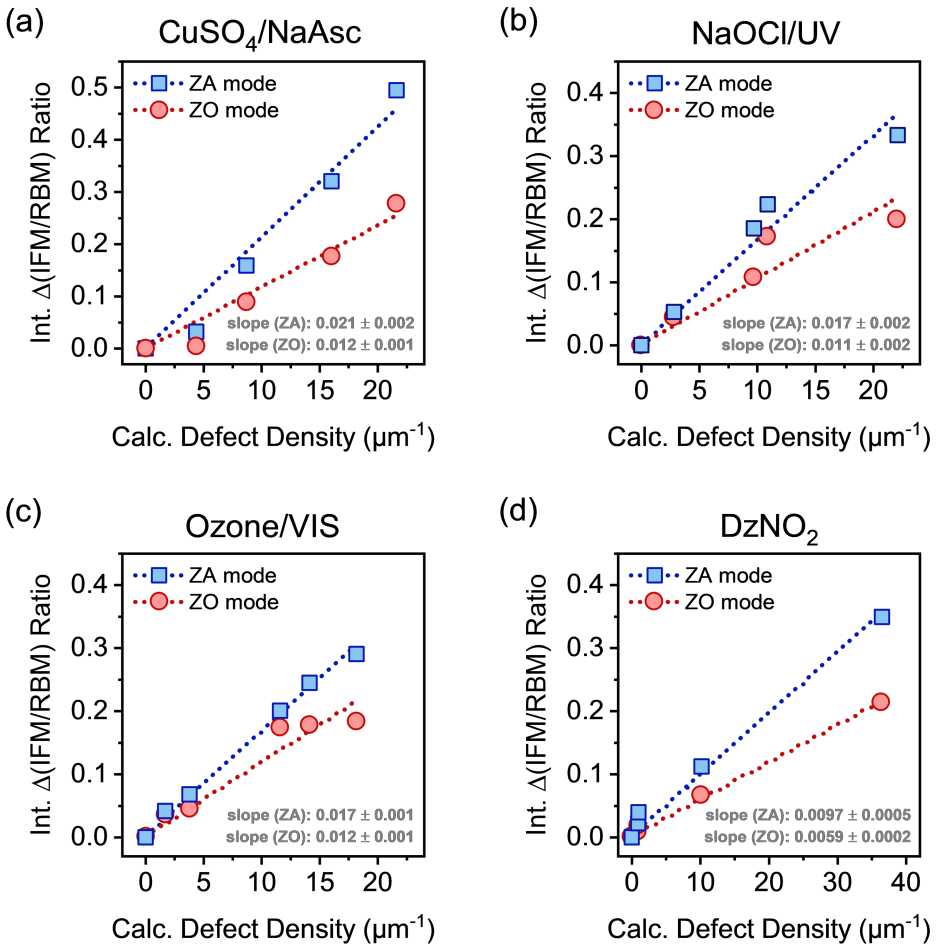

Figure S10. Integrated Raman Δ(ZA/RBM) and Δ(ZO/RBM) ratios versus calculated defect densities n_d for pristine and functionalized (6,5) SWCNTs (drop cast films) for all functionalization methods; **(a)** $CuSO_4$/NaAsc, **(b)** NaOCl/UV-light, **(c)** ozone/visible light, **(d)** $DzNO_2$. Dashed lines are linear fits to the data (slopes of the fits and respective R^2 values are noted in the graphs).

Extracted Raman Δ(IFM/RBM) *vs* n_d slopes

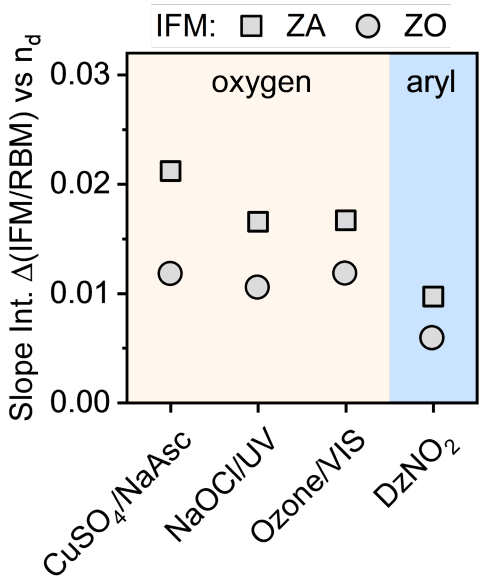

Figure S11. Extracted slopes of the integrated Δ(IFM/RBM) ratios versus calculated defect densities n_d for different functionalization methods.

Additional low-temperature single-SWCNT PL spectra

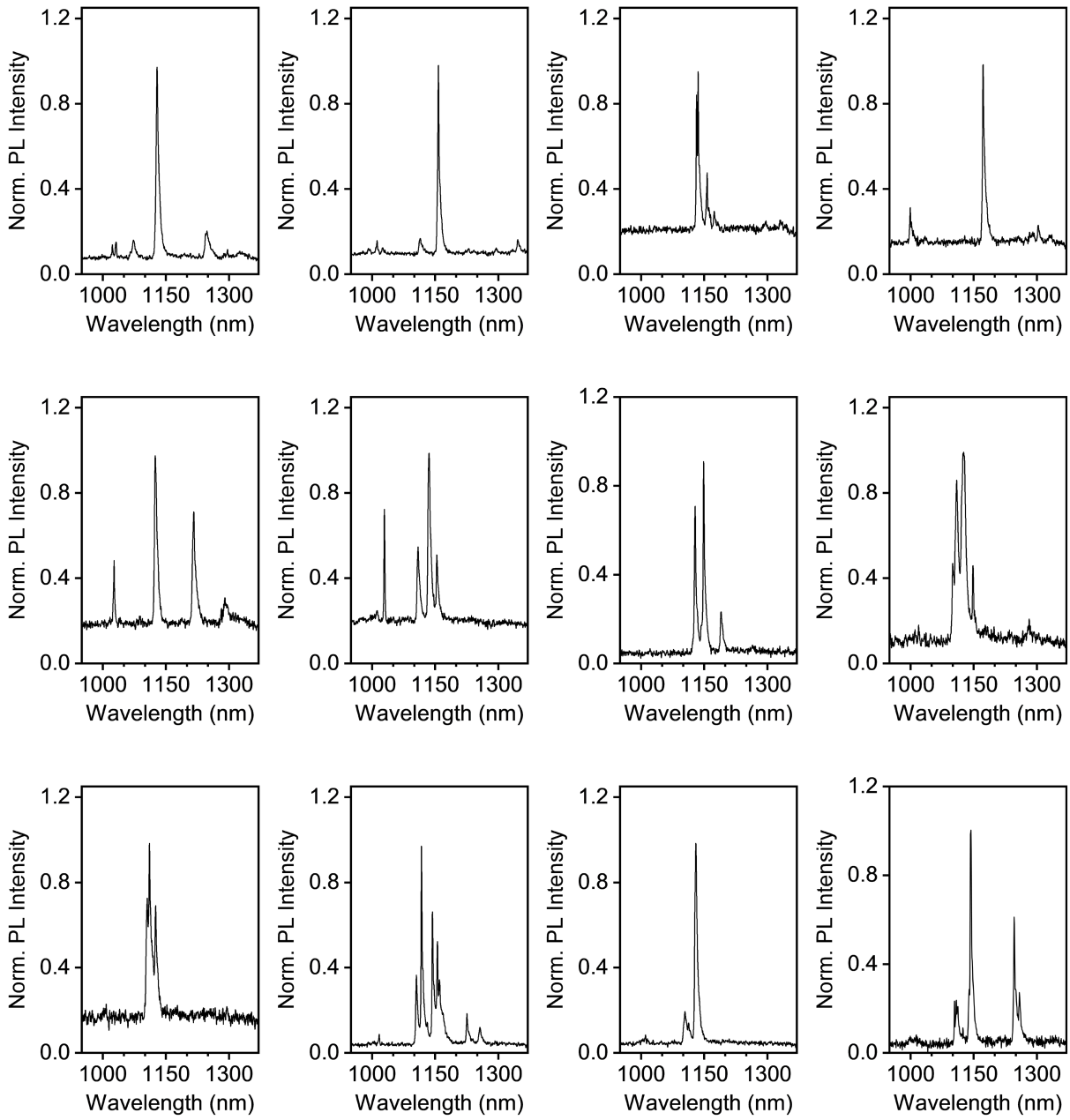

Figure S12. Additional low-temperature (4.7 K) PL spectra of single SWCNTs functionalized with $CuSO_4$/NaAsc, embedded in a polystyrene matrix (continued on the next page).

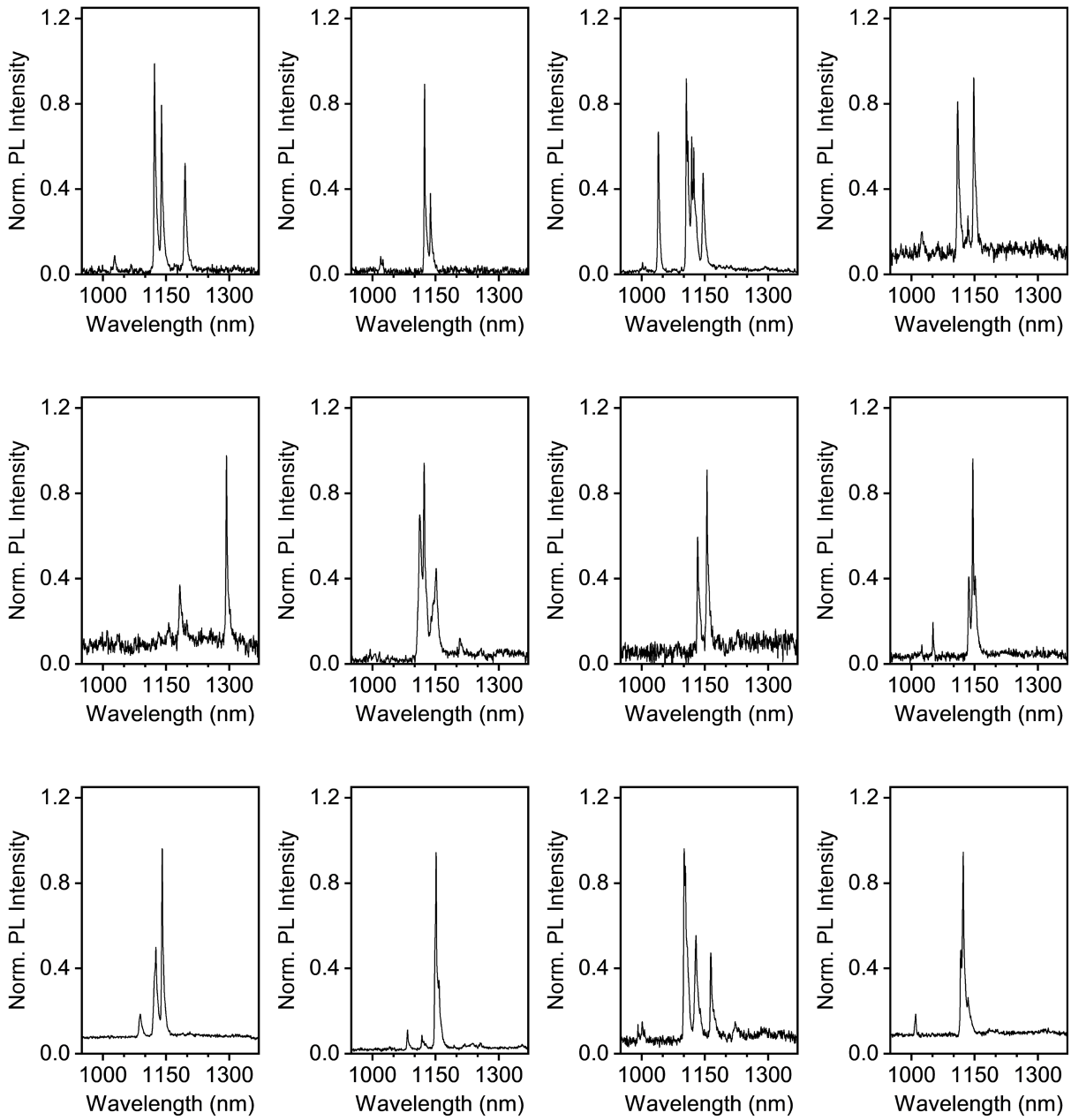

Figure S13. Additional low-temperature (4.7 K) PL spectra of single SWCNTs functionalized with $CuSO_4$/NaAsc, embedded in a polystyrene matrix.

AFM length statistics of functionalized SWCNTs

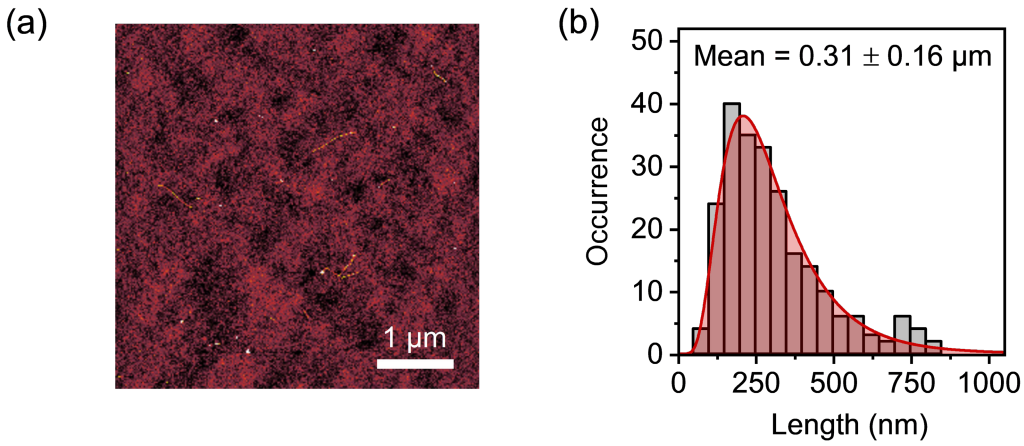

Figure S14. **(a)** Representative Atomic force micrograph and **(b)** length histogram (log-normal distribution, red line) of functionalized (6,5) SWCNTs ($CuSO_4$/NaAsc) after transfer from aqueous dispersion (0.3 % w/v SDS) to toluene/PFO-BPy.

References

(1) Sebastian, F. L., Zorn, N. F., Settele, S., Lindenthal, S., Berger, F. J., Bendel, C., Li, H., Flavel, B. S. and Zaumseil, J. Absolute Quantification of sp^3 Defects in Semiconducting Single-Wall Carbon Nanotubes by Raman Spectroscopy. *J. Phys. Chem. Lett.* **2022**, *13*, 3542-3548.

(2) Settele, S., Stammer, F., Sebastian, F. L., Lindenthal, S., Wald, S. R., Li, H., Flavel, B. S. and Zaumseil, J. Easy Access to Bright Oxygen Defects in Biocompatible Single-Walled Carbon Nanotubes Via a Fenton-Like Reaction. *ACS Nano* **2024**, *18*, 20667-20678.

(3) Lin, C.-W., Bachilo, S. M., Zheng, Y., Tsedev, U., Huang, S., Weisman, R. B. and Belcher, A. M. Creating Fluorescent Quantum Defects in Carbon Nanotubes Using Hypochlorite and Light. *Nat. Commun.* **2019**, *10*, 2874.

(4) Ghosh, S., Bachilo, S. M., Simonette, R. A., Beckingham, K. M. and Weisman, R. B. Oxygen Doping Modifies near-Infrared Band Gaps in Fluorescent Single-Walled Carbon Nanotubes. *Science* **2010**, *330*, 1656-1659.

(5) Pfohl, M., Tune, D. D., Graf, A., Zaumseil, J., Krupke, R. and Flavel, B. S. Fitting Single-Walled Carbon Nanotube Optical Spectra. *ACS Omega* **2017**, *2*, 1163-1171.

(6) Graf, A., Zakharko, Y., Schießl, S. P., Backes, C., Pfohl, M., Flavel, B. S. and Zaumseil, J. Large Scale, Selective Dispersion of Long Single-Walled Carbon Nanotubes with High Photoluminescence Quantum Yield by Shear Force Mixing. *Carbon* **2016**, *105*, 593-599.

(7) Berger, F. J., Lüttgens, J., Nowack, T., Kutsch, T., Lindenthal, S., Kistner, L., Müller, C. C., Bongartz, L. M., Lumsargis, V. A., Zakharko, Y. and Zaumseil, J. Brightening of Long, Polymer-Wrapped Carbon Nanotubes by sp^3 Functionalization in Organic Solvents. *ACS Nano* **2019**, *13*, 9259-9269.

(8) Hertel, T., Himmelein, S., Ackermann, T., Stich, D. and Crochet, J. Diffusion Limited Photoluminescence Quantum Yields in 1-D Semiconductors: Single-Wall Carbon Nanotubes. *ACS Nano* **2010**, *4*, 7161-7168.

(9) Hofmann, M. S., Glückert, J. T., Noe, J., Bourjau, C., Dehmel, R. and Högele, A. Bright, Long-Lived and Coherent Excitons in Carbon Nanotube Quantum Dots. *Nat. Nanotechnol.* **2013**, *8*, 502-505.

(10) Raynaud, C., Claude, T., Borel, A., Amara, M. R., Graf, A., Zaumseil, J., Lauret, J.-S., Chassagneux, Y. and Voisin, C. Superlocalization of Excitons in Carbon Nanotubes at Cryogenic Temperature. *Nano Lett.* **2019**, *19*, 7210-7216.

(11) Settele, S., Berger, F. J., Lindenthal, S., Zhao, S., El Yumin, A. A., Zorn, N. F., Asyuda, A., Zharnikov, M., Högele, A. and Zaumseil, J. Synthetic Control over the Binding Configuration of Luminescent sp^3-Defects in Single-Walled Carbon Nanotubes. *Nat. Commun.* **2021**, *12*, 2119.

(12) Fantini, C., Jorio, A., Souza, M., Ladeira, L. O., Souza Filho, A. G., Saito, R., Samsonidze, G. G., Dresselhaus, G., Dresselhaus, M. S. and Pimenta, M. A. One-Dimensional Character of Combination Modes in the Resonance Raman Scattering of Carbon Nanotubes. *Phys. Rev. Lett.* **2004**, *93*, 087401.

(13) Sebastian, F. L., Becker, F., Yomogida, Y., Hosokawa, Y., Settele, S., Lindenthal, S., Yanagi, K. and Zaumseil, J. Unified Quantification of Quantum Defects in Small-Diameter Single-Walled Carbon Nanotubes by Raman Spectroscopy. *ACS Nano* **2023**, *17*, 21771-21781.

(14) Soltani, N., Zheng, Y., Bachilo, S. M. and Weisman, R. B. Structure-Resolved Monitoring of Single-Wall Carbon Nanotube Functionalization from Raman Intermediate Frequency Modes. *J. Phys. Chem. Lett.* **2023**, *14*, 7960-7966.

5 Photocatalytic creation and circular dichroism of luminescent defects

This Chapter includes a publication which introduces photocatalytic oxygen functionalization of SWCNTs and reveals the intrinsic chiral properties of defect-trapped excitons, which exhibit near-infrared circular dichroism.

For the original publication, refer to Sebastian *et al.*, *Nat. Commun.* **16**, 5107 (2024).

Formblatt Kumulative Dissertation

1. Publikation/*Publication:*
Vollständige bibliographische Referenz/*Complete bibliographic reference:*

Finn L. Sebastian, Leon Kaminski, Christoph Bendel, Yohei Yomogida, Yuuya Hosokawa, Han Li, Sebastian Lindenthal, Benjamin S. Flavel, Kazuhiro Yanagi, and Jana Zaumseil. *Circular dichroism of quantum defects in carbon nanotubes created by photocatalytic oxygen functionalization*. *Nat. Commun.* **16**, 5107 (2025), DOI: 10.1038/s41467-025-60342-y.

2. Erstautorenschaft/*First authorship:* **Ja/*Yes***

3. Veröffentlicht/*Published:* **Ja/*Yes***

4. Beteiligungen/*Contributions (according to Contributor Role Taxonomy, CRediT):*

Contributor role	Doctoral student
Last name, first name	Sebastian, Finn Luca
Methodology	×
Software	
Validation	×
Formal analysis	×
Investigation	×
Resources	
Data curation	×
Writing - original draft	×
Writing - review and editing	×
Visualization	×
Supervision	×
Project administration	
Funding acquisition	

Hiermit bestätige ich, dass alle obigen Angaben korrekt sind.
I confirm that all declarations made above are correct.



Finn Luca Sebastian
Doktorand/*Doctoral student*

Betreuungsperson/*Supervisor:*
Hiermit bestätige ich, dass alle obigen Angaben korrekt sind und dass die selbstständigen Arbeitsanteile des Doktoranden an der aufgeführten Publikation hinreichend und signifikant sind.
I confirm that all declarations made above are correct and that the doctoral student's independent contribution to this publication is significant and sufficient to be considered for the cumulative dissertation.



04.08.2025

Prof. Dr. Jana Zaumseil

Datum/*Date*

nature communications

Article

https://doi.org/10.1038/s41467-025-60342-y

Circular dichroism of quantum defects in carbon nanotubes created by photocatalytic oxygen functionalization

Received: 3 February 2025

Accepted: 20 May 2025

Published online: 02 June 2025

Check for updates

Finn L. Sebastian[1], Leon Kaminski[1], Christoph Bendel[2], Yohei Yomogida[3], Yuuya Hosokawa[4], Han Li[5,6], Sebastian Lindenthal[1], Benjamin S. Flavel[7], Kazuhiro Yanagi[4] & Jana Zaumseil[1]

Control over the chiroptical properties of low-dimensional semiconductors is a promising route toward next-generation optoelectronics and photonics. With their helical chirality, single-wall carbon nanotubes (SWCNTs) offer a suitable framework for exploring chiral excitonic states. In addition to intrinsic, one-dimensional excitons, the targeted functionalization of SWCNTs with luminescent defects introduces zero-dimensional quantum states that enhance photoluminescence quantum yields and exhibit single-photon emission at room temperature. Here, we demonstrate that these defect states inherit the chirality of the respective SWCNT enantiomer, as evident from near-infrared circular dichroism. This observation is achieved by utilizing photocatalysis for efficient and versatile functionalization of SWCNTs with luminescent oxygen defects. The employed approach, based on anthraquinone derivatives as photocatalysts, is applicable to SWCNTs with different diameters, in aqueous or organic dispersions, with different surfactants, and even enables lateral patterning of defects in SWCNT networks. Low catalyst concentrations and the absence of cytotoxic metals or reactants make this functionalization method highly biocompatible. Introducing luminescent defects with uniform binding configurations in sorted nanotube enantiomers represents a key step toward chirality control of quantum defects in SWCNTs.

Structural chirality in low-dimensional semiconductors leads to the formation of chiral excitonic states, which are fundamental to chiroptical effects such as circular dichroism (CD) and circularly polarized luminescence (CPL)[1]. Chiral excitons have been studied extensively in two-dimensional systems such as transition metal dichalcogenides[2], their twisted bilayer structures[3], and hybrid organic-inorganic perovskites[4]. With the integration of chirality as an additional degree of freedom in nanoscale systems, the precise control of chiral excitons and an understanding of the impact of their confinement or localization at lattice defects or edges have become essential. The question to what degree chirality persists in such confined states is particularly important for applications that rely on quasi zero-dimensional excitons, e.g., circularly polarized single-photon emission (SPE)[5].

Due to their helical chirality, single-wall carbon nanotubes (SWCNTs) represent a model system for exploring the properties of chiral excitons. Their structural diversity as well as their optical and

[1]Institute for Physical Chemistry, Universität Heidelberg, Heidelberg, Germany. [2]Institute for Inorganic Chemistry, Universität Heidelberg, Heidelberg, Germany. [3]Research Institute for Electronic Science, Hokkaido University, Sapporo, Hokkaido, Japan. [4]Department of Physics, Tokyo Metropolitan University, Hachioji, Tokyo, Japan. [5]Department of Mechanical and Materials Engineering, University of Turku, Turku, Finland. [6]Turku Collegium for Science, Medicine and Technology, University of Turku, Turku, Finland. [7]Institute of Nanotechnology, Karlsruhe Institute of Technology, Karlsruhe, Germany. e-mail: zaumseil@uni-heidelberg.de

electronic properties continue to drive fundamental insights into the photophysics of nanoscale systems[6,7] and their application in optoelectronics[8,9], as near-infrared (NIR) single-photon emitters[10,11], for biological imaging[12–14], and optical sensing[15,16]. Highly optimized techniques for nanotube dispersion and sorting[17] are the prerequisite for all of the above. The separation of not only specific (*n*,*m*) species but SWCNT enantiomers currently presents the most advanced level of sorting[18,19]. SWCNT enantiomer separation has been achieved by density gradient centrifugation[20], wrapping with chiral polymers in organic solvents[21], aqueous two-phase extraction (ATPE)[19], and gel chromatography[22] where the enantiomeric purities can exceed 90%[23]. Enantiomer-separated SWCNTs were employed for chirality-selective recognition of amino acids[24], the investigation of their Raman optical activity[25], and enantiomer-specific DNA-wrapping kinetics[26]. As the interaction of circularly polarized light with helically chiral carbon nanotubes enables the observation of cross-polarized E_{ij} optical transitions in CD spectroscopy, enantiomer-separated SWCNTs were also crucial for determining their complete exciton band structure[18].

Simultaneously with these advancements in enantiomer separation, the targeted covalent functionalization of SWCNTs with luminescent defects (also referred to as organic color centers or quantum defects) was discovered[27,28] and optimized for various applications[29]. These luminescent defects can be created through the controlled reaction of SWCNTs with reactive oxygen species[27,30,31] or aryl diazonium salts[28,32]. This covalent functionalization leads to changes in the local electronic band structure and facilitates exciton localization at the defect sites. New NIR photoluminescence (PL) peaks appear that are red-shifted in comparison to the intrinsic E_{11} PL of SWCNTs and exhibit PL lifetimes on the order of hundreds of ps[33]. The energy difference between the intrinsic exciton and the defect emission (100 meV or more) corresponds to the optical trap depth (ΔE_{opt}) of the defect. As free excitons are efficiently funneled to these luminescent defects, they also lead to higher PL quantum yields (PLQYs). The precise PLQY values and enhancement factors depend on the initial nanotube length, defect density (ideally 5 − 8 per μm), functionalization method, and dispersion solvent[28,31,32,34]. The combination of exceptional photostability and narrow-band emission in the second biological window render SWCNTs with luminescent defects as excellent nanoscale emitters for high-contrast deep-tissue imaging with unprecedented spatial resolution[13,35,36]. The nearly zero-dimensional state of luminescent defects and their deep trap depth enable NIR SPE from SWCNTs even at room temperature[37,38], making them promising candidates for quantum light sources at telecommunication wavelengths[10,11].

Despite the many potential applications of luminescent defects, the handedness of the functionalized SWCNTs and its impact on the chiroptical properties of the defects themselves has not yet been explored. As defect-trapped excitons remain localized on the nanotube lattice instead of the introduced functional group[39], the chiral nature of the SWCNT should be retained in the defect states. However, so far this has not been shown experimentally. Furthermore, the extent to which localized excitons inherit the chirality of the surrounding SWCNT is currently unknown. To answer this question, a highly efficient and tunable method for the introduction of quantum defects is necessary that proceeds under mild reaction conditions to prevent excessive side reactions. These demands can be fulfilled by photocatalytic functionalization approaches, which are still unexplored for SWCNTs.

Photocatalysis has been a rapidly expanding area within organic synthesis. Current developments are driven by its inherent compatibility with higher atom economy and sustainability of chemical transformations[40]. Furthermore, photocatalysis can be used to control reaction pathways and rates by adjusting the irradiation wavelength and intensity. Among the various organic photocatalysts, anthraquinones (AQs) are particularly suitable for oxidative processes and have been employed in alcohol and C-H bond oxidation as well as for light-driven hydrogen peroxide production[41,42]. AQs combine large absorptivity in the UV-Vis spectral region with high excited state redox potentials. They can be easily derivatized to tune their solubility in water or organic solvents, which, together with their low cost, makes them excellent candidates for scalable and versatile photocatalytic reactions[43].

Here, we introduce AQs as organic photocatalysts for the controlled and efficient functionalization of SWCNTs with luminescent oxygen defects. The metal-free functionalization reaction yields SWCNTs with narrow defect emission peaks, high PLQYs and can be applied to nanotubes with different diameters in aqueous or organic dispersions, at low and high concentrations, and even with spatial resolution for SWCNTs thin films. Using photocatalysis with AQ, the functionalization of concentrated dispersions of separated (6,5) and (11,−5) SWCNT enantiomers with high defect densities and without detrimental side reactions becomes possible and thus enables CD spectroscopy of these defects states. We find that the chiral properties of the nanotubes indeed persist within the luminescent defects and even enable us to determine the relative size of free and localized excitons in functionalized SWCNTs.

Results

Photocatalytic functionalization of SWCNTs

For the development of a photocatalytic functionalization strategy for SWCNTs, CoMoCAT raw material was subjected to aqueous two-phase extraction (ATPE) to prepare monochiral (6,5) SWCNTs (see Methods and Supplementary Fig. 1) stabilized by sodium dodecyl sulfate (SDS) in water[34]. Luminescent oxygen defects (with E_{11}^* emission at 1120 nm) were introduced to the nanotube lattice at room temperature via a photocatalytic cycle with anthraquinone-2-sulfonate (AQS) that produced reactive oxygen species (ROS) as shown in Fig. 1a. UV irradiation (UVA, excitation wavelength λ_{ex} = 365 nm) of AQS leads to the formation of an excited-state anthraquinone (for a comparison of the AQS absorption bands and the spectral output of the illuminating light-emitting diode see Supplementary Fig. 2). In the presence of water and oxygen, the excited-state AQS transforms into a hydroquinone species under generation of ROS. While the precise mechanism of this step and the structure of reactive intermediates, especially in water are still a subject of debate, the generation of strong hydroxylation agents has been confirmed[44–46]. The created ROS directly attack the nanotube sidewalls to form luminescent oxygen defects as evident from the new defect emission peaks in the PL spectra[31,47]. Subsequent autoxidation of the hydroquinone under ambient conditions produces hydrogen peroxide and completes the catalytic cycle. To a very limited extent, continuous irradiation with UVA-light will also drive the photodissociation of the generated H_2O_2, which supplies additional reactive hydroxyl radicals[48]. The rate of ROS production under these mild conditions is low and thus enables a high degree of control over the SWCNT functionalization reaction.

The bright, red-shifted E_{11}^* emission feature of the luminescent oxygen defects appears within minutes of UVA-irradiation of a dispersion of (6,5) SWCNTs in the presence of the photocatalyst AQS (concentration 6 μM). The absolute PL intensity of the narrow defect emission peak (full width at half maximum of 49 nm) increases with the duration of UV-light exposure and reaches over 3 times the value of the initial absolute E_{11} peak intensity. Notably, no other emission features or broadening are observed in PL spectra or PL excitation (PLE) maps (see Fig. 1b), demonstrating exceptional selectivity of the photocatalytic functionalization with AQS towards a single oxygen defect binding configuration.

Continued UV-light irradiation of the (6,5) SWCNT dispersion with AQS further increases the E_{11}^* defect emission until a maximum is reached followed by a decrease of the absolute PL intensity, while the E_{11}^*/E_{11} PL intensity ratio continues to increase (see Supplementary

Fig. 3a, b). The reduction in overall PL results from the significant perturbation of the electronic structure of the SWCNTs at very high degrees of functionalization, which also impedes the formation and transport of mobile E_{11} excitons to the luminescent defect sites. SWCNT samples collected after different irradiation times were used to determine their absolute PLQY (see Methods)[34,49] and confirmed that the photocatalytic functionalization method produces highly emissive (6,5) SWCNTs with PLQYs of up to 3.6% in aqueous dispersion at optimum defect density compared to 0.6% before functionalization (see Fig. 1c). The required duration of irradiation to reach the maximum PLQY can be extended by reducing the AQS concentration from 6 to 4 μM, thus offering more accurate control over the degree of functionalization. NIR PL images of pristine and functionalized SWCNT dispersions under identical conditions further visualize the almost six-fold enhancement of the PLQY (see Supplementary Fig. 3c). This increase of SWCNT PLQY and thus brightness with functionalization is significantly higher than values obtained with other common methods for the introduction of oxygen defects[27,30,47]. It is similar to a recently reported metal-catalyzed functionalization reaction[31], but does not require removal of the catalyst before assessing the degree of functionalization.

Functionalization mechanism and properties of oxygen defects

To gain further insights into the mechanism of the photocatalytic functionalization, several reference experiments were performed. First, adding only AQS to the (6,5) SWCNT dispersion or prolonged exposure to UV-light (2 h) without the catalyst does not lead to any changes in the nanotube PL spectra (see Supplementary Fig. 4a). Irradiation with 525 nm light for 1 h at an AQS concentration of 6 μM also did not result in any functionalization, corroborating that it is

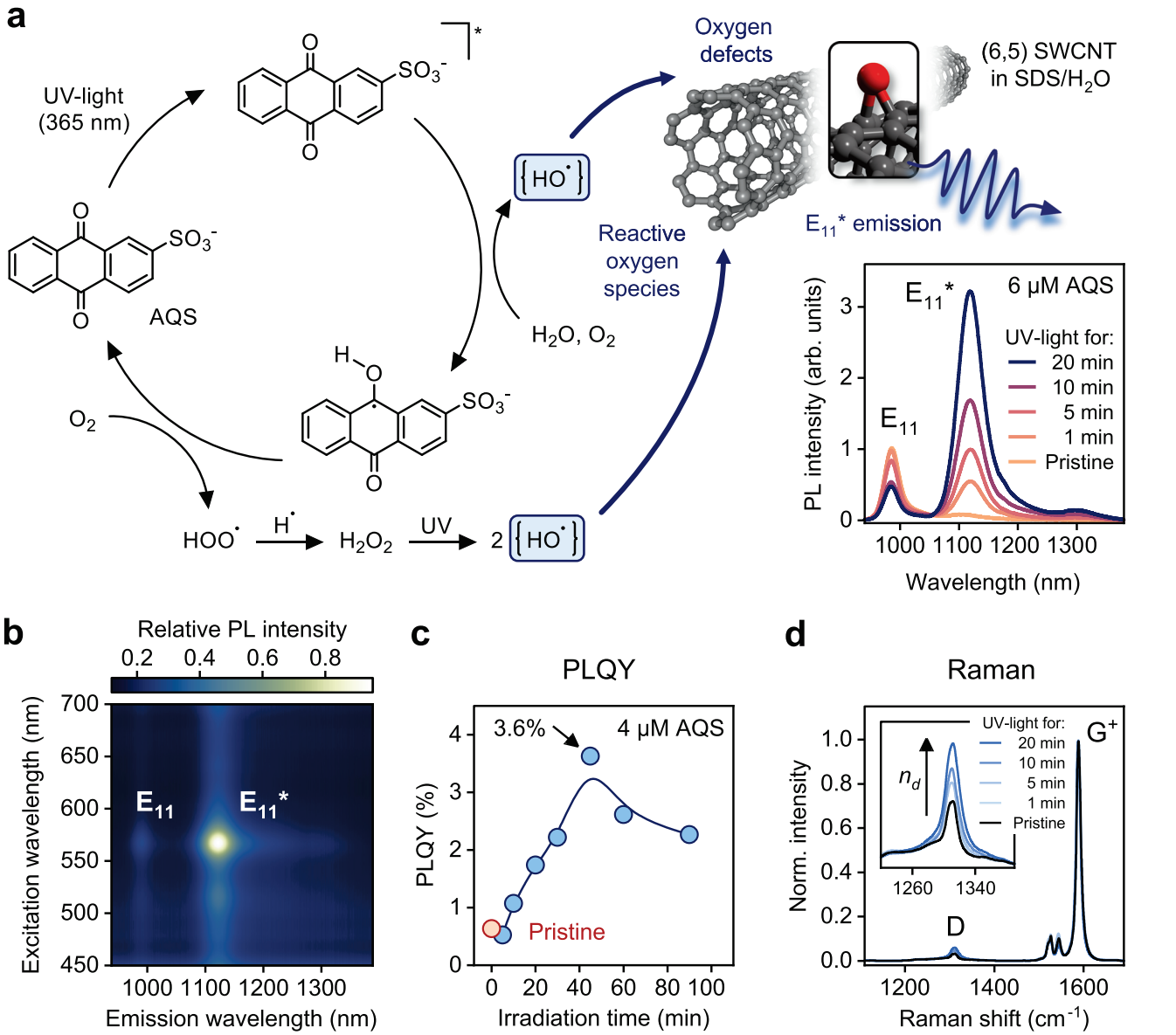

Fig. 1 | Photocatalytic oxygen functionalization of (6,5) SWCNTs. **a** Photocatalytic generation of ROS using AQS (concentration 6 μM) as photocatalyst and UV-light (λ_{ex} = 365 nm). Reaction of ROS with the SWCNT lattice creates luminescent oxygen defects leading to strong E_{11}* photoluminescence (PL, excitation at E_{22} transition, λ_{ex} = 570 nm), as fast-diffusing excitons are localized at the defect site. **b** PLE map of functionalized (6,5) SWCNTs (concentration AQS 6 μM, UV irradiation for 20 min) in aqueous dispersion (SDS, 0.33% w/v). **c** Evolution of the total PL quantum yield (PLQY) of (6,5) SWCNT dispersions with increasing oxygen defect density (PLQY of the pristine sample: 0.6%, concentration AQS 4 μM, the blue line is a guide to the eye). **d** Averaged and normalized Raman spectra of (6,5) SWCNTs (λ_{ex} = 532 nm) at different degrees of functionalization and detail of the Raman D-mode showing its relative increase in intensity compared to the G^+-mode with defect density n_d. Source data are provided as a Source Data file.

indeed the excitation of AQS that drives the reaction (see Supplementary Fig. 4b) and not the optical excitation of the nanotubes. A limited degree of functionalization through exposure to daylight for two days suggests that AQS remains catalytically active for an extended period of time (Supplementary Fig. 4c).

Stopping the UV-light exposure immediately interrupts the photocatalytic reaction, as visible from the identical PL spectra acquired directly after irradiation and 1 h later (see Supplementary Fig. 5a). Even after prolonged UV exposure of the dispersion, no further functionalization occurs after the irradiation is stopped, which suggests that short-lived reactive hydroxylation intermediates are responsible for the SWCNT functionalization and must be generated continuously. From a practical perspective, these short-lived ROS provide unparalleled reaction control, as continuous PL measurements are possible and no quenching or washing steps are required to shield the SWCNTs from reactants (e.g., by addition of sodium deoxycholate, DOC[31]). Supplementary Movie 1 shows the progressing photocatalytic SWCNT functionalization under UV irradiation and the simultaneous changes of the NIR PL of (6,5) nanotube dispersions with and without AQS. After reaching the desired PL brightness or E_{11}/E_{11}^* ratio, the water-soluble catalyst and any potential reaction byproducts can be removed by spin-filtration to obtain pure nanotube dispersions (see Supplementary Fig. 5b).

The properties of luminescent oxygen defects created by photocatalytically produced ROS were further investigated by Raman spectroscopy. The resonant Raman spectra of functionalized (6,5) SWCNTs (see Fig. 1d) show an increase of the relative Raman D/G^+ mode ratio with increasing irradiation time. The Raman D/G^+ ratio is frequently used as a relative metric for defect densities in carbon nanotubes and recently has been expanded to determine absolute defect densities[34]. Importantly, Raman D/G^+ ratios for SWCNTs with luminescent oxygen and aryl defects scale differently in relation to the defect densities calculated from the decrease of the E_{11} PLQY due to the formation of clusters in the case of oxygen defects[50]. This difference in scaling can help to distinguish between luminescent oxygen and aryl defects. For our photocatalytic approach, we find the same correlation between the Raman D/G^+ ratio and calculated defect densities as previously seen for oxygen defects. Maximum SWCNT PL intensities are obtained for ≈ 6 defect clusters per μm. While the E_{11}^* emission wavelength (≈ 1120 nm, corresponding to an optical trap depth of 141 meV) already suggests the presence of oxygen defects[27,30,31,51], the D/G^+ scaling further corroborates the nature of the luminescent defects and excludes any direct reaction of the AQS with the nanotube lattice. This notion is further supported by examining the RBM/IFM region of the Raman spectra (see Supplementary Fig. 6)[50,52].

Luminescent quantum defects have significantly longer PL lifetimes compared to those of mobile E_{11} excitons (few ps), as localization at the defect sites prevents fast non-radiative decay elsewhere on the nanotube lattice or at the nanotube ends[33,35]. Time-correlated single-photon counting (TCSPC) measurements of the E_{11}^* PL decay at 1120 nm gave an amplitude-averaged lifetime of 158 ps (see Supplementary Fig. 7), which agrees well with literature data on luminescent defects[31,33,37]. Excitation density-dependent PL measurements further show the characteristic sub-linear scaling and eventual saturation of the E_{11}^* emission (see Supplementary Fig. 8) due to defect state-filling[32]. Finally, temperature-dependent PL spectra yield a thermal trap depth $\Delta E_{\mathrm{therm}}$ of 102 meV (see Supplementary Fig. 9), which is also in agreement with previous reports on oxygen defects[27,31,53]. The difference between the optical and thermal defect trap depth of ≈ 39 meV can be attributed to vibrational reorganization of the local nanotube lattice upon exciton trapping[53].

Versatility of photocatalytic SWCNT functionalization

To explore the robustness and versatility of the presented photocatalytic functionalization of SWCNTs with AQS, different reaction conditions, nanotube environments and starting materials were tested. First, a range of common surfactants for the stabilization of (6,5) SWCNTs in water were employed leading to variations in the accessibility of the nanotube surface. Normalized PL spectra of (6,5) SWCNTs functionalized under otherwise identical conditions with SDS, DOC, sodium dodecylbenzene sulfonate (SDBS), or sodium cholate (SC) as surfactants at concentrations above their respective critical micelle concentration are shown in Supplementary Fig. 10. While no functionalization occurs in dispersions with DOC due to its dense surface coverage[54], comparable degrees of functionalization were achieved with the other surfactants. Dispersions with SDS showed the highest degree of functionalization in terms of the E_{11}^*/E_{11} peak intensity ratio.

The small-diameter (6,5) SWCNTs (0.76 nm) are particularly well-suited for covalent functionalization, as the bond strain due to the lattice curvature leads to high reactivity. To investigate the effectiveness of the photocatalytic functionalization approach for other and especially larger diameter carbon nanotube species, (7,3), (8,3), (10,0), (9,2), (9,4), and (10,3) SWCNTs (diameter 0.71–0.92 nm) were sorted by gel chromatography[55] and transferred to SDS dispersions (see Supplementary Figs. 11 and 12 for absorption spectra and PLE maps). PL spectra of the different SWCNT species after functionalization in the presence of AQS and under UV-light irradiation are shown in Fig. 2a (see Supplementary Fig. 13 for corresponding PLE maps), confirming efficient functionalization even of larger diameter nanotubes without any changes to the reaction protocol. In agreement with data on luminescent aryl defects[56], an overall trend of decreasing optical trap depths for larger diameter nanotubes is observed (see Supplementary Fig. 14).

Their narrow-band PL in the second biological window (NIR-II) combined with high photostability have made SWCNTs promising fluorophores for biological imaging[12–14]. However, their application as emitters in biological environments or even living organisms requires a high degree of biocompatibility, which is usually achieved by biocompatible polymers such as ssDNA or pegylated phospholipids (PL-PEG)[24,36,57]. Since functional groups on the nanotube surface often disrupt surfactant coverage or polymer wrapping[31,38] and thus make post-functionalization surfactant exchange less efficient, protocols for functionalizing already biocompatible SWCNTs are highly desirable. As a proof of concept, pristine (6,5) SWCNTs were transferred by dialysis to PL-PEG_{5000} and $(GT)_6$-ssDNA dispersions, respectively. Successful wrapping with these biocompatible polymers was corroborated by the significant redshifts of the corresponding E_{11} emission and absorption peaks (see Supplementary Figs. 15 and 16). Without any additional treatment after dialysis, the PL-PEG-wrapped (6,5) SWCNTs were functionalized photocatalytically in the presence of AQS and emission from luminescent oxygen defects was evident. The integrated PL intensities were more than four times higher than pristine PL-PEG-wrapped nanotubes (see Fig. 2b). For $(GT)_6$-wrapped (6,5) SWCNTs, the photocatalytic functionalization was also possible but led to lower final E_{11}^*/E_{11} PL intensity ratios (see Supplementary Fig. 16c). The apparently lower reactivity of ssDNA-wrapped SWCNTs may result from a difference in nanotube surface coverage[58]. Possible unwanted side reactions between ROS and the buffer system (PBS) may also contribute in addition to a lower colloidal stability due to alterations of DNA strands by ROS. The functionalization efficiency might be improved by optimizing the oligomer sequence or ssDNA concentration[59]. After functionalization, the AQS could be easily and completely removed from the dispersions by spin-filtration, ensuring biocompatibility of the final sample (see Supplementary Fig. 5b).

As the cost and effort to prepare monochiral SWCNT dispersions is still high, unsorted SWCNTs are often employed for biological imaging and sensing applications, as they can be obtained in high concentrations from commercially available raw materials (e.g., CoMoCAT)[12,60]. Oxygen-functionalized CoMoCAT SWCNTs have been shown to enable sensing of metabolites such as dopamine or

https://doi.org/10.1038/s41467-025-60342-y

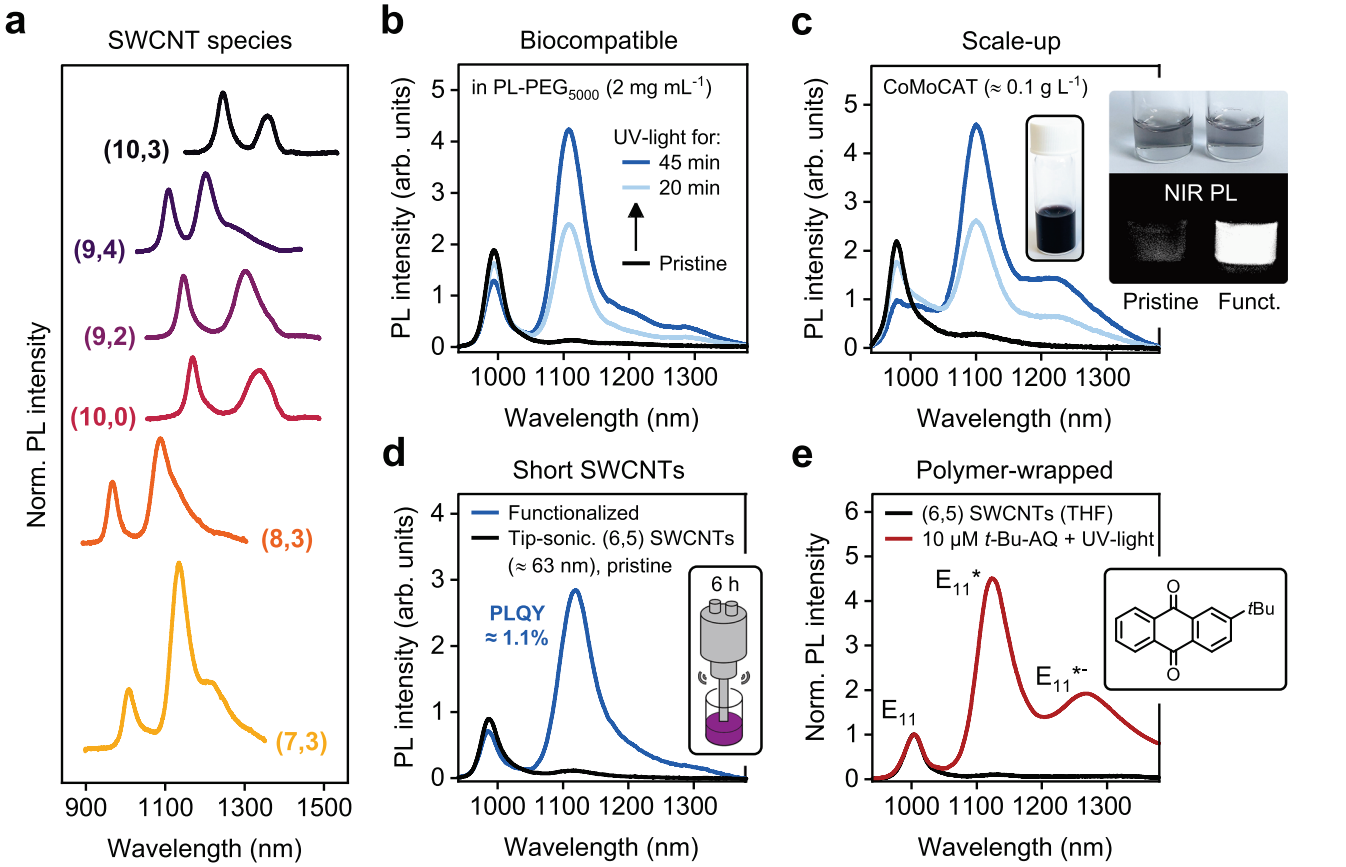

Fig. 2 | Versatility of photocatalytic SWCNT functionalization. a Normalized PL spectra of different oxygen-functionalized SWCNT species with diameters ranging from 0.71 nm to 0.92 nm (excitation at respective E_{22} optical transition wavelengths as determined from UV-Vis-NIR absorption spectra, see Supplementary Fig. 11). **b** Functionalization of (6,5) SWCNTs after surfactant exchange to biocompatible polymer PL-PEG_{5000} (concentration 2 mg mL^{-1}, without any post-treatment after dialysis). **c** Scale-up of photocatalytic functionalization using CoMoCAT raw material (SDS, 0.33% w/v) at high SWCNT concentrations (≈ 0.1 g L^{-1}); black line: pristine SWCNTs; light blue: 10 min UV irradiation; dark blue: 20 min UV irradiation. The inset shows NIR PL images (950–1600 nm) of diluted pristine and functionalized CoMoCAT dispersions at identical concentration (525 nm excitation). **d** Functionalization of (6,5) SWCNTs shortened by tip sonication (6 h, average length of ≈ 63 nm). **e** Photocatalytic functionalization of PFO-BPy-wrapped (6,5) SWCNTs in THF using 2-*tert*-butylanthraquinone as photocatalyst. Source data are provided as a Source Data file.

cholesterol[60,61]. Their sensitivity and applicability could be enhanced by overall brighter luminescent defects. For this purpose, the photocatalytic introduction of oxygen defects was scaled-up to highly concentrated CoMoCAT dispersions (0.1 g L^{-1}) in SDS (for absorption spectra and PLE maps see Supplementary Fig. 17). PL spectra of CoMoCAT SWCNTs before and after functionalization with AQS/UV-light illustrate a strong brightening effect (see Fig. 2c). The functionalized SWCNTs exhibit a 4.5× higher integrated PL intensity compared to the pristine CoMoCAT dispersion as also evident from the NIR PL images of pristine and oxygen-functionalized dispersions under the same conditions.

In addition to the choice of coating, short SWCNTs (<100 nm) are significantly more biocompatible than long nanotubes. They are also better suited for real-time imaging with high spatial resolution[62]. However, shortening nanotubes by oxidative cutting or ultrasonication severely reduces their PLQY due to quenching of mobile excitons at the nanotube ends[32,63]. Luminescent aryl and oxygen defects offer a way to alleviate this problem by efficient exciton localization[31,35]. To assess the brightening effect by photocatalytic functionalization for short SWCNTs, dispersions of pristine (6,5) SWCNTs (average length ≈ 580 nm) were subjected to 6 h of tip sonication, which shortened them to an average length of ≈ 63 nm (for absorption and PL spectra as well as AFM images, see Supplementary Figs. 18 and 19). As shown in Fig. 2d, irradiation with UV-light at an AQS concentration of 6 µM led to efficient functionalization with luminescent oxygen defects and an exceptionally high PLQY of 1.1% (at optimal defect density) for such short nanotubes. With such brightness values these oxygen-functionalized SWCNTs are highly suitable for in-vivo, high-resolution imaging.

So far, all functionalization experiments were performed in aqueous dispersions. However, to create thin films, networks and finally devices with functionalized SWCNTs, the dispersions must be compatible with established film deposition techniques such as spin coating or aerosol-jet printing, which often rely on organic solvents[10,32,64,65]. The advantages of organic solvents compared to water in this context include their high vapor pressure, lower surface tension, and compatibility with processing under inert conditions. To test the photocatalytic functionalization of SWCNTs in organic solvents, 2-*tert*-butylanthraquinone (*t*-Bu-AQ) was chosen as photocatalyst due to its solubility in many organic solvents and its already established commercial application (e.g., in the industrial anthraquinone process)[42]. Monochiral dispersions of (6,5) SWCNTs were prepared by shear-force mixing (SFM) with a polyfluorene-bipyridine (PFO-BPy) copolymer in toluene, which yields long nanotubes with high PLQYs of 2% (for absorption spectra and PLE maps see Supplementary Figs. 20 and 21)[49]. When the prepared dispersions of (6,5) SWCNTs in toluene were mixed with *t*-Bu-AQ (10 µM) and exposed to UV-light, no functionalization reaction occurred (see Supplementary Fig. 22), presumably due to insufficient stabilization of the reactive hydroxylation species in a non-polar environment[66]. In contrast to that,

(6,5) SWCNTs that were dispersed in the more polar THF were easily functionalized and reached high E_{11}^*/E_{11} PL intensity ratios (see Fig. 2e).

The functionalization with oxygen defects instead of aryl sp^3 defects for polymer-wrapped SWCNTs in organic solvent was corroborated by the spectral position of the respective E_{11}^* peak at 1124 nm, with the expected blueshift by ≈ 40 nm compared to aryl defects[32]. In general, three possible binding configurations (E_{11}^{*+}, E_{11}^*, E_{11}^{*-}) can be distinguished for luminescent oxygen defects based on previous theoretical studies[51]. The E_{11}^{*+} (≈ 1050 nm) and the more prevalent E_{11}^* (≈ 1120 nm) PL peaks are associated with a longitudinally- and circumferentially-oriented ether-type binding motif (ether-L and ether-D, respectively). A further redshifted E_{11}^{*-} PL peak (≈ 1250 nm) results from an epoxide-like defect structure (epoxide-L). PL spectra of individual, oxygen-functionalized SWCNTs in a polymer matrix at cryogenic temperature (4.6 K, see Supplementary Fig. 23) indicated the presence of all three possible defect binding geometries, although the defect (binding configuration shown in Fig. 1a) with E_{11}^*emission is clearly dominant. Notably, a reduction of the selectivity towards the ether-D oxygen defect binding geometry in organic solvents compared to aqueous environments was evident from the additional, more redshifted E_{11}^{*-} emission feature (epoxide-L defect configuration) in Fig. 2e. This constitutes the first report of intentional oxygen-functionalization of polymer-wrapped nanotubes directly in organic dispersions rather than on reactive oxide surfaces[37,67].

Spatially resolved SWCNT thin-film functionalization

As the photocatalytic functionalization of SWCNTs with anthraquinones is driven by UV-light, it also allows for the spatially controlled introduction of oxygen quantum defects in thin films and networks of nanotubes. To date, the solid-state functionalization of SWCNTs with luminescent oxygen defects requires a direct and permanent contact between SWCNTs and reactive surfaces such as SiO_2 or metal oxides under inert conditions[37,67]. However this is often impractical for the fabrication of optoelectronic devices or SWCNT-coupled nanocavities, e.g., for collecting single photons from luminescent defects[8]. To perform photocatalytic functionalization of thin films of SWCNTs with AQS, we employed an irradiation setup as detailed in Fig. 3a. Glass or Si/SiO_2 substrates were coated with a thin and chemically inert layer of a crosslinked bis-benzocyclobutene polymer (BCB, ≈ 30 nm) to exclude any unintentional surface reactions or trap states[68]. Subsequently, polymer-wrapped (6,5) SWCNTs were spin-coated from toluene onto the BCB-covered substrates to achieve network densities similar to those for light-emitting field-effect transistors (see Fig. 3b)[9]. Finally, a shadow mask and a droplet of an aqueous AQS solution (2 mg mL^{-1}) were placed on top of the nanotube film. Subsequent irradiation with UV-light (λ_{ex} = 365 nm) led to oxygen defect functionalization within minutes as visualized by Raman D/G^+ ratio mapping in Fig. 3c. Only areas that were not covered by the shadow mask were functionalized. The corresponding averaged PL spectra only show the intrinsic E_{11} and narrow E_{11}^* defect PL (see Fig. 3d, e), confirming the high selectivity of the photocatalytic functionalization with AQS in water for creating a single oxygen defect binding configuration even in polymer-wrapped SWCNT networks on a solid substrate.

By applying an absolute defect quantification approach based on Raman spectroscopy[34,50], we calculated an average defect density of ≈ 13 ± 4 oxygen atom defects per μm of nanotube (integrated Raman $\Delta(D/G^+)$ ratio of 0.03 ± 0.01). This value is within a reasonable range for the observed E_{11}^*/E_{11} PL intensity ratios of ≈ 1:1 (see Fig. 3e and Supplementary Fig. 24) and supports the assumption that no significant side reactions have occurred.

The spatial resolution of the functionalization method tested here was limited by the features of the shadow mask, as indicated by a nanotube thin film exposed with a stripe pattern (see Supplementary Fig. 24). However, the maximum spatial resolution of the process is most likely limited by the diffusion of the short-lived reactive hydroxylation species.

Circular dichroism of luminescent oxygen defects

Chirality in low-dimensional semiconductors, such as hybrid organic-inorganic perovskites[1], quantum dots[69] or transition metal dichalcogenides[2,70] can be induced via geometrical distortion or supramolecular interactions with chiral ligands or additives. In contrast to that, SWCNTs exhibit intrinsic chirality across multiple length scales from few nm up to several μm as a direct consequence of the intrinsic helicity of the rolled-up carbon lattice. Except for zig-zag SWCNTs, all semiconducting SWCNTs are chiral and can be classified as left- or right-handed enantiomers according to their optical activity in CD spectra. The corresponding mirror image of a (*n*,*m*) nanotube is a (*n* + *m*,−*m*) nanotube, as exemplified by the SWCNT enantiomers (6,5) and (11,−5)[71].

The excitons in SWCNTs represent an intermediate regime between delocalized Wannier-Mott and tightly-bound Frenkel excitons due to their one-dimensional confinement. They exhibit coherence lengths of several nm but also large binding energies[72]. Consequently, SWCNTs offer a suitable framework for the characterization of free and defect-localized excitons and their interactions with a chiral carbon lattice. Due to limited light absorption by the few luminescent defects (5–30 defects per μm of nanotube) that are usually introduced by covalent functionalization[32] it was not yet possible to determine their chiroptical properties, e.g., by CD spectroscopy. The photocatalytic functionalization of SWCNTs enables the introduction of large numbers of oxygen defects. At the same time, the method proceeds with remarkably high selectivity for the ether-D (E_{11}^*) binding configuration even in highly concentrated SWCNT dispersions. Thus, the E_{11}^* absorbance values and well-defined absorption peaks necessary to obtain reliable CD spectra become accessible.

To take advantage of this possibility, (6,5) and (11,-5) SWCNT enantiomers were separated by gel chromatography[18,22] and transferred to SDS dispersions (see Supplementary Figs. 25 and 26 for absorption spectra and PLE maps). CD spectra of pristine (6,5) and (11,−5) SWCNTs show the expected E_{ii} and E_{ij} transitions in the UV-Vis and NIR spectral range (see Fig. 4a, b). Enantiomeric purities of 84% for (6,5) and 89% for (11,−5) SWCNTs were determined from the normalized ellipticity ($CD_{norm} = CD_{E_{ii}}/Abs_{E_{ii}}$) at the E_{22} transition[71].

For ideal signal-to-noise ratios in CD measurements, optical densities (OD) of ≈ 0.8 – 1 cm^{-1} are desired. To obtain these values for the E_{11}^* transition, the pristine (6,5) and (11,−5) enantiomer dispersions were concentrated by spin-filtration to an OD of ≈ 3.5 cm^{-1} at the E_{11} transition. Subsequently, the SWCNT dispersions were functionalized with luminescent oxygen defects using AQS (10 μM) and UV irradiation. As this method enables frequent checks after each step of irradiation, direct tuning of the degree of functionalization was possible for both dispersions. The absorption spectra (see Fig. 4c) of both (6,5) and (11,-5) dispersions show the expected broadening of the E_{11} transition upon extensive functionalization (see also Supplementary Fig. 27 for E_{22} transitions) and an additional absorption peak at ≈ 1105 nm, which we attribute to direct absorption into the E_{11}^* defect state. The corresponding CD spectra (see Fig. 4d) also show a new CD feature with the same energy as the E_{11}^* defect absorption and the same sign as the E_{11} transition. Hence, we can assign this new CD peak to the defect-related E_{11}^* exciton with clear evidence that the chirality of the nanotube also determines the chiroptical properties of the quantum defects.

As noted above, a large defect density is necessary to reach sufficient optical densities for CD measurements. The absolute quantification of the total defect densities of the functionalized (6,5) and (11,-5) SWCNT dispersions by Raman spectroscopy[50] yielded remarkably high values of about 70 oxygen atom defects per μm of SWCNT (see

https://doi.org/10.1038/s41467-025-60342-y

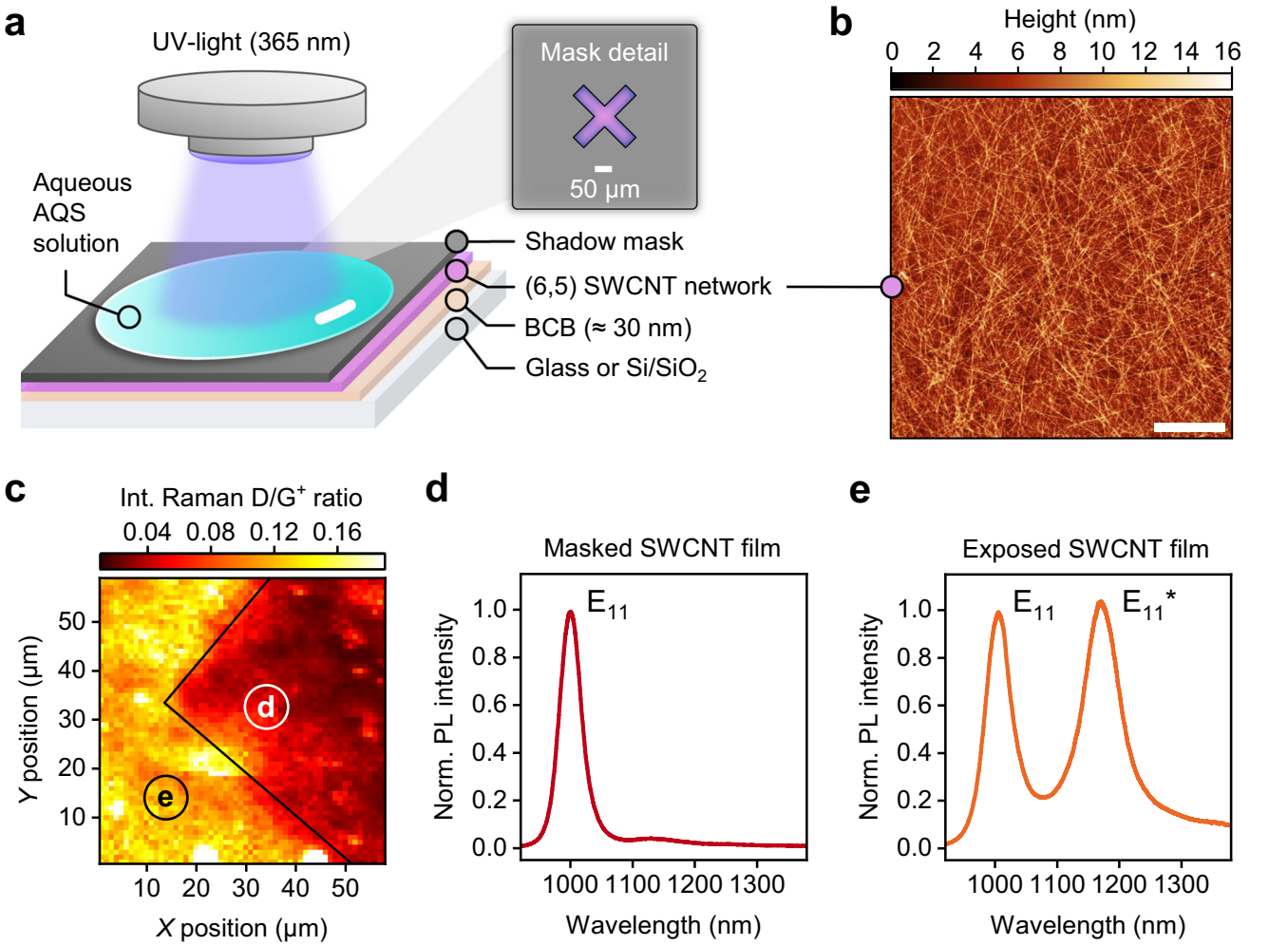

Fig. 3 | Spatially resolved functionalization of SWCNT thin films. a Schematic illustration of the functionalization procedure using UV-light (λ_{ex} = 365 nm) and a shadow mask, which is placed on top of a spin-coated nanotube network (polymer-wrapped (6,5) SWCNTs) on BCB-coated glass or silicon substrates. Irradiation through an aqueous AQS solution (2 mg mL^{-1}) in contact with the nanotube film leads to the formation of luminescent defects in the exposed areas. **b** AFM image of SWCNT network used for functionalization (scale bar, 1 µm). **c** Map of integrated Raman D/G$^+$ ratios at the shadow mask edge (solid black line) after functionalization. **d**, **e** Averaged, normalized PL spectra (>100 averaged spectra) of masked and exposed areas after functionalization. Source data are provided as a Source Data file.

Supplementary Fig. 28). Nevertheless, the corresponding PL spectra of these dispersions still show good spectral purity of the E_{11}* PL with only minor side band contributions (see Fig. 4c) while the E_{11} emission is almost negligible and the E_{11}*/E_{11} PL intensity ratio reaches more than 30.

Extracting the CD_{norm} values (or absorption dissymmetry factors g_{abs}) of the E_{11} and E_{11}* transitions from the CD and absorption spectra of the same SWCNT sample enables the direct quantification of the relative size of the free and localized exciton. Functionalized (6,5) and (11, −5) SWCNTs exhibit very similar CD_{norm} values of −27 and 31 mdeg at the E_{11} and -15 and 14 mdeg at the E_{11}* transition, respectively. From the approximately two-fold difference in CD_{norm} values between the free and defect-localized exciton, a reduction of the exciton size by a factor of ≈ 2 upon trapping can be estimated (see Fig. 4e, and Supplementary Note 1). Such a contraction of the exciton upon confinement at luminescent quantum defects was previously proposed based on theoretical considerations[39,73]. The CD data presented here provides direct experimental evidence for this assumption and corroborates that the trapped E_{11}* exciton remains strongly coupled to the surrounding nanotube lattice. Thus, the broken mirror symmetry of the helically chiral SWCNT lattice is maintained even in the confined excitonic states of the quantum defects. Based on reported values of ≈ 5–10 nm for the coherence length of the free exciton[74], our analysis suggests a confinement of the localized E_{11}* exciton to ≈ 2–5 nm, which is in good agreement with theoretical predictions[51]. Overall, the observation of CD in luminescent quantum defects provides a tool for exploring and exploiting the chiroptical properties of SWCNT enantiomers and could be utilized for chirality-sensitive optical readout schemes.

Discussion

We have demonstrated a simple but highly efficient and versatile photocatalytic approach for the covalent functionalization of SWCNTs with luminescent oxygen defects. It is based on the photocatalytic activity of anthraquinones, which produces strong hydroxylation agents under UV illumination. These ROS react with the nanotube lattice to create oxygen defects of a specific binding type (ether-D), resulting in narrow defect emission peaks in the NIR. The reactivity of the system is controlled by variation of irradiation time and photocatalyst concentration, offering flexibility and scalability to create samples with precise defect densities, narrow defect emission, and high PL brightness (PLQY of 3.6%). No toxic, air-sensitive or metal-containing reagents are required for this simple photocatalytic transformation. Very low photocatalyst concentrations (µM) in combination

https://doi.org/10.1038/s41467-025-60342-y

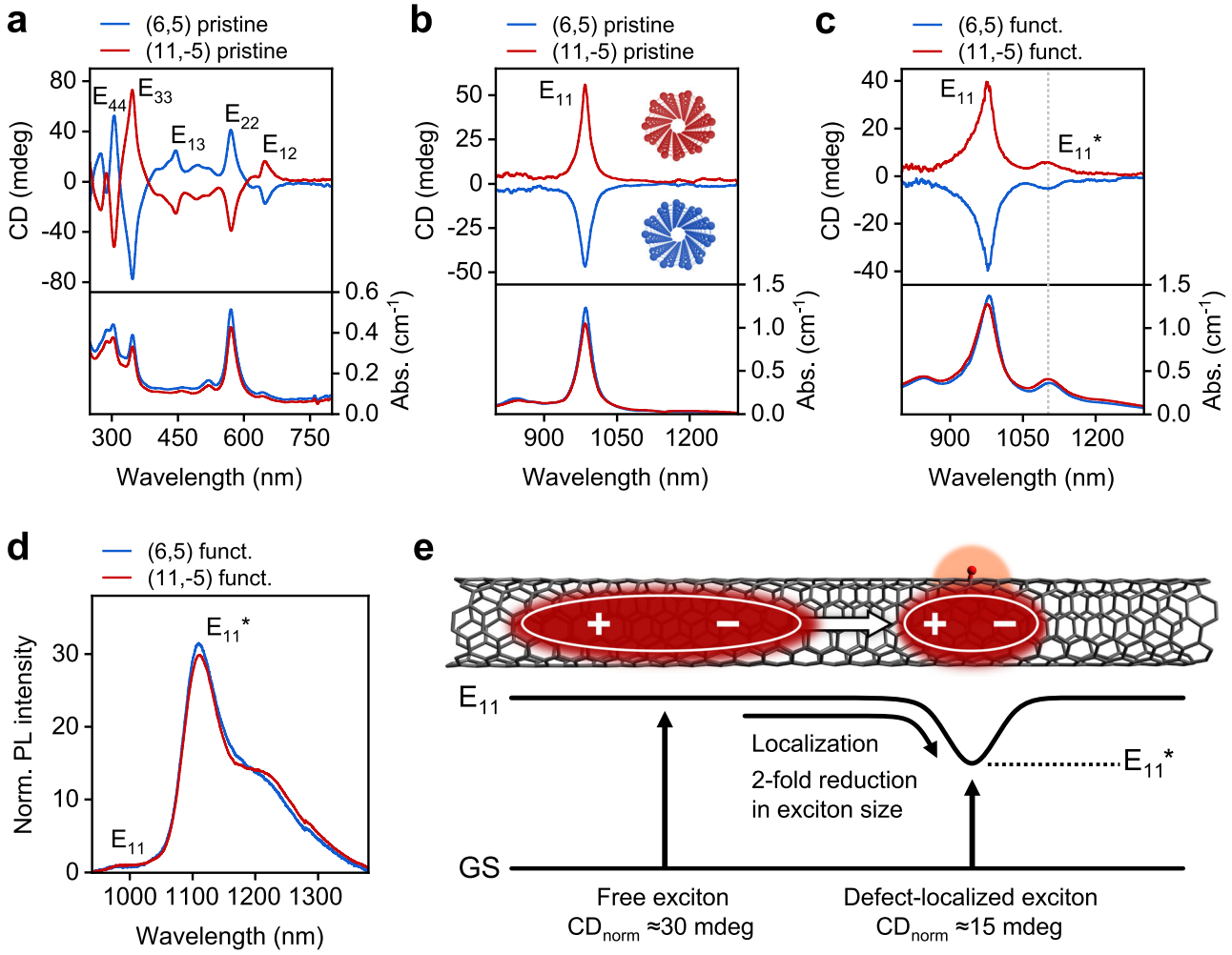

Fig. 4 | Chirality of luminescent quantum defects. a CD and absorbance spectra of pristine (6,5) and (11,−5) SWCNT enantiomers in the visible spectral region. **b** CD and absorbance spectra of pristine SWCNT enantiomers in the NIR spectral region (inset with front view of helically chiral SWCNT enantiomers). **c** CD and absorbance spectra of oxygen-functionalized SWCNT enantiomers in the NIR spectral region, demonstrating CD of E_{11}^* defects. **d** PL spectra of oxygen-functionalized SWCNT dispersions in (**c**). **e** Schematic illustration of the reduction in exciton size by a factor of ≈ 2 upon confinement of the free exciton at the oxygen defect site as determined from the ratio of the respective CD_{norm} values. Source data are provided as a Source Data file.

with their straightforward removal upon work-up are key advantages of this easy, sustainable and cost-efficient nanotube functionalization procedure.

The photocatalytic introduction of luminescent oxygen defects is suitable for various small-diameter SWCNTs (0.71 – 0.92 nm), providing access to photostable NIR emitters throughout the telecommunication O-band and NIR-II biological window. Our approach can be applied to SWCNTs in different surfactant systems, to biocompatible carbon nanotubes that are coated with pegylated phospholipids or DNA and to short (<100 nm) SWCNTs suitable for in-vivo bioimaging. It can be easily scaled-up for highly concentrated and unsorted SWCNT dispersions (e.g., CoMoCAT). Importantly, this broad versatility is achieved without any adaptations of the reaction protocol. Furthermore, a simple exchange of the water-soluble anthraquinone photocatalyst with a less polar derivative enables the functionalization of polymer-wrapped carbon nanotubes in THF. Even the spatially controlled introduction of luminescent oxygen defects in SWCNT networks is possible with high spectral purity and low levels of unfavorable side reactions, which is highly valuable for the fabrication of light-emitting devices, nanocavities, and integrated photonic circuits with NIR carbon nanotube emitters.

Finally, the photocatalytic introduction of oxygen defects in carbon nanotubes can be utilized to answer fundamental questions about the interactions of excitons in one-dimensional and chiral SWCNTs. The controlled functionalization of concentrated dispersions of (6,5) and (11,-5) SWCNT enantiomers with high defect densities allowed us to characterize the chiroptical properties of luminescent quantum defects in carbon nanotubes. The circular dichroism of the defect absorption with the same sign as the exciton absorption clearly demonstrates that the helical chirality of the nanotube lattice is retained in the quasi zero-dimensional defect state. This intrinsic chirality of the luminescent defects may enable circularly polarized light emission or chiral single photon emission from functionalized SWCNTs. Furthermore, the absorption dissymmetry factors calculated from the CD spectra give access to the relative sizes of the E_{11} versus the E_{11}^* excitons. The rather large mobile excitons in SWCNTs are reduced in size by a factor of two upon localization by the quantum defect. These values provide direct experimental insights into the fundamental properties of luminescent defects and can be used to further develop and benchmark theoretical models.

Methods

Preparation of (6,5) SWCNT dispersions

Monochiral (6,5) SWCNT dispersions in water were obtained by aqueous two-phase extraction (ATPE) from CoMoCAT raw material (CHASM SG65i-L58)[34]. For this purpose, a two-phase system of dextran

(M_W = 70 kg mol^{-1}, TCI) and polyethylene glycol (PEG, M_W = 6 kg mol^{-1}, Alfa Aesar) was employed. The separation protocol used sodium deoxycholate (DOC, BioXtra, ≥ 98.0%) and sodium dodecyl sulfate (SDS, Sigma-Aldrich, ≥ 99.0%) for diameter-specific sorting of SWCNTs. Initially, the SDS concentration was increased to 1.1% (w/v) at a fixed DOC concentration of 0.04% (w/v) to transfer all species with diameters larger than (6,5) SWCNTs to the upper phase. Next, the SDS concentration was adjusted to 1.2% (w/v) and gradually increased to 1.5% (w/v) for the collection of fractions enriched in (6,5) SWCNTs. Metallic and semiconducting species were separated by addition of sodium cholate (SC, Sigma-Aldrich, ≥ 99.0%) and sodium hypochlorite as oxidant. Sorted (6,5) SWCNTs were concentrated in an ultrafiltration stirred cell (Millipore) using a 300 kg mol^{-1} cut-off membrane, and adjusted to a 1% (w/v) SDS before further processing.

Highly-purified (6,5) SWCNT dispersions in toluene were obtained from CoMoCAT raw material (SG65i, Sigma-Aldrich, Lot No. MKC1004) via selective polymer-wrapping using shear-force mixing[49]. Briefly, the raw material was mixed with poly[(9,9-dioctylfluorenyl-2,7-diyl)-*alt*-(6,6′-(2,2′-bipyridine))] (PFO-BPy, American Dye Source, M_W = 38 kg mol^{-1}, 0.5 g L^{-1}) in toluene, and dispersed by shear-force mixing (Silverson L2/Air, 10230 rpm, 72 h, 20 °C), followed by centrifugation (2×, 45 min, 60000 × *g*, Beckman Coulter Avanti J26XP) and filtration of the combined supernatants through a PTFE syringe filter (5 μm pore size).

Sorting of additional SWCNT species

Monochiral (7,3), (8,3), (9,2), (9,4), (10,0), and (10,3) SWCNTs were obtained by gel chromatography employing a mixed surfactant system[55,75]. For (7,3), (10,0), (8,3), (9,2) SWCNTs, HiPco SWCNT raw material (NanoIntegris, Inc., diameter distribution 1.0 ± 0.3 nm) was dispersed in an aqueous solution of SC (0.8%, w/v) by ultrasonication (Branson Sonifier 250D) for 1–2 h. After ultracentrifugation at 210,000 × *g* for 2 h, the supernatant was collected and mixed with aqueous solutions of SDS and SC to modify the surfactant concentration to 0.6% SDS + 0.4% SC. The separation was carried out with a HPLC system (Cytiva AKTAexplorer 10S) and columns (Cytiva HiScale 26/20) filled with gel beads (Cytiva Sephacryl S-200 HR) at a temperature of 17 °C. After loading with the SWCNT dispersion, adsorbed SWCNTs were eluted using a mixed surfactant solution of 0.6% SDS + 0.4% SC + *x*% sodium lithocholate (LC, >98%, Tokyo Chemical Industry Co., Ltd.). Adjustment of the LC concentration to 0.030%, 0.048%, 0.056%, and 0.065% yielded fractions highly enriched in (7,3), (10,0), (8,3), and (9,2) SWCNTs, respectively. For (9,4) and (10,3) SWCNTs, HiPco SWCNT raw material was dispersed in an aqueous solution of SC (1%, w/v) by ultrasonication for 2 h. After ultracentrifugation, the collected supernatant was mixed with aqueous solutions of SDS to modify the surfactant concentration (1.0% SDS + 0.5% SC). The separation was carried out with a HPLC system and columns (Cytiva HiScale 50/20) at a temperature of 20 °C. After loading with the SWCNT dispersion, adsorbed SWCNTs were eluted using a mixed surfactant solution of 1.0% SDS + 0.5% SC + *x*% DOC. The concentration *x*% of DOC was adjusted to 0.14% and 0.16% to obtain (9,4) and (10,3) SWCNT fractions, respectively. Prior to functionalization, the surfactant was exchanged to SDS (0.33%, w/v) by spin-filtration (Amicon Ultra-4, 100 kg mol^{-1}).

Enantiomer separation of (6,5) and (11,-5) SWCNTs

Enantiomer separation of (6,5) SWCNT dispersions in water was performed by gel chromatography[22]. CoMoCAT SWCNTs (Sigma-Aldrich SG65, 704148) were dispersed in an aqueous solution of SC (1.0%, w/v) by ultrasonication (Branson Sonifier 250D). Following ultracentrifugation at 210,000 × *g* for 2 h, the supernatant solution was collected and mixed with an aqueous solution of SDS to obtain a 2.0% (w/v) SDS + 0.5% (w/v) SC dispersion. The separation was performed in a two-step procedure, and the temperature was kept constant at 20 °C. A high-performance liquid chromatography system (NGC, BIO-RAD) was equipped with columns filled with gel beads (GE healthcare Sephacryl S-200 HR) and the SWCNT dispersion was loaded into the first column equilibrated with 2.0% (w/v) SDS + 0.5% (w/v) SC. The non-adsorbed filtrate containing (6,5) and (11,-5) SWCNTs was collected and subjected to the second purification step. This fraction was combined with an aqueous solution of SC to prepare a 0.5% (w/v) SDS + 0.5% (w/v) SC dispersion, which was loaded into another column after equilibration with 0.5% (w/v) SDS + 0.5% (w/v) SC. Adsorbed SWCNTs were eluted using a mixed surfactant solution containing LC. A stepwise increase of the LC concentration yielded fractions containing 0.5% (w/v) SDS + 0.5% (w/v) SC + *x*% (w/v) LC, where high-purity (11,-5) and (6,5) SWCNTs were eluted at LC concentrations of 0.029% and 0.034%, respectively. Prior to functionalization, the obtained enantiopure dispersions were transferred to 0.33% (w/v) SDS by spin-filtration (Amicon Ultra-4, 100 kg mol^{-1}).

Shortening of SWCNTs

Dispersions of pristine (6,5) SWCNTs (1% w/v SDS) were tip-sonicated for 6 h (Sonic Vibra Cell VCX500, amplitude 25%, on/off cycle 8 s/2 s) in a water-cooling bath (5 °C). After centrifugation at 60,000 × *g* for 30 min (Beckman Coulter Avanti J-26S XP), the supernatant was removed and used for functionalization.

Transfer of SWCNTs to PL-PEG$_{5000}$

Pristine (6,5) SWCNTs were transferred to PL-PEG$_{5000}$ using an adapted procedure as reported by Welsher et al.[36]. SWCNT dispersions were mixed with appropriate amounts of 18:0 PEG5000 PE (1,2-distearoyl-*sn*-glycero-3-phosphoethanolamine-*N*-[methoxy(polyethylene glycol)-5000], PL-PEG$_{5000}$, Avanti Polar Lipids, Inc.) to obtain a final concentration of 2 mg mL^{-1}. After dialysis against ultrapure water in a 1 kg mol^{-1} dialysis bag (Spectra/Por, Spectrum Laboratories Inc.) for 5 days, the obtained dispersion was subjected to bath sonication for 10 min.

Transfer of SWCNTs to ssDNA

For coating of pristine (6,5) SWCNTs with ssDNA, a protocol by Ackermann et al. was applied[57]. SWCNT dispersions (5 mL, OD at E_{11} = 1 cm^{-1}) were mixed with 500 μL of $(GT)_6$ ssDNA (Sigma-Aldrich, 2 mg mL^{-1}) in phosphate buffered saline (1× PBS, Carl Roth) and dialyzed against PBS for 4 days (1 kg mol^{-1} dialysis bag, Spectra/Por, Spectrum Laboratories Inc.). Following centrifugation at 20,000 × *g* for 20 min (Hettich Micro 220 R), the supernatant was used without further treatment.

Photocatalytic SWCNT functionalization in dispersion

Photocatalytic functionalization of aqueous SWCNT dispersions was carried out in standard borosilicate glassware. Typically, 4 mL screw cap vials were employed as reaction vessels. SWCNT dispersions were adjusted to a SDS concentration of 0.33% (w/v), followed by addition of appropriate amounts of a fresh stock solution of sodium anthraquinone-2-sulfonate (AQS, 1 mg mL^{-1}, Sigma-Aldrich, ≥ 98.0%) to achieve a final concentration of 6 μM. The reaction mixture was irradiated with UV-light (365 nm, 1.3 mW mm^{-2}, Thorlabs SOLIS-365C) until the desired defect density was reached. Spin-filtration (Amicon Ultra-4, 100 kg mol^{-1}) was employed for removal of AQS and transfer of functionalized SWCNTs to different surfactants (e.g., 1% (w/v) DOC for long-term storage).

The photocatalytic functionalization of PFO-BPy-wrapped (6,5) SWCNTs in THF was carried out similarly using 2-*tert*-butylanthraquinone (Sigma-Aldrich, ≥ 98.0%) at a final concentration of 10 μM in the reaction mixture. Before functionalization, the content of free PFO-BPy polymer in the dispersion was reduced by filtration of toluene dispersions of (6,5) SWCNTs through PTFE membranes (Millipore

JVWP, pore size 0.1 μm) and redispersion of the filter cake by bath sonication (20 min) in fresh THF.

Photocatalytic functionalization of SWCNT thin films

Thin films of (6,5) SWCNTs were prepared by spin-coating (3 × 80 μL, 2000 rpm, 30 s) of highly concentrated dispersions of PFO-BPy-wrapped (6,5) SWCNTs in toluene (OD at $E_{11} \approx 8\,cm^{-1}$) onto BCB-passivated glass or Si/SiO_2 substrates[68], with washing (THF, isopropanol) and annealing steps (100 °C, 1 min) in-between.

Photocatalytic functionalization was performed by placement of a shadow mask above the thin film, followed by a droplet of an aqueous AQS solution (2 mg mL^{-1}). The desired functionalization density was controlled by varying the duration of UV-light irradiation (365 nm, 1.9 mW mm^{-2}, Thorlabs SOLIS-365C). Following removal of the shadow mask, the substrate was gently washed with ultrapure water and blow-dried with nitrogen.

UV-Vis-NIR absorption spectroscopy

Baseline-corrected UV-Vis-NIR absorption spectra were acquired with a Cary 6000i UV-Vis-NIR absorption spectrometer (Varian Inc.). A background $S(\lambda) = S_0 e^{-b\lambda}$ was subtracted from absorption spectra to account for scattering[76,77].

Raman spectroscopy

Raman spectra were recorded using a Renishaw inVia Reflex confocal Raman microscope in backscattering configuration equipped with a 50× long-working distance objective (Olympus, N.A. 0.5). For the determination of D/G^+ and IFM/RBM ratios, samples were prepared by drop casting of SWCNT dispersions onto glass slides (Schott AF32eco) and careful washing with ultrapure water for surfactant removal. Over 3000 individual spectra were recorded and averaged for each sample under 532 nm (D/G spectral region) or 785 nm (RBM region) laser excitation.

Atomic force microscopy

Atomic force microscope (AFM) images were acquired with a Bruker Dimension Icon AFM under ambient conditions. For AFM images of SWCNT thin films, the instrument was operated in ScanAsyst mode, whereas AFM images for SWCNT length statistics were recorded in tapping mode. Samples for SWCNT length statistics were prepared by incubation of Si/SiO_2 substrates with aqueous poly-L-lysine hydrobromide (PLL, 0.1 g L^{-1}) for 10 min, followed by rinsing with ultrapure water. Diluted SWCNT dispersions (OD at $E_{11} = 0.1\,cm^{-1}$) were placed on the PLL-covered Si/SiO_2 substrate for 10 min, followed by removal of the droplet and rinsing with ultrapure water.

Photoluminescence spectroscopy (laser excitation)

For excitation power-dependent PL, PL lifetime, and PLQY measurements, a home-built setup was used as detailed in the following.

Excitation-power dependent PL

For PL measurements at different excitation power, the wavelength-filtered output (570 nm) of a picosecond pulsed supercontinuum laser (NKT Photonics SuperK Extreme) was focused onto the sample with a 50× NIR-optimized objective (Olympus, N.A 0.65). Emitted light passed through a dichroic mirror (875 nm) and was guided through a long-pass filter (830 nm) to reject scattered laser light. An Acton SpectraPro SP2358 spectrograph (grating blaze 1200 nm, 150 lines mm^{-1}) coupled to a liquid nitrogen-cooled InGaAs line camera (Princeton Instruments, OMAV:1024) was used for spectra acquisition.

PL lifetime measurements

Wavelength-resolved PL lifetime measurements were conducted in a time-correlated single-photon counting (TCSPC) scheme, and the output of the spectrograph was focused onto a gated InGaAs/InP avalanche photodiode (Micro Photon Devices) using a NIR-optimized 20× objective (Mitutoyo, NA 0.4). TCSPC histograms were obtained with a photon-counting module (PicoQuant PicoHarp 300) and biexponential reconvolution-based fits were used to fit the SWCNT E_{11}^* PL decay (SymPhoTime 64 software). The instrument-limited E_{11} excitonic decay in (6,5) SWCNT thin films was used to obtain the instrument response function.

PL quantum yield determination

Spectrally-resolved PL quantum yields (PLQYs) of pristine and functionalized SWCNTs were obtained with an absolute method employing an integrating sphere[34,49]. The PLQY was determined as the ratio of emitted (N_{em}) to absorbed photons (N_{abs}):

$$\eta = \frac{N_{em}}{N_{abs}} \tag{1}$$

A quartz glass cuvette (Hellma Analytics, QX) was filled with 1 mL of the analyte (solvent or SWCNT dispersion, OD at $E_{11} < 0.2\,cm^{-1}$) and centered in an integrating sphere (LabSphere, Spectralon coating). Samples were excited at the respective SWCNT E_{22} transition and the light exiting the integrating sphere was guided into the spectrometer with an optical fiber. Light absorption and scattering by the solvent were corrected for by repetition of the sample measurements using only the solvent. Integration of emission spectra yielded a value proportional to N_{em}. By subtracting the integrated attenuated laser signals of the sample and the pure solvent, values proportional to N_{abs} were obtained. A stabilized tungsten halogen light source with known spectral power distribution (Thorlabs SLS201/M, 300 – 2600 nm) was employed for correction of the wavelength-dependent detection efficiency of the detector and absorption characteristics of optical components.

Low-temperature single-nanotube PL spectroscopy

Low-temperature PL spectroscopy of individual SWCNTs was performed at 4.6 K in a closed-cycle liquid helium-cooled optical cryostat (Montana Instruments, Cryostation s50). Samples were prepared by dilution of oxygen-functionalized (6,5) SWCNT dispersions in THF to an optical density of 0.005 cm^{-1} at the E_{11} transition with a solution of polystyrene (PS, Polymer Source Inc., $M_W = 230$ kg mol^{-1}) to achieve a final PS concentration of 20 g L^{-1}. Spin coating (2000 rpm, 60 s) onto glass substrates coated with a thermally-evaporated layer of gold (150 nm) yielded individualized SWCNTs in a polymer matrix.

For acquisition of single-nanotube PL spectra, the output of a continuous wave laser diode (Coherent Inc., OBIS 640 nm, 1 mW) was focused onto the sample plane with a NIR-optimized 50× long-working distance objective (Mitutoyo, N.A. 0.42). Scattered laser light was rejected by placement of appropriate long-pass filters. The emitted light was guided to a grating spectrograph (Princeton Instruments, IsoPlane SCT-320, grating blaze 1200 nm, 85 grooves mm^{-1}). PL spectra were recorded with a thermoelectrically-cooled two-dimensional InGaAs camera array (Princeton Instruments, NIRvana 640ST). A custom script was employed for automated collection of PL spectra using a piezo-based nanopositioning system (Attocube ANC350, equipped with ANPx101 and ANPz102 nanopositioners).

Photoluminescence spectroscopy and PLE mapping (lamp excitation)

Photoluminescence (PL) spectra and PL excitation-emission (PLE) maps were recorded with a Fluorolog-3 spectrometer (Horiba Jobin-Yvon) equipped with a liquid nitrogen-cooled InGaAs line camera (Symphony II) and a xenon arc-discharge light source (450 W). A Peltier-based temperature controller was used to perform

temperature-dependent PL measurements of liquid samples between 283 and 328 K.

NIR PL imaging

PL images of SWCNT dispersions in the NIR (950–1600 nm) were recorded with a thermoelectrically-cooled InGaAs camera (Xenics XEVA-CL-TE3, 252 × 320 pixels) under excitation with LED light sources (Thorlabs SOLIS-365C or SOLIS-525C). Emitted light was guided through a long-pass filter (950 nm) and focused onto the 2D focal plane array using a tube lens.

Circular dichroism spectroscopy

Baseline-corrected UV-Vis-NIR circular dichroism (CD) and corresponding absorption spectra of pristine and oxygen-functionalized dispersions of SWCNT enantiomers were recorded with a JASCO J-1700 CD spectrometer at a scanning speed of 50 nm min^{-1}.

Reporting summary

Further information on research design is available in the Nature Portfolio Reporting Summary linked to this article.

Data availability

The data that support the findings of this study are available from the heiDATA repository[78] and from the corresponding author upon request. Source data are provided with this paper.

References

1. Sercel, P. C., Hautzinger, M. P., Song, R., Blum, V. & Beard, M. C. Optical activity of chiral excitons. *Adv. Mater.* **37**, e2415901 (2025).
2. Purcell-Milton, F. et al. Induction of chirality in two-dimensional nanomaterials: chiral 2D MoS_2 nanostructures. *ACS Nano* **12**, 954–964 (2018).
3. Scuri, G. et al. Electrically tunable valley dynamics in twisted WSe_2/WSe_2 bilayers. *Phys. Rev. Lett.* **124**, 217403 (2020).
4. Long, G. et al. Chiral-perovskite optoelectronics. *Nat. Rev. Mater.* **5**, 423–439 (2020).
5. Koperski, M. et al. Single photon emitters in exfoliated WSe_2 structures. *Nat. Nanotechnol.* **10**, 503–506 (2015).
6. Li, Z. et al. Breakdown of the Nernst–Einstein relation in carbon nanotube porins. *Nat. Nanotechnol.* **18**, 177–183 (2023).
7. Tang, D.-M. et al. Semiconductor nanochannels in metallic carbon nanotubes by thermomechanical chirality alteration. *Science* **374**, 1616–1620 (2021).
8. Ovvyan, A. P. et al. An electroluminescent and tunable cavity-enhanced carbon-nanotube-emitter in the telecom band. *Nat. Commun.* **14**, 3933 (2023).
9. Zorn, N. F., Settele, S., Sebastian, F. L., Lindenthal, S. & Zaumseil, J. Tuning electroluminescence from functionalized SWCNT networks further into the near-infrared. *ACS Appl. Opt. Mater.* **1**, 1706–1714 (2023).
10. Li, M.-K., Dehm, S., Kappes, M. M., Hennrich, F. & Krupke, R. Correlation measurements for carbon nanotubes with quantum defects. *ACS Nano* **18**, 9525–9534 (2024).
11. He, X. et al. Carbon nanotubes as emerging quantum-light sources. *Nat. Mater.* **17**, 663–670 (2018).
12. Antonucci, A. et al. Carbon nanotube uptake in cyanobacteria for near-infrared imaging and enhanced bioelectricity generation in living photovoltaics. *Nat. Nanotechnol.* **17**, 1111–1119 (2022).
13. Mandal, A. K. et al. Fluorescent sp^3 defect-tailored carbon nanotubes enable NIR-II single particle imaging in live brain slices at ultra-low excitation doses. *Sci. Rep.* **10**, 5286 (2020).
14. Paviolo, C. et al. Near-infrared carbon nanotube tracking reveals the nanoscale extracellular space around synapses. *Nano Lett.* **22**, 6849–6856 (2022).
15. Ackermann, J., Metternich, J. T., Herbertz, S. & Kruss, S. Biosensing with fluorescent carbon nanotubes. *Angew. Chem. Int. Ed.* **61**, e202112372 (2022).
16. Settele, S. et al. Ratiometric fluorescent sensing of pyrophosphate with sp^3-functionalized single-walled carbon nanotubes. *Nat. Commun.* **15**, 706 (2024).
17. Wei, X. et al. Recent advances in structure separation of single-wall carbon nanotubes and their application in optics, electronics, and optoelectronics. *Adv. Sci.* **9**, 2200054 (2022).
18. Wei, X. et al. Experimental determination of excitonic band structures of single-walled carbon nanotubes using circular dichroism spectra. *Nat. Commun.* **7**, 12899 (2016).
19. Li, H. et al. Isolation of the (6,5) single-wall carbon nanotube enantiomers by surfactant-assisted aqueous two-phase extraction. *Carbon* **204**, 475–483 (2023).
20. Green, A. A., Duch, M. C. & Hersam, M. C. Isolation of single-walled carbon nanotube enantiomers by density differentiation. *Nano Res.* **2**, 69–77 (2009).
21. Xu, L. et al. Enantiomeric separation of semiconducting single-walled carbon nanotubes by acid cleavable chiral polyfluorene. *ACS Nano* **15**, 4699–4709 (2021).
22. Wei, X. et al. High-yield and high-throughput single-chirality enantiomer separation of single-wall carbon nanotubes. *Carbon* **132**, 1–7 (2018).
23. Wei, X. et al. Length-dependent enantioselectivity of carbon nanotubes by gel chromatography. *ACS Nano* **17**, 8393–8402 (2023).
24. De los Santos, Z. A., Lin, Z. & Zheng, M. Optical detection of stereoselective interactions with DNA-wrapped single-wall carbon nanotubes. *J. Am. Chem. Soc.* **143**, 20628–20632 (2021).
25. Magg, M., Kadria-Vili, Y., Oulevey, P., Weisman, R. B. & Bürgi, T. Resonance Raman optical activity spectra of single-walled carbon nanotube enantiomers. *J. Phys. Chem. Lett.* **7**, 221–225 (2016).
26. Zheng, Y., Bachilo, S. M. & Weisman, R. B. Enantiomers of single-wall carbon nanotubes show distinct coating displacement kinetics. *J. Phys. Chem. Lett.* **9**, 3793–3797 (2018).
27. Ghosh, S., Bachilo, S. M., Simonette, R. A., Beckingham, K. M. & Weisman, R. B. Oxygen doping modifies near-infrared band gaps in fluorescent single-walled carbon nanotubes. *Science* **330**, 1656–1659 (2010).
28. Piao, Y. et al. Brightening of carbon nanotube photoluminescence through the incorporation of sp^3 defects. *Nat. Chem.* **5**, 840–845 (2013).
29. Zaumseil, J. Luminescent defects in single-walled carbon nanotubes for applications. *Adv. Opt. Mater.* **10**, 2101576 (2022).
30. Lin, C.-W. et al. Creating fluorescent quantum defects in carbon nanotubes using hypochlorite and light. *Nat. Commun.* **10**, 2874 (2019).
31. Settele, S. et al. Easy access to bright oxygen defects in biocompatible single-walled carbon nanotubes via a Fenton-like reaction. *ACS Nano* **18**, 20667–20678 (2024).
32. Berger, F. J. et al. Brightening of long, polymer-wrapped carbon nanotubes by sp^3 functionalization in organic solvents. *ACS Nano* **13**, 9259–9269 (2019).
33. Hartmann, N. F. et al. Photoluminescence dynamics of aryl sp^3 defect states in single-walled carbon nanotubes. *ACS Nano* **10**, 8355–8365 (2016).
34. Sebastian, F. L. et al. Absolute quantification of sp^3 defects in semiconducting single-wall carbon nanotubes by Raman spectroscopy. *J. Phys. Chem. Lett.* **13**, 3542–3548 (2022).
35. Danné, N. et al. Ultrashort carbon nanotubes that fluoresce brightly in the near-infrared. *ACS Nano* **12**, 6059–6065 (2018).
36. Welsher, K. et al. A route to brightly fluorescent carbon nanotubes for near-infrared imaging in mice. *Nat. Nanotechnol.* **4**, 773–780 (2009).

37. Ma, X., Hartmann, N. F., Baldwin, J. K. S., Doorn, S. K. & Htoon, H. Room-temperature single-photon generation from solitary dopants of carbon nanotubes. *Nat. Nanotechnol.* **10**, 671–675 (2015).
38. Settele, S. et al. Synthetic control over the binding configuration of luminescent sp^3-defects in single-walled carbon nanotubes. *Nat. Commun.* **12**, 2119 (2021).
39. Gifford, B. J., Kilina, S., Htoon, H., Doorn, S. K. & Tretiak, S. Exciton localization and optical emission in aryl-functionalized carbon nanotubes. *J. Phys. Chem. C.* **122**, 1828–1838 (2018).
40. Marzo, L., Pagire, S. K., Reiser, O. & König, B. Visible-light photocatalysis: does it make a difference in organic synthesis?. *Angew. Chem. Int. Ed.* **57**, 10034–10072 (2018).
41. Zhang, W., Gacs, J., Arends, I. W. C. E. & Hollmann, F. Selective photooxidation reactions using water-soluble anthraquinone photocatalysts. *ChemCatChem* **9**, 3821–3826 (2017).
42. Vibbert, H. B., Bendel, C., Norton, J. R. & Moment, A. J. On-demand photochemical synthesis of hydrogen peroxide from alkylated anthraquinones. *ACS Sustain. Chem. Eng.* **10**, 11106–11116 (2022).
43. Cervantes-González, J. et al. Anthraquinones: versatile organic photocatalysts. *ChemCatChem* **12**, 3811–3827 (2020).
44. Clark, K. P. & Stonehill, H. I. Photochemistry and radiation chemistry of 9,10-anthraquinone-2-sodium sulphonate in aqueous solution. Part 2. - Photochemical products. *J. Chem. Soc. Faraday Trans.* **68**, 1676–1686 (1972).
45. Loeff, I., Treinin, A. & Linschitz, H. Photochemistry of 9,10-anthraquinone-2-sulfonate in solution. 1. Intermediates and mechanism. *J. Phys. Chem.* **87**, 2536–2544 (1983).
46. Maddigapu, P. R. et al. The pH-dependent photochemistry of anthraquinone-2-sulfonate. *Photochem. Photobiol. Sci.* **9**, 323–330 (2010).
47. Espinoza, V. B., Bachilo, S. M., Zheng, Y., Htoon, H. & Weisman, R. B. Complexity in the photofunctionalization of single-wall carbon nanotubes with hypochlorite. *ACS Nano* **19**, 2497–2506 (2025).
48. Chu, L. & Anastasio, C. Formation of hydroxyl radical from the photolysis of frozen hydrogen peroxide. *J. Phys. Chem. A* **109**, 6264–6271 (2005).
49. Graf, A. et al. Large scale, selective dispersion of long single-walled carbon nanotubes with high photoluminescence quantum yield by shear force mixing. *Carbon* **105**, 593–599 (2016).
50. Sebastian, F. L., Settele, S., Li, H., Flavel, B. S. & Zaumseil, J. How to recognize clustering of luminescent defects in single-wall carbon nanotubes. *Nanoscale Horiz.* **9**, 2286–2294 (2024).
51. Ma, X. et al. Electronic structure and chemical nature of oxygen dopant states in carbon nanotubes. *ACS Nano* **8**, 10782–10789 (2014).
52. Sebastian, F. L. et al. Unified quantification of quantum defects in small-diameter single-walled carbon nanotubes by Raman spectroscopy. *ACS Nano* **17**, 21771–21781 (2023).
53. Kim, M. et al. Fluorescent carbon nanotube defects manifest substantial vibrational reorganization. *J. Phys. Chem. C.* **120**, 11268–11276 (2016).
54. Fagan, J. A. et al. Analyzing surfactant structures on length and chirality resolved (6,5) single-wall carbon nanotubes by analytical ultracentrifugation. *ACS Nano* **7**, 3373–3387 (2013).
55. Yomogida, Y., Tanaka, T., Tsuzuki, M., Wei, X. & Kataura, H. Automatic sorting of single-chirality single-wall carbon nanotubes using hydrophobic cholates: implications for multicolor near-infrared optical technologies. *ACS Appl. Nano Mater.* **3**, 11289–11297 (2020).
56. Kim, M. et al. Mapping structure-property relationships of organic color centers. *Chem* **4**, 2180–2191 (2018).
57. Ackermann, J. et al. High sensitivity near-infrared imaging of fluorescent nanosensors. *Small* **19**, 2206856 (2023).
58. Bisker, G. et al. Protein-targeted corona phase molecular recognition. *Nat. Commun.* **7**, 10241 (2016).
59. Lei, K., Bachilo, S. M. & Weisman, R. B. Kinetics of single-wall carbon nanotube coating displacement by single-stranded DNA depends on nanotube structure. *ACS Nano* **17**, 17568–17575 (2023).
60. Basu, S., Hendler-Neumark, A. & Bisker, G. Role of oxygen defects in eliciting a divergent fluorescence response of single-walled carbon nanotubes to dopamine and serotonin. *ACS Nano* **18**, 34134–34146 (2024).
61. Basu, S., Hendler-Neumark, A. & Bisker, G. Ratiometric normalization of near-infrared fluorescence in defect-engineered single-walled carbon nanotubes for cholesterol detection. *J. Phys. Chem. Lett.* **15**, 10425–10434 (2024).
62. Hemmer, E., Benayas, A., Légaré, F. & Vetrone, F. Exploiting the biological windows: current perspectives on fluorescent bioprobes emitting above 1000 nm. *Nanoscale Horiz.* **1**, 168–184 (2016).
63. Li, Y. et al. Fluorescent ultrashort nanotubes from defect-induced chemical cutting. *Chem. Mater.* **31**, 4536–4544 (2019).
64. Rother, M. et al. Aerosol-jet printing of polymer-sorted (6,5) carbon nanotubes for field-effect transistors with high reproducibility. *Adv. Electron. Mater.* **3**, 1700080 (2017).
65. Lu, S. et al. Flexible, print-in-place 1D–2D thin-film transistors using aerosol jet printing. *ACS Nano* **13**, 11263–11272 (2019).
66. Mitroka, S., Zimmeck, S., Troya, D. & Tanko, J. M. How solvent modulates hydroxyl radical reactivity in hydrogen atom abstractions. *J. Am. Chem. Soc.* **132**, 2907–2913 (2010).
67. Wieland, S., El Yumin, A. A., Settele, S. & Zaumseil, J. Photo-activated, solid-state introduction of luminescent oxygen defects into semiconducting single-walled carbon nanotubes. *J. Phys. Chem. C.* **128**, 2012–2021 (2024).
68. Zorn, N. F. et al. Near-intrinsic photo- and electroluminescence from single-walled carbon nanotube thin films on BCB-passivated surfaces. *Adv. Opt. Mater.* **11**, 2300236 (2023).
69. Abendroth, J. M. et al. Spin selectivity in photoinduced charge-transfer mediated by chiral molecules. *ACS Nano* **13**, 4928–4946 (2019).
70. Wada, N. et al. Efficient and chiral electroluminescence from in-plane heterostructure of transition metal dichalcogenide monolayers. *Adv. Funct. Mater.* **32**, 2203602 (2022).
71. Wei, X., Tanaka, T., Hirakawa, T., Yomogida, Y. & Kataura, H. Determination of enantiomeric purity of single-wall carbon nanotubes using flavin mononucleotide. *J. Am. Chem. Soc.* **139**, 16068–16071 (2017).
72. Nguyen, D. T. et al. Elastic exciton-exciton scattering in photoexcited carbon nanotubes. *Phys. Rev. Lett.* **107**, 127401 (2011).
73. Miyauchi, Y. et al. Brightening of excitons in carbon nanotubes on dimensionality modification. *Nat. Photonics* **7**, 715–719 (2013).
74. Gifford, B. J., Kilina, S., Htoon, H., Doorn, S. K. & Tretiak, S. Controlling defect-state photophysics in covalently functionalized single-walled carbon nanotubes. *Acc. Chem. Res.* **53**, 1791–1801 (2020).
75. Yomogida, Y. et al. Industrial-scale separation of high-purity single-chirality single-wall carbon nanotubes for biological imaging. *Nat. Commun.* **7**, 12056 (2016).
76. Pfohl, M. et al. Fitting single-walled carbon nanotube optical spectra. *ACS Omega* **2**, 1163–1171 (2017).
77. Naumov, A. V., Ghosh, S., Tsyboulski, D. A., Bachilo, S. M. & Weisman, R. B. Analyzing absorption backgrounds in single-walled carbon nanotube spectra. *ACS Nano* **5**, 1639–1648 (2011).
78. Sebastian, F. L. et al. Circular dichroism of quantum defects in carbon nanotubes created by photocatalytic oxygen functionalization. *heiDATA*, https://doi.org/10.11588/DATA/BTVHDH (2025).

Acknowledgements

This project has received funding from the European Research Council (ERC) under the European Union's Horizon 2020 research and innovation programme (Grant Agreement No. 817494 "TRIFECTs", F.L.S., S.L., J.Z.).

B.S.F. acknowledges support by the Helmholtz Research Programs Natural Artificial and Cognitive Information Processing (NACIP) and Materials Systems Engineering (MSE). H.L. gratefully acknowledges support from the Turku Collegium for Science, Medicine and Technology (TCSMT, Starttiraha 26005020). Y.Y. acknowledges support from JSPS KAKENHI through Grant Nos. JP22H05468, JP22H01911, and JST FOREST No. JPMJFR235Z, and from Konica Minolta Imaging Science Foundation and Iketani Science and Technology Foundation, Japan. K.Y. acknowledges support from JSPS KAKENHI through Grant Nos. JP21H05017, JP23H00259, and JP24H01200, international joint research program (JPJSBP120252302) and U.S.-JAPAN PIRE through Grant No. JPJSJRP20221202, Japan. K.Y. and J.Z. acknowledge support by the ASPIRE-EXAR project through Grant No. JPMJAP2310, Japan. The authors acknowledge financial support by Heidelberg University for open access fees.

Author contributions

F.L.S. fabricated samples, performed all measurements, and analyzed the data. L.K. and C.B. prepared selected samples and contributed to the development of the functionalization method. Y.Y. and Y.H. prepared enantiomer-separated (6,5) SWCNTs and other nanotube chirality dispersions under supervision of K.Y. H.L. and B.S.F. performed ATPE and provided (6,5) SWCNT dispersions in water. S.L. contributed to Raman measurements of SWCNT thin films. J.Z. conceived and supervised the project. F.L.S. and J.Z. wrote the manuscript with input from all authors.

Funding

Open Access funding enabled and organized by Projekt DEAL.

Competing interests

The authors declare no competing interests.

Additional information

Supplementary information The online version contains supplementary material available at https://doi.org/10.1038/s41467-025-60342-y.

Correspondence and requests for materials should be addressed to Jana Zaumseil.

Peer review information *Nature Communications* thanks Sergei Tretiak and the other, anonymous, reviewer(s) for their contribution to the peer review of this work. A peer review file is available.

Reprints and permissions information is available at http://www.nature.com/reprints

Publisher's note Springer Nature remains neutral with regard to jurisdictional claims in published maps and institutional affiliations.

Open Access This article is licensed under a Creative Commons Attribution 4.0 International License, which permits use, sharing, adaptation, distribution and reproduction in any medium or format, as long as you give appropriate credit to the original author(s) and the source, provide a link to the Creative Commons licence, and indicate if changes were made. The images or other third party material in this article are included in the article's Creative Commons licence, unless indicated otherwise in a credit line to the material. If material is not included in the article's Creative Commons licence and your intended use is not permitted by statutory regulation or exceeds the permitted use, you will need to obtain permission directly from the copyright holder. To view a copy of this licence, visit http://creativecommons.org/licenses/by/4.0/.

© The Author(s) 2025

SUPPLEMENTARY INFORMATION

Circular dichroism of quantum defects in carbon nanotubes created by photocatalytic oxygen functionalization

Finn L. Sebastian[1], Leon Kaminski[1], Christoph Bendel[2], Yohei Yomogida[3], Yuuya Hosokawa[4], Han Li[5,6], Sebastian Lindenthal[1], Benjamin S. Flavel[7], Kazuhiro Yanagi[4], and Jana Zaumseil[1,]*

[1]Institute for Physical Chemistry, Universität Heidelberg, D-69120 Heidelberg, Germany

[2]Institute for Inorganic Chemistry, Universität Heidelberg, D-69120 Heidelberg, Germany

[3]Research Institute for Electronic Science, Hokkaido University, Sapporo, Hokkaido 001-0021, Japan

[4]Department of Physics, Tokyo Metropolitan University, Hachioji, Tokyo 192-0397, Japan

[5]Department of Mechanical and Materials Engineering, University of Turku, FI-20014 Turku, Finland

[6]Turku Collegium for Science, Medicine and Technology, University of Turku, FI-20520 Turku, Finland

[7]Institute of Nanotechnology, Karlsruhe Institute of Technology, D-76131 Karlsruhe, Germany

Corresponding author

*E-mail: zaumseil@uni-heidelberg.de

CONTENTS

Supplementary Figures **3**
Suppl. Fig. 1 | Characterization of pristine (6,5) SWCNTs **3**
Suppl. Fig. 2 | LED output and AQS absorption **4**
Suppl. Fig. 3 | SWCNT functionalization tracking **5**
Suppl. Fig. 4 | Reference experiments I **6**
Suppl. Fig. 5 | Reference experiments II **6**
Suppl. Fig. 6 | Raman spectroscopy of SWCNTs **7**
Suppl. Fig. 7 | TCSPC measurements **8**
Suppl. Fig. 8 | Excitation density-dependent PL **9**
Suppl. Fig. 9 | Temperature-dependent PL **10**
Suppl. Fig. 10 | Different surfactants **11**
Suppl. Fig. 11 | Absorption spectra of additional nanotube species **12**
Suppl. Fig. 12 | PLE maps of pristine SWCNTs **13**
Suppl. Fig. 13 | PLE maps of functionalized SWCNTs **14**
Suppl. Fig. 14 | Optical trap depths for different SWCNT species **15**
Suppl. Fig. 15 | SWCNT dispersions in PL-PEG **16**
Suppl. Fig. 16 | SWCNTs wrapped by ssDNA **17**
Suppl. Fig. 17 | Functionalization of CoMoCAT SWCNTs **18**
Suppl. Fig. 18 | Tip-sonicated SWCNTs **19**
Suppl. Fig. 19 | AFM length statistics **20**
Suppl. Fig. 20 | Organic solvent SWCNT dispersions **21**
Suppl. Fig. 21 | PLE maps of organic solvent SWCNT dispersions **22**
Suppl. Fig. 22 | Treatment of (6,5) SWCNTs with *t*-Bu-AQ in toluene **23**
Suppl. Fig. 23 | Single-nanotube PL spectra at cryogenic temperature **24**
Suppl. Fig. 24 | Spatial resolution of film functionalization **25**
Suppl. Fig. 25 | Absorption spectra of SWCNT enantiomers **26**
Suppl. Fig. 26 | PLE maps of SWCNT enantiomers **27**
Suppl. Fig. 27 | UV-Vis CD spectra of functionalized SWCNTs **28**
Suppl. Fig. 28 | Raman spectra of SWCNT enantiomers **29**
Supplementary Note 1 ..... **30**
Supplementary References **32**

Supplementary Figures

Suppl. Fig. 1 | Characterization of pristine (6,5) SWCNTs

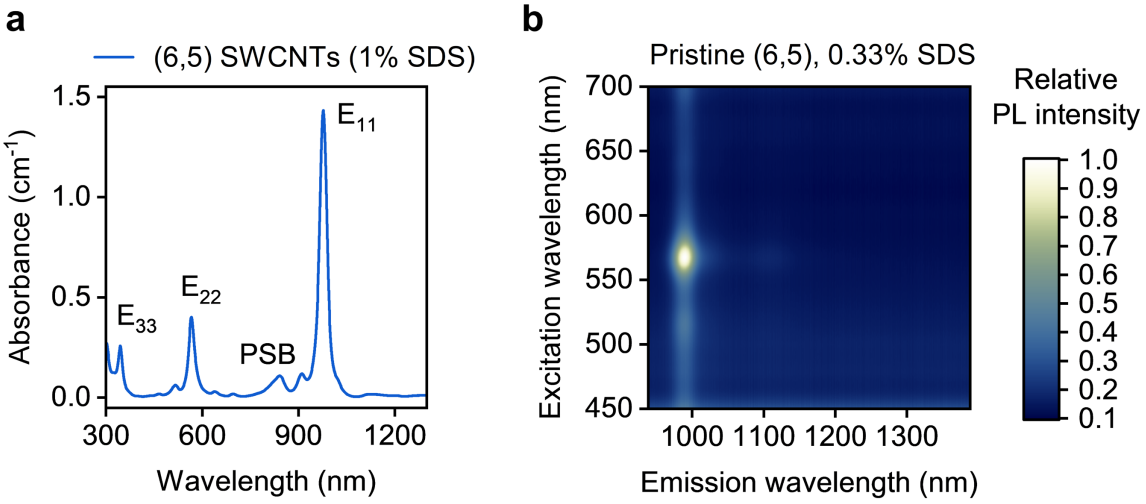

Supplementary Fig. 1 | Characterization of pristine (6,5) SWCNTs. a UV-Vis-NIR absorption spectrum of a pristine (6,5) SWCNT dispersion in H_2O (1% w/v SDS) and assignment of main absorption features (E_{ii} transitions and phonon side band (PSB)). **b** PL excitation-emission (PLE) map of a diluted dispersion (0.33% w/v SDS).

Suppl. Fig. 2 | LED output and AQS absorption

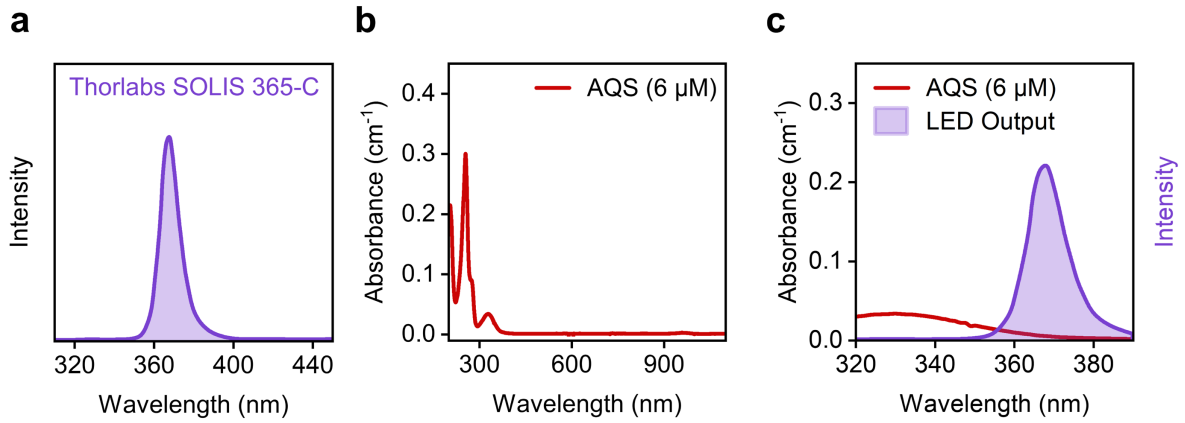

Supplementary Fig. 2 | LED output characteristics and UV-Vis absorption spectrum of AQS. **a** Spectral output of the LED employed for the photocatalytic functionalization reaction (Thorlabs SOLIS 365-C). **b** UV-Vis-NIR absorption spectrum of anthraquinone-2-sulfonate (AQS) at identical concentration as used for the functionalization of (6,5) SWCNTs in H_2O. **c** Overlay of the absorption spectrum of AQS and the spectral output of the LED (note that the scaling of the LED output intensity was chosen arbitrarily in reference to the absorption spectrum to highlight the spectral overlap).

Suppl. Fig. 3 | SWCNT functionalization tracking

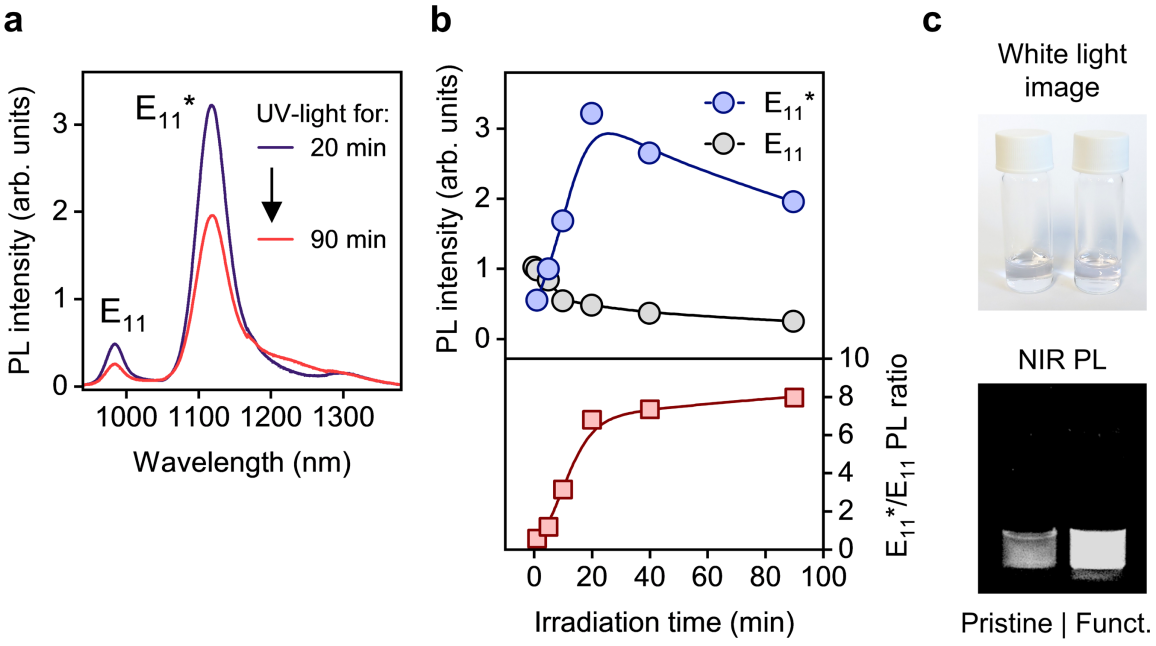

Supplementary Fig. 3 | Tracking of the photocatalytic functionalization reaction and NIR PL imaging. a Reduction in absolute PL intensity under further irradiation with UV-light (365 nm) after absolute E_{11}* PL emission intensity maximum was reached. **b** Evolution of the absolute and relative E_{11} and E_{11}* PL intensities with increasing duration of UV-light irradiation (lines are a guide to the eye). **c** White light image and NIR PL image (950 – 1600 nm, excitation with 525 nm LED) of pristine and functionalized (6,5) SWCNT dispersions (0.33% w/v SDS) at identical concentration.

Suppl. Fig. 4 | Reference experiments I

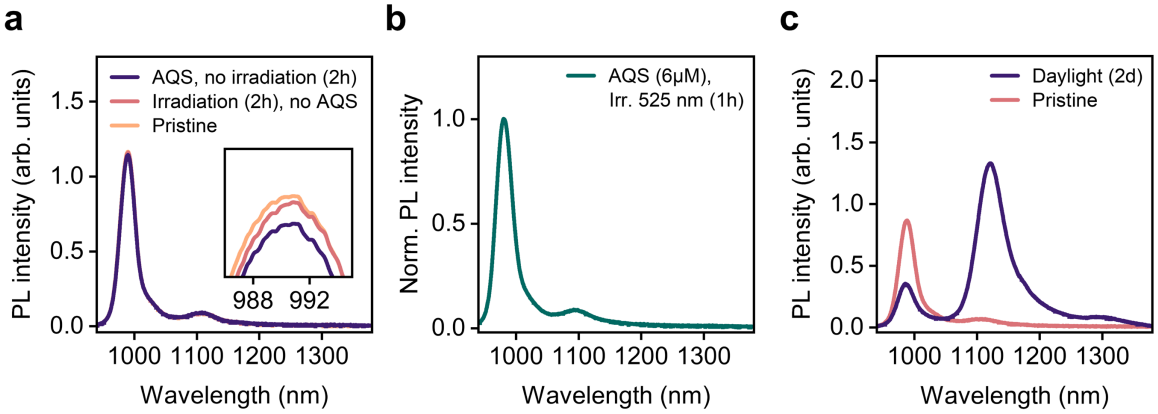

Supplementary Fig. 4 | a PL spectra of a pristine aqueous (6,5) SWCNT dispersion (0.33% w/v SDS), the same dispersion 2 h after addition of AQS (6 µM) but without irradiation, and dispersion 2 h after continuous irradiation (365 nm LED) but without prior addition of AQS. **b** PL spectrum of (6,5) SWCNT dispersion after addition of AQS (6 µM) and continuous irradiation with a 525 nm LED (Thorlabs SOLIS 525-C), showing no signs of functionalization. **c** Limited functionalization after exposure to daylight for 2 days (6 µM AQS).

Suppl. Fig. 5 | Reference experiments II

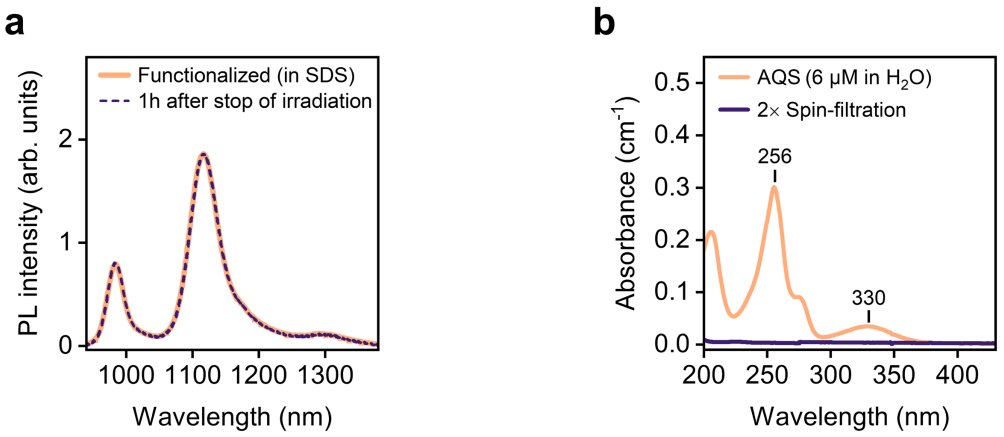

Supplementary Fig. 5 | a PL spectra of a functionalized (6,5) SWCNT dispersion (in 0.33% w/v SDS), directly after stopping UV-light irradiation and 1 h later. **b** UV-Vis absorption spectra of an aqueous AQS solution as it is used in the functionalization procedure (concentration 6 µM) and after the standard work-up of functionalized SWCNT dispersions (two consecutive rounds of spin-filtration), showing no residual AQS in the dispersion.

Suppl. Fig. 6 | Raman spectroscopy of SWCNTs

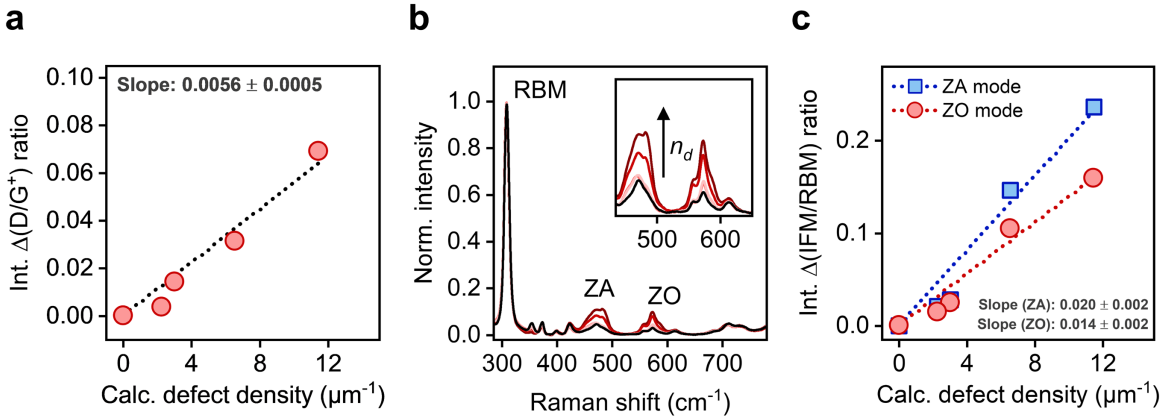

Supplementary Fig. 6 | Raman spectroscopy of pristine and functionalized (6,5) SWCNTs. **a** Correlation of integrated Raman $\Delta(D/G^+)$ ratios vs calculated defect density for functionalized (6,5) SWCNTs as depicted in Figure 1d (main text) and linear fit to the data (R^2 = 0.97). **b** Averaged and normalized Raman spectra of pristine and functionalized (6,5) SWCNTs in the RBM and IFM region (λ_{exc} = 785 nm). **c** Correlation of integrated Raman Δ(IFM/RBM) ratios vs calculated defect densities (linear fits to the data, R^2(ZA) = 0.97, R^2(ZO) = 0.97)[1,2].

Suppl. Fig. 7 | TCSPC measurements

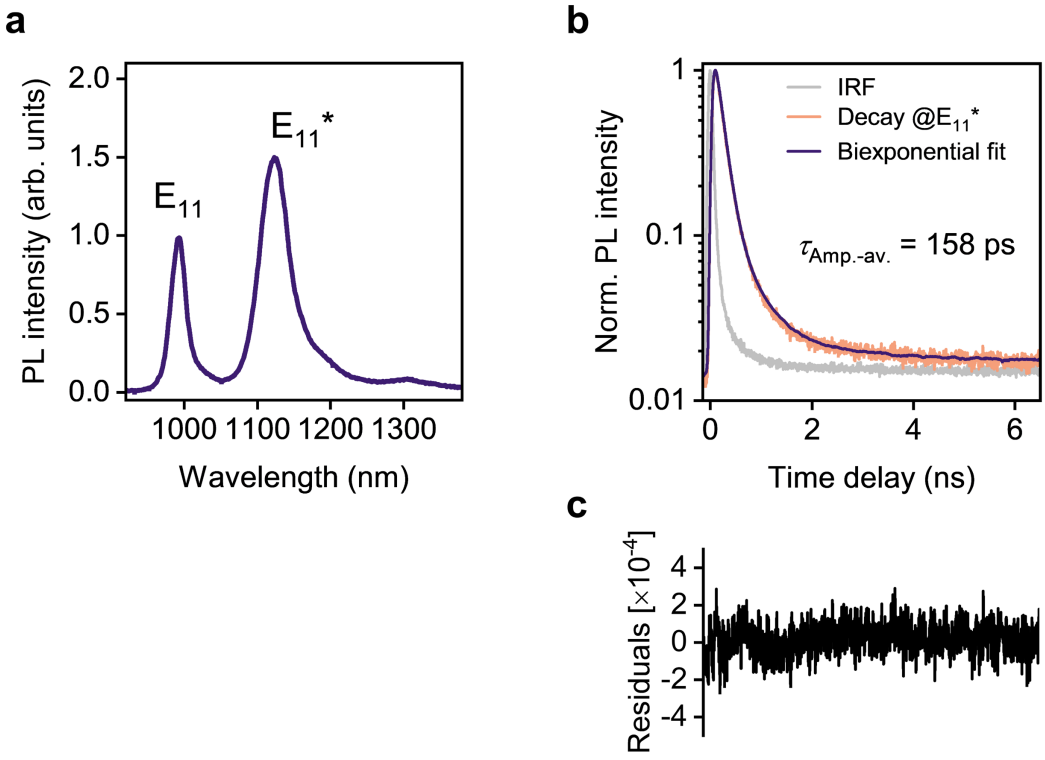

Supplementary Fig. 7 | Time-resolved photoluminescence measurements. a PL spectrum of aqueous (6,5) SWCNT dispersion used for time-resolved PL measurements. **b** TCSPC (time-correlated single-photon counting) histogram of the E_{11}* PL decay measured at 1120 nm (orange) and biexponential fit to the data (dark blue) according to Hartmann et al.[3] The instrument-limited decay of the E_{11} emission was used to obtain the instrument-response function (IRF, gray). An amplitude-averaged lifetime ($\tau_{Amp.-av.}$) of 158 ps was extracted. **c** Corresponding residuals of the biexponential fit from **b**.

Suppl. Fig. 8 | Excitation density-dependent PL

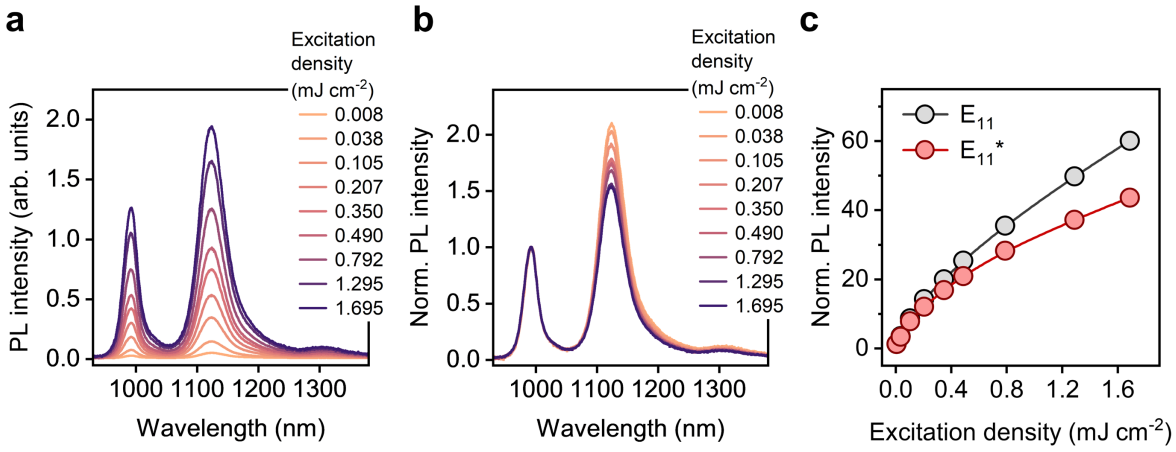

Supplementary Fig. 8 | Dependence of E_{11} and E_{11}* PL emission on excitation density. a PL spectra of oxygen-functionalized (6,5) SWCNTs (aqueous dispersion, 1% w/v DOC) at different laser excitation densities (pulsed excitation at E_{22}, λ_{exc} = 570 nm). **b** Normalized (to E_{11}) PL spectra at different laser excitation densities. **c** Intensities of E_{11} (gray) and E_{11}* (red) emission normalized to their respective value at the lowest laser excitation density, lines are guides to the eye.

Suppl. Fig. 9 | Temperature-dependent PL

The thermal detrapping energy ΔE_{therm} can be extracted from temperature-dependent PL measurements of functionalized SWCNTs using van't Hoff plots as introduced by Kim et al.[4] This analysis assumes reversibility of exciton trapping at defect sites if the thermal energy kT exceeds the depth of the defect state potential. Thus, the relative PL intensity of the E_{11} and E_{11}* emission exhibits a dependence on the temperature according to:

$$\frac{A_{E_{11}}}{A_{E_{11}^*}} \propto \exp\left(-\frac{\Delta E_{\text{therm}}}{\text{k}T}\right) \tag{2}$$

$$\ln\left(\frac{A_{E_{11}}}{A_{E_{11}^*}}\right) \propto -\frac{\Delta E_{\text{therm}}}{\text{k}T} + C \tag{3}$$

Integrated PL intensities are denoted by $A_{E_{11}}$and $A_{E_{11}^*}$; k is the Boltzmann constant, T the absolute temperature, and C is a correction factor. PL spectra of functionalized (6,5) SWCNTs were acquired in a temperature range from 283 K to 328 K in increments of 5 K. Integrated PL intensities were extracted from normalized spectra (see Suppl. Fig. 9a, b). A linear fit according to Equation (2) yields ΔE_{therm} = 102.4 meV (see Suppl. Fig. 9c).

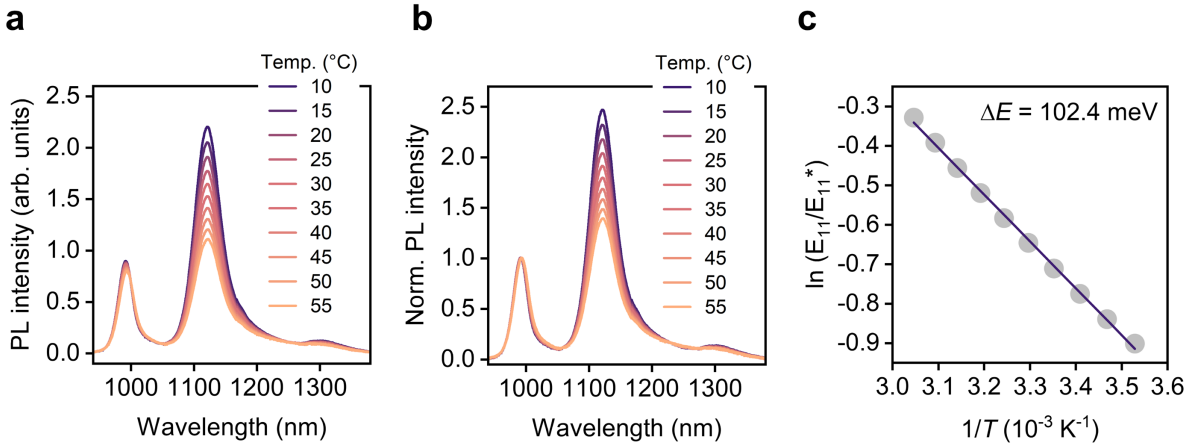

Supplementary Fig. 9 | Temperature-dependent photoluminescence measurements. **a** Temperature-dependent (283 K to 328 K) PL spectra of oxygen-functionalized (6,5) SWCNTs (aqueous dispersion, 1% w/v DOC). **b** Corresponding normalized (to E_{11}) PL spectra. **c** van't Hoff plot for the E_{11}* emissive state, linear fit to the data (R^2 = 0.99) and extraction of a thermal detrapping energy ΔE_{therm} = 102.4 meV.

Suppl. Fig. 10 | Different surfactants

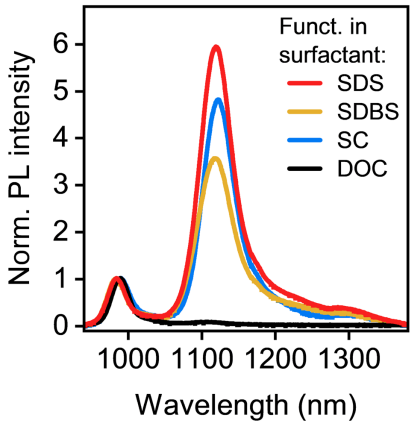

Supplementary Fig. 10 | Functionalization in dispersions with different surfactants. Photocatalytic functionalization (6 µM AQS, 20 min UV irradiation) of (6,5) SWCNTs stabilized by different surfactants (concentrations: SDS 0.33% (red), SDBS 0.33% (orange), SC 0.80% (blue), DOC 0.33% (black), all in (w/v)).

Suppl. Fig. 11 | Absorption spectra of additional nanotube species

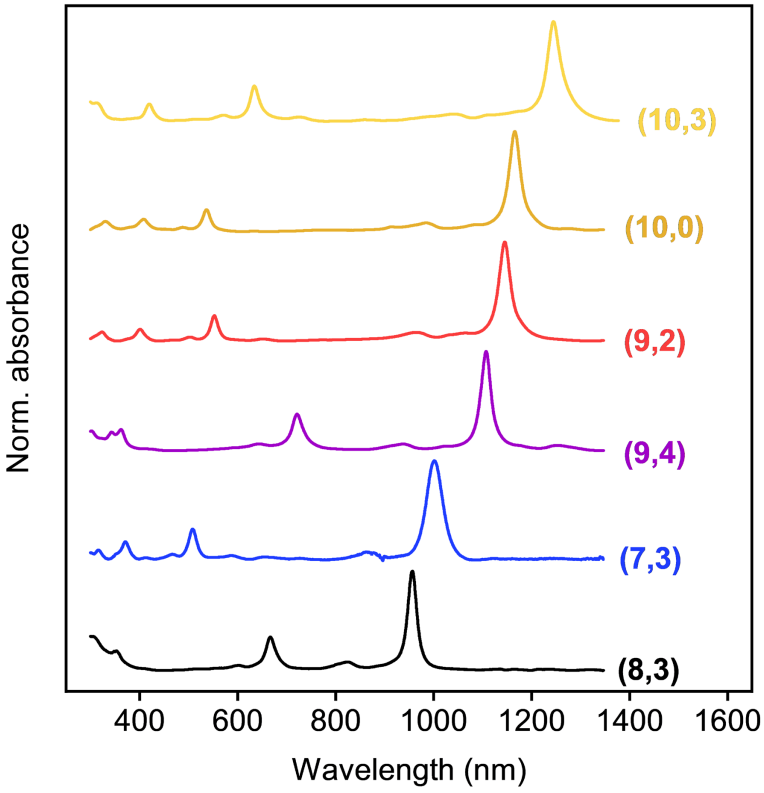

Supplementary Fig. 11 | Absorption spectra of different SWCNT species. UV-Vis-NIR absorption spectra of sorted (10,3), (10,0), (9,2), (9,4), (8,3), and (7,3) SWCNT dispersions before functionalization (in 0.33% w/v SDS). E_{22} optical transition wavelengths for optical excitation in PL spectroscopy were determined from the depicted spectra: (8,3) – 668 nm, (7,3) – 509 nm, (9,4) – 723 nm, (9,2) – 554 nm, (10,0) – 538 nm, (10,3) – 636 nm.

Suppl. Fig. 12 | PLE maps of pristine SWCNTs

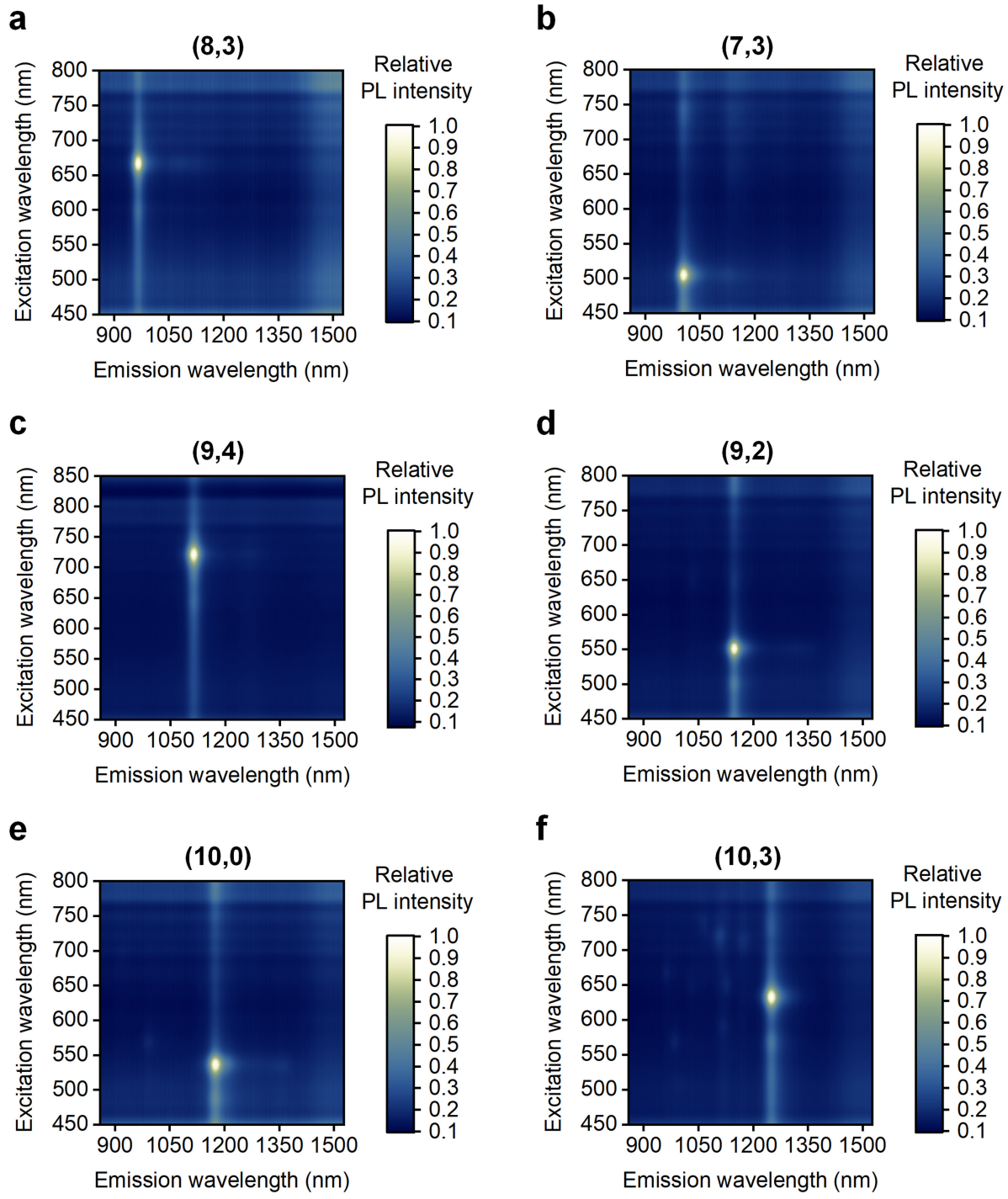

Supplementary Fig. 12 | PLE maps of different pristine SWCNT species. Aqueous dispersions (0.33% w/v SDS) of (8,3) (**a**), (7,3) (**b**), (9,4) (**c**), (9,2) (**d**), (10,0) (**e**), and (10,3) (**f**) SWCNTs.

Suppl. Fig. 13 | PLE maps of functionalized SWCNTs

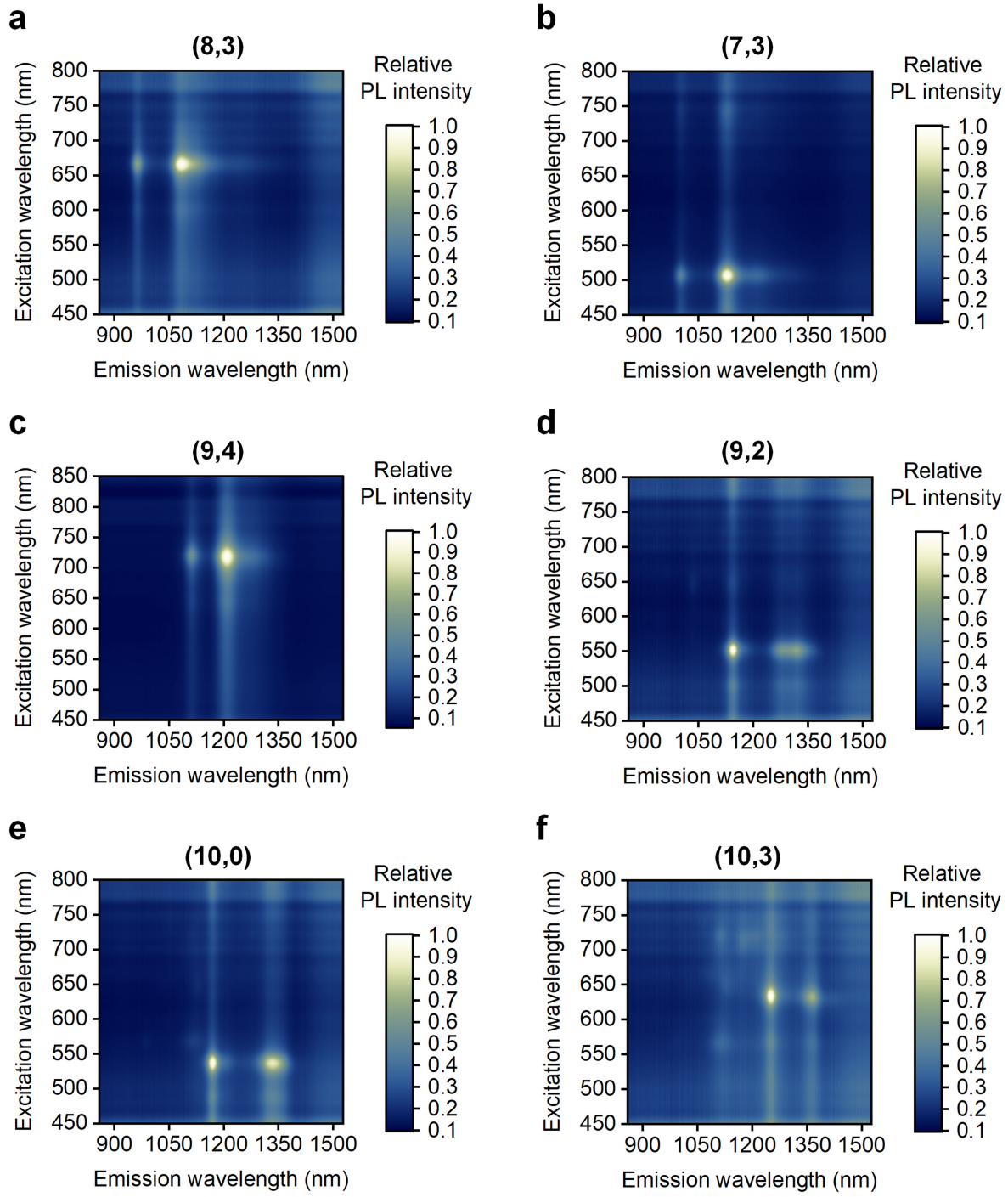

Supplementary Fig. 13 | PLE maps of different functionalized SWCNT species. Aqueous dispersions (0.2% w/v DOC) of (8,3) (**a**), (7,3) (**b**), (9,4) (**c**), (9,2) (**d**), (10,0) (**e**), and (10,3) (**f**) SWCNTs.

Suppl. Fig. 14 | Optical trap depths for different SWCNT species

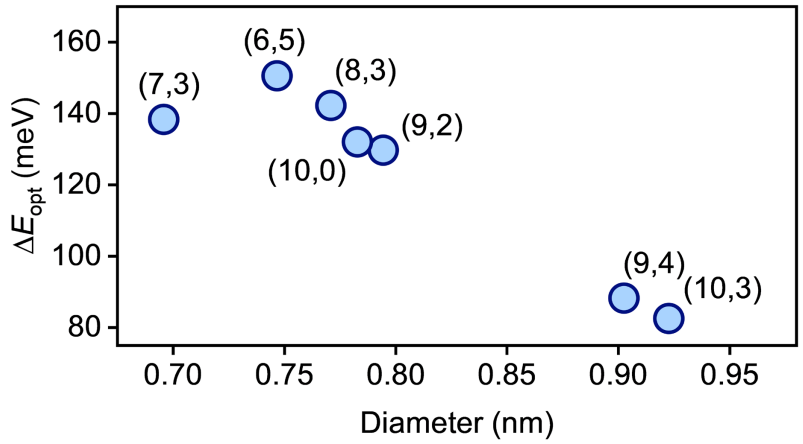

Supplementary Fig. 14 | Diameter dependence of optical trap depth. Optical trap depths ΔE_{opt} vs SWCNT diameter (data extracted from E_{11} and E_{11}* PL peaks of different oxygen-functionalized SWCNT species, see Fig. 2c, main text).

Suppl. Fig. 15 | SWCNT dispersions in PL-PEG

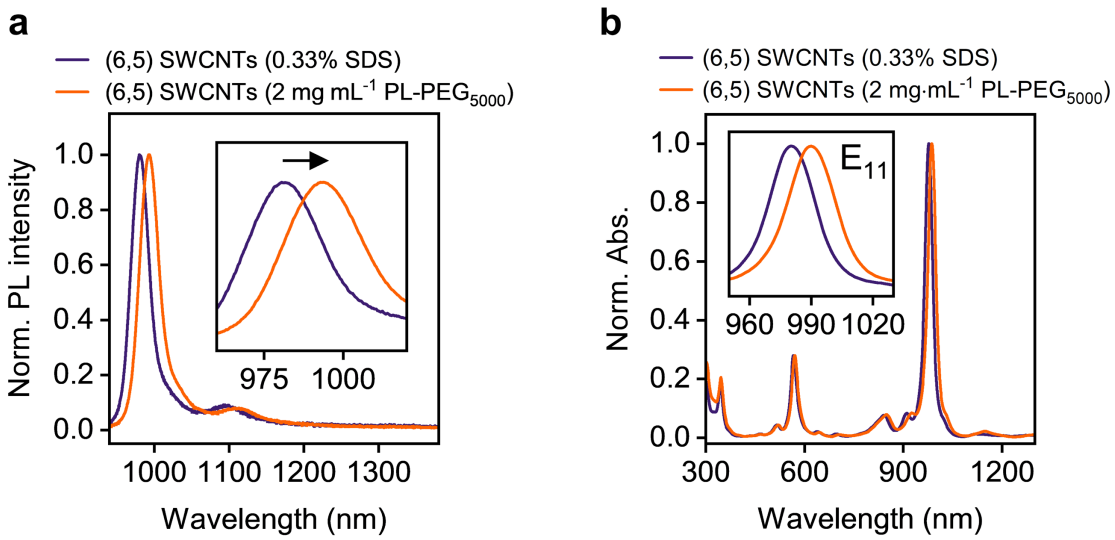

Supplementary Fig. 15 | Transfer of (6,5) SWCNTs to PL-PEG$_{5000}$. a Normalized PL spectra of (6,5) SWCNTs before and after exchange of surfactant system from SDS (0.33% w/v) to PL-PEG$_{5000}$ (2 mg mL^{-1}). The successful exchange to PL-PEG$_{5000}$ is indicated by a redshift (≈ 13 nm) of the E_{11} peak. **b** UV-Vis-NIR absorption spectra of (6,5) SWCNTs before and after transfer to PL-PEG$_{5000}$.

Suppl. Fig. 16 | SWCNTs wrapped by ssDNA

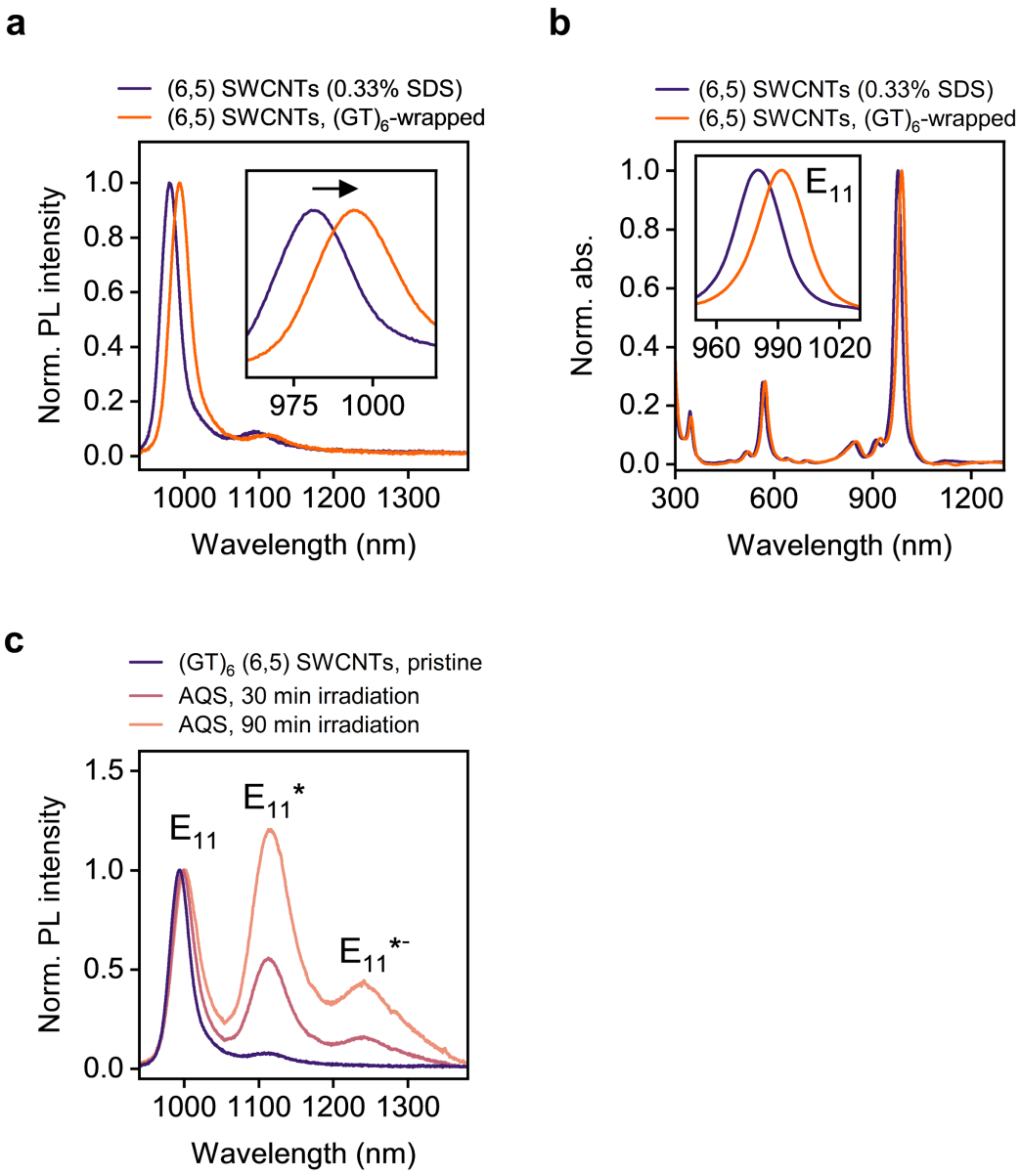

Supplementary Fig. 16 | Functionalization of ssDNA-wrapped SWCNTs. a PL spectra of pristine (6,5) SWCNTs before and after transfer from SDS surfactant to $(GT)_6$-ssDNA, indicated by a redshift of ≈ 14 nm. **b** UV-Vis-NIR absorption spectra of (6,5) SWCNTs before and after transfer to $(GT)_6$-ssDNA. **c** Photocatalytic functionalization of $(GT)_6$-wrapped (6,5) SWCNTs using AQS in 1× PBS buffer.

Suppl. Fig. 17 | Functionalization of CoMoCAT SWCNTs

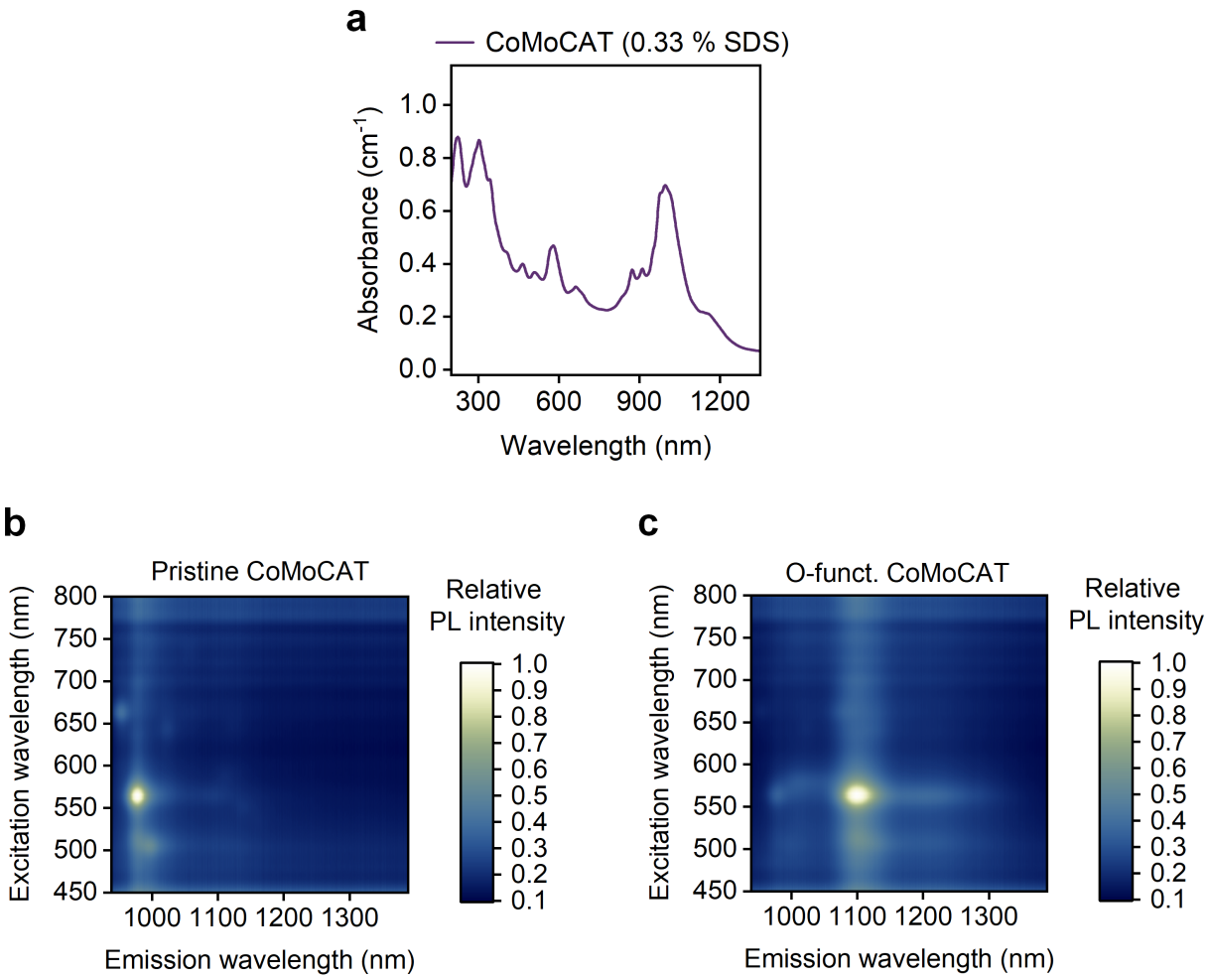

Supplementary Fig. 17 | Functionalization of CoMoCAT raw material. a UV-Vis-NIR absorption spectrum of CoMoCAT raw material dispersed in 0.33% (w/v) SDS. **b** PLE map of CoMoCAT raw material dispersed in 0.33% (w/v) SDS. **c** PLE map of oxygen-functionalized CoMoCAT raw material (0.33% w/v SDS).

Suppl. Fig. 18 | Tip-sonicated SWCNTs

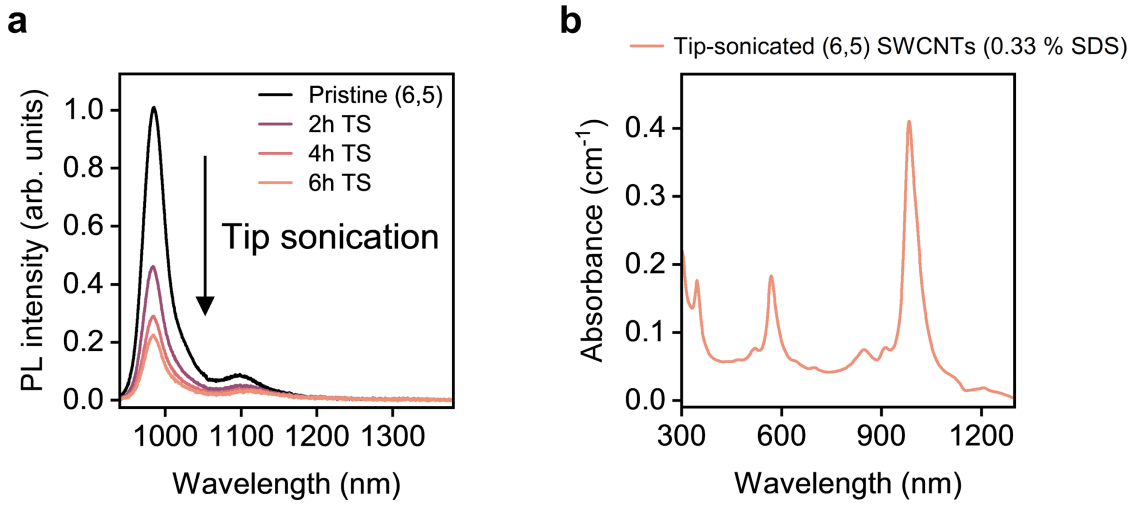

Supplementary Fig. 18 | Shortening of SWCNTs by tip sonication. a PL spectra of (6,5) SWCNTs (1% w/v SDS) after different durations of tip sonication (TS). **b** UV-Vis-NIR absorption spectrum of (6,5) SWCNTs after 6 h of tip sonication (1% w/v SDS).

Suppl. Fig. 19 | AFM length statistics

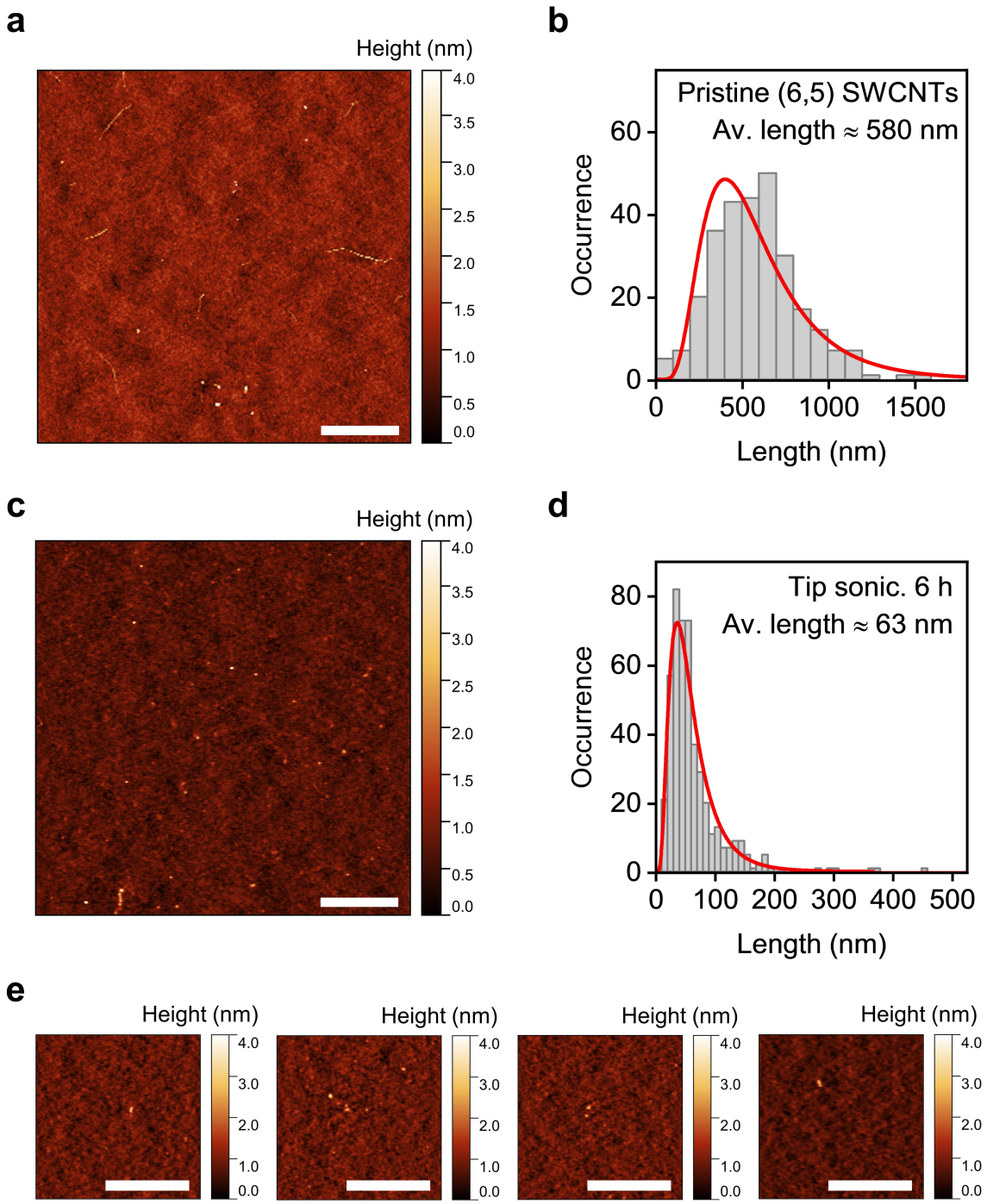

Supplementary Fig. 19 | AFM length statistics of tip-sonicated SWCNTs. a Representative atomic force micrograph of pristine (6,5) SWCNTs (scale bar, 1 µm). **b** Length histogram of pristine (6,5) SWCNTs with an average length of 580 nm (log-normal distribution, red curve. **c** Representative atomic force micrograph of (6,5) SWCNTs after 6 h of tip sonication (scale bar, 1 µm). **d** Length histogram of (6,5) SWCNTs after 6 h of tip sonication with an average length of 63 nm (log-normal distribution, red curve). **e** Zoomed-in atomic force micrographs (1 µm × 1 µm) of shortened (6,5) SWCNTs (scale bar, 500 nm).

Suppl. Fig. 20 | Organic solvent SWCNT dispersions

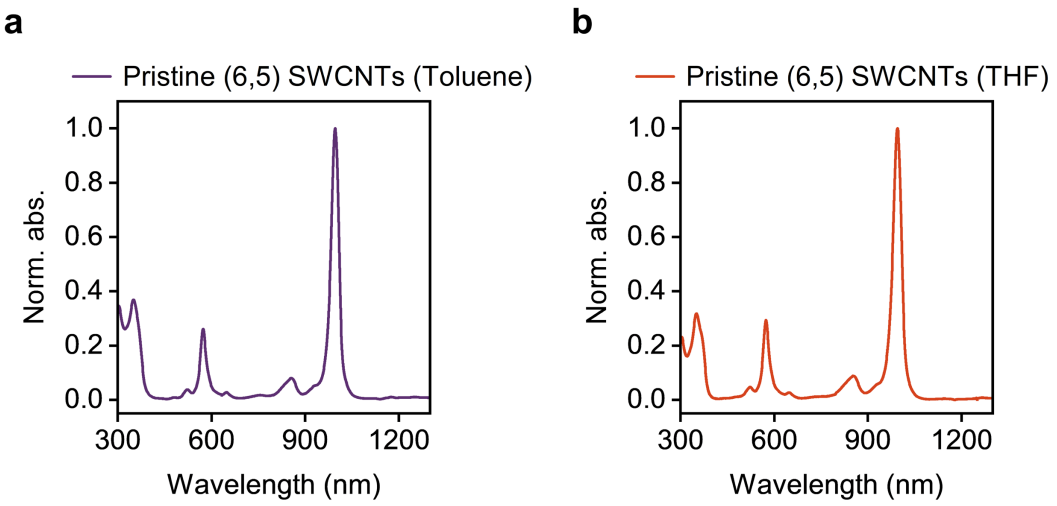

Supplementary Fig. 20 | Absorption spectra of (6,5) SWCNT dispersions in organic solvents. Normalized UV-Vis-NIR absorption spectra of PFO-BPy-wrapped (6,5) SWCNTs in toluene (**a**) or THF (**b**).

Suppl. Fig. 21 | PLE maps of organic solvent SWCNT dispersions

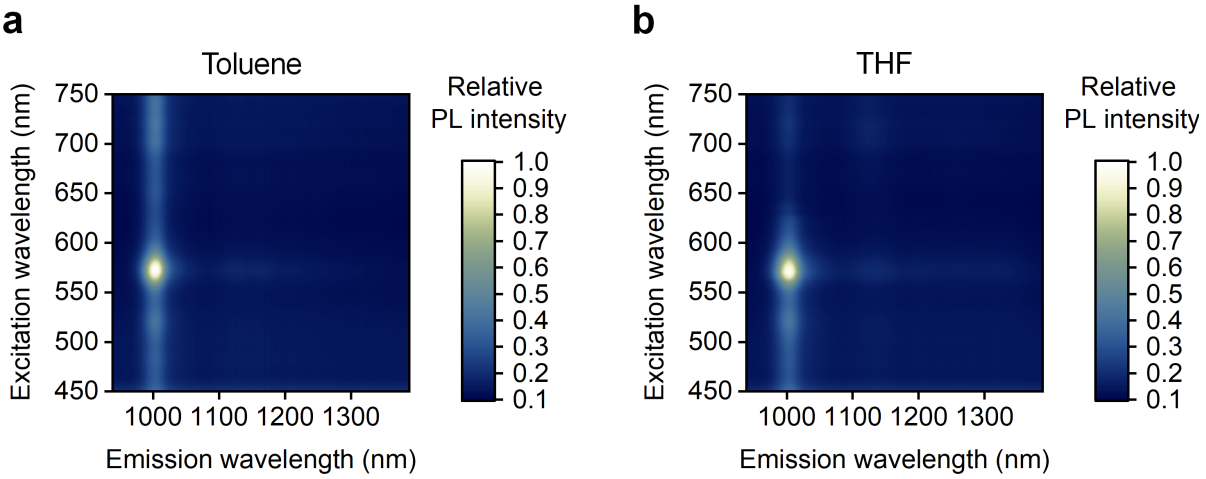

Supplementary Fig. 21 | SWCNT dispersions in organic solvents. PLE maps of PFO-BPy-wrapped (6,5) SWCNTs in toluene (**a**) and THF (**b**).

Suppl. Fig. 22 | Treatment of (6,5) SWCNTs with *t*-Bu-AQ in toluene

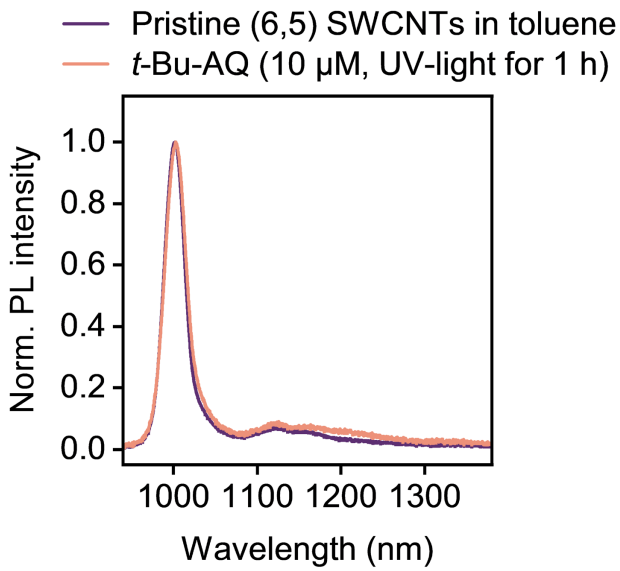

Supplementary Fig. 22 | Treatment of toluene dispersions of (6,5) SWCNTs with *t*-Bu-AQ. PL spectra of (6,5) SWCNTs (wrapped by PFO-BPy in toluene) before and after treatment with *t*-Bu-AQ and UV-light (365 nm) for 1 h.

Suppl. Fig. 23 | Single-nanotube PL spectra at cryogenic temperature

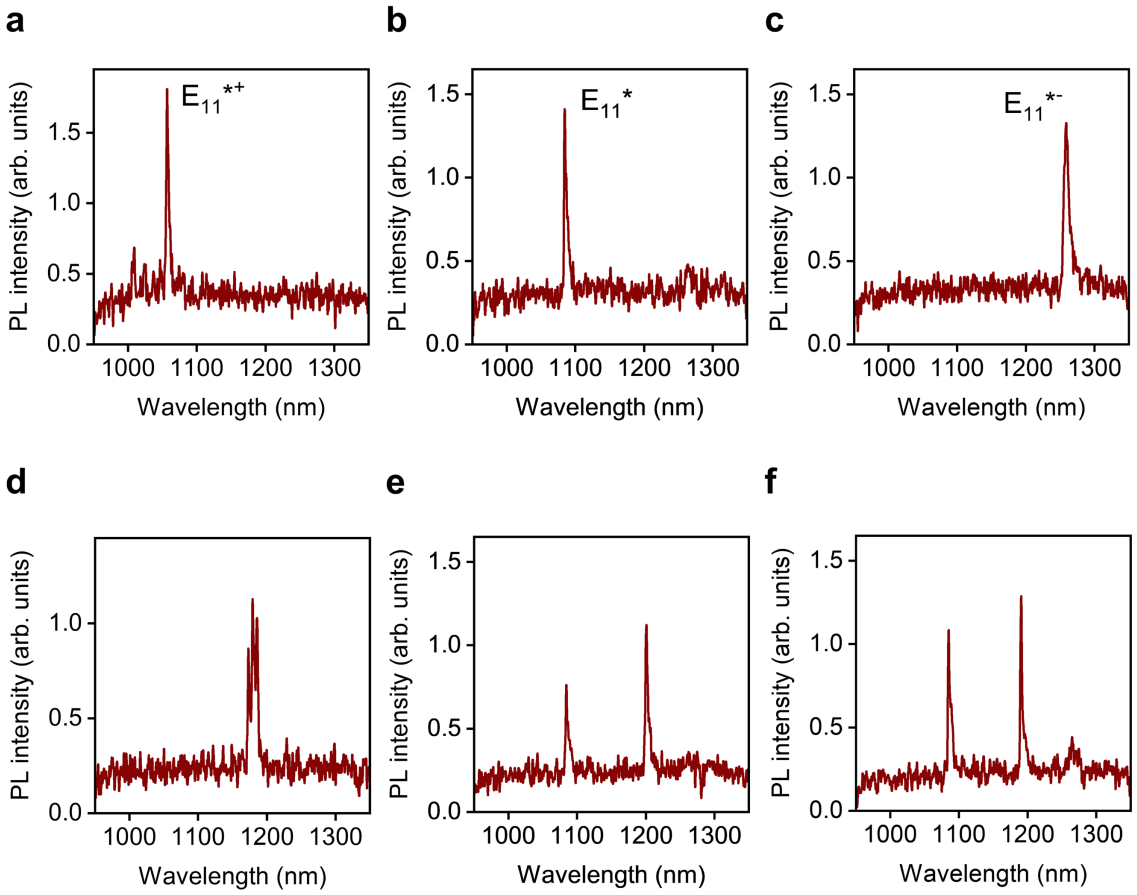

Supplementary Fig. 23 | Low-temperature (4.6 K) single-SWCNT spectra of PFO-BPy-wrapped (6,5) SWCNTs functionalized using 2-*tert*-butylanthraquinone in THF. Single-nanotube PL spectra with E_{11}^{*+} (**a**), E_{11}^{*} (**b**) and E_{11}^{*-} (**c**) emission peaks[5]. **d, e, f** Single-nanotube PL spectra with spectral signatures of multiple defects.

Suppl. Fig. 24 | Spatial resolution of film functionalization

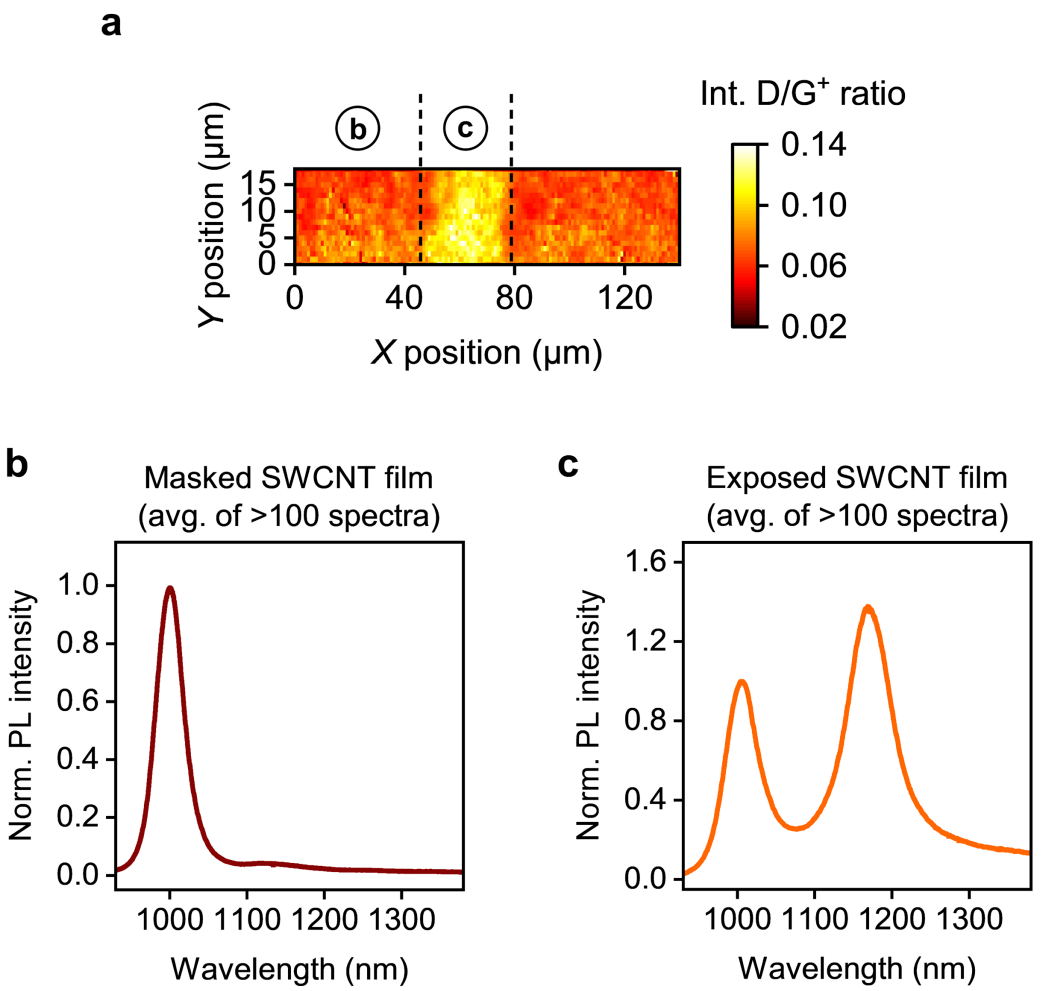

Supplementary Fig. 24 | Spatial resolution of photocatalytic SWCNT film functionalization. a Map of integrated Raman D/G$^+$ ratio of a thin-film of PFO-BPy-wrapped (6,5) SWCNTs after photocatalytic functionalization with aqueous AQS solution (2 mg mL^{-1}) and UV irradiation (365 nm, 1 h). The employed shadow mask consisted of a line structure (width 50 µm). Average PL spectra of masked (**b**) and exposed area (**c**) after functionalization (>100 randomly sampled positions for each area).

Suppl. Fig. 25 | Absorption spectra of SWCNT enantiomers

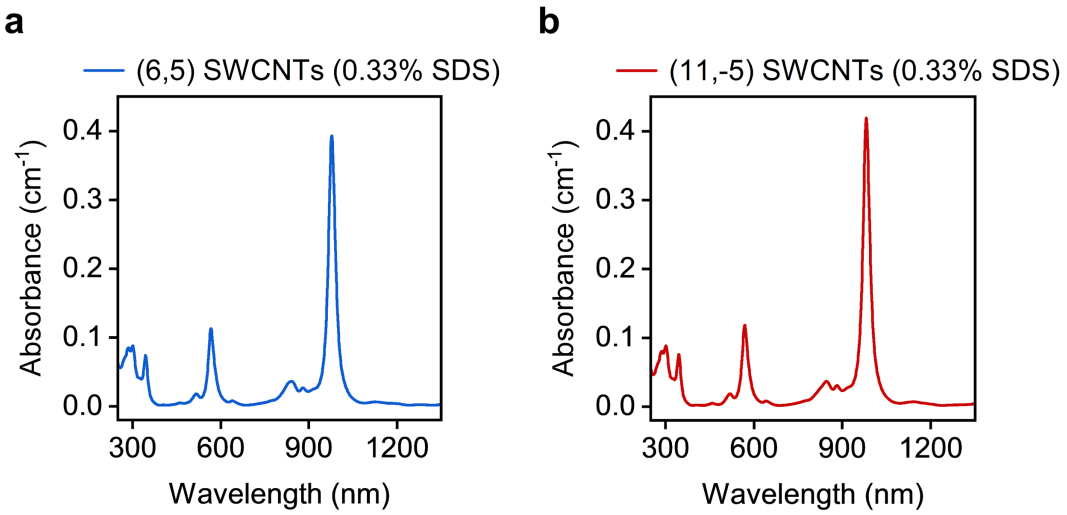

Supplementary Fig. 25 | Absorption spectra of enantiopure SWCNTs. UV-Vis-NIR absorption spectra of aqueous dispersions of enantiopure (6,5) (**a**) and (11,-5) (**b**) SWCNTs.

Suppl. Fig. 26 | PLE maps of SWCNT enantiomers

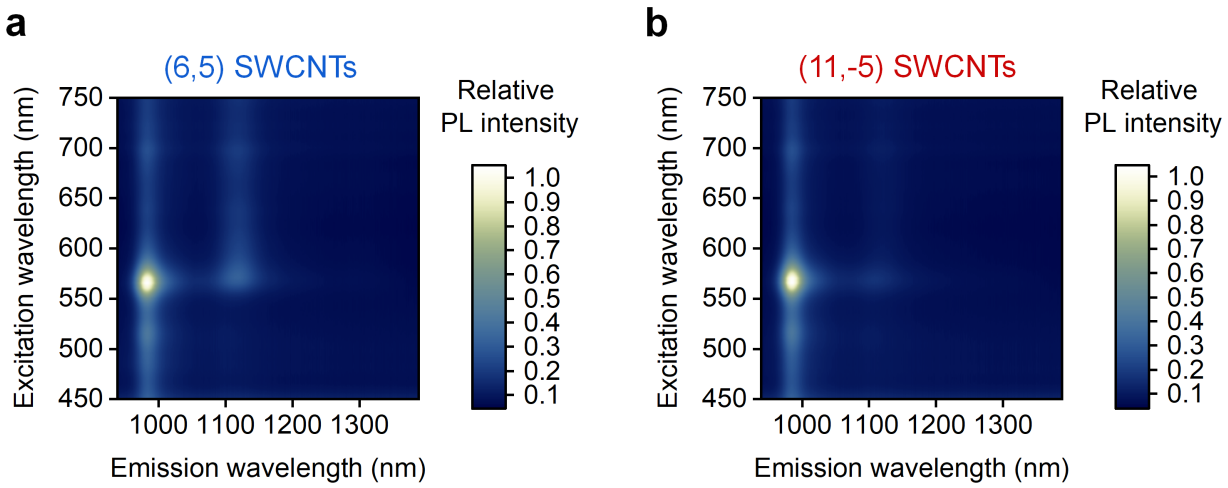

Supplementary Fig. 26 | PLE maps of SWCNT enantiomers. Photoluminescence excitation-emission maps of (6,5) (**a**) and (11,-5) (**b**) SWCNTs (aqueous dispersions). Note, the (6,5) SWCNT dispersion in (**a**) shows weak emission from a few unintentional luminescent defects. Due to their low density, they do not affect the absorption or CD spectra.

Suppl. Fig. 27 | UV-Vis CD spectra of functionalized SWCNTs

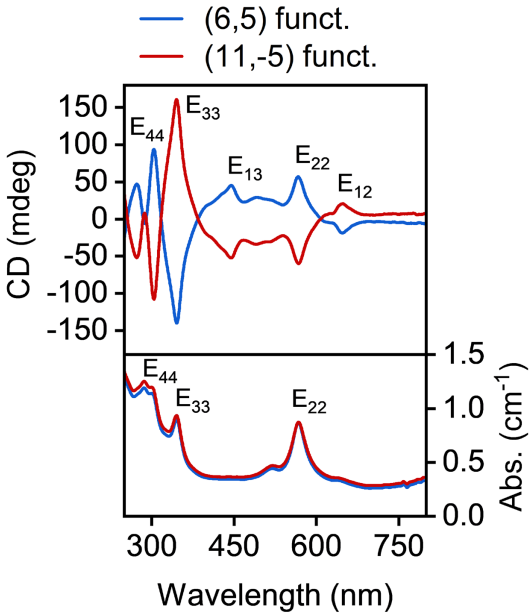

Supplementary Fig. 27 | CD and absorption spectra of functionalized SWCNT enantiomers. Circular dichroism and UV-Vis absorption spectra (250 – 800 nm) of oxygen-functionalized (6,5) and (11,-5) SWCNT enantiomers (in aqueous dispersion, 1% w/v DOC).

Suppl. Fig. 28 | Raman spectra of SWCNT enantiomers

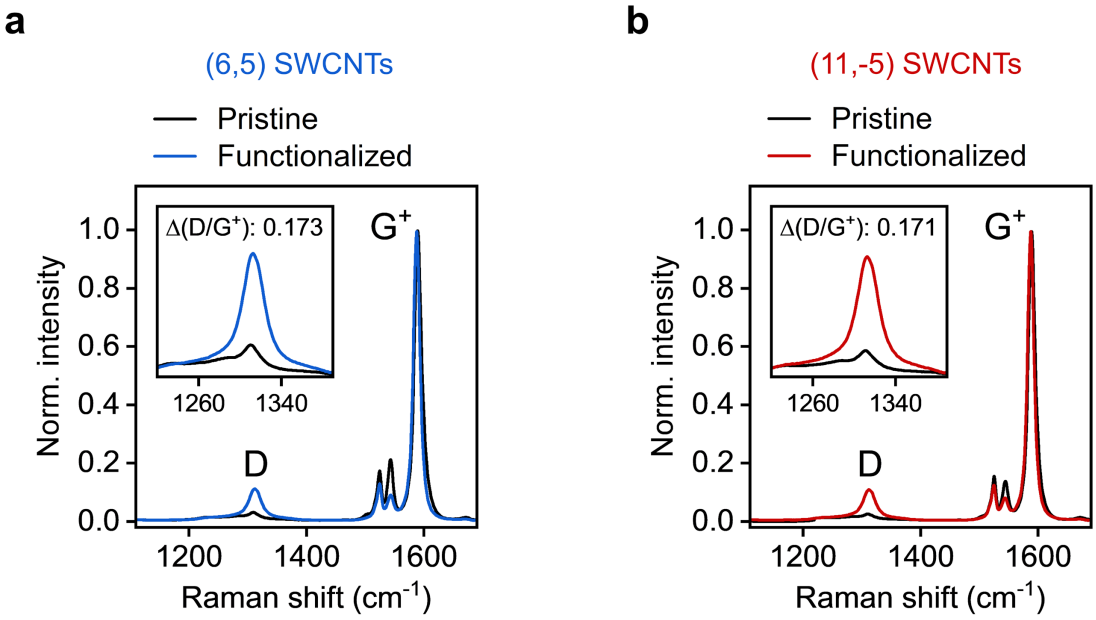

Supplementary Fig. 28 | Raman spectroscopy of pristine and functionalized SWCNT enantiomers. Normalized and averaged (>3000 spectra) Raman spectra (λ_{exc} = 532 nm) of pristine and highly functionalized (6,5) (**a**) and (11,-5) (**b**) SWCNTs as used for circular dichroism measurements. Insets show the D-mode and integrated $\Delta(D/G^+)$ ratio.

Supplementary Note 1| Influence of exciton trapping on absorption dissymmetry factor

The absorption dissymmetry factor g_{abs} (or equivalently, the normalized circular dichroism signal $\mathrm{CD_{norm}}$) of an optical transition can be calculated from the rotational strength R and dipole strength D of a molecule according to

$$g_{\mathrm{abs}} = \frac{4R}{D}, \tag{4}$$

where

$$R = |\mu||m| \cos\theta \tag{5}$$

and

$$D = |\mu|^2 + |m|^2. \tag{6}$$

μ and m denote the electronic and magnetic transition dipole moments, respectively, which include the angle θ.[6] For alternating $\mathrm{E_{ii}}$ transitions in SWCNTs (i = 1, 2, 3…), the orientation of μ and m changes, resulting in opposite signs for odd and even E_{ii} transitions in CD spectra of single-enantiomer SWCNTs[7] (see also Supplementary Fig. 27). In contrast to that, the CD signals of the $\mathrm{E_{11}}$ and $\mathrm{E_{11}}$* optical transitions have the same sign, indicating that the orientation of the transition dipole moments is not reversed for free and defect-localized excitons (see Fig. 4c of the main text).

For a comparative, semi-quantitative estimate of absorption dissymmetry factors g_{abs} of the $\mathrm{E_{11}}$ and $\mathrm{E_{11}}$* transitions, we assume that exciton localization at a luminescent defect site leads to a reduction in exciton size, while the symmetry of the excitonic wavefunction remains unchanged. In agreement with previous TD-DFT simulations[5,8], the magnitude of the interaction with the nanotube lattice is assumed to remain identical for free and defect-localized exciton, as the respective electron and hole densities are strongly confined on the nanotube lattice (instead of the attached functional group or atom defect). A reduction in exciton size due to trapping at a luminescent defect results in a three- to four-fold reduction in oscillator strength f_{12},[8] which is related to the electronic transition dipole moment μ_{12} for a transition between two states $|1\rangle$ and $|2\rangle$ according to

$$f_{12} = \frac{2}{3}\Delta E_{12}\,|\mu_{12}|^2. \tag{7}$$

Here, ΔE_{12} denotes the difference in energy between the initial and final states $|1\rangle$ and $|2\rangle$. Consequently, for the $\mathrm{E_{11}}$ and $\mathrm{E_{11}}$* optical transitions, a difference in electronic transition dipole

moments of ≈ 1.7 – 1.9 is found from the aforementioned difference in oscillator strength. Based on theoretical work on SWCNTs and data from synthesized nanotube segments[9-11], μ and m can be estimated to be on the order of 1 D and 0.1 μ_B, which are typical values found in helically chiral organic molecules with comparable absorption dissymmetry factors as observed for the E_{11} transition in SWCNTs (~ 10^{-4} – 10^{-3})[12-14]. Any change in magnetic transition dipole moment between the E_{11} and E_{11}* state is assumed to be negligible, as they are practically identical in geometry[11,12].

Overall, these values result in an estimate for g_{abs} of ≈ $4 \cdot 10^{-4}$ and ≈ $2 \cdot 10^{-4}$ for the E_{11} and E_{11}* absorption, respectively, which aligns well with our findings ($g_{abs}(E_{11}) \approx 9 \cdot 10^{-4}$ and $g_{abs}(E_{11}^*) \approx 5 \cdot 10^{-4}$). Thus, we conclude that a reduction in exciton size by a factor of ≈ 2 – 3, accompanied by a proportional decrease in oscillator strength and electronic transition dipole moment, results in the observed reduction of the absorption dissymmetry factor from the E_{11} to the E_{11}* optical transition, which in turn enables the direct calculation of relative exciton sizes based on CD spectroscopy.

Supplementary References

1. Sebastian, F. L. et al. Absolute quantification of sp^3 defects in semiconducting single-wall carbon nanotubes by Raman spectroscopy. *J. Phys. Chem. Lett.* **13**, 3542-3548 (2022).

2. Sebastian, F. L. et al. Unified quantification of quantum defects in small-diameter single-walled carbon nanotubes by Raman spectroscopy. *ACS Nano* **17**, 21771-21781 (2023).

3. Hartmann, N. F. et al. Photoluminescence dynamics of aryl sp^3 defect states in single-walled carbon nanotubes. *ACS Nano* **10**, 8355-8365 (2016).

4. Kim, M. et al. Fluorescent carbon nanotube defects manifest substantial vibrational reorganization. *J. Phys. Chem. C* **120**, 11268-11276 (2016).

5. Ma, X. et al. Electronic structure and chemical nature of oxygen dopant states in carbon nanotubes. *ACS Nano* **8**, 10782-10789 (2014).

6. Covington, C. L. & Polavarapu, P. L. Similarity in dissymmetry factor spectra: a quantitative measure of comparison between experimental and predicted vibrational circular dichroism. *J. Phys. Chem. A* **117**, 3377-3386 (2013).

7. Wei, X. et al. Experimental determination of excitonic band structures of single-walled carbon nanotubes using circular dichroism spectra. *Nat. Commun.* **7**, 12899 (2016).

8. Gifford, B. J., Kilina, S., Htoon, H., Doorn, S. K. & Tretiak, S. Exciton localization and optical emission in aryl-functionalized carbon nanotubes. *J. Phys. Chem. C* **122**, 1828-1838 (2018).

9. Motavas, S., Ivanov, A. & Nojeh, A. Optical transitions in semiconducting zigzag carbon nanotubes with small diameters: a first-principles broad-range study. *Phys. Rev. B* **82**, 085442 (2010).

10. Sato, S. et al. Chiral intertwined spirals and magnetic transition dipole moments dictated by cylinder helicity. *Proc. Natl. Acad. Sci. U.S.A.* **114**, 13097-13101 (2017).

11. Kogashi, K., Matsuno, T., Sato, S. & Isobe, H. Narrowing segments of helical carbon nanotubes with curved aromatic panels. *Angew. Chem. Int. Ed.* **58**, 7385-7389 (2019).

12. Qiu, Z. et al. Amplification of dissymmetry factors in π-extended [7]- and [9]helicenes. *J. Am. Chem. Soc.* **143**, 4661-4667 (2021).

13. Xu, F. et al. Supramolecular polymerization as a tool to reveal the magnetic transition dipole moment of heptazines. *J. Am. Chem. Soc.* **146**, 15843-15849 (2024).

14. Tanaka, H., Inoue, Y. & Mori, T. Circularly polarized luminescence and circular dichroisms in small organic molecules: correlation between excitation and emission dissymmetry factors. *ChemPhotoChem* **2**, 386-402 (2018).

6 Conclusion and Outlook

At the beginning of this thesis, many fundamental aspects of luminescent defects in SWCNTs had been addressed by detailed experimental and theoretical studies, paving the way towards their integration in light-emitting devices,[106,367] single-photon sources[50,221] and nanophotonic cavities,[368,369] as well as enabling their use in biological sensing applications[265–267,269,370] and high-contrast tissue imaging.[54,55] The enhancement of photoluminescence quantum yields (PLQYs) of SWCNTs upon introduction of luminescent defects and the ability to synthetically attach various chemical groups to the carbon nanotube lattice and create unique functionalities promises solutions to a variety of problems in near-infrared photonics, optical read-out schemes, and biomarker identification. The successful integration of functionalized SWCNTs in these fields of technology beyond proof-of-concept studies will depend critically on the degree of tunability, reproducibility, spatial control, and uniformity with which luminescent defects can be introduced in SWCNTs. While the synthetic toolbox for the introduction of luminescent defects continuously expands, the metrological approaches to investigate their structure, density and distribution have remained largely the same. However, precise knowledge about the density and distribution of luminescent defects is valuable, both in terms of purely practical aspects (*e.g.*, identification of high-quality samples), but also to provide a reference for other nanotube properties (*e.g.*, number of available sensor binding sites). To this end, a reliable and universally applicable method for the absolute quantification of luminescent defects in SWCNTs was developed in this thesis, as presented in Chapter 3. A subsequent comparative study of oxygen and aryl defects, detailed in Chapter 4, revealed the potential of this method to identify differences in the distribution of luminescent defects on nanotube sidewalls, and indicates how synthetic methods can be designed to obtain brightly luminescent SWCNTs. Building on this knowledge, Chapter 5 explored photocatalysis as a method to obtain bright oxygen defects with uniform binding configuration, which facilitated the first exploration of the impact of helical nanotube chirality on strongly confined excitons at luminescent defect sites.

Unified quantification of defects by Raman spectroscopy

To quantitatively relate the optical, electronic and thermal properties of functionalized SWCNTs to the density of defect sites on the nanotube lattice, a simple and reliable metric is required. Prior to this thesis, the relative assessment of defect densities was usually performed by comparing PL intensity ratios for the intrinsic E_{11} and defect state emission, from Raman $D/G^{(+)}$ ratios, or by X-ray photoelectron spectroscopy (XPS).[13,221,230,240,288] PL intensity ratios are an unreliable metric

for defect densities due to their dependence on excitation power,[239] while XPS measurements are insufficient to identify the minor changes in nanotube structure that occur at ideal defect densities leading to maximum PLQYs. Raman spectroscopy, on the other hand, is sufficiently sensitive, but $D/G^{(+)}$ ratios can only serve as a relative metric and depend on the quality of the starting material. However, for graphene, the sp^2-hybridized 2D analogue of SWCNTs, an absolute quantification method is well-established and has served as a versatile tool to assess graphene quality and functionalization.[347,349,350,353,371,372]

Chapter 3 presented a unified and absolute quantification method for luminescent defects in small-diameter semiconducting carbon nanotubes, which was established from a linear correlation of integrated Raman D/G^+ ratios with defect densities calculated from spectrally resolved PLQY measurements *via* the diffusion-limited contact quenching model (for a summary, see Figure 6.1). A prerequisite for the development of this method was the availability of highly purified samples of SWCNTs, which was enabled by continuous improvements in nanotube sorting and selection techniques.[17] Based on results obtained prior to and in the beginning of this thesis on (6,5) SWCNTs,[19] this work significantly expanded the fundamental quantification approach by screening different small-diameter SWCNTs ((7,3), (6,5), (8,3), (9,2), and (7,5) species) at various Raman laser excitation wavelengths (532 nm, 633 nm, 785 nm). Similar to the work on graphene, a normalization of the D/G^+ ratio to the Raman excitation laser wavelength by λ^4 was required to account for the scattering efficiency of optical phonons.[347] This provides a unified expression for the absolute quantification of defects independent of excitation energy and has proven particularly valuable for the assessment of new synthetic strategies and characterization of defect structures.[257,373]

Beyond this practical aspect, the precise determination of defect densities also enabled further insights into the nature of luminescent defects in SWCNTs. For the small-diameter species investigated in this work, the slope of the linear correlation between integrated Raman D/G^+ ratios and calculated defect densities scales inversely proportional with nanotube diameter. While the challenges of large-diameter nanotube functionalization due to reduced reactivity prevented a more extensive analysis, the results strongly point towards a complicated relationship between nanotube diameter and Raman response in functionalized SWCNTs. This observation could serve as motivation for future experimental and theoretical studies on the relation between nanotube curvature, defect structure, and optical properties.

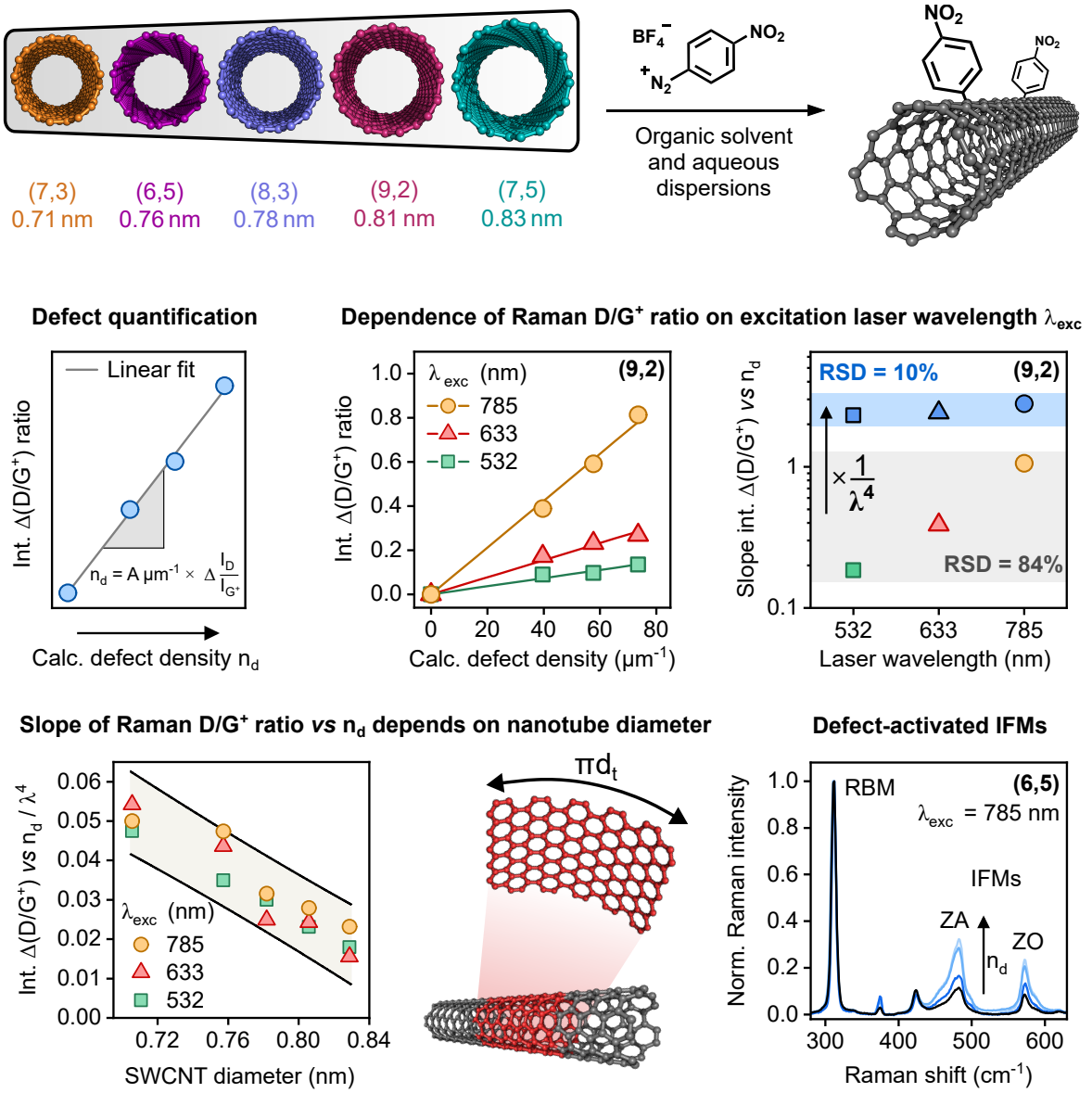

Figure 6.1: Main results presented in Chapter 3, published in Sebastian *et al.*, *ACS Nano* **17**, 21771-21781 (2023).[20]

As sp^3 functionalization of liquid-dispersed SWCNTs introduces lattice defects in a highly controlled environment without additional sidewall damage (*e.g.*, by sonication), the dependence of other Raman modes on the presence of defects could be studied in detail. This enabled the unambiguous identification of two defect-related intermediate frequency modes (IFMs) in Raman spectra of the low-frequency region: Raman spectra of pristine and functionalized SWCNTs with different defect densities revealed that ZA- and ZO-derived phonon modes at $\approx 480\,\mathrm{cm}^{-1}$ and $\approx 570\,\mathrm{cm}^{-1}$, respectively, are second-order processes that involve elastic phonon scattering at sp^3 defect sites. Similar to the Raman D/G^+ ratio, the integrated IFM/RBM ratio increases linearly with calculated defect densities, but with a difference in slope. In practice, the low intensity of IFMs limits their applicability as an absolute defect den-

sity metric, but they can provide quantitative information on nanotube modification and functionalization beyond the standard Raman D/G^+ ratio for selected samples.

Overall, this unified defect quantification approach should enable a better comparability of SWCNT samples across laboratories and different nanotube raw materials. By incorporation of the Raman excitation laser wavelength into the established empirical relation between D/G^+ ratios and calculated defect densities, the defect quantification can be performed with practically any Raman spectroscopy setup. Notably, the dependence of the linear relation between D/G^+ and n_d on the nanotube diameter demonstrates that the defectiveness of different SWCNT species cannot be compared based on Raman spectra alone. The quantification approach is currently limited to the small-diameter, semiconducting SWCNTs investigated in Chapter 3. For metallic SWCNTs, a universally applicable defect quantification method is equally important with regard to their use in conductive inks, transparent electronics, or flexible integrated circuits, but remains a significant challenge.[374–376]

Identification of luminescent defect clustering

Among the different types of luminescent defects, oxygen and aryl motifs are the ones which have received the most attention in experiment and theory. In the case of oxygen defects, this interest was driven by the fact that the first observation of defect PL in SWCNTs was observed by ozonolysis of nanotubes.[12] Oxygen defects were also crucial for the initial demonstration of room-temperature single-photon emission from SWCNTs.[14] However, in comparison to luminescent sp^3 aryl defects, oxygen defects were generally assumed to result in lower emission brightness due to reverse ordering of dark and bright defect states.[210,211,218] The harsh conditions under which oxygen defects are created from reactive oxygen species in the established functionalization methods (*e.g.*, ozonolysis,[12] photodissociation of sodium hypochlorite[287]) could also facilitate over-oxidation and lead to non-radiative quenching sites. A previously identified preference for oxidative processes to occur at already defective areas of nanotube sidewalls may result in a tendency of oxygen defects to form clusters,[295,296] but the spectroscopic identification of defect clustering and its effect on SWCNT emission was challenging.

The work presented in Chapter 4 employed the absolute defect quantification method introduced in Chapter 3 for a comparative analysis of luminescent aryl and oxygen defects (see Figure 6.2 for a summary). For this purpose, aqueous dispersions of (6,5) SWCNTs were functionalized with aryl sp^3 defects and oxygen defects using previously reported methods.[12,13,222,287] A systematic evaluation of Raman spectra and PLQY measurements revealed that the linear correlation between integrated

D/G^+ ratios and calculated defect densities was fundamentally different for oxygen and aryl sp^3 defects. The observed deviation by a factor of 2.3 suggests that the structural modification of the SWCNT lattice at which the same degree of E_{11} PLQY reduction occurs is greater for oxygen defects compared to aryl sp^3 defects. Notably, a very similar deviation was observed for the ZA- and ZO-derived intermediate frequency phonon modes. This difference, which is similar for all oxygen functionalization methods, can be attributed to a higher tendency of oxygen defects to form clusters on nanotube sidewalls. As a result, the overall exciton trapping efficiency – per atomic defect site – is lower for oxygen defects, *i.e.*, a cluster of 2 – 3 oxygen defects acts as a single defect for a mobile exciton. Consequently, more single oxygen defects are required to achieve maximum PLQYs.

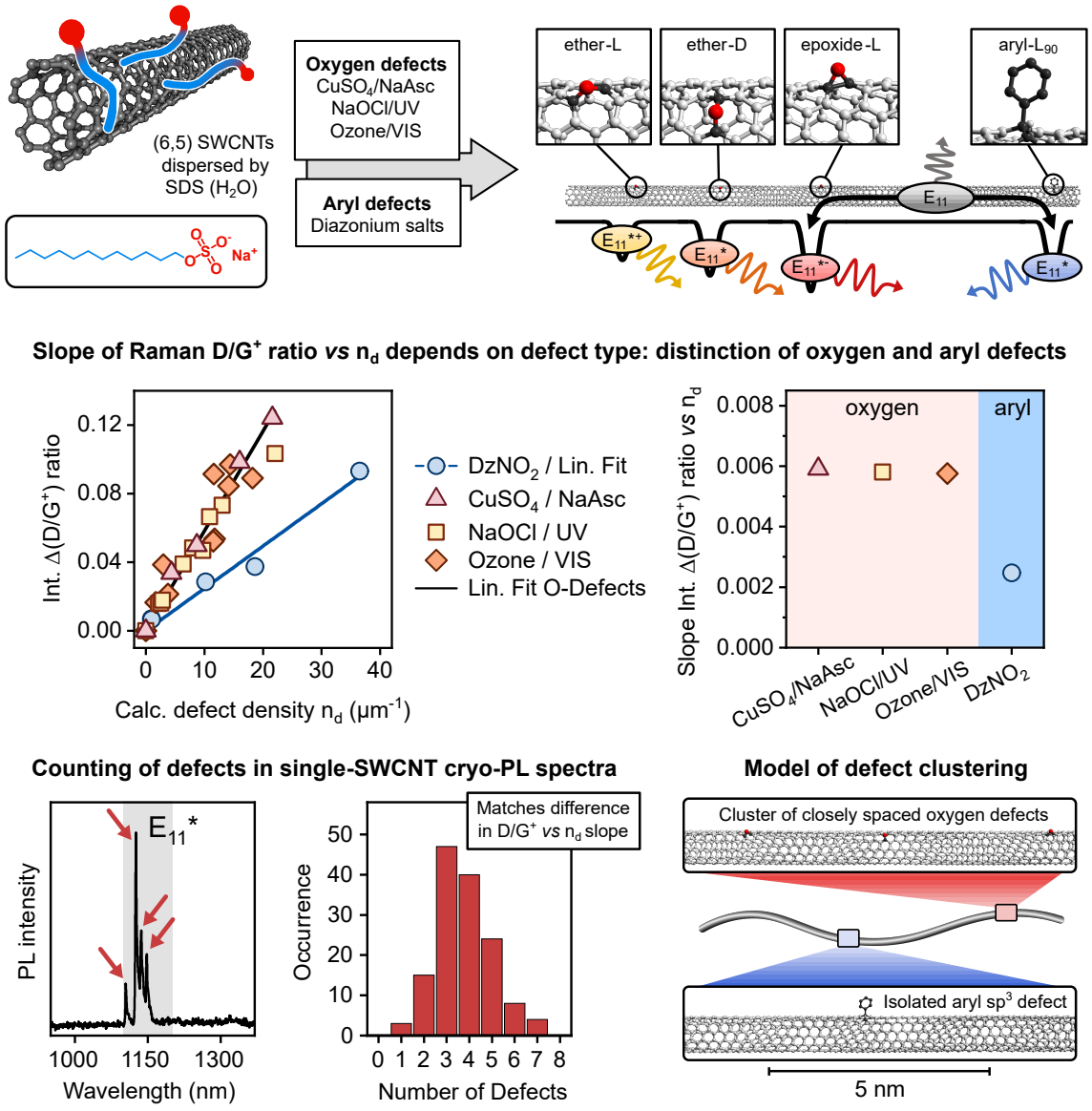

Figure 6.2: Main results presented in Chapter 4, published in Sebastian *et al.*, *Nanoscale Horiz.* **9**, 2286-2294 (2024).[21]

In order to independently assess whether the number of single oxygen defects is actually higher than the calculation of the defect density by PLQY measurements indicates, PL spectra of individual, oxygen-functionalized SWCNTs were recorded at cryogenic temperature (4.7 K). Under these conditions, strong localization of excitons and narrowing of the corresponding emission peaks enables the identification of single atomic defect states, which exhibit minor differences in emission energy due to small variations in the dielectric environment of the nanotube. A statistical analysis of over 150 single-SWCNT cryo-PL spectra in combination with the average nanotube lengths (from atomic force microscopy, AFM) supported the hypothesis of defect clustering. The deviation by a factor of 2.3 in the slope of Raman D/G^+ ratios *vs* calculated defect densities was closely matched by this analysis, which found ≈ 12 defects μm^{-1} compared to $n_d = 5\,\mu m^{-1}$ obtained from E_{11} PLQYs.

This work simplifies the identification of luminescent defect types (oxygen or aryl sp^3) and enables the assessment of the degree of defect clustering by providing empirical equations applicable to (6,5) SWCNTs. Although (6,5) SWCNTs are the material of choice for the development of new functionalization methods, other nanotube species can also offer advantages (*e.g.*, further red-shifted defect emission). A corresponding expansion of the presented method to other species should be straightforward. In addition to this analytical protocol, the presented work demonstrated the validity of the absolute quantification method by Raman spectroscopy even for slightly p-doped SWCNTs, which is observed upon liquid-phase processing in the presence of oxidants or oxidative functionalization. Despite these advances, a method with sufficient spatial resolution to directly identify the distribution of luminescent defects on SWCNTs is still missing. Future directions could include the use of near-field methods such as tip-enhanced Raman spectroscopy (TERS) to gain spatially resolved information on the decoration of nanotube sidewalls with defects before and after functionalization.

Photocatalytic creation and circular dichroism of luminescent defects

The development of new functionalization methods for the introduction of luminescent defects in SWCNTs has shifted the limit of attainable nanotube PLQYs,[13,221,230] enabled a manifold of optical sensing schemes[18,263,264,266,267,269,377–379] and revealed fundamental insights into the nature of zero-dimensional luminescent defect states (*e.g*, room-temperature single-photon emission).[50] However, the possible chiral nature of luminescent defects in SWCNTs, which exhibit an intrinsic helical chirality along the nanotube axis, has remained elusive up to now. In order to study this potential phenomenon, highly purified and concentrated dispersions of SWCNT enantiomers need to be functionalized with large numbers of luminescent defects of

uniform binding configuration, a requirement which could not be met by currently available synthetic strategies.

In Chapter 5, the development of a nanotube functionalization method was presented that uses photocatalysis to achieve dense coverage of SWCNTs with luminescent E_{11}^* oxygen defects without detrimental side reactions (see Figure 6.3). Photoexcitation of water-soluble anthraquinone derivatives at 365 nm (UV-A) was shown to create sufficiently reactive oxygen species in the form of strong hydroxylation agents in a catalytic cycle. By adjustment of the catalyst concentration and irradiation time, E_{11}^* defects could be introduced with high selectivity to produce brightly fluorescent, oxygen-functionalized (6,5) SWCNTs with PLQYs of up to 3.6%. Stopping the exposure to UV-light immediately interrupts the supply of reactive species. This makes the previously required quenching of the reaction (*e.g.*, by addition of DOC) redundant and simplifies subsequent work-up protocols.

Even in larger-diameter nanotube species ((10,0), (9,2), (9,4), and (10,3)), luminescent defects can be created reliably by this photocatalytic approach. Provided that suitable SWCNT species are available, this method could become an essential tool to reliably create quantum defects with strongly red-shifted single-photon emission (SPE) in the telecom C- (1530 – 1565 nm) or even L-band (1565 – 1625 nm).[14] Furthermore, the functionalization method proceeds under mild conditions without the need for toxic chemicals, metal-containing reagents or air-sensitive compounds. It is even suitable for the functionalization of biocompatible (6,5) SWCNTs wrapped by PL-PEG. The functionalization approach also works for CoMoCAT raw material essential for biomonitoring at low cost and large scale,[380] for intentionally shortened SWCNTs ideally suited for high-contrast bioimaging,[55] and for polymer-wrapped carbon nanotubes advantageous for thin film deposition and device fabrication.[51,163]

The integration of SWCNTs with luminescent defects in nanophotonics and quantum technology requires the controlled introduction of luminescent defects at specific positions on nanotube sidewalls. A major step in this direction was made by employing aqueous solutions of the anthraquinone photocatalyst to perform direct functionalization of SWCNT thin films, where the placement of a shadow mask provided spatial resolution down to several μm. This represents the first demonstration of luminescent oxygen defect creation in the solid state without the need for reactive oxide surfaces or deposition of metal oxides. By using anthraquinones or other suitable photocatalysts in combination with focused laser irradiation, patterning of SWCNTs with bright oxygen defects in the sub-μm range appears feasible. With regard to the use of oxygen defects as optical sensors for neurotransmitters or metabolites,[370,381]

such a patterning could enable multi-channel read-out arrays on single substrates, even after nanotube film deposition.

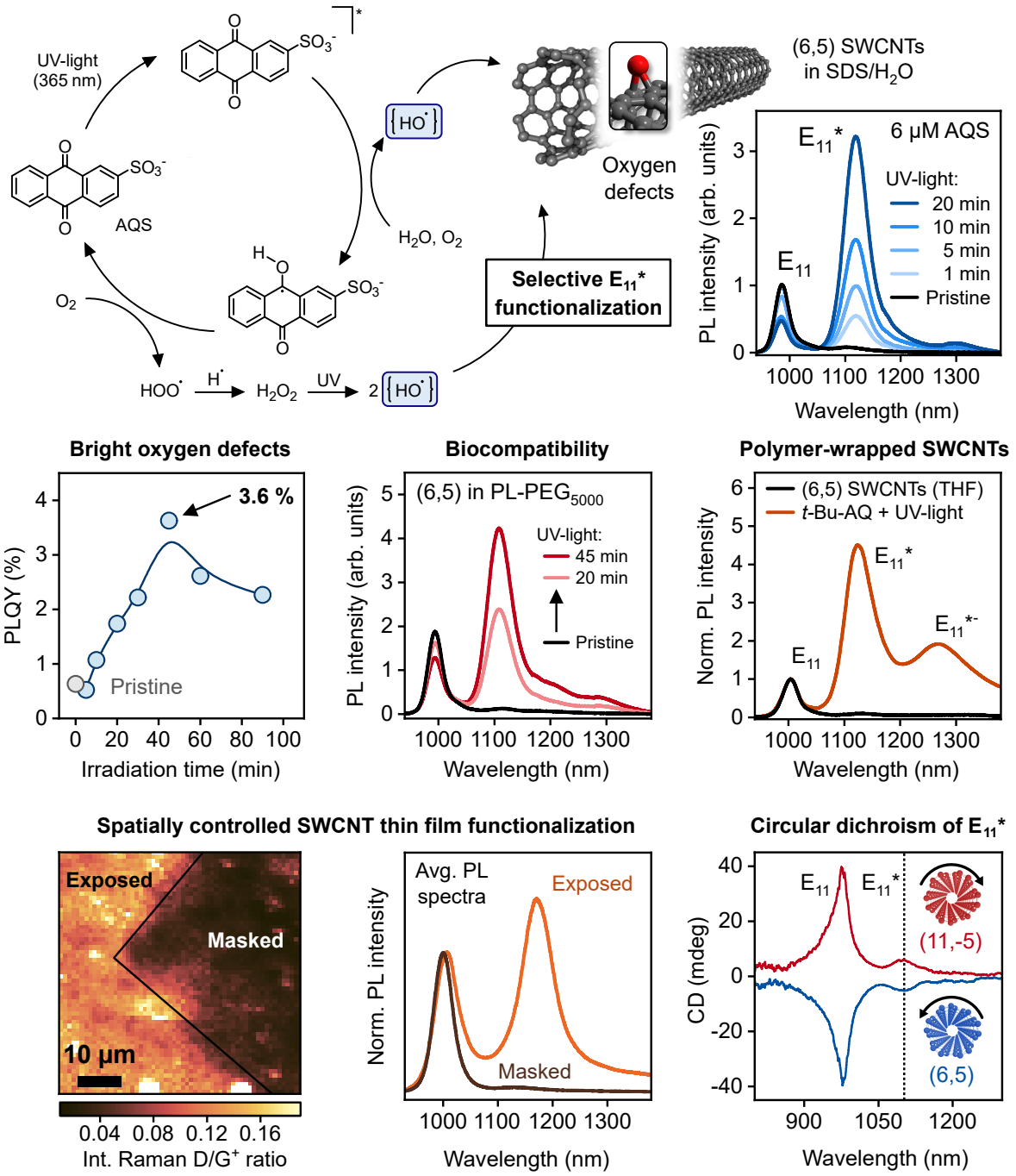

Figure 6.3: Main results presented in Chapter 5, published in Sebastian *et al.*, *Nat. Commun.* **16**, 5107 (2025).[22]

In combination with the progress that has been made in carbon nanotube enantiomer sorting,[112,127,129] the possibility to create large numbers of luminescent E_{11}^* defects in highly concentrated samples prompted the investigation into the potential

chiral nature of luminescent defect states. Indeed, circular dichroism spectroscopy of oxygen-functionalized (6,5) and (11,-5) SWCNT enantiomers in the NIR revealed that the zero-dimensional defect states inherit the chirality of the nanotube lattice. In addition, the direct comparison of the absorption-normalized circular dichroism of the intrinsic and defect optical transitions provides a straightforward metric to assess the relative change of the exciton size upon confinement at nanotube lattice defects. The deterministic manipulation of chirality and spin states in semiconductors has emerged as an important goal for next-generation photonics and electronics. In particular, chiral excitons in hybrid organic/inorganic semiconductor systems receive increasing attention as they combine the favorable transport properties of inorganic layers with the tunability and chirality of organic additives.[382] Control over the chirality of 1D and 0D excitonic states in SWCNTs, which combine several beneficial properties of inorganic and organic materials, could contribute to these developments. Overall, the chirality of confined excitonic states in SWCNTs should offer a valuable additional degree of freedom for the application of luminescent defects in optical sensing and nanophotonics.

To date, many fundamental questions regarding the structural characteristics and photophysical properties of luminescent defects in SWCNTs have been addressed in great detail. Synthetic approaches have advanced to a point where spectral tunability of defect emission across the NIR region and relevant telecommunication bands can be achieved by choice of suitable SWCNT species and reaction conditions.[13,18,212,221,246] Efficient integration of functionalized SWCNTs into luminescent devices has been achieved,[106,367,383] and significant progress towards electrically stimulated single-photon emission[51] and the implementation of electronic spin qubits has been made.[384] Functionalized SWCNTs are also becoming increasingly relevant for healthcare applications such as diagnostics[269] or high-resolution 3D tissue imaging.[55] The observation of chiral, quasi zero-dimensional excitons in SWCNTs raises the exciting question whether circularly polarized luminescence (CPL) from these confined states is also achievable. While currently limited by the performance of CPL detection schemes,[385,386] the experimental determination of CPL from luminescent defects should be a central aspect of future studies. In light of these advancements, it is evident that innovative methods for the controlled introduction and precise characterization of luminescent defects in SWCNTs form the basis for optimizing their performance in current applications and for identifying novel functionalities.

Abbreviations

0D	Zero-dimensional
1D	One-dimensional
2D	Two-dimensional
arb. unit	Arbitrary unit
AFM	Atomic force microscopy
ATPE	Aqueous two-phase extraction
CD	Circular dichroism
CMC	Critical micelle concentration
CPL	Circularly polarized luminescence
CVD	Chemical vapor deposition
DFT	Density functional theory
DGU	Density gradient ultracentrifugation
DLCQ	Diffusion-limited contact quenching
DOC	Sodium deoxycholate
DOS	Density of states
EEA	Exciton-exciton annihilation
EVET	Electronic-to-vibrational energy transfer
FRET	Förster resonance energy transfer
FWHM	Full width at half maximum
IFM	Intermediate frequency mode
LC	Sodium lithocholate
LCPL	Left-handed circularly polarized light
MeCN	Acetonitrile
MPD	Multi-phonon decay
MWCNT	Multi-wall carbon nanotube
NIR	Near-infrared
OD	Optical density
PEG	Poly(ethylene glycol)
PFO	Poly(9,9-di-*n*-octylfluorenyl-2,7-diyl)
PFO-BPy	Poly[(9,9-di-*n*-octylfluorenyl-2,7-diyl)-*alt*-*co*-(6,6′-2,2′-bipyridine)]
PL	Photoluminescence

PL-PEG	Phospholipid–poly(ethylene glycol)
PLQY	Photoluminescence quantum yield
PSB	Phonon sideband
PTFE	Poly(tetrafluoroethylene)
RBM	Radial breathing mode
RCPL	Right-handed circularly polarized light
REM	Raman excitation mapping
ROS	Reactive oxygen species
RSD	Relative standard deviation
SC	Sodium cholate
SDS	Sodium dodecyl sulfate
SPE	Single-photon emission
SRM	Super-resolution microscopy
SWCNT	Single-wall carbon nanotube
TCSPC	Time-correlated single-photon counting
TD	Thermal detrapping
TERS	Tip-enhanced Raman spectroscopy
THF	Tetrahydrofuran
UV	Ultraviolet
vH	van Hove
XPS	X-ray photoelectron spectroscopy

Bibliography

1. Osgood Jr., R. & Meng, X. *Principles of photonic integrated circuits: Materials, device physics, guided wave design* (Springer, Cham, 2021).
2. Eliseeva, S. V. & Bünzli, J.-C. G. Lanthanide luminescence for functional materials and bio-sciences. *Chem. Soc. Rev.* **39,** 189–227 (2010).
3. Liu, Y. *et al.* Near-infrared light emitting metal halides: Materials, mechanisms, and applications. *Adv. Mater.* **36,** e2312482 (2024).
4. Cho, H.-H. *et al.* Efficient near-infrared organic light-emitting diodes with emission from spin doublet excitons. *Nat. Photonics* **18,** 905–912 (2024).
5. Aharonovich, I., Englund, D. & Toth, M. Solid-state single-photon emitters. *Nat. Photonics* **10,** 631–641 (2016).
6. Ding, F., Zhan, Y., Lu, X. & Sun, Y. Recent advances in near-infrared II fluorophores for multifunctional biomedical imaging. *Chem. Sci.* **9,** 4370–4380 (2018).
7. Zaumseil, J. Single-walled carbon nanotube networks for flexible and printed electronics. *Semicond. Sci. Technol.* **30,** 074001 (2015).
8. Zaumseil, J. Semiconducting single-walled carbon nanotubes or very rigid conjugated polymers: A comparison. *Adv. Electron. Mater.* **5,** 1800514 (2019).
9. Nandi, S., Caicedo, K. & Cognet, L. When super-resolution localization microscopy meets carbon nanotubes. *Nanomaterials* **12,** 1433 (2022).
10. Ackermann, J., Metternich, J. T., Herbertz, S. & Kruss, S. Biosensing with fluorescent carbon nanotubes. *Angew. Chem. Int. Ed.* **61,** e202112372 (2022).
11. Graf, A. *et al.* Electrical pumping and tuning of exciton-polaritons in carbon nanotube microcavities. *Nat. Mater.* **16,** 911–917 (2017).
12. Ghosh, S., Bachilo, S. M., Simonette, R. A., Beckingham, K. M. & Weisman, R. B. Oxygen doping modifies near-infrared band gaps in fluorescent single-walled carbon nanotubes. *Science* **330,** 1656–1659 (2010).
13. Piao, Y. *et al.* Brightening of carbon nanotube photoluminescence through the incorporation of sp^3 defects. *Nat. Chem.* **5,** 840–845 (2013).
14. He, X. *et al.* Tunable room-temperature single-photon emission at telecom wavelengths from defects in carbon nanotubes. *Nat. Photonics* **11,** 577–582 (2017).
15. Comandar, L. C. *et al.* Room temperature single-photon detectors for high bit rate quantum key distribution. *Appl. Phys. Lett.* **104,** 021101 (2014).

16. Diamanti, E., Lo, H.-K., Qi, B. & Yuan, Z. Practical challenges in quantum key distribution. *npj Quantum Inf.* **2,** 16025 (2016).

17. Wei, X. *et al.* Recent advances in structure separation of single-wall carbon nanotubes and their application in optics, electronics, and optoelectronics. *Adv. Sci.* **9,** e2200054 (2022).

18. Zaumseil, J. Luminescent defects in single-walled carbon nanotubes for applications. *Adv. Opt. Mater.* **10,** 2101576 (2022).

19. Sebastian, F. L. *et al.* Absolute quantification of sp^3 defects in semiconducting single-wall carbon nanotubes by Raman spectroscopy. *J. Phys. Chem. Lett.* **13,** 3542–3548 (2022).

20. Sebastian, F. L. *et al.* Unified quantification of quantum defects in small-diameter single-walled carbon nanotubes by Raman spectroscopy. *ACS Nano* **17,** 21771–21781 (2023).

21. Sebastian, F. L., Settele, S., Li, H., Flavel, B. S. & Zaumseil, J. How to recognize clustering of luminescent defects in single-wall carbon nanotubes. *Nanoscale Horiz.* **9,** 2286–2294 (2024).

22. Sebastian, F. L. *et al.* Circular dichroism of quantum defects in carbon nanotubes created by photocatalytic oxygen functionalization. *Nat. Commun.* **16,** 5107 (2025).

23. Liu, X. & Hersam, M. C. 2D materials for quantum information science. *Nat. Rev. Mater.* **4,** 669–684 (2019).

24. Chhowalla, M., Jena, D. & Zhang, H. Two-dimensional semiconductors for transistors. *Nat. Rev. Mater.* **1,** 16052 (2016).

25. Bao, C., Tang, P., Sun, D. & Zhou, S. Light-induced emergent phenomena in 2D materials and topological materials. *Nat. Rev. Phys.* **4,** 33–48 (2022).

26. Liu, X., Guo, Q. & Qiu, J. Emerging low-dimensional materials for nonlinear optics and ultrafast photonics. *Adv. Mater.* **29,** 1605886 (2017).

27. Meunier, V., Souza Filho, A. G., Barros, E. B. & Dresselhaus, M. S. Physical properties of low-dimensional sp^2-based carbon nanostructures. *Rev. Mod. Phys.* **88,** 025005 (2016).

28. Novoselov, K. S. *et al.* Electric field effect in atomically thin carbon films. *Science* **306,** 666–669 (2004).

29. Wang, Q. H., Kalantar-Zadeh, K., Kis, A., Coleman, J. N. & Strano, M. S. Electronics and optoelectronics of two-dimensional transition metal dichalcogenides. *Nat. Nanotechnol.* **7,** 699–712 (2012).

30. Manzeli, S., Ovchinnikov, D., Pasquier, D., Yazyev, O. V. & Kis, A. 2D transition metal dichalcogenides. *Nat. Rev. Mater.* **2,** 17033 (2017).

31. Geim, A. K. & Grigorieva, I. V. Van der Waals heterostructures. *Nature* **499,** 419–425 (2013).

32. Andrei, E. Y. *et al.* The marvels of moiré materials. *Nat. Rev. Mater.* **6,** 201–206 (2021).

33. Novoselov, K. S., Mishchenko, A., Carvalho, A. & Castro Neto, A. H. 2D materials and van der Waals heterostructures. *Science* **353,** aac9439 (2016).

34. Cao, Y. *et al.* Unconventional superconductivity in magic-angle graphene superlattices. *Nature* **556,** 43–50 (2018).

35. Ōsawa, E., Kroto, H. W., Fowler, P. W. & Wasserman, E. The evolution of the football structure for the C_{60} molecule: A retrospective. *Philos. Trans. R. Soc. A* **343,** 1–8 (1993).

36. Kroto, H. W., Heath, J. R., O'Brien, S. C., Curl, R. F. & Smalley, R. E. C_{60}: Buckminsterfullerene. *Nature* **318,** 162–163 (1985).

37. Brabec, C. J. *et al.* Polymer-fullerene bulk-heterojunction solar cells. *Adv. Mater.* **22,** 3839–3856 (2010).

38. Tan, Z. *et al.* Atomically defined angstrom-scale all-carbon junctions. *Nat. Commun.* **10,** 1748 (2019).

39. Castro, E., Hernandez Garcia, A., Zavala, G. & Echegoyen, L. Fullerenes in biology and medicine. *J. Mater. Chem. B* **5,** 6523–6535 (2017).

40. Wang, H. *et al.* Graphene nanoribbons for quantum electronics. *Nat. Rev. Phys.* **3,** 791–802 (2021).

41. Iijima, S. Helical microtubules of graphitic carbon. *Nature* **354,** 56–58 (1991).

42. White, C. T. & Todorov, T. N. Carbon nanotubes as long ballistic conductors. *Nature* **393,** 240–242 (1998).

43. Javey, A., Guo, J., Wang, Q., Lundstrom, M. & Dai, H. Ballistic carbon nanotube field-effect transistors. *Nature* **424,** 654–657 (2003).

44. Ericson, L. M. *et al.* Macroscopic, neat, single-walled carbon nanotube fibers. *Science* **305,** 1447–1450 (2004).

45. Treacy, M. M. J., Ebbesen, T. W. & Gibson, J. M. Exceptionally high Young's modulus observed for individual carbon nanotubes. *Nature* **381,** 678–680 (1996).

46. Komatsu, N. *et al.* Macroscopic weavable fibers of carbon nanotubes with giant thermoelectric power factor. *Nat. Commun.* **12,** 4931 (2021).

47. Massetti, M. *et al.* Unconventional thermoelectric materials for energy harvesting and sensing applications. *Chem. Rev.* **121,** 12465–12547 (2021).

48. Avouris, P., Freitag, M. & Perebeinos, V. Carbon-nanotube photonics and optoelectronics. *Nat. Photonics* **2,** 341–350 (2008).

49. Ovvyan, A. P. *et al.* An electroluminescent and tunable cavity-enhanced carbon-nanotube-emitter in the telecom band. *Nat. Commun.* **14,** 3933 (2023).

50. He, X. *et al.* Carbon nanotubes as emerging quantum-light sources. *Nat. Mater.* **17,** 663–670 (2018).

51. Li, M.-K., Dehm, S., Kappes, M. M., Hennrich, F. & Krupke, R. Correlation measurements for carbon nanotubes with quantum defects. *ACS Nano* **18,** 9525–9534 (2024).

52. Husel, L. *et al.* Cavity-enhanced photon indistinguishability at room temperature and telecom wavelengths. *Nat. Commun.* **15,** 3989 (2024).

53. Bianco, A., Kostarelos, K. & Prato, M. Applications of carbon nanotubes in drug delivery. *Curr. Opin. Chem. Biol.* **9,** 674–679 (2005).

54. Mandal, A. K. *et al.* Fluorescent sp^3 defect-tailored carbon nanotubes enable NIR-II single particle imaging in live brain slices at ultra-low excitation doses. *Sci. Rep.* **10,** 5286 (2020).

55. Nandi, S. *et al.* Ultrashort carbon nanotubes with luminescent color centers are bright NIR-II nanoemitters. *ACS Nano* **19,** 19818–19830 (2025).

56. Wong, H.-S. P. & Akinwande, D. *Carbon nanotube and graphene device physics* (Cambridge University Press, Cambridge, 2011).

57. Saito, R., Dresselhaus, G. & Dresselhaus, M. S. *Physical properties of carbon nanotubes* (Imperial College Press, London, 1998).

58. Odom, T. W., Huang, J.-L., Kim, P. & Lieber, C. M. Structure and electronic properties of carbon nanotubes. *J. Phys. Chem. B* **104,** 2794–2809 (2000).

59. Prasek, J. *et al.* Methods for carbon nanotubes synthesis-review. *J. Mater. Chem.* **21,** 15872–15884 (2011).

60. Yan, Y. *et al.* Carbon nanotube catalysts: Recent advances in synthesis, characterization and applications. *Chem. Soc. Rev.* **44,** 3295–3346 (2015).

61. Shi, Z. *et al.* Mass-production of single-wall carbon nanotubes by arc discharge method. *Carbon* **37,** 1449–1453 (1999).

62. Ando, Y. *et al.* Mass production of single-wall carbon nanotubes by the arc plasma jet method. *Chem. Phys. Lett.* **323,** 580–585 (2000).

63. Guo, T., Nikolaev, P., Thess, A., Colbert, D. T. & Smalley, R. E. Catalytic growth of single-walled nanotubes by laser vaporization. *Chem. Phys. Lett.* **243,** 49–54 (1995).

64. Yudasaka, M., Komatsu, T., Ichihashi, T. & Iijima, S. Single-wall carbon nanotube formation by laser ablation using double-targets of carbon and metal. *Chem. Phys. Lett.* **278,** 102–106 (1997).

65. Zhang, Y., Gu, H. & Iijima, S. Single-wall carbon nanotubes synthesized by laser ablation in a nitrogen atmosphere. *Appl. Phys. Lett.* **73,** 3827–3829 (1998).

66. Kim, K. S. *et al.* Large-scale production of single-walled carbon nanotubes by induction thermal plasma. *J. Phys. D: Appl. Phys.* **40,** 2375–2387 (2007).

67. Maruyama, S., Kojima, R., Miyauchi, Y., Chiashi, S. & Kohno, M. Low-temperature synthesis of high-purity single-walled carbon nanotubes from alcohol. *Chem. Phys. Lett.* **360,** 229–234 (2002).

68. Cassell, A. M., Raymakers, J. A., Kong, J. & Dai, H. Large scale CVD synthesis of single-walled carbon nanotubes. *J. Phys. Chem. B* **103,** 6484–6492 (1999).

69. Jourdain, V. & Bichara, C. Current understanding of the growth of carbon nanotubes in catalytic chemical vapour deposition. *Carbon* **58,** 2–39 (2013).

70. Ding, L. P. *et al.* Why carbon nanotubes grow. *J. Am. Chem. Soc.* **144,** 5606–5613 (2022).

71. Cassell, A. M. *et al.* Directed growth of free-standing single-walled carbon nanotubes. *J. Am. Chem. Soc.* **121,** 7975–7976 (1999).

72. Teo, K. B. K. *et al.* Uniform patterned growth of carbon nanotubes without surface carbon. *Appl. Phys. Lett.* **79,** 1534–1536 (2001).

73. Nikolaev, P. *et al.* Gas-phase catalytic growth of single-walled carbon nanotubes from carbon monoxide. *Chem. Phys. Lett.* **313,** 91–97 (1999).

74. Chiang, I. W. *et al.* Purification and characterization of single-wall carbon nanotubes (SWNTs) obtained from the gas-phase decomposition of CO (HiPco process). *J. Phys. Chem. B* **105,** 8297–8301 (2001).

75. Kitiyanan, B., Alvarez, W. E., Harwell, J. H. & Resasco, D. E. Controlled production of single-wall carbon nanotubes by catalytic decomposition of CO on bimetallic Co-Mo catalysts. *Chem. Phys. Lett.* **317,** 497–503 (2000).

76. Wang, B. *et al.* (n,m) selectivity of single-walled carbon nanotubes by different carbon precursors on Co-Mo catalysts. *J. Am. Chem. Soc.* **129,** 9014–9019 (2007).

77. Lolli, G. *et al.* Tailoring (n,m) structure of single-walled carbon nanotubes by modifying reaction conditions and the nature of the support of CoMo catalysts. *J. Phys. Chem. B* **110,** 2108–2115 (2006).

78. Bachilo, S. M. *et al.* Narrow (n,m)-distribution of single-walled carbon nanotubes grown using a solid supported catalyst. *J. Am. Chem. Soc.* **125,** 11186–11187 (2003).

79. Charlier, J.-C., De Vita, A., Blase, X. & Car, R. Microscopic growth mechanisms for carbon nanotubes. *Science* **275,** 646–649 (1997).

80. Sinnott, S. B. *et al.* Model of carbon nanotube growth through chemical vapor deposition. *Chem. Phys. Lett.* **315,** 25–30 (1999).

81. Artyukhov, V. I., Penev, E. S. & Yakobson, B. I. Why nanotubes grow chiral. *Nat. Commun.* **5,** 4892 (2014).

82. Magnin, Y., Amara, H., Ducastelle, F., Loiseau, A. & Bichara, C. Entropy-driven stability of chiral single-walled carbon nanotubes. *Science* **362,** 212–215 (2018).

83. Hedman, D. *et al.* Dynamics of growing carbon nanotube interfaces probed by machine learning-enabled molecular simulations. *Nat. Commun.* **15,** 4076 (2024).

84. Sun, S., Maruyama, S. & Li, Y. Chirality-dependent kinetics of single-walled carbon nanotubes from machine-learning force fields. *J. Am. Chem. Soc.* **147,** 7103–7112 (2025).

85. Yang, F. *et al.* Chirality pure carbon nanotubes: Growth, sorting, and characterization. *Chem. Rev.* **120,** 2693–2758 (2020).

86. Sanchez-Valencia, J. R. *et al.* Controlled synthesis of single-chirality carbon nanotubes. *Nature* **512,** 61–64 (2014).

87. Yang, F. *et al.* Chirality-specific growth of single-walled carbon nanotubes on solid alloy catalysts. *Nature* **510,** 522–524 (2014).

88. Wang, X. & Ding, F. How a solid catalyst determines the chirality of the single-wall carbon nanotube grown on it. *J. Phys. Chem. Lett.* **10,** 735–741 (2019).

89. Coleman, J. N. Liquid-phase exfoliation of nanotubes and graphene. *Adv. Funct. Mater.* **19,** 3680–3695 (2009).

90. Hasan, T. *et al.* Stabilization and "debundling" of single-wall carbon nanotube dispersions in *N*-Methyl-2-pyrrolidone (NMP) by polyvinylpyrrolidone (PVP). *J. Phys. Chem. C* **111,** 12594–12602 (2007).

91. Bergin, S. D. *et al.* Towards solutions of single-walled carbon nanotubes in common solvents. *Adv. Mater.* **20,** 1876–1881 (2008).

92. Bergin, S. D. *et al.* Multicomponent solubility parameters for single-walled carbon nanotube-solvent mixtures. *ACS Nano* **3,** 2340–2350 (2009).

93. Cheng, Q., Debnath, S., Gregan, E. & Byrne, H. J. Ultrasound-assisted SWNTs dispersion: Effects of sonication parameters and solvent properties. *J. Phys. Chem. C* **114,** 8821–8827 (2010).

94. Wenseleers, W. *et al.* Efficient isolation and solubilization of pristine single-walled nanotubes in bile salt micelles. *Adv. Funct. Mater.* **14,** 1105–1112 (2004).

95. Graf, A. *et al.* Large scale, selective dispersion of long single-walled carbon nanotubes with high photoluminescence quantum yield by shear force mixing. *Carbon* **105,** 593–599 (2016).

96. Hwang, J.-Y. *et al.* Polymer structure and solvent effects on the selective dispersion of single-walled carbon nanotubes. *J. Am. Chem. Soc.* **130,** 3543–3553 (2008).

97. Lee, H. W. *et al.* Selective dispersion of high purity semiconducting single-walled carbon nanotubes with regioregular poly(3-alkylthiophene)s. *Nat. Commun.* **2,** 541 (2011).

98. Gomulya, W. *et al.* Semiconducting single-walled carbon nanotubes on demand by polymer wrapping. *Adv. Mater.* **25,** 2948–2956 (2013).

99. Samanta, S. K. *et al.* Conjugated polymer-assisted dispersion of single-wall carbon nanotubes: The power of polymer wrapping. *Acc. Chem. Res.* **47,** 2446–2456 (2014).

100. Gu, J. *et al.* Solution-processable high-purity semiconducting SWCNTs for large-area fabrication of high-performance thin-film transistors. *Small* **12,** 4993–4999 (2016).

101. Nish, A., Hwang, J.-Y., Doig, J. & Nicholas, R. J. Highly selective dispersion of single-walled carbon nanotubes using aromatic polymers. *Nat. Nanotechnol.* **2,** 640–646 (2007).

102. Ozawa, H., Ide, N., Fujigaya, T., Niidome, Y. & Nakashima, N. One-pot separation of highly enriched (6,5)-single-walled carbon nanotubes using a fluorene-based copolymer. *Chem. Lett.* **40,** 239–241 (2011).

103. Gao, J., Loi, M. A., de Carvalho, E. J. & dos Santos, M. C. Selective wrapping and supramolecular structures of polyfluorene-carbon nanotube hybrids. *ACS Nano* **5,** 3993–3999 (2011).

104. Joo, Y. *et al.* Isolation of pristine electronics grade semiconducting carbon nanotubes by switching the rigidity of the wrapping polymer backbone on demand. *ACS Nano* **9,** 10203–10213 (2015).

105. Derenskyi, V. *et al.* Semiconducting SWNTs sorted by polymer wrapping: How pure are they? *Appl. Phys. Lett.* **112,** 072106 (2018).

106. Zorn, N. F., Berger, F. J. & Zaumseil, J. Charge transport in and electroluminescence from sp^3-functionalized carbon nanotube networks. *ACS Nano* **15,** 10451–10463 (2021).

107. Khripin, C. Y., Fagan, J. A. & Zheng, M. Spontaneous partition of carbon nanotubes in polymer-modified aqueous phases. *J. Am. Chem. Soc.* **135,** 6822–6825 (2013).

108. Fagan, J. A. *et al.* Isolation of specific small-diameter single-wall carbon nanotube species *via* aqueous two-phase extraction. *Adv. Mater.* **26,** 2800–2804 (2014).

109. Fagan, J. A. Aqueous two-polymer phase extraction of single-wall carbon nanotubes using surfactants. *Nanoscale Adv.* **1,** 3307–3324 (2019).

110. Sims, C. M., Zheng, M. & Fagan, J. A. Single-wall carbon nanotube separations *via* aqueous two-phase extraction: New prospects enabled by high-throughput methods. *Chem. Commun.* **61,** 2026–2039 (2025).

111. Li, H. *et al.* Separation of specific single-enantiomer single-wall carbon nanotubes in the large-diameter regime. *ACS Nano* **14,** 948–963 (2020).

112. Li, H. *et al.* Isolation of the (6,5) single-wall carbon nanotube enantiomers by surfactant-assisted aqueous two-phase extraction. *Carbon* **204,** 475–483 (2023).

113. Blanch, A. J., Lenehan, C. E. & Quinton, J. S. Optimizing surfactant concentrations for dispersion of single-walled carbon nanotubes in aqueous solution. *J. Phys. Chem. B* **114,** 9805–9811 (2010).

114. Sims, C. M. & Fagan, J. A. Orthogonal determination of competing surfactant adsorption onto single-wall carbon nanotubes during aqueous two-polymer phase extraction *via* fluorescence spectroscopy and analytical ultracentrifugation. *J. Phys. Chem. C* **128,** 13064–13073 (2024).

115. Subbaiyan, N. K. *et al.* Role of surfactants and salt in aqueous two-phase separation of carbon nanotubes toward simple chirality isolation. *ACS Nano* **8,** 1619–1628 (2014).

116. Zeng, X. *et al.* Detecting and tuning the interactions between surfactants and carbon nanotubes for their high-efficiency structure separation. *Adv. Mater. Interfaces* **5,** 1700727 (2018).

117. Alizadehmojarad, A. A., Bachilo, S. M., Kolomeisky, A. B. & Weisman, R. B. Morphology transitions of SDS coatings on single-walled carbon nanotubes. *J. Phys. Chem. C* **128,** 6126–6132 (2024).

118. Tummala, N. R. & Striolo, A. SDS surfactants on carbon nanotubes: Aggregate morphology. *ACS Nano* **3,** 595–602 (2009).

119. Duan, W. H., Wang, Q. & Collins, F. Dispersion of carbon nanotubes with SDS surfactants: A study from a binding energy perspective. *Chem. Sci.* **2,** 1407–1413 (2011).

120. Wei, L., Flavel, B. S., Li, W., Krupke, R. & Chen, Y. Exploring the upper limit of single-walled carbon nanotube purity by multiple-cycle aqueous two-phase separation. *Nanoscale* **9,** 11640–11646 (2017).

121. Sims, C. M. & Fagan, J. A. An automated gradient titration fluorescence methodology for high-resolution identification of aqueous two-polymer phase extraction conditions for single-wall carbon nanotubes. *Carbon* **219,** 118813 (2024).

122. Moshammer, K., Hennrich, F. & Kappes, M. M. Selective suspension in aqueous sodium dodecyl sulfate according to electronic structure type allows simple separation of metallic from semiconducting single-walled carbon nanotubes. *Nano Res.* **2,** 599–606 (2009).

123. Liu, H., Nishide, D., Tanaka, T. & Kataura, H. Large-scale single-chirality separation of single-wall carbon nanotubes by simple gel chromatography. *Nat. Commun.* **2,** 309 (2011).

124. Flavel, B. S., Moore, K. E., Pfohl, M., Kappes, M. M. & Hennrich, F. Separation of single-walled carbon nanotubes with a gel permeation chromatography system. *ACS Nano* **8,** 1817–1826 (2014).

125. Yomogida, Y., Tanaka, T., Tsuzuki, M., Wei, X. & Kataura, H. Automatic sorting of single-chirality single-wall carbon nanotubes using hydrophobic cholates: Implications for multicolor near-infrared optical technologies. *ACS Appl. Nano Mater.* **3,** 11289–11297 (2020).

126. Zhao, Y. *et al.* Selective desorption of high-purity (6,5) SWCNTs from hydrogels through surfactant modulation. *Chem. Commun.* **52,** 2928–2931 (2016).

127. Wei, X. *et al.* Experimental determination of excitonic band structures of single-walled carbon nanotubes using circular dichroism spectra. *Nat. Commun.* **7,** 12899 (2016).

128. Wei, X., Tanaka, T., Hirakawa, T., Yomogida, Y. & Kataura, H. Determination of enantiomeric purity of single-wall carbon nanotubes using flavin mononucleotide. *J. Am. Chem. Soc.* **139,** 16068–16071 (2017).

129. Wei, X. *et al.* High-yield and high-throughput single-chirality enantiomer separation of single-wall carbon nanotubes. *Carbon* **132,** 1–7 (2018).

130. Wei, X. *et al.* Length-dependent enantioselectivity of carbon nanotubes by gel chromatography. *ACS Nano* **17,** 8393–8402 (2023).

131. Tvrdy, K. *et al.* A kinetic model for the deterministic prediction of gel-based single-chirality single-walled carbon nanotube separation. *ACS Nano* **7,** 1779–1789 (2013).

132. Liu, H., Tanaka, T., Urabe, Y. & Kataura, H. High-efficiency single-chirality separation of carbon nanotubes using temperature-controlled gel chromatography. *Nano Lett.* **13,** 1996–2003 (2013).

133. Mintmire, J. W. & White, C. T. Electronic and structural properties of carbon nanotubes. *Carbon* **33,** 893–902 (1995).

134. Charlier, J.-C., Blase, X. & Roche, S. Electronic and transport properties of nanotubes. *Rev. Mod. Phys.* **79,** 677–732 (2007).

135. Reich, S., Maultzsch, J., Thomsen, C. & Ordejón, P. Tight-binding description of graphene. *Phys. Rev. B* **66,** 035412 (2002).

136. Barros, E. B. *et al.* Review on the symmetry-related properties of carbon nanotubes. *Phys. Rep.* **431,** 261–302 (2006).

137. Weisman, R. B. & Bachilo, S. M. Dependence of optical transition energies on structure for single-walled carbon nanotubes in aqueous suspension: An empirical Kataura plot. *Nano Lett.* **3,** 1235–1238 (2003).

138. Strano, M. S. Probing chiral selective reactions using a revised Kataura plot for the interpretation of single-walled carbon nanotube spectroscopy. *J. Am. Chem. Soc.* **125,** 16148–16153 (2003).

139. Saito, R., Dresselhaus, G. & Dresselhaus, M. S. Trigonal warping effect of carbon nanotubes. *Phys. Rev. B* **61,** 2981–2990 (2000).

140. Carlson, L. J. & Krauss, T. D. Photophysics of individual single-walled carbon nanotubes. *Acc. Chem. Res.* **41,** 235–243 (2008).

141. Reich, S., Thomsen, C. & Ordejón, P. Electronic band structure of isolated and bundled carbon nanotubes. *Phys. Rev. B* **65,** 155411 (2002).

142. Zólyomi, V. & Kürti, J. First-principles calculations for the electronic band structures of small diameter single-wall carbon nanotubes. *Phys. Rev. B* **70,** 085403 (2004).

143. Miyauchi, Y., Oba, M. & Maruyama, S. Cross-polarized optical absorption of single-walled nanotubes by polarized photoluminescence excitation spectroscopy. *Phys. Rev. B* **74,** 205440 (2006).

144. Wang, Y. *et al.* Receiving and transmitting light-like radio waves: Antenna effect in arrays of aligned carbon nanotubes. *Appl. Phys. Lett.* **85,** 2607–2609 (2004).

145. Blancon, J.-C. *et al.* Direct measurement of the absolute absorption spectrum of individual semiconducting single-wall carbon nanotubes. *Nat. Commun.* **4,** 2542 (2013).

146. Plentz, F., Ribeiro, H. B., Jorio, A., Strano, M. S. & Pimenta, M. A. Direct experimental evidence of exciton-phonon bound states in carbon nanotubes. *Phys. Rev. Lett.* **95,** 247401 (2005).

147. Dresselhaus, M. S., Dresselhaus, G., Saito, R. & Jorio, A. Exciton photophysics of carbon nanotubes. *Annu. Rev. Phys. Chem.* **58,** 719–747 (2007).

148. Amori, A. R., Hou, Z. & Krauss, T. D. Excitons in single-walled carbon nanotubes and their dynamics. *Annu. Rev. Phys. Chem.* **69,** 81–99 (2018).

149. Spataru, C. D., Ismail-Beigi, S., Benedict, L. X. & Louie, S. G. Excitonic effects and optical spectra of single-walled carbon nanotubes. *Phys. Rev. Lett.* **92,** 077402 (2004).

150. Wang, F., Dukovic, G., Brus, L. E. & Heinz, T. F. The optical resonances in carbon nanotubes arise from excitons. *Science* **308,** 838–841 (2005).

151. Nguyen, D. T. *et al.* Elastic exciton-exciton scattering in photoexcited carbon nanotubes. *Phys. Rev. Lett.* **107,** 127401 (2011).

152. Perebeinos, V., Tersoff, J. & Avouris, P. Radiative lifetime of excitons in carbon nanotubes. *Nano Lett.* **5,** 2495–2499 (2005).

153. Mortimer, I. B. & Nicholas, R. J. Role of bright and dark excitons in the temperature-dependent photoluminescence of carbon nanotubes. *Phys. Rev. Lett.* **98,** 027404 (2007).

154. Blackburn, J. L., Holt, J. M., Irurzun, V. M., Resasco, D. E. & Rumbles, G. Confirmation of K-momentum dark exciton vibronic sidebands using ^{13}C-labeled, highly enriched (6,5) single-walled carbon nanotubes. *Nano Lett.* **12,** 1398–1403 (2012).

155. Harrah, D. M. *et al.* Intensity-dependent exciton dynamics of (6,5) single-walled carbon nanotubes: Momentum selection rules, diffusion, and nonlinear interactions. *ACS Nano* **5,** 9898–9906 (2011).

156. Soavi, G., Scotognella, F., Lanzani, G. & Cerullo, G. Ultrafast photophysics of single-walled carbon nanotubes. *Adv. Opt. Mater.* **4,** 1670–1688 (2016).

157. Jones, M. *et al.* Analysis of photoluminescence from solubilized single-walled carbon nanotubes. *Phys. Rev. B* **71,** 115426 (2005).

158. Lefebvre, J., Fraser, J. M., Finnie, P. & Homma, Y. Photoluminescence from an individual single-walled carbon nanotube. *Phys. Rev. B* **69,** 075403 (2004).

159. Moritsubo, S. *et al.* Exciton diffusion in air-suspended single-walled carbon nanotubes. *Phys. Rev. Lett.* **104,** 247402 (2010).

160. Amori, A. R., Rossi, J. E., Landi, B. J. & Krauss, T. D. Defects enable dark exciton photoluminescence in single-walled carbon nanotubes. *J. Phys. Chem. C* **122,** 3599–3607 (2018).

161. Tumiel, T. M., Amin, M. & Krauss, T. D. Single-walled carbon nanotube dark exciton photoluminescence dynamics. *J. Phys. Chem. C* **125,** 25022–25029 (2021).

162. Kadria-Vili, Y., Bachilo, S. M., Blackburn, J. L. & Weisman, R. B. Photoluminescence side band spectroscopy of individual single-walled carbon nanotubes. *J. Phys. Chem. C* **120,** 23898–23904 (2016).

163. Zorn, N. F. *et al.* Near-intrinsic photo- and electroluminescence from single-walled carbon nanotube thin films on BCB-passivated surfaces. *Adv. Opt. Mater.* **11,** 2300236 (2023).

164. Matsunaga, R., Matsuda, K. & Kanemitsu, Y. Observation of charged excitons in hole-doped carbon nanotubes using photoluminescence and absorption spectroscopy. *Phys. Rev. Lett.* **106,** 037404 (2011).

165. Santos, S. M. *et al.* All-optical trion generation in single-walled carbon nanotubes. *Phys. Rev. Lett.* **107,** 187401 (2011).

166. Nishihara, T., Yamada, Y., Okano, M. & Kanemitsu, Y. Trion formation and recombination dynamics in hole-doped single-walled carbon nanotubes. *Appl. Phys. Lett.* **103,** 023101 (2013).

167. Hertel, T., Himmelein, S., Ackermann, T., Stich, D. & Crochet, J. Diffusion limited photoluminescence quantum yields in 1-D semiconductors: Single-wall carbon nanotubes. *ACS Nano* **4,** 7161–7168 (2010).

168. Liu, T. & Xiao, Z. W. Exact and closed form solutions for the quantum yield, exciton diffusion length, and lifetime to reveal the universal behaviors of the photoluminescence of defective single-walled carbon nanotubes. *J. Phys. Chem. C* **115,** 16920–16927 (2011).

169. Hofmann, M. S., Noe, J., Kneer, A., Crochet, J. J. & Högele, A. Ubiquity of exciton localization in cryogenic carbon nanotubes. *Nano Lett.* **16,** 2958–2962 (2016).

170. Birkmeier, K., Hertel, T. & Hartschuh, A. Probing the ultrafast dynamics of excitons in single semiconducting carbon nanotubes. *Nat. Commun.* **13,** 6290 (2022).

171. Ishii, A., Machiya, H. & Kato, Y. K. High efficiency dark-to-bright exciton conversion in carbon nanotubes. *Phys. Rev. X* **9,** 041048 (2019).

172. Ishii, A., Yoshida, M. & Kato, Y. K. Exciton diffusion, end quenching, and exciton-exciton annihilation in individual air-suspended carbon nanotubes. *Phys. Rev. B* **91,** 125427 (2015).

173. Ohno, Y. *et al.* Excitonic transition energies in single-walled carbon nanotubes: Dependence on environmental dielectric constant. *Phys. Status Solidi B* **244,** 4002–4005 (2007).

174. Larsen, B. A. *et al.* Effect of solvent polarity and electrophilicity on quantum yields and solvatochromic shifts of single-walled carbon nanotube photoluminescence. *J. Am. Chem. Soc.* **134,** 12485–12491 (2012).

175. Nishida, J., Otsuka, K., Minato, T., Kato, Y. K. & Kumagai, T. Ultrafast infrared nano-imaging of local electron-hole dynamics in CVD-grown single-walled carbon nanotubes. *Sci. Adv.* **11,** eadv9584 (2025).

176. Choi, J. H. & Strano, M. S. Solvatochromism in single-walled carbon nanotubes. *Appl. Phys. Lett.* **90,** 223114 (2007).

177. Silvera-Batista, C. A., Wang, R. K., Weinberg, P. & Ziegler, K. J. Solvatochromic shifts of single-walled carbon nanotubes in nonpolar microenvironments. *Phys. Chem. Chem. Phys.* **12,** 6990–6998 (2010).

178. Zhao, H. & Mazumdar, S. Electron-electron interaction effects on the optical excitations of semiconducting single-walled carbon nanotubes. *Phys. Rev. Lett.* **93,** 157402 (2004).

179. McDonald, T. J., Engtrakul, C., Jones, M., Rumbles, G. & Heben, M. J. Kinetics of PL quenching during single-walled carbon nanotube rebundling and diameter-dependent surfactant interactions. *J. Phys. Chem. B* **110,** 25339–25346 (2006).

180. Satishkumar, B. C. *et al.* Reversible fluorescence quenching in carbon nanotubes for biomolecular sensing. *Nat. Nanotechnol.* **2,** 560–564 (2007).

181. Cognet, L. *et al.* Stepwise quenching of exciton fluorescence in carbon nanotubes by single-molecule reactions. *Science* **316,** 1465–1468 (2007).

182. Sato, N., Tatsumi, Y. & Saito, R. Circular dichroism of single-wall carbon nanotubes. *Phys. Rev. B* **95,** 155436 (2017).

183. Tasaki, S., Maekawa, K. & Yamabe, T. π-band contribution to the optical properties of carbon nanotubes: Effects of chirality. *Phys. Rev. B* **57,** 9301–9318 (1998).

184. Ivchenko, E. L. & Spivak, B. Chirality effects in carbon nanotubes. *Phys. Rev. B* **66,** 155404 (2002).

185. Samsonidze, G. G. *et al.* Interband optical transitions in left- and right-handed single-wall carbon nanotubes. *Phys. Rev. B* **69,** 205402 (2004).

186. Sánchez-Castillo, A., Román-Velázquez, C. E. & Noguez, C. Optical circular dichroism of single-wall carbon nanotubes. *Phys. Rev. B* **73,** 045401 (2006).

187. Sánchez-Castillo, A. & Noguez, C. Understanding optical activity in single-walled carbon nanotubes from first-principles studies. *J. Phys. Chem. C* **114,** 9640–9644 (2010).

188. Dukovic, G. *et al.* Racemic single-walled carbon nanotubes exhibit circular dichroism when wrapped with DNA. *J. Am. Chem. Soc.* **128,** 9004–9005 (2006).

189. Peng, X. *et al.* Optically active single-walled carbon nanotubes. *Nat. Nanotechnol.* **2,** 361–365 (2007).

190. Wang, F. *et al.* Simultaneous discrimination of handedness and diameter of single-walled carbon nanotubes (SWNTs) with chiral diporphyrin nanotweezers leading to enrichment of a single enantiomer of (6,5)-SWNTs. *J. Am. Chem. Soc.* **132,** 10876–10881 (2010).

191. Green, A. A., Duch, M. C. & Hersam, M. C. Isolation of single-walled carbon nanotube enantiomers by density differentiation. *Nano Res.* **2,** 69–77 (2009).

192. Ao, G., Streit, J. K., Fagan, J. A. & Zheng, M. Differentiating left- and right-handed carbon nanotubes by DNA. *J. Am. Chem. Soc.* **138,** 16677–16685 (2016).

193. Liu, H., Tanaka, T. & Kataura, H. Optical isomer separation of single-chirality carbon nanotubes using gel column chromatography. *Nano Lett.* **14,** 6237–6243 (2014).

194. Tanaka, T., Urabe, Y., Hirakawa, T. & Kataura, H. Simultaneous chirality and enantiomer separation of metallic single-wall carbon nanotubes by gel column chromatography. *Anal. Chem.* **87,** 9467–9472 (2015).

195. Xu, L. *et al.* Enantiomeric separation of semiconducting single-walled carbon nanotubes by acid cleavable chiral polyfluorene. *ACS Nano* **15,** 4699–4709 (2021).

196. Magg, M., Kadria-Vili, Y., Oulevey, P., Weisman, R. B. & Bürgi, T. Resonance Raman optical activity spectra of single-walled carbon nanotube enantiomers. *J. Phys. Chem. Lett.* **7,** 221–225 (2016).

197. Yao, F. *et al.* Complete structural characterization of single carbon nanotubes by Rayleigh scattering circular dichroism. *Nat. Nanotechnol.* **16,** 1073–1078 (2021).

198. Erkens, M. *et al.* Hyperspectral detection of the fluorescence shift between chirality-sorted empty and water-filled single-wall carbon nanotube enantiomers. *ACS Nano* **18,** 14532–14545 (2024).

199. Diederich, F. & Thilgen, C. Covalent fullerene chemistry. *Science* **271,** 317–323 (1996).

200. Niyogi, S. *et al.* Chemistry of single-walled carbon nanotubes. *Acc. Chem. Res.* **35,** 1105–1113 (2002).

201. Hirsch, A. Functionalization of single-walled carbon nanotubes. *Angew. Chem. Int. Ed.* **41,** 1853–1859 (2002).

202. Holzinger, M. *et al.* Sidewall functionalization of carbon nanotubes. *Angew. Chem. Int. Ed.* **40,** 4002–4005 (2001).

203. Bahr, J. L. *et al.* Functionalization of carbon nanotubes by electrochemical reduction of aryl diazonium salts: A bucky paper electrode. *J. Am. Chem. Soc.* **123,** 6536–6542 (2001).

204. Bahr, J. L. & Tour, J. M. Highly functionalized carbon nanotubes using *in situ* generated diazonium compounds. *Chem. Mater.* **13,** 3823–3824 (2001).

205. Mawhinney, D. B. *et al.* Infrared spectral evidence for the etching of carbon nanotubes: Ozone oxidation at 298 K. *J. Am. Chem. Soc.* **122,** 2383–2384 (2000).

206. Banerjee, S., Kahn, M. G. C. & Wong, S. S. Rational chemical strategies for carbon nanotube functionalization. *Chem. Eur. J.* **9,** 1898–1908 (2003).

207. Kuznetsova, A. *et al.* Oxygen-containing functional groups on single-wall carbon nanotubes: NEXAFS and vibrational spectroscopic studies. *J. Am. Chem. Soc.* **123,** 10699–10704 (2001).

208. Georgakilas, V. *et al.* Organic functionalization of carbon nanotubes. *J. Am. Chem. Soc.* **124,** 760–761 (2002).

209. Sun, Y. P., Fu, K., Lin, Y. & Huang, W. Functionalized carbon nanotubes: Properties and applications. *Acc. Chem. Res.* **35,** 1096–1104 (2002).

210. Miyauchi, Y. *et al.* Brightening of excitons in carbon nanotubes on dimensionality modification. *Nat. Photonics* **7,** 715–719 (2013).

211. Hartmann, N. F. *et al.* Photoluminescence dynamics of aryl sp^3 defect states in single-walled carbon nanotubes. *ACS Nano* **10,** 8355–8365 (2016).

212. Brozena, A. H., Kim, M., Powell, L. R. & Wang, Y. Controlling the optical properties of carbon nanotubes with organic colour-centre quantum defects. *Nat. Rev. Chem.* **3,** 375–392 (2019).

213. Janas, D. Perfectly imperfect: A review of chemical tools for exciton engineering in single-walled carbon nanotubes. *Mater. Horiz.* **7,** 2860–2881 (2020).

214. Shiraki, T., Miyauchi, Y., Matsuda, K. & Nakashima, N. Carbon nanotube photoluminescence modulation by local chemical and supramolecular chemical functionalization. *Acc. Chem. Res.* **53,** 1846–1859 (2020).

215. Gifford, B. J., Kilina, S., Htoon, H., Doorn, S. K. & Tretiak, S. Controlling defect-state photophysics in covalently functionalized single-walled carbon nanotubes. *Acc. Chem. Res.* **53,** 1791–1801 (2020).

216. Ma, X., Hartmann, N. F., Baldwin, J. K., Doorn, S. K. & Htoon, H. Room-temperature single-photon generation from solitary dopants of carbon nanotubes. *Nat. Nanotechnol.* **10,** 671–675 (2015).

217. Kilina, S., Ramirez, J. & Tretiak, S. Brightening of the lowest exciton in carbon nanotubes *via* chemical functionalization. *Nano Lett.* **12,** 2306–2312 (2012).

218. Kim, M. *et al.* Fluorescent carbon nanotube defects manifest substantial vibrational reorganization. *J. Phys. Chem. C* **120,** 11268–11276 (2016).

219. Ma, X. *et al.* Electronic structure and chemical nature of oxygen dopant states in carbon nanotubes. *ACS Nano* **8,** 10782–10789 (2014).

220. Hartmann, N. F. *et al.* Photoluminescence imaging of solitary dopant sites in covalently doped single-wall carbon nanotubes. *Nanoscale* **7,** 20521–20530 (2015).

221. Settele, S. *et al.* Synthetic control over the binding configuration of luminescent sp^3-defects in single-walled carbon nanotubes. *Nat. Commun.* **12,** 2119 (2021).

222. Settele, S. *et al.* Easy access to bright oxygen defects in biocompatible single-walled carbon nanotubes *via* a Fenton-like reaction. *ACS Nano* **18,** 20667–20678 (2024).

223. Spataru, C. D., Ismail-Beigi, S., Capaz, R. B. & Louie, S. G. Theory and ab initio calculation of radiative lifetime of excitons in semiconducting carbon nanotubes. *Phys. Rev. Lett.* **95,** 247402 (2005).

224. He, X. *et al.* Solvent- and wavelength-dependent photoluminescence relaxation dynamics of carbon nanotube sp^3 defect states. *ACS Nano* **12,** 8060–8070 (2018).

225. Cherukuri, T. K., Tsyboulski, D. A. & Weisman, R. B. Length- and defect-dependent fluorescence efficiencies of individual single-walled carbon nanotubes. *ACS Nano* **6,** 843–850 (2012).

226. Sykes, M. E. *et al.* Ultrafast exciton trapping at sp^3 quantum defects in carbon nanotubes. *ACS Nano* **13,** 13264–13270 (2019).

227. Danné, N. *et al.* Ultrashort carbon nanotubes that fluoresce brightly in the near-infrared. *ACS Nano* **12,** 6059–6065 (2018).

228. Kozawa, D. *et al.* Formation of organic color centers in air-suspended carbon nanotubes using vapor-phase reaction. *Nat. Commun.* **13,** 2814 (2022).

229. Shiraki, T., Shiraishi, T., Juhasz, G. & Nakashima, N. Emergence of new red-shifted carbon nanotube photoluminescence based on proximal doped-site design. *Sci. Rep.* **6,** 28393 (2016).

230. Berger, F. J. *et al.* Brightening of long, polymer-wrapped carbon nanotubes by sp^3 functionalization in organic solvents. *ACS Nano* **13,** 9259–9269 (2019).

231. Yu, B. *et al. ortho*-substituted aryldiazonium design for the defect configuration-controlled photoluminescent functionalization of chiral single-walled carbon nanotubes. *ACS Nano* **16,** 21452–21461 (2022).

232. Kim, Y. *et al.* Photoluminescence intensity fluctuations and temperature-dependent decay dynamics of individual carbon nanotube sp^3 defects. *J. Phys. Chem. Lett.* **10,** 1423–1430 (2019).

233. Perebeinos, V. & Avouris, P. Phonon and electronic nonradiative decay mechanisms of excitons in carbon nanotubes. *Phys. Rev. Lett.* **101,** 057401 (2008).

234. Englman, R. & Jortner, J. The energy gap law for radiationless transitions in large molecules. *Mol. Phys.* **18,** 145–164 (1970).

235. Gifford, B. J., Kilina, S., Htoon, H., Doorn, S. K. & Tretiak, S. Exciton localization and optical emission in aryl-functionalized carbon nanotubes. *J. Phys. Chem. C* **122,** 1828–1838 (2018).

236. Kwon, H. *et al.* Probing trions at chemically tailored trapping defects. *ACS Cent. Sci.* **5,** 1786–1794 (2019).

237. He, X. *et al.* Intrinsic limits of defect-state photoluminescence dynamics in functionalized carbon nanotubes. *Nanoscale* **11,** 9125–9132 (2019).

238. Borel, A., Rapisarda, F., Doorn, S. K., Voisin, C. & Chassagneux, Y. Luminescence properties of closely packed organic color centers grafted on a carbon nanotube. *Nano Lett.* **24,** 3456–3461 (2024).

239. Iwamura, M. *et al.* Nonlinear photoluminescence spectroscopy of carbon nanotubes with localized exciton states. *ACS Nano* **8,** 11254–11260 (2014).

240. Kwon, H. *et al.* Molecularly tunable fluorescent quantum defects. *J. Am. Chem. Soc.* **138,** 6878–6885 (2016).

241. Gifford, B. J. *et al.* Optical effects of divalent functionalization of carbon nanotubes. *Chem. Mater.* **31,** 6950–6961 (2019).

242. Maeda, Y. *et al.* Influence of local strain caused by cycloaddition on the band gap control of functionalized single-walled carbon nanotubes. *RSC Adv.* **9,** 13998–14003 (2019).

243. Hayashi, K. *et al.* Azide modification forming luminescent sp^2 defects on single-walled carbon nanotubes for near-infrared defect photoluminescence. *Chem. Commun.* **58,** 11422–11425 (2022).

244. Wang, P. *et al.* Quantum defects: What pairs with the aryl group when bonding to the sp^2 carbon lattice of single-wall carbon nanotubes? *J. Am. Chem. Soc.* **144,** 13234–13241 (2022).

245. He, X. *et al.* Low-temperature single carbon nanotube spectroscopy of sp^3 quantum defects. *ACS Nano* **11,** 10785–10796 (2017).

246. Saha, A. *et al.* Narrow-band single-photon emission through selective aryl functionalization of zigzag carbon nanotubes. *Nat. Chem.* **10,** 1089–1095 (2018).

247. Zheng, Y. *et al.* Photochemical spin-state control of binding configuration for tailoring organic color center emission in carbon nanotubes. *Nat. Commun.* **13,** 4439 (2022).

248. Banerjee, S., Hemraj-Benny, T. & Wong, S. S. Covalent surface chemistry of single-walled carbon nanotubes. *Adv. Mater.* **17,** 17–29 (2005).

249. Tasis, D., Tagmatarchis, N., Bianco, A. & Prato, M. Chemistry of carbon nanotubes. *Chem. Rev.* **106,** 1105–1136 (2006).

250. Doyle, C. D., Rocha, J. D., Weisman, R. B. & Tour, J. M. Structure-dependent reactivity of semiconducting single-walled carbon nanotubes with benzenediazonium salts. *J. Am. Chem. Soc.* **130,** 6795–6800 (2008).

251. Yurekli, K., Mitchell, C. A. & Krishnamoorti, R. Small-angle neutron scattering from surfactant-assisted aqueous dispersions of carbon nanotubes. *J. Am. Chem. Soc.* **126,** 9902–9903 (2004).

252. Przypis, L. *et al.* Enhancing near-infrared photoluminescence from single-walled carbon nanotubes by defect-engineering using benzoyl peroxide. *Sci. Rep.* **10,** 19877 (2020).

253. Huang, Z. *et al.* Photolithographic patterning of organic color-centers. *Adv. Mater.* **32,** e1906517 (2020).

254. Dou, Q., Xu, B., Wu, X., Mo, J. & Wang, Y. Tunable photo-patterning of organic color-centers. *Mater. Des.* **212,** 110252 (2021).

255. Gordeev, G., Rosenkranz, T., Hennrich, F., Reich, S. & Krupke, R. Light control over chirality selective functionalization of substrate supported carbon nanotubes. *J. Phys. Chem. C* **126,** 9803–9812 (2022).

256. Just, D., Siedlecki, R., Podleśny, B. & Janas, D. Synchronous sorting and functionalization of single-walled carbon nanotubes using organic derivatives of hydrazine. *Adv. Opt. Mater.* **13,** 2402873 (2025).

257. Taborowska, P., Dzienia, A. & Janas, D. Unraveling aryl peroxide chemistry to enrich optical properties of single-walled carbon nanotubes. *Chem. Sci.* **16,** 1374–1389 (2025).

258. Luo, H.-B. *et al.* One-pot, large-scale synthesis of organic color center-tailored semiconducting carbon nanotubes. *ACS Nano* **13,** 8417–8424 (2019).

259. Wu, X., Kim, M., Kwon, H. & Wang, Y. Photochemical creation of fluorescent quantum defects in semiconducting carbon nanotube hosts. *Angew. Chem. Int. Ed.* **57,** 648–653 (2018).

260. Zheng, Y., Bachilo, S. M. & Weisman, R. B. Photoexcited aromatic reactants give multicolor carbon nanotube fluorescence from quantum defects. *ACS Nano* **14,** 715–723 (2020).

261. Maeda, Y., Takehana, Y., Yamada, M., Suzuki, M. & Murakami, T. Control of the photoluminescence properties of single-walled carbon nanotubes by alkylation and subsequent thermal treatment. *Chem. Commun.* **51,** 13462–13465 (2015).

262. He, X., Kevlishvili, I., Murcek, K., Liu, P. & Star, A. [$2\pi + 2\pi$] photocycloaddition of enones to single-walled carbon nanotubes creates fluorescent quantum defects. *ACS Nano* **15,** 4833–4844 (2021).

263. Kwon, H. *et al.* Optical probing of local pH and temperature in complex fluids with covalently functionalized, semiconducting carbon nanotubes. *J. Phys. Chem. C* **119,** 3733–3739 (2015).

264. Kim, M. *et al.* Nanosensor-based monitoring of autophagy-associated lysosomal acidification *in vivo*. *Nat. Chem. Biol.* **19,** 1448–1457 (2023).

265. Spreinat, A. *et al.* Quantum defects in fluorescent carbon nanotubes for sensing and mechanistic studies. *J. Phys. Chem. C* **125,** 18341–18351 (2021).

266. Settele, S. *et al.* Ratiometric fluorescent sensing of pyrophosphate with sp^3-functionalized single-walled carbon nanotubes. *Nat. Commun.* **15,** 706 (2024).

267. Ma, C. *et al.* Ratiometric imaging of catecholamine neurotransmitters with nanosensors. *Nano Lett.* **24,** 2400–2407 (2024).

268. Kim, M. *et al.* Quantum defect sensitization *via* phase-changing supercharged antibody fragments. *J. Am. Chem. Soc.* **146,** 12454–12462 (2024).

269. Kim, M. *et al.* Detection of ovarian cancer *via* the spectral fingerprinting of quantum-defect-modified carbon nanotubes in serum by machine learning. *Nat. Biomed. Eng.* **6,** 267–275 (2022).

270. Dyke, C. A., Stewart, M. P., Maya, F. & Tour, J. M. Diazonium-based functionalization of carbon nanotubes: XPS and GC-MS analysis and mechanistic implications. *Synlett* **1,** 155–160 (2004).

271. Usrey, M. L., Lippmann, E. S. & Strano, M. S. Evidence for a two-step mechanism in electronically selective single-walled carbon nanotube reactions. *J. Am. Chem. Soc.* **127,** 16129–16135 (2005).

272. Nair, N., Kim, W.-J., Usrey, M. L. & Strano, M. S. A structure-reactivity relationship for single walled carbon nanotubes reacting with 4-hydroxybenzene diazonium salt. *J. Am. Chem. Soc.* **129,** 3946–3954 (2007).

273. Schmidt, G., Gallon, S., Esnouf, S., Bourgoin, J.-P. & Chenevier, P. Mechanism of the coupling of diazonium to single-walled carbon nanotubes and its consequences. *Chem. Eur. J.* **15,** 2101–2110 (2009).

274. Gomberg, M. & Bachmann, W. E. The synthesis of biaryl compounds by means of the diazo reaction. *J. Am. Chem. Soc.* **46,** 2339–2343 (1924).

275. Powell, L. R., Piao, Y. & Wang, Y. Optical excitation of carbon nanotubes drives localized diazonium reactions. *J. Phys. Chem. Lett.* **7,** 3690–3694 (2016).

276. Powell, L. R., Kim, M. & Wang, Y. Chirality-selective functionalization of semiconducting carbon nanotubes with a reactivity-switchable molecule. *J. Am. Chem. Soc.* **139,** 12533–12540 (2017).

277. Mann, F. A., Galonska, P., Herrmann, N. & Kruss, S. Quantum defects as versatile anchors for carbon nanotube functionalization. *Nat. Protoc.* **17,** 727–747 (2022).

278. Zhang, Y. *et al.* Propagative sidewall alkylcarboxylation that induces red-shifted near-IR photoluminescence in single-walled carbon nanotubes. *J. Phys. Chem. Lett.* **4,** 826–830 (2013).

279. Gebhardt, B. *et al.* Carbon nanotube sidewall functionalization with carbonyl compounds-modified Birch conditions *vs* the organometallic reduction approach. *J. Am. Chem. Soc.* **133,** 7985–7995 (2011).

280. Zhang, K. S. *et al.* Overcoming catalyst residue inhibition of the functionalization of single-walled carbon nanotubes *via* the Billups-Birch reduction. *ACS Appl. Mater. Interfaces* **9,** 37972–37980 (2017).

281. Liang, F. *et al.* A convenient route to functionalized carbon nanotubes. *Nano Lett.* **4,** 1257–1260 (2004).

282. Deng, S. *et al.* Confined propagation of covalent chemical reactions on single-walled carbon nanotubes. *Nat. Commun.* **2,** 382 (2011).

283. Maeda, Y. *et al.* Selective emergence of photoluminescence at telecommunication wavelengths from cyclic perfluoroalkylated carbon nanotubes. *Commun. Chem.* **6,** 159 (2023).

284. Setaro, A. *et al.* Preserving π-conjugation in covalently functionalized carbon nanotubes for optoelectronic applications. *Nat. Commun.* **8,** 14281 (2017).

285. Zheng, Y., Bachilo, S. M. & Weisman, R. B. Controlled patterning of carbon nanotube energy levels by covalent DNA functionalization. *ACS Nano* **13,** 8222–8228 (2019).

286. Alizadehmojarad, A. A., Bachilo, S. M. & Weisman, R. B. Guanine functionalization of single-wall carbon nanotubes: A quantum chemical study. *ACS Nano* **19,** 21038–21045 (2025).

287. Lin, C.-W. *et al.* Creating fluorescent quantum defects in carbon nanotubes using hypochlorite and light. *Nat. Commun.* **10,** 2874 (2019).

288. Chiu, C. F., Saidi, W. A., Kagan, V. E. & Star, A. Defect-induced near-infrared photoluminescence of single-walled carbon nanotubes treated with polyunsaturated fatty acids. *J. Am. Chem. Soc.* **139,** 4859–4865 (2017).

289. Espinoza, V. B., Bachilo, S. M., Zheng, Y., Htoon, H. & Weisman, R. B. Complexity in the photofunctionalization of single-wall carbon nanotubes with hypochlorite. *ACS Nano* **19,** 2497–2506 (2025).

290. Ma, X., Baldwin, J. K. S., Hartmann, N. F., Doorn, S. K. & Htoon, H. Solid-state approach for fabrication of photostable, oxygen-doped carbon nanotubes. *Adv. Funct. Mater.* **25,** 6157–6164 (2015).

291. Wieland, S., El Yumin, A. A., Settele, S. & Zaumseil, J. Photo-activated, solid-state introduction of luminescent oxygen defects into semiconducting single-walled carbon nanotubes. *J. Phys. Chem. C* **128,** 2012–2021 (2024).

292. Yim, W.-L. & Johnson, J. K. Ozone oxidation of single walled carbon nanotubes from density functional theory. *J. Phys. Chem. C* **113,** 17636–17642 (2009).

293. Eremin, T., Eremina, V., Svirko, Y. & Obraztsov, P. Over two-fold photoluminescence enhancement from single-walled carbon nanotubes induced by oxygen doping. *Nanomaterials* **13,** 1561 (2023).

294. Simmons, J. M. *et al.* Effect of ozone oxidation on single-walled carbon nanotubes. *J. Phys. Chem. B* **110,** 7113–7118 (2006).

295. Li, Y. *et al.* Fluorescent ultrashort nanotubes from defect-induced chemical cutting. *Chem. Mater.* **31,** 4536–4544 (2019).

296. Yang, M. *et al.* Rapid room temperature degradation of carbon nanotubes by sodium hypochlorite and UV-light irradiation. *Carbon* **208,** 238–246 (2023).

297. Dresselhaus, M. S., Dresselhaus, G., Saito, R. & Jorio, A. Raman spectroscopy of carbon nanotubes. *Phys. Rep.* **409,** 47–99 (2005).

298. Wolverson, D., Crampin, S., Kazemi, A. S., Ilie, A. & Bending, S. J. Raman spectra of monolayer, few-layer, and bulk $ReSe_2$: An anisotropic layered semiconductor. *ACS Nano* **8,** 11154–11164 (2014).

299. Zhang, X., Tan, Q.-H., Wu, J.-B., Shi, W. & Tan, P.-H. Review on the Raman spectroscopy of different types of layered materials. *Nanoscale* **8,** 6435–6450 (2016).

300. Jorio, A. & Saito, R. Raman spectroscopy for carbon nanotube applications. *J. Appl. Phys.* **129,** 021102 (2021).

301. Jorio, A. *et al.* Structural (n,m) determination of isolated single-wall carbon nanotubes by resonant Raman scattering. *Phys. Rev. Lett.* **86,** 1118–1121 (2001).

302. Dresselhaus, M. S., Dresselhaus, G., Jorio, A., Souza, A. G. & Saito, R. Raman spectroscopy on isolated single wall carbon nanotubes. *Carbon* **40,** 2043–2061 (2002).

303. Dresselhaus, M. S., Jorio, A. & Saito, R. Characterizing graphene, graphite, and carbon nanotubes by Raman spectroscopy. *Ann. Rev. Condens. Matter Phys.* **1,** 89–108 (2010).

304. Araujo, P. T. *et al.* Phonon self-energy corrections to nonzero wave-vector phonon modes in single-layer graphene. *Phys. Rev. Lett.* **109,** 046801 (2012).

305. Samsonidze, G. G. *et al.* Electron-phonon coupling mechanism in two-dimensional graphite and single-wall carbon nanotubes. *Phys. Rev. B* **75,** 155420 (2007).

306. Finnie, P., Ouyang, J. & Fagan, J. A. Broadband full-spectrum Raman excitation mapping reveals intricate optoelectronic-vibrational resonance structure of chirality-pure single-walled carbon nanotubes. *ACS Nano* **17,** 7285–7295 (2023).

307. Jorio, A. *et al.* Resonance Raman spectra of carbon nanotubes by cross-polarized light. *Phys. Rev. Lett.* **90,** 107403 (2003).

308. Souza, M. *et al.* Single- and double-resonance Raman G-band processes in carbon nanotubes. *Phys. Rev. B* **69,** 241403 (2004).

309. Reich, S., Thomsen, C. & Ordejón, P. Phonon eigenvectors of chiral nanotubes. *Phys. Rev. B* **64,** 195416 (2001).

310. Jorio, A. *et al.* Polarized Raman study of single-wall semiconducting carbon nanotubes. *Phys. Rev. Lett.* **85,** 2617–2620 (2000).

311. Telg, H. *et al.* Chiral index dependence of the G^+ and G^- Raman modes in semiconducting carbon nanotubes. *ACS Nano* **6,** 904–911 (2012).

312. Brown, S. D. M. *et al.* Origin of the Breit-Wigner-Fano lineshape of the tangential G-band feature of metallic carbon nanotubes. *Phys. Rev. B* **63,** 155414 (2001).

313. Jorio, A. *et al.* Characterizing carbon nanotube samples with resonance Raman scattering. *New J. Phys.* **5,** 139 (2003).

314. Grimm, S. *et al.* Doping-dependent G-mode shifts of small diameter semiconducting single-walled carbon nanotubes. *Carbon* **118,** 261–267 (2017).

315. Xu, J.-L. *et al.* Efficient and reversible electron doping of semiconductor-enriched single-walled carbon nanotubes by using decamethylcobaltocene. *Sci. Rep.* **7,** 6751 (2017).

316. Fantini, C. *et al.* Optical transition energies for carbon nanotubes from resonant Raman spectroscopy: Environment and temperature effects. *Phys. Rev. Lett.* **93,** 147406 (2004).

317. Uchida, T., Tazawa, M., Sakai, H., Yamazaki, A. & Kobayashi, Y. Radial breathing modes of single-walled carbon nanotubes in resonance Raman spectra at high temperature and their chiral index assignment. *Appl. Surf. Sci.* **254,** 7591–7595 (2008).

318. Mahan, G. D. Oscillations of a thin hollow cylinder: Carbon nanotubes. *Phys. Rev. B* **65,** 235402 (2002).

319. Araujo, P. T. *et al.* Nature of the constant factor in the relation between radial breathing mode frequency and tube diameter for single-wall carbon nanotubes. *Phys. Rev. B* **77,** 241403 (2008).

320. Araujo, P. T., Fantini, C., Lucchese, M. M., Dresselhaus, M. S. & Jorio, A. The effect of environment on the radial breathing mode of supergrowth single wall carbon nanotubes. *Appl. Phys. Lett.* **95,** 261902 (2009).

321. Dresselhaus, M. S., Jorio, A., Hofmann, M., Dresselhaus, G. & Saito, R. Perspectives on carbon nanotubes and graphene Raman spectroscopy. *Nano Lett.* **10,** 751–758 (2010).

322. Piao, Y. *et al.* Intensity ratio of resonant Raman modes for (n,m) enriched semiconducting carbon nanotubes. *ACS Nano* **10,** 5252–5259 (2016).

323. Souza Filho, A. G. *et al.* Effect of quantized electronic states on the dispersive Raman features in individual single-wall carbon nanotubes. *Phys. Rev. B* **65,** 035404 (2001).

324. Souza Filho, A. G. *et al.* Anomalous two-peak G'-band Raman effect in one isolated single-wall carbon nanotube. *Phys. Rev. B* **65,** 085417 (2002).

325. Souza Filho, A. G. *et al.* Competing spring constant versus double resonance effects on the properties of dispersive modes in isolated single-wall carbon nanotubes. *Phys. Rev. B* **67,** 035427 (2003).

326. Samsonidze, G. G. *et al.* Phonon trigonal warping effect in graphite and carbon nanotubes. *Phys. Rev. Lett.* **90,** 027403 (2003).

327. Saito, R. *et al.* Probing phonon dispersion relations of graphite by double resonance Raman scattering. *Phys. Rev. Lett.* **88,** 027401 (2002).

328. Cronin, S. B. *et al.* Resonant Raman spectroscopy of individual metallic and semiconducting single-wall carbon nanotubes under uniaxial strain. *Phys. Rev. B* **72,** 035425 (2005).

329. Maciel, I. O. *et al.* Electron and phonon renormalization near charged defects in carbon nanotubes. *Nat. Mater.* **7,** 878–883 (2008).

330. Maultzsch, J., Reich, S. & Thomsen, C. Chirality-selective Raman scattering of the D mode in carbon nanotubes. *Phys. Rev. B* **64,** 121407 (2001).

331. Pimenta, M. A. *et al.* Studying disorder in graphite-based systems by Raman spectroscopy. *Phys. Chem. Chem. Phys.* **9,** 1276–1291 (2007).

332. Graupner, R. Raman spectroscopy of covalently functionalized single-wall carbon nanotubes. *J. Raman Spectrosc.* **38,** 673–683 (2007).

333. Laudenbach, J., Hennrich, F., Telg, H., Kappes, M. & Maultzsch, J. Resonance behavior of the defect-induced Raman mode of single-chirality enriched carbon nanotubes. *Phys. Rev. B* **87,** 165423 (2013).

334. Pimenta, M. A. *et al.* Diameter dependence of the Raman D-band in isolated single-wall carbon nanotubes. *Phys. Rev. B* **64,** 041401 (2001).

335. Herziger, F., Vierck, A., Laudenbach, J. & Maultzsch, J. Understanding double-resonant Raman scattering in chiral carbon nanotubes: Diameter and energy dependence of the D mode. *Phys. Rev. B* **92,** 235409 (2015).

336. Laudenbach, J. *et al.* Diameter dependence of the defect-induced Raman modes in functionalized carbon nanotubes. *Carbon* **112,** 1–7 (2017).

337. Zólyomi, V., Kürti, J., Grüneis, A. & Kuzmany, H. Origin of the fine structure of the Raman D band in single-wall carbon nanotubes. *Phys. Rev. Lett.* **90,** 157401 (2003).

338. Tyborski, C., Herziger, F. & Maultzsch, J. Raman spectroscopy of nondispersive intermediate frequency modes and their overtones in carbon nanotubes. *Phys. Status Solidi B* **252,** 2551–2557 (2015).

339. Saito, R., Takeya, T., Kimura, T., Dresselhaus, G. & Dresselhaus, M. S. Finite-size effect on the Raman spectra of carbon nanotubes. *Phys. Rev. B* **59,** 2388–2392 (1999).

340. Fantini, C. *et al.* One-dimensional character of combination modes in the resonance Raman scattering of carbon nanotubes. *Phys. Rev. Lett.* **93,** 087401 (2004).

341. Fantini, C. *et al.* Steplike dispersion of the intermediate-frequency Raman modes in semiconducting and metallic carbon nanotubes. *Phys. Rev. B* **72,** 085446 (2005).

342. Luo, Z. T., Papadimitrakopoulos, F. & Doorn, S. K. Intermediate-frequency Raman modes for the lower optical transitions of semiconducting single-walled carbon nanotubes. *Phys. Rev. B* **75,** 205438 (2007).

343. Skákalová, V., Maultzsch, J., Osváth, Z., Biró, L. P. & Roth, S. Intermediate frequency modes in Raman spectra of Ar^+-irradiated single-wall carbon nanotubes. *Phys. Status Solidi RRL* **1,** 138–140 (2007).

344. Singh, D. K., Iyer, P. K. & Giri, P. K. Distinguishing defect induced intermediate frequency modes from combination modes in the Raman spectrum of single walled carbon nanotubes. *J. Appl. Phys.* **111,** 064304 (2012).

345. Vierck, A., Gannott, F., Schweiger, M., Zaumseil, J. & Maultzsch, J. ZA-derived phonons in the Raman spectra of single-walled carbon nanotubes. *Carbon* **117,** 360–366 (2017).

346. Lucchese, M. M. *et al.* Quantifying ion-induced defects and Raman relaxation length in graphene. *Carbon* **48,** 1592–1597 (2010).

347. Cançado, L. G. *et al.* Quantifying defects in graphene *via* Raman spectroscopy at different excitation energies. *Nano Lett.* **11,** 3190–3196 (2011).

348. Venezuela, P., Lazzeri, M. & Mauri, F. Theory of double-resonant Raman spectra in graphene: Intensity and line shape of defect-induced and two-phonon bands. *Phys. Rev. B* **84,** 035433 (2011).

349. Eckmann, A. *et al.* Probing the nature of defects in graphene by Raman spectroscopy. *Nano Lett.* **12,** 3925–3930 (2012).

350. Englert, J. M. *et al.* Scanning-Raman-microscopy for the statistical analysis of covalently functionalized graphene. *ACS Nano* **7,** 5472–5482 (2013).

351. Ferrari, A. C. & Basko, D. M. Raman spectroscopy as a versatile tool for studying the properties of graphene. *Nat. Nanotechnol.* **8,** 235–246 (2013).

352. Beams, R., Cançado, L. G. & Novotny, L. Raman characterization of defects and dopants in graphene. *J. Phys. Condens. Matter* **27,** 083002 (2015).

353. Cançado, L. G. *et al.* Disentangling contributions of point and line defects in the Raman spectra of graphene-related materials. *2D Mater.* **4,** 025039 (2017).

354. Turner, P. *et al.* International interlaboratory comparison of Raman spectroscopic analysis of CVD-grown graphene. *2D Mater.* **9,** 035010 (2022).

355. Hennrich, F. *et al.* Raman spectroscopy of individual single-walled carbon nanotubes from various sources. *J. Phys. Chem. B* **109,** 10567–10573 (2005).

356. Dillon, A. C. *et al.* Systematic inclusion of defects in pure carbon single-wall nanotubes and their effect on the Raman D-band. *Chem. Phys. Lett.* **401,** 522–528 (2005).

357. Anderson, N., Hartschuh, A. & Novotny, L. Chirality changes in carbon nanotubes studied with near-field Raman spectroscopy. *Nano Lett.* **7,** 577–582 (2007).

358. Simpson, J. R., Fagan, J. A., Becker, M. L., Hobbie, E. K. & Walker, A. R. H. The effect of dispersant on defects in length-separated single-wall carbon nanotubes measured by Raman spectroscopy. *Carbon* **47,** 3238–3241 (2009).

359. Miyata, Y., Mizuno, K. & Kataura, H. Purity and defect characterization of single-wall carbon nanotubes using Raman spectroscopy. *J. Nanomater.* **2011,** 786763 (2011).

360. Kalbac, M. *et al.* Defects in individual semiconducting single wall carbon nanotubes: Raman spectroscopic and *in situ* Raman spectroelectrochemical study. *Nano Lett.* **10,** 4619–4626 (2010).

361. Georgi, C. & Hartschuh, A. Tip-enhanced Raman spectroscopic imaging of localized defects in carbon nanotubes. *Appl. Phys. Lett.* **97,** 143117 (2010).

362. Hofmann, M. S. *et al.* Bright, long-lived and coherent excitons in carbon nanotube quantum dots. *Nat. Nanotechnol.* **8,** 502–505 (2013).

363. Zheng, W., Zorn, N. F., Bonn, M., Zaumseil, J. & Wang, H. I. Probing carrier dynamics in sp^3-functionalized single-walled carbon nanotubes with time-resolved terahertz spectroscopy. *ACS Nano* **16,** 9401–9409 (2022).

364. Sander, M., Metternich, J. T., Dippner, P., Kruss, S. & Borchardt, L. Controlled introduction of sp^3 quantum defects in fluorescent carbon nanotubes by mechanochemistry. *Angew. Chem. Int. Ed.* **64,** e202421021 (2025).

365. Townsend, W. J. V. *et al.* The role of carbon catalyst coatings in the electrochemical water splitting reaction. *Nat. Commun.* **16,** 4460 (2025).

366. Finnie, P., Ouyang, J. & Fagan, J. A. Static and dynamic Raman excitation mapping of chirality-pure carbon nanotube films. *Commun. Mater.* **6,** 10 (2025).

367. Li, M.-K. *et al.* Electroluminescence from single-walled carbon nanotubes with quantum defects. *ACS Nano* **16,** 11742–11754 (2022).

368. Ishii, A. *et al.* Enhanced single-photon emission from carbon-nanotube dopant states coupled to silicon microcavities. *Nano Lett.* **18,** 3873–3878 (2018).

369. Luo, Y. *et al.* Carbon nanotube color centers in plasmonic nanocavities: A path to photon indistinguishability at telecom bands. *Nano Lett.* **19,** 9037–9044 (2019).

370. Basu, S., Hendler-Neumark, A. & Bisker, G. Ratiometric normalization of near-infrared fluorescence in defect-engineered single-walled carbon nanotubes for cholesterol detection. *J. Phys. Chem. Lett.* **15,** 10425–10434 (2024).

371. Parvez, K. *et al.* Exfoliation of graphite into graphene in aqueous solutions of inorganic salts. *J. Am. Chem. Soc.* **136,** 6083–6091 (2014).

372. Cançado, L. G. *et al.* Science and metrology of defects in graphene using Raman spectroscopy. *Carbon* **220,** 118801 (2024).

373. Pan, Y. *et al.* Triphenylphosphine oxide: A versatile covalent functionality for carbon nanotubes. *Angew. Chem. Int. Ed.* **63,** e202412084 (2024).

374. Park, S., Vosguerichian, M. & Bao, Z. A review of fabrication and applications of carbon nanotube film-based flexible electronics. *Nanoscale* **5,** 1727–1752 (2013).

375. Fan, Y., Goldsmith, B. R. & Collins, P. G. Identifying and counting point defects in carbon nanotubes. *Nat. Mater.* **4,** 906–911 (2005).

376. Cai, L. & Wang, C. Carbon nanotube flexible and stretchable electronics. *Nanoscale Res. Lett.* **10,** 1013 (2015).

377. Shiraki, T., Onitsuka, H., Shiraishi, T. & Nakashima, N. Near infrared photoluminescence modulation of single-walled carbon nanotubes based on a molecular recognition approach. *Chem. Commun.* **52,** 12972–12975 (2016).

378. Onitsuka, H., Fujigaya, T., Nakashima, N. & Shiraki, T. Control of the near infrared photoluminescence of locally functionalized single-walled carbon nanotubes *via* doping by azacrown-ether modification. *Chem. Eur. J.* **24,** 9393–9398 (2018).

379. Liu, F. *et al.* Viscosity sensitive near-infrared fluorescent probes based on functionalized single-walled carbon nanotubes. *Chem. Commun.* **56,** 8301–8304 (2020).

380. Giraldo, J. P. & Kruss, S. Nanosensors for monitoring plant health. *Nat. Nanotechnol.* **18,** 107–108 (2023).

381. Basu, S., Hendler-Neumark, A. & Bisker, G. Role of oxygen defects in eliciting a divergent fluorescence response of single-walled carbon nanotubes to dopamine and serotonin. *ACS Nano* **18,** 34134–34146 (2024).

382. Sercel, P. C., Hautzinger, M. P., Song, R., Blum, V. & Beard, M. C. Optical activity of chiral excitons. *Adv. Mater.* **37,** e2415901 (2025).

383. Zorn, N. F., Settele, S., Sebastian, F. L., Lindenthal, S. & Zaumseil, J. Tuning electroluminescence from functionalized SWCNT networks further into the near-infrared. *ACS Appl. Opt. Mater.* **1,** 1706–1714 (2023).

384. Chen, J.-S. *et al.* Long-lived electronic spin qubits in single-walled carbon nanotubes. *Nat. Commun.* **14,** 848 (2023).

385. Arrico, L., Di Bari, L. & Zinna, F. Quantifying the overall efficiency of circularly polarized emitters. *Chem. Eur. J.* **27,** 2920–2934 (2021).

386. Baguenard, B. *et al.* Theoretical and experimental analysis of circularly polarized luminescence spectrophotometers for artifact-free measurements using a single CCD camera. *Nat. Commun.* **14,** 1065 (2023).

Eidesstattliche Versicherung

Eidesstattliche Versicherung gemäß §8 der Promotionsordnung für die Gesamtfakultät für Mathematik, Ingenieurs- und Naturwissenschaften der Universität Heidelberg

1. Bei der eingereichten Dissertation zu dem Thema "Raman and Chiroptical Spectroscopy of Carbon Nanotubes with Luminescent Defects" handelt es sich um meine eigenständig erbrachte Leistung.

2. Ich habe nur die angegebenen Quellen und Hilfsmittel (inkl. KI-basierter Hilfsmittel) benutzt und mich keiner unzulässigen Hilfe Dritter bedient. Insbesondere habe ich wörtlich oder sinngemäß aus anderen Werken übernommene Inhalte als solche kenntlich gemacht.

3. Die Arbeit oder Teile davon habe ich bislang nicht an einer Hochschule des In- oder Auslands als Bestandteil einer Prüfungs- oder Qualifikationsleistung vorgelegt.

4. Die Richtigkeit der vorstehenden Erklärungen bestätige ich.

5. Die Bedeutung der eidesstattlichen Versicherung und die strafrechtlichen Folgen einer unrichtigen oder unvollständigen eidesstattlichen Versicherung sind mir bekannt.

Ich versichere an Eides statt, dass ich nach bestem Wissen die reine Wahrheit erklärt und nichts verschwiegen habe.

Heidelberg, 01.09.2025

_____

Finn Luca Sebastian